UNIVERSITÀ DELLA CALABRIA

Università della Calabria
Dipartimento di Fisica

Dottorato di Ricerca in
Scienze e Tecnologie Fisiche, Chimiche e dei Materiali

CICLO
XXXV

Nonlinear processes in general relativity: from vacuum spacetimes to turbulent plasmas near compact objects

Settore Scientifico Disciplinare FIS/05

Coordinatore: Ch.ma Prof.ssa Gabriella Cipparrone

Firma oscurata in base alle linee
guida del Garante della privacy

Supervisore: Ch.mo Prof. Sergio Servidio

Firma oscurata in base alle linee
guida del Garante della privacy
[redacted]

Dottorando: Dott. Claudio Meringolo

Firma oscurata in base alle linee
guida del Garante della privacy
[redacted]

Turbulent Starry Night at Unical

Abstract

Strong gravitational fields are well-described by Einstein's theory of gravity. In the last decades, observational breakthroughs have supported the milestones of general relativity, stimulating increasing scientific activity. Together with observations, numerical relativity became a very important instrument to validate and extend the comprehension of such observations.

In the first part of this thesis, we present new results through the full three-dimensional (3D) evolution of black holes, in binary- and multiple-body systems. After a brief review of Einstein's theory and of the "3+1" formalism adopted, we describe the Spectral FIltered Numerical Gravity CodE (`SFINGE`). This is a numerical code based on the Fourier decomposition, accompanied by different filtering techniques. The accuracy of the model has been validated through standard testbeds, revealing that the filtered pseudo-spectral technique is highly accurate. We evolve black hole dynamics in vacuum conditions and small domains. The gravitational wave signals have been inspected by employing both Fourier and wavelet analyses, showing net differences among the global configurations. We observe strong nonlinear emission in the case of three-black holes, which can be a template for future observational campaigns. Finally, we introduced also the presence of matter in spacetime, presenting some preliminary results of general relativistic hydrodynamics.

In the second part of the thesis, we focus on the plasma in the neighboring regions of black holes, by using numerical models for plasmas in trans-relativistic regimes. We present a very comprehensive campaign of two-dimensional (2D) kinetic Particle-In-Cell (PIC) simulations of special-relativistic turbulence by using the `Zeltron` code. Imposing a realistic mass ratio between electrons and protons, we analyze the energization of electrons, by varying several plasma parameters. The simulations have been designed to cover several regimes of turbulence in the vicinity of compact objects. These results can find application in a wide range of astrophysical scenarios, including the accretion and the jet emission onto supermassive black holes, such as M87* and Sgr A*.

Contents

List of Figures

List of Tables

List of Abbreviations and Acronyms

BH	**B**lack **H**ole
GW	**G**ravitational **W**ave
EHT	**E**vent **H**orizon **T**elescope
VLBI	**V**ery **L**ong **B**aseline **I**nterferometry
GMVA	**G**lobal **M**illimiter **V**LBI **A**rray
ADM	**A**rnowit **D**eser **M**isner
BSSN	**B**aumarte **S**hapiro **S**hibata **N**akamura
BSSNOK	**B**aumarte **S**hapiro **S**hibata **N**akamura **O**ohara **K**ojima
HD	**H**ydro**D**inamics
MHD	**M**agneto**H**ydro**D**inamics
GRHD	**G**eneral **R**elativistic **H**ydro**D**inamics
GRMHD	**G**eneral **R**elativistic **M**agneto**H**ydro**D**inamics
CFL	**C**ourant **F**riedrichs **L**ewy
FFT	**F**ast **F**ourier **T**ransform
IHB	**I**mplicit **H**yperviscous **B**oundary
RSC	**R**unning **S**tability **C**heck
ISCO	**I**nnermost **S**table **C**ircular **O**rbit
MAD	**M**agnetically **A**rrested **D**isk
GRRT	**G**eneral **R**elativistic **R**adiative **T**ransfer
PIC	**P**article **I**n **C**ell
`SFINGE`	**S**pectral **FI**ltered **N**umerical **G**ravity cod**E**
`BHAC`	**B**lach **H**ole **A**ccretion **C**ode
`BHOSS`	**B**lack **H**ole **O**bservations in **S**tationary **S**pacetimes

Physical Constants

FUNDAMENTAL CONSTANTS

Speed of Light	$c \simeq 2.997 \times 10^{10}\,\mathrm{cm\,s^{-1}}$
Boltzamm constant	$k_B \simeq 1.381 \times 10^{-16}\,(\mathrm{erg\,K^{-1}} = \mathrm{g\,cm^2\,s^{-2}\,K^{-1}})$
Planck's constant	$h \simeq 6.626 \times 10^{-27}\,(\mathrm{cm^2\,g\,s} = \mathrm{erg\,s})$
Reduced Planck's constant	$\hbar \simeq 1.055 \times 10^{-27}\,(\mathrm{cm^2\,g\,s} = \mathrm{erg\,s})$
Gravitational constant	$G \simeq 6.674 \times 10^{-8}\,\mathrm{cm^3\,g^{-1}\,s^{-2}}$
Electron mass	$m_e \simeq 9.109 \times 10^{-28}\,\mathrm{g}$
Proton mass	$m_p \simeq 1.673 \times 10^{-24}\,\mathrm{g}$
Neutron mass	$m_n \simeq 1.675 \times 10^{-24}\,\mathrm{g}$
Electron charge	$e \simeq 4.805 \times 10^{-10}\,\mathrm{statC}$

ASTRONOMICAL CONSTANTS

astronomical unit	$1\,\mathrm{A.U.} \simeq 1.5 \times 10^{13}\,\mathrm{cm}$
light year	$1\,ly \simeq 9.46 \times 10^{17}\mathrm{cm} \simeq 6.3 \times 10^{4}\,\mathrm{A.U.}$
parsec	$1\,pc \simeq 3.26\,ly \simeq 2.06 \times 10^{5}\mathrm{A.U.} \simeq 3.09 \times 10^{18}\,\mathrm{cm}$
Sun	
mass	$M_\odot \simeq 1.989 \times 10^{33}\,\mathrm{g}$
radius	$R_\odot \simeq 6.963 \times 10^{10}\,\mathrm{cm}$
surface gravity	$g_\odot \simeq 2.741 \times 10^{4}\,\mathrm{cm\,s^{-2}}$
Earth	
mass	$M_\oplus \simeq 5.972 \times 10^{27}\,\mathrm{g}$
equatorial radius	$R_\oplus^E \simeq 6.378 \times 10^{8}\,\mathrm{cm}$
polar radius	$R_\oplus^P \simeq 6.356 \times 10^{8}\,\mathrm{cm}$
surface gravity	$g_\oplus \simeq 9.806 \times 10^{2}\,\mathrm{cm\,s^{-2}}$
Sagittarius A*	
mass	$M_{A*} \simeq 4.1 \times 10^{6} M_\odot \simeq 8.155 \times 10^{33}\,\mathrm{g}$
radius	$R_{A*} \simeq 18.7\,R_\odot \simeq 1.3 \times 10^{12}\,\mathrm{cm}$

surface gravity	$g_{A^*} \simeq 3.3 \times 10^7 \, g_{\oplus} \simeq 3.3 \times 10^8 \, \mathrm{cm\,s^{-2}}$
mean distance from Sun	$d_{\odot,A^*} \simeq 2.6 \times 10^4 \, \mathrm{ly} \simeq \ 2.5 \times 10^{22} \ \mathrm{cm}$

M87

mass	$M_{M87} \simeq 6.6 \times 10^9 M_{\odot} \simeq 1.32 \times 10^{43} \ \mathrm{g}$
radius	$R_{M87} \simeq 2.6 \times 10^4 \, R_{\odot} \simeq 1.8 \times 10^{12} \, \mathrm{cm}$
surface gravity	$g_{M87} \simeq 3.3 \times 10^7 \, g_{\oplus} \simeq 3.3 \times 10^8 \, \mathrm{cm\,s^{-2}}$
mean distance from Sun	$d_{\odot,M87} \simeq 5.5 \times 10^7 \, ly \simeq \ 5.2 \times 10^{25} \ \mathrm{cm}$

Notation and conventions

Throughout this thesis, we will use the so-called *geometric units*, in which the speed of light c and Newton's gravitational constant G are taken to be equal to one. In geometric units, all physical quantities have dimensions of length to some power. In particular, time will be measured in meters: a meter of time being equal to the time it takes light to travel one meter. Mass will also be measured in meters: a meter of mass is equal to the mass of a point particle that in Newton's theory has an escape velocity equal to the speed of light at a distance of two meters. (The reason for using two meters instead of one comes from the factor 2 in the expression for the kinetic energy $E_K = mv^2/2$). In these units, a meter of time is $\simeq 3 \times 10^{-9}$ seconds, and a meter of mass is $\simeq 1.3 \times 10^{27}$ kilograms, i.e. roughly 200 times the mass of the Earth. So, the mass of the Earth is about half a centimeter and the mass of the Sun is about one and a half kilometers. We will also adopt Einstein's summation rule: unless otherwise stated, repeated indices are summed over all their possible values. An example is: $A_k A^k = \sum_k A_k A^k = A_1 A^1 + A_2 A^2 + A_3 A^3 + ... + A_n A^n$, where n is the space dimension of A_k. We will display a tensor in spacetime by a symbol in boldface when emphasizing its coordinate-free character, or by its components when the tensor has been expanded in a particular set of basis tensors.

As follows, we present, in a more schematic way, the basic conventions used.

Signature

We will use the conventions of Misner, Thorne, and Wheeler (Misner, Thorne, and Wheeler, 1973) for the metric signature together with all the sign conventions. In particular, the signature of the Minkowski 4-metric will be taken to be:

$$\eta_{\mu\nu} = \begin{pmatrix} -1 & 0 & 0 & 0 \\ 0 & +1 & 0 & 0 \\ 0 & 0 & +1 & 0 \\ 0 & 0 & 0 & +1 \end{pmatrix}.$$

Objects in four-dimensional spacetime

Greek indices $(\mu, \nu, \rho, \sigma, ...)$ refer to four-dimensional spacetime and can take values from 0 to 3, with 0 indicating the time variable, while the other refers to spatial, Cartesian coordinates:

- The 4-metric tensor is $g_{\mu\nu}$ which depends on the four-vector $x^\mu = (t, x, y, z)$;
- The proper distance is $ds^2 = \eta_{\mu\nu}\, dx^\mu dx^\nu = -dt^2 + dx^2 + dy^2 + dz^2$;
- Covariant derivatives along x^μ are defined as ∇_μ.

Objects in three-dimensional space

Latin indices $(i, j, k, l, ...)$ refer to three-dimensional space and take values from 1 to 3:

- The 3-metric tensor is γ_{ij}, the three-vector $x^i = (x, y, z)$;
- The proper distance is $dl^2 = \eta_{ij}\, dx^i dx^j = dx^2 + dy^2 + dz^2$;
- Covariant spatial derivatives along x^i are defined as D_i;
- Partial derivatives along x^i are defined in both cases as $\partial_i = \dfrac{\partial}{\partial x^i}$.

Indices symmetries

- The symmetric part of a tensor $T_{\mu\nu}$ is defined as $T_{(\mu\nu)} = \frac{1}{2}(T_{\mu\nu} + T_{\nu\mu})$;
- The antisymmetric part of a tensor $T_{\mu\nu}$ is defined as $T_{[\mu\nu]} = \frac{1}{2}(T_{\mu\nu} - T_{\nu\mu})$.

The above relations are used to simplify notations, for example:

$$T_{\mu\,(\nu}T_{\rho\,)\sigma} = \frac{1}{2}\Big(T_{\mu\nu}\;T_{\rho\sigma} + T_{\mu\rho}\;T_{\nu\sigma}\Big)\,,$$

$$T_{\mu\,[\nu}T_{\rho\,]\sigma} = \frac{1}{2}\Big(T_{\mu\nu}\;T_{\rho\sigma} - T_{\mu\rho}\;T_{\nu\sigma}\Big).$$

Introduction

Massive compact bodies such as black holes and neutron stars represent the most suggestive and extraordinary objects in astrophysics. Their incredible compactness leads to a strong curvature of the spacetime. The real challenge today is the comprehension of the spacetime dynamics whenever such compact bodies interact with each other, especially during their collapsing stage where the evolution is fully non-linear. In these extreme events, the mass of the final object is smaller than the sum of the two separate bodies, and the missing mass is converted into energy via *gravitational waves*, following the Einstein theory. Gravitational waves are only one of the predictions of Einstein's theory of general relativity and give us the possibility to collect several pieces of information that cannot be obtained from direct observations.

The main result of general relativity are the *Einstein's field equations*, ten coupled nonlinear partial differential equations, that relate the curvature of spacetime to the presence of mass-energy. The famous equation reads

$$G_{\mu\nu} = \frac{8\pi G}{c^4} T_{\mu\nu}. \tag{1}$$

Apart from the elegance and compactness, the *take-home* message of the above equation is that the curvature of spacetime (left-hand side) is proportional to the presence of energy-matter (right-hand side)[1]. The proportional constant is extremely small, since one has $G/c^4 \sim 10^{-50}$, and this means that the spacetime is relatively *stiff*[2]. In other words, a large amount of mass-energy – in a relatively small volume – is required to have appreciable curvatures of spacetime.

Since the presence of plasma is ubiquitous in the Universe, it plays a central role in the detection of black holes, otherwise non-emitting objects by definition. The plasma can be captured by the extreme curvature and rotate around supermassive compact objects. And plasma, actually, is what the Event Horizon Telescope Collaboration captured, for the first-ever images of the two supermassive black holes, M87* in April 2019 (Event Horizon Telescope Collaboration et al., 2019a), and Sgr A* in May 2022 (Event Horizon Telescope Collaboration et al., 2022a), captured by the EHT astronomers of four continents who coordinated their efforts.

In order to understand phenomena such as multi-body collisions, production of gravitational waves, and plasma dynamics around black holes, numerical methods are needed. Numerical approaches become very important to modeling and supporting these breakthroughs, helping to improve the comprehension of the Universe. Given the high non-linearity and complexity of Einstein's equations, is necessary to solve them through the use of supercomputers. Many efforts have been dedicated over the last years to modeling the plasma onto supermassive black holes and neutron stars (Font, 2008), and many codes to solve general relativistic magnetohydrodynamic (GRMHD) equations have been developed worldwide. They are worth mentioning, among all, `BHAC` (Porth et al., 2017), `WhiskyMHD` (Giacomazzo and

---

[1] For the purpose of this thesis, in equation (1) we have neglected the cosmological term $\Lambda g_{\mu\nu}$.

[2] Note that the above result holds in CGS units, but in geometric units one has $G/c^4 = 1$.

Rezzolla, 2007), `SpEC` (Szilágyi, 2014), IllinoisGRMHD (Etienne et al., 2015), `GRHydro` (Mösta et al., 2014), CAFE (Lora-Clavijo, Cruz-Osorio, and Guzmán, 2015), `Athena++` (Stone et al., 2008), `ECHO` (Londrillo and Del Zanna, 2000), `H-AMR` (Gammie, McKinney, and Tóth, 2003), and many others. With modern computational resources and due to the intrinsic huge physical dimensions, fluid (global) approaches can describe the entire system.[3] These equations can only describe the thermal (fluid) behavior of the plasma, leaving completely undetermined the non-thermal particle phenomena and the electron scales dynamics. It becomes important, at this point, to support global fluid simulations by local, *kinetic* approaches, in order to capture microphysical plasma dynamics otherwise not modeled.

The thesis is essentially composed of two parts.

In the first part, we focus on the dynamics of a vacuum spacetime, and in a variety of different conditions. We start with a brief overview of general relativity, and we introduce the main concepts of the theory and the recent detections that confirmed Einstein's predictions. Then, we move to the needful numerical treatments of the field equations, namely the Arnowit-Deser-Misner (ADM), and the Baumgarte-Shapiro-Shibata-Nakamura-Oohara-Kojima (BSSNOK) formulation. Here we introduce the "3+1" formulation, in which a foliation of spacetime is employed to overcome the intrinsic coupling between space and time of Einstein formalism. We then present the ADM and the BSSNOK set of equations, that have to be solved together with the constraint prescriptions. To model the field equations (1), we present the Spectral FIltered Numerical Gravity CodE (`SFINGE`), a new numerical algorithm based on a filtered pseudo-spectral scheme, and developed entirely at the University of Calabria. Our code solves the Einstein equations using either the ADM or the BSSNOK formulation, in fully three-dimensional space. The main approach is as follows: products are computed in the physical space, while derivatives are computed in the spectral space via simple and efficient Fast Fourier Transforms (FFTs). The code shows a very low violation of the constraints via standard gravitational testbeds, due to the precision of spectral methods which are high-order accurate.

We introduce a number of techniques to improve the stability of the algorithm, such as the Running Stability Check (RSC), which monitors the strength of the time derivatives and provides an optimal time-step. The Implicit Hyperviscous Boundary (IHB) method, borrowed from fluid and plasma dynamics, is used to model non-periodic problems such as black hole dynamics. In particular, it is able to suppress spurious boundary effects, typical limitations of periodicity in pseudo-spectral, FFT-based methods. In practice, we match the ideal solution in the center of the domain, based on the pseudo-spectral solution equations, with a semi-implicit, second-order Crank-Nicholson technique at the boundaries, where we added hyper-viscous diffusion. We test this strategy via a simple gravitational wavepacket absorption, as well as more challenging singular dynamical spacetimes. We present a detailed analysis of the aliasing instabilities by monitoring, in the complex Fourier space, the behavior of higher harmonics, both for the ADM and BSSNOK variables. Two types of anti-aliasing filters are used, in order to suppress numerical artifacts that are due to the intrinsic nonlinear nature of the governing equations.

We move then to a more realistic and nonlinear scenario, namely the dynamics of multiple BHs collisions. We consider both the evolution of the binary and the three black hole problem, in a number of different initial configurations. We

---

[3] Also other models are being developed, such as pair-plasma, kinetic simulations of accreting supermassive black hole (Parfrey, Philippov, and Cerutti, 2019; Crinquand et al., 2022).

compare the binary merger and the three-body gravitational signals, by computing the Fourier and the Shannon wavelet spectra, revealing net differences between the two- and three-body cases. These results could be of interest for future observational campaigns, in which one can achieve better signal-to-noise sensibility, investigating whether such extreme events might occur and be detected. Finally, we move towards simulations in which the matter is taken into account. In particular, by using our `SFINGE` algorithm, we simulate the propagation of a simple 1D sound wave in a nonlinear regime. We make use of an implicit Crank-Nicolson method and a smoothed filter technique, to handle the correct dynamics and suppress numerical artifacts.

In the second part of the thesis, we start presenting a GRMHD simulation making use of the `BHAC` code (Porth et al., 2017). We evolve a toroidal structure immersed in the equatorial plane of a rotating Kerr black hole, showing that the dynamic of the plasma becomes highly turbulent and leads to large-scale vortexes. Such fluid approaches are widely used to describe astrophysical compact objects, in a number of realistic scenarios, but leave completely unmodeled the nonthermal plasma and the electron scales of the plasma.

With the focus to obtain a deeper understanding of the microphysical properties of accreting black holes, we finally study the plasma in trans-relativistic regimes via kinetic models. To this scope, we briefly introduce the Particle-In-Cell method, in flat geometry and Cartesian coordinates. In particular, we make use of the `Zeltron` code (Cerutti et al., 2013) to carry out a large campaign of 2D simulations of special-relativistic, decaying plasma turbulence. We span over a large portion of the parameter space encountered in astrophysical plasmas. Our goal is to connect the microphysical properties of the plasma with the macrophysical ones. In particular, this campaign of simulations allows us to present 2D fitting functions, relating the electron spectral index, the efficiency in generating nonthermal particles, and the ratio between the electron and proton temperatures, with the magnetization σ and the plasma$-\beta$ parameters. Our work represents a very systematic PIC exploration of trans-relativistic turbulence, and these expressions provide compact and reasonably accurate descriptions of the behavior of the microphysical plasma properties. The results that we obtain can be employed in a wide range of astrophysical systems, such as jets and accretion disks around supermassive black holes, and their imaging campaign (Event Horizon Telescope Collaboration et al., 2019b; Event Horizon Telescope Collaboration et al., 2022b). In the very last part, we present preliminary results by performing direct, global GRMHD simulations of the morphology of M87 jet. To this scope, we used both the `BHAC` and the `BHOSS` codes, employing our self-consistent prescriptions obtained from our kinetic simulations. The results of such analysis will be material for future works.

The thesis is structured as follows.

In Chapter 1, we introduce the main concepts of general relativity, presenting the formulation of the theory in the tensorial, standard form. We discuss the recent detections that confirmed Einstein's predictions, and the importance to build numerical methods in order to model the gravitational equations.

In Chapter 2, we present `SFINGE`, a new numerical algorithm that solves Einstein's equations in vacuum conditions, and with matter distributions. We introduce the "3+1" formulation of spacetime, in which "space" and "time" have been decoupled, making the equations more suitable for numerical modeling.

In Chapter 3, by performing direct numerical simulations, we test our algorithm in vacuum conditions through a variety of different standard testbeds. Then we move to the more challenging, singular spacetimes, evolving the full three-dimensional dynamics of multiple black holes. We analyze the gravitational waves emitted from such systems via Fourier and wavelet spectra, revealing net differences among the two- and the three-body configuration.

In Chapter 4, by introducing one of the main novelties of our work, we show results from a campaign of large-scale PIC simulations, by using the `Zeltron` code. Here, we present important relationships between microphysical and global properties of relativistic plasmas surrounding black holes. These expressions can be employed in a wide range of astrophysical systems, such as jets and accretion disks around supermassive black holes, and, of course, their imaging.

Chapter 1

The Einstein theory of gravity

In this Chapter, we will introduce the main objects that are at the basis of Einstein's theory of gravity and the formulation adopted for the Einstein field equations. We write down the *Schwarzchild* and the *Kerr–Newman* metric, two analytical solutions that describe the curvature around singular and stationary spacetimes. Finally, we present recent breakthroughs and observations, discussing the importance to build numerical methods in order to model such extraordinary phenomena.

1.1 A brief introduction

The main result of Einstein's theory of general relativity are the celebrated field equations, ten coupled nonlinear partial differential equations given by [1]

$$G_{\mu\nu} = R_{\mu\nu} - \frac{1}{2} g_{\mu\nu} R = 8\pi T_{\mu\nu}, \tag{1.1}$$

where $G_{\mu\nu}$ is the *Einstein tensor*, $R = g^{\mu\nu} R_{\mu\nu}$ is the *Ricci scalar*, $g_{\mu\nu} = g_{\mu\nu}(x^{\sigma})$ is the *4-metric tensor*, and the *Ricci tensor* $R_{\mu\nu} = g^{\rho}{}_{\sigma}\, g^{\delta}{}_{\rho}\, R^{\sigma}{}_{\nu\delta\mu}$ is the trace of the *Riemann tensor*. The latter is defined as

$$R^{\mu}{}_{\nu\rho\sigma} = \begin{vmatrix} \partial_{\rho} & \partial_{\sigma} \\ \Gamma^{\mu}_{\nu\rho} & \Gamma^{\mu}_{\nu\sigma} \end{vmatrix} + \begin{vmatrix} \Gamma^{\mu}_{\gamma\rho} & \Gamma^{\mu}_{\gamma\sigma} \\ \Gamma^{\gamma}_{\nu\rho} & \Gamma^{\gamma}_{\nu\sigma} \end{vmatrix}.$$

In the above, we made use of the *Christoffel symbols* expressed in terms of $g_{\mu\nu}$, namely:

$$\Gamma^{\mu}_{\nu\rho} = \frac{1}{2} g^{\mu\sigma} \left(\partial_{\rho} g_{\sigma\nu} + \partial_{\nu} g_{\sigma\rho} - \partial_{\sigma} g_{\nu\rho} \right).$$

An equivalent way to define the Riemann tensor is given by

$$R^{\sigma}{}_{\rho\nu\mu} A_{\sigma} = 2 \nabla_{[\nu} \nabla_{\mu]} A_{\rho},$$

for any tensor A_{ν}, where $\nabla_{\mu} A_{\nu} = \partial_{\mu} A_{\nu} - \Gamma^{\rho}_{\mu\nu} A_{\rho}$ are the *covariant derivatives* in terms of the 4-metric.

One of the most important identities for the Riemann tensor, among the others, is the *Bianchi identities*, which reads

$$\nabla_{\kappa} R_{\mu\nu\rho\sigma} + \nabla_{\sigma} R_{\mu\nu\kappa\rho} + \nabla_{\rho} R_{\mu\nu\sigma\kappa} = 0.$$

As a consequence of the above relation, the covariant divergence of the Einstein tensor vanishes, i.e. $\nabla_{\mu} G^{\mu\nu} = 0$.

---

[1] Note that we keep using the geometric units.

For $n = 4$ dimensions, the Riemann tensor $R^{\sigma}{}_{\mu\rho\nu}$ contains 20 independent components, of which 10 are expressed in its trace $R_{\mu\nu}$. The other 10 independent components of the Riemann tensor are expressed in its traceless part, the *Weyl tensor*, and can be obtained by subtracting out various traces, as follows:

$$C_{\mu\nu\rho\sigma} = R_{\mu\nu\rho\sigma} - \left(g_{\mu[\rho}\, R_{\sigma]\nu} - g_{\nu[\rho}\, R_{\sigma]\mu} \right) + \frac{1}{3} g_{\mu[\rho} g_{\sigma]\nu} R.$$

Proof

One can easily see that the Weyl tensor is traceless:

$$\begin{aligned}
C_{\nu\sigma} =& g^{\mu\rho} C_{\mu\nu\rho\sigma} \\
=& g^{\mu\rho} R_{\mu\nu\rho\sigma} - \frac{1}{2} g^{\mu\rho} \left(g_{\mu\rho}\, R_{\sigma\nu} - g_{\mu\sigma}\, R_{\rho\nu} - g_{\nu\rho}\, R_{\sigma\mu} + g_{\nu\sigma}\, R_{\rho\mu} \right) \\
& \qquad + \frac{1}{6} g^{\mu\rho} \left(g_{\mu\rho} g_{\sigma\nu} - g_{\mu\sigma} g_{\rho\nu} \right) R \\
=& R_{\nu\sigma} - 2R_{\nu\sigma} + \frac{1}{2} \left(\delta^{\rho}_{\sigma}\, R_{\rho\nu} + \delta^{\mu}_{\nu}\, R_{\sigma\mu} - g_{\nu\sigma}\, R \right) + \frac{1}{6} \left(4 g_{\sigma\nu} - \delta^{\mu}_{\nu} g_{\mu\sigma} \right) R \\
=& - R_{\nu\sigma} + R_{\nu\sigma} - \frac{1}{2} g_{\nu\sigma}\, R + \frac{1}{2} g_{\sigma\nu} R \\
=& 0,
\end{aligned} \qquad (1.2)$$

where we have used the property of the metric tensor $g_{\mu\nu} g^{\mu\sigma} = \delta^{\sigma}_{\nu}$.

In Einstein field equations (1.1) also appear source terms through the $T_{\mu\nu}$ tensor, which is called the *stress-energy* tensor (or sometimes the *energy-momentum tensor*). In a *locally inertial frame* T^{00} is the energy density, T^{0i} is the energy which flows per unit time across the unit surface orthogonal to the axis x^i, and T^{ij} is the amount of the $i-$th-component of momentum which flows per unit time across the unit surface orthogonal to the axis x^j[2]. Let us consider a fluid element and the associated *locally inertial comoving frame*. In this frame, the fluid is at rest and the (fluid) stress-energy tensor can be written as[3]

$$T^{\mu\nu} = (\varepsilon + P) u^{\mu} u^{\nu} + P g^{\mu\nu} = T^{\mu\nu}_{\text{fluid}}. \qquad (1.3)$$

In this comoving frame, T^{00} is again the energy density, while $T^{0i} = 0$ means that the fluid element does not exchange energy with its surroundings, because there is no heat flow. On the other hand, $T^{ij} = P\,\delta^{ij}$ means that the force exerted on the surface orthogonal to the axis x^j must be orthogonal to the surface, and this force per unit surface is, by definition, the pressure[4]. A schematic picture of $T^{\mu\nu}$ in the local rest frame of a comoving observer is reported in figure 1.1.

Equation (1.3) is a tensorial expression and it must be valid in any other reference frame, by the general covariance principle. Note that ε and P are defined as the energy density and the pressure of the fluid element measured by a locally inertial, comoving observer. These quantities are, by definition, scalar fields on the manifold, and their value in a given point does not depend on the coordinate frame. Also, note that a comoving observer sees the fluid as isotropic.

---

[2] In a perfect fluid, both viscosity and heat flow are absent.

[3] Note that in a locally inertial comoving frame one has $g^{\mu\nu} = \eta^{\mu\nu}$.

[4] In other words, in a perfect fluid no tangential stresses are allowed.

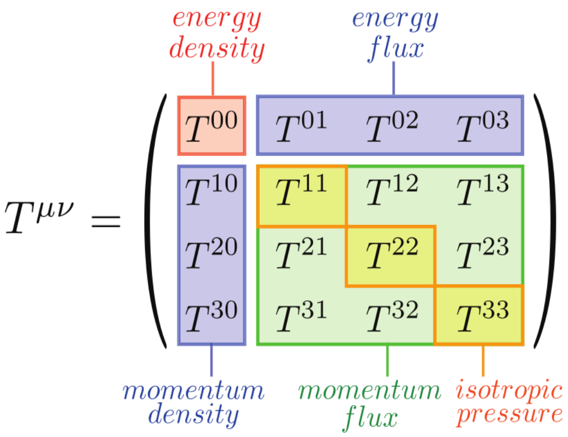

FIGURE 1.1: Schematic diagram illustrating the different parts composing the energy–momentum tensor of a perfect fluid in the local rest frame of a comoving observer. Note the location of the energy density T^{00} (red), of the energy flux T^{0i} and momentum density T^{i0} (violet), of the momentum flux T^{ij} (green), and of the isotropic pressure T^{ii} (yellow). Figure from Rezzolla and Zanotti, 2013

In many scenarios, the effect of the magnetized gas on the metric cannot be ignored, and the gas, the magnetic fields, and the metric must be evolved self-consistently. Consider the case of an electromagnetic field described by the potential 4-vector $\boldsymbol{A} = (\varphi, A^i)$, with φ the scalar potential and A^i the vector potential[5]

In such cases, one has to consider the total stress-energy tensor defined as

$$T^{\mu\nu} = T^{\mu\nu}_{\text{fluid}} + T^{\mu\nu}_{\text{EM}} = \begin{pmatrix} \varepsilon + \frac{1}{8\pi}\left(E^2 + B^2\right) & \zeta_x & \zeta_y & \zeta_z \\ \zeta_x & P - \sigma_{xx} & -\sigma_{xy} & -\sigma_{xz} \\ \zeta_y & -\sigma_{yx} & P - \sigma_{yy} & -\sigma_{yz} \\ \zeta_z & -\sigma_{zx} & -\sigma_{zy} & P - \sigma_{zz} \end{pmatrix},$$

where $T^{\mu\nu}_{EM} = \left[F^{\mu\rho}F^{\nu}_{\rho} - \frac{1}{4}\eta^{\mu\nu}F_{\rho\sigma}F^{\rho\sigma}\right]/(4\pi)$ is the purely electromagnetic stress-energy tensor, $F_{\mu\nu} = 2\nabla_{[\mu}A_{\nu]}$ is the *Faraday tensor*, $\zeta^i = \boldsymbol{E} \times \boldsymbol{B}/(4\pi)$ is the Poynting vector, and

$$\sigma_{ij} = \frac{1}{4\pi}\left[E_iE_j + B_iB_j\right] - \frac{1}{8\pi}\left[E^2 + B^2\right]\delta_{ij}$$

is the *Maxwell stress tensor*. As a consequence of the divergenceless of the Einstein tensor, from the Einstein equations (1.1) one has

$$\nabla_\mu T^{\mu\nu} = 0.$$

The above is the equation of motion governing the flow of energy and momentum for the matter, and is the statement that the total energy-momentum of the Universe is conserved (Alcubierre, 2006).

Obviously, the high complexity of the Einstein equations implies that it is very difficult (and often impossible) to find an analytical solution for a generic case. The simplicity of the compact form of the Einstein equations is only apparent since each term is a short-hand for considerably more complex mathematical objects. Written

---

[5] Notice that in tensorial terms neither φ is a scalar nor A^i a vector; they are in fact different components of the same 4-vector.

in their most general form, in an arbitrary coordinate system, and with all terms expanded out, the Einstein equations become a system of ten coupled, nonlinear, second-order partial differential equations with hundreds of terms. However, it is possible to find a few simple solutions in vacuum conditions to the field equations that are worth mentioning, as we describe in the following Section.

1.2 Analytical solutions

One particularly important application of general relativity is related to the exterior gravitational field of a static and spherically symmetric object. In early 1916, the astrophysicist Karl Schwarzschild found the first non-trivial exact solution to the Einstein field equations in vacuum, for a spherical, non-rotating, and non-electrically charged mass distribution, that can be written as:

$$ds^2 = -\left(1 - \frac{2M}{r}\right) dt^2 + \left(1 - \frac{2M}{r}\right)^{-1} dr^2 + r^2 \left(d\theta^2 + sin^2\theta \, d\phi^2\right), \tag{1.4}$$

where M is the gravitational mass, r is the distance from the singularity and $\left(d\theta^2 + sin^2\theta \, d\phi^2\right) = d\Omega^2$. Equation (1.4) is known as *Schwartzschild metric*.[6]

This solution holds in the vacuum region of any spherical spacetime, including a spacetime containing matter. The mass of this spacetime, as measured by a distant static observer in the vacuum exterior, is M. When the vacuum extends down to $r = 2M$, the interior spacetime corresponds to a vacuum black hole of mass M. The black hole event horizon is located at $r = 2M$ and is called the Schwarzschild radius. It is also referred to as the "surface of infinite redshift" because photons emitted by a static source just outside $r = 2M$ will have infinite wavelength when measured by a static observer at infinity. The Schwartzschild metric seems to have two singularities, namely at $r = 0$ and at $r = 2M$, but only the first one is a physical singularity; the second point is just a singularity due to the choice of the coordinates that can be eliminated, for example, by using *Kruskal coordinates* (Alcubierre, 2006).

A solution for a spherical black hole with an electric charge was found independently by Reissner and Nordstrom soon after Schwarzschild's work (Reissner, 1916). For a non-spherically symmetric black hole solution, we have to wait until 1963 when Kerr found the spacetime metric for a rotating black hole (Kerr, 1963). Finally, in 1965 the charged rotating black hole solution, which contains all other previous solutions as special cases, was found by Newman et al. (Newman et al., 1965). The metric is uniquely specified by just three parameters: the mass M, the angular momentum parameter a, and the charge Q of the black hole. The metric for this so-called *Kerr–Newman* black hole is given by:

$$\begin{aligned} ds^2 = &- \left[\frac{\Delta - a^2 \sin^2\theta}{\rho^2}\right] dt^2 - \frac{2a \sin^2\theta (r^2 + a^2 - \Delta)}{\rho^2} dt d\phi \\ &+ \left[\frac{(r^2 + a^2)^2 - \Delta a^2 \sin^2\theta}{\rho^2}\right] sin^2\theta d\phi^2 + \frac{\rho^2}{\Delta} dr^2 + \rho^2 d\theta^2, \end{aligned} \tag{1.5}$$

---

[6] Even though the Schwartzschild metric is a vacuum solution, the mass M appears in the metric. Similarly to electrostatic, masses are sources of gravitational perturbations.

where

$$\begin{cases} \Delta = r^2 + a^2 + Q^2 - 2Mr, \\ \\ \rho^2 = r^2 + a^2 \cos^2\theta, \end{cases}$$

and $a = J/M$ is an angular momentum parameter. Note that for $a = Q = 0$ the solution reduces to the Schwarzschild metric (1.4), for $a = 0$ and $Q \neq 0$ it reduces to the *Reissner–Nordstrom* solution, while for $Q = 0$ and $a \neq 0$ it reduces to the Kerr solution.

Still today, it is not clear how Kerr obtained this solution, and is not that easy to obtain it starting from first principles (Teukolsky, 2015). A detailed mathematical study of the metric in Equation (1.5) reveals that black holes might have two distinct event horizons, one inside the other. Moreover, the solution includes a narrow shell that surrounds the outer horizon, in which the matter is trapped and rotate very fast, co-moving with the spinning black hole. This region is called *ergosphere* and is supposed to be a very energetic plasma-sphere, with trapped, energetic matter and light. The Kerr–Newman spacetime is clearly stationary (i.e. the metric coefficients are time-independent), and axisymmetric (the metric is independent of the angle ϕ).

Another analytical solution that is worth mentioning is related to gravitational waves (GWs). The perturbations caused by the propagation of GWs through the detectors are incredibly small, of the order of $\mathcal{O}(h) \sim 10^{-22}$, where h is proportional to the amplitude of the waves. Keeping only terms linear in h at very large distances from the sources is therefore an excellent approximation, in analytical models. The main approach is to start from the Minkowski metric $\eta_{\mu\nu}$ adding a small perturbation, namely

$$g_{\mu\nu} = \eta_{\mu\nu} + h_{\mu\nu},$$

where $h_{\mu\nu} \ll 1$ is a tensor field defined on Minkowski spacetime which transforms as a rank-2 tensor. From the assumption that $\partial_\sigma \eta_{\mu\nu} = 0$ and after some algebra, one can write the variation of the Ricci tensor as

$$\delta R_{\mu\nu} = \delta R^{\sigma}_{\ \mu\sigma\nu} = \frac{1}{2}\Big(\partial_\sigma \partial_\mu h^{\sigma}_{\ \nu} + \partial_\nu \partial^\sigma h_{\mu\sigma}\Big) - \partial_\sigma \partial^\sigma h_{\mu\nu} - \partial_\mu \partial_\nu h, \tag{1.7}$$

with $h = \eta^{\mu\nu} h_{\mu\nu}$ the trace of the perturbation. Introducing a new vector field $\zeta_\mu = \partial_\nu h^{\nu}_{\ \mu} - (\partial_\mu h)/2$ and the d'Alembert operator $\Box = \eta^{\mu\nu}\partial_\mu\partial_\nu$, equation (1.7) becomes

$$\delta R_{\mu\nu} = \frac{1}{2}\Big(-\Box h_{\mu\nu} + \partial_\mu \zeta_\nu + \partial_\nu \zeta_\mu \Big). \tag{1.8}$$

We now make an infinitesimal coordinate transformation of the type

$$(x^\mu)' = x^\mu + \epsilon^\mu,$$

where ϵ^μ is an arbitrary vector such that $\partial \epsilon^\mu / \partial x^\nu \sim h_{\mu\nu}$. Then it is possible to show that, up to $\mathcal{O}(h^2)$, holds the relation

$$h'_{\mu\nu} = h_{\mu\nu} - \partial_\mu \epsilon_\nu - \partial_\nu \epsilon_\mu. \tag{1.9}$$

Note that both $h'_{\mu\nu}$ and $h_{\mu\nu}$ describe the same physical situation, since the (linearized) Einstein's equations do not fix uniquely $h_{\mu\nu}$. Applying the transformation (1.9) to the variation of the Ricci tensor (1.8) and in vacuum conditions, one finally obtains

$$\Box h_{\mu\nu} = 0, \tag{1.10}$$

where the *harmonic gauge* $\zeta = 0$ is employed. The above is the familiar wave equation and holds for all the ten independent components of the perturbation $h_{\mu\nu}$. In the so-called *transverse and traceless (TT) gauge*, GWs have only two physical degrees of freedom, which correspond to the two possible polarization states, named h_+ and $h_\times$.

Because of the complexity of Einstein's equations, exact solutions are only known in such a few cases with high symmetry, either in space or in time, and making some assumptions. The wave equation (1.10), for instance, is valid only in the weak-field limit and at very large distances from the sources. The same holds for the black hole solutions (1.4) and (1.5), in which certain symmetries are assumed. If we are interested in studying systems with astrophysical relevance, which involve strong and dynamical gravitational fields with no assumption of any symmetry, it is simply impossible to obtain exact analytical solutions. The need to study this type of system has given birth to the field of *numerical relativity*, which solves the Einstein field equations using numerical techniques and complex computational codes.

1.3 Recent breakthroughs

More than a century has passed since Einstein's theory of general relativity has been formulated, but only in the last years, with the improvement of technology and engineering equipment, we are able to observe and measure some of Einstein's predictions.

The first-ever direct detection of gravitational waves has been made on September 2015 (exactly one century later the formulation of Einstein's theory) by researchers working on the Laser Interferometer Gravitational-wave Observatory (LIGO) and announced by the LIGO and Virgo collaborations on February 2016 (Abbott et al., 2016b). The signal was named GW150914 (from the date of observation). In this event, the waveform detected by observatories matched the predictions of general relativity for a gravitational wave, emanating from the inspiraling and merger of a pair of spinning black holes of 29 and 36 solar masses. After the subsequent *ringdown* of the single new-born black hole, about 3 solar masses are lost via gravitational waves. The single black hole created by such a violent collision is initially highly distorted and loses its deformity almost instantly by ringing like a bell and producing further gravitational radiation. The signal also revealed that the resulting black hole is a rotating Kerr black hole, with a *spin* parameter of 0.67.

Figure 1.2 shows the two waveforms measured by the LIGO detectors, with different colors. Apart from the background noise, it is possible to distinguish the two sinusoidal-type signals, arrived within seven milliseconds of each other and lasted for about 0.2 seconds on the detectors. A time-frequency representation of the strain data is also reported, showing that the signal increases in frequency and amplitude in about 8 cycles, from 35 to 200 Hz, revealing the *inspiral, chirp* and *ringdown* features.

The gravitational waves of this event were detected only by the two LIGO's interferometers, (located in Hanford, Washington, and in Livingstone, Louisiana). The Virgo detector (Cascina, Pisa) was being upgraded, and GEO 600 (Sarstedt, Hannover), though not sufficiently sensitive to detect this event was operating but not in observational mode. The data showed that gravitational waves travel at the speed

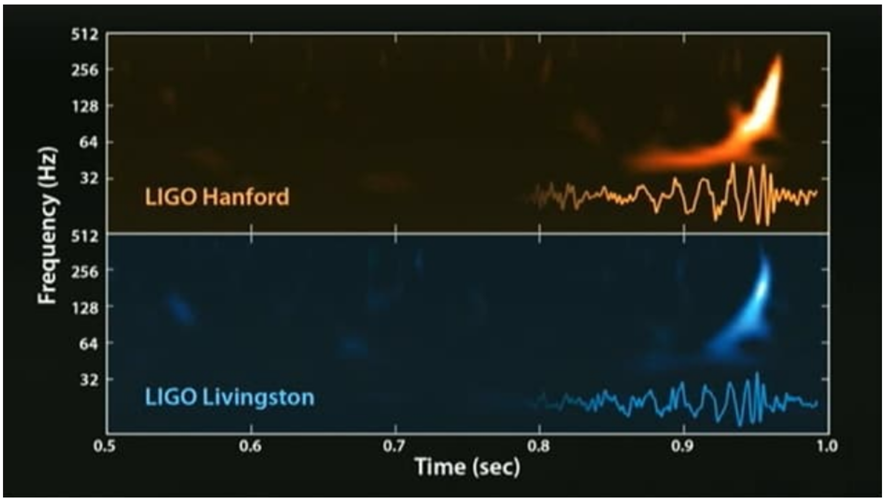

FIGURE 1.2: GW150914 signal detected by the LIGO Hanford and LIGO Livingstone interferometers. A time-frequency representation of the strain data is also reported, revealing that the signal increases in frequency and amplitude. Image credit: https://www.ligo.caltech.edu

of light and that the currently unknown carriers of the force, the *gravitions*, are massless, as predicted by general relativity. This event was also the first observation of a stellar-mass binary black hole merger, demonstrating the existence of binary stellar-mass black hole systems and the fact that such mergers could occur.

In April 2019 and in May 2022, the Event Horizon Telescope (EHT) collaboration produced images of two supermassive black holes: the one in the center of a galaxy Messier 87 (also called Virgo A), and the one at the center of our galaxy, the Milky Way (Event Horizon Telescope Collaboration et al., 2019b; Event Horizon Telescope Collaboration et al., 2022b). This project involved hundreds of scientists worldwide and made use of the very long baseline interferometry (VLBI) technique. In particular, the VLBI used a global network of radio telescopes spread across different continents to form a "virtual" giant (Earth-sized) telescope. The radio wave signals emitted by the hot plasma surrounding the black holes are recorded separately at the individual telescopes. Afterward, the signals are cross-correlated for all pairs of antennas at a central location, and an image of the emission surrounding the black holes has been reconstructed.

The two supermassive objects are called, respectively, M87* and SgrA*, and are both Kerr-type black holes, described in the previous Section. The estimated masses are, respectively, about 6 billion and 4 million solar masses, with a distance from the Earth of 55 million and 27000 light years. In particular, M87* interested scientists not only because is one of the largest known supermassive black holes. Unlike SgrA*, it is an active black hole, with matter falling into it and throwing out in the form of relativistic jets of particles that are accelerated to velocities near the speed of light. The two images obtained by the EHT are shown in figure 1.3. The central compact objects are resolved and show a circular ring of emission, which encompasses a depression in brightness. It is also evident the asymmetry of the rings in both images, likely due to doppler boosting of material orbiting the black holes.

Magnetic fields pervade the relativistic plasma that envelops black holes. As the electrons turn around the field lines, they lose energy via synchrotron radiation, which is linearly polarized in the plane of the gyration. As the radiation makes its way through the plasma along the observer's line of sight, another electromagnetic process, the Faraday rotation, comes into play. The turbulence of the field causes

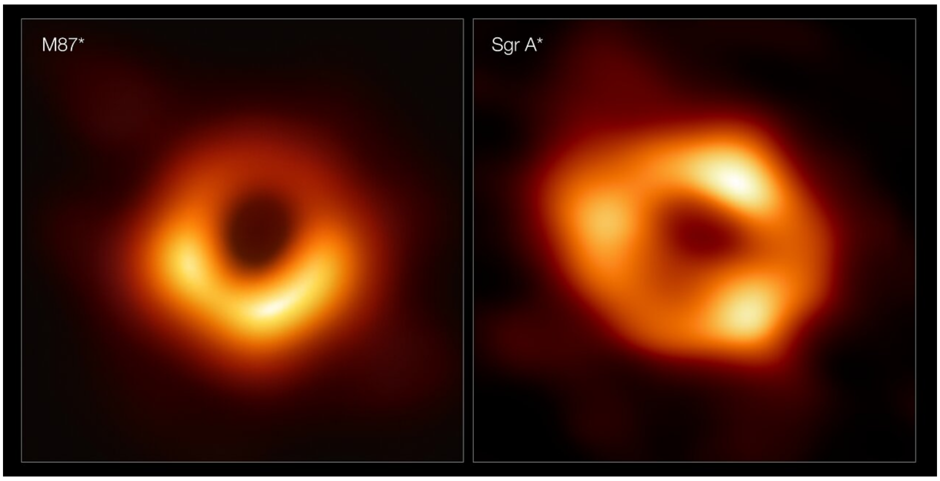

FIGURE 1.3: The two supermassive black holes captured by the EHT collaboration, M87* to the left, and SgrA* to the right. Image credit: http://eventhorizontelescope.org

particles to collide and lose energy and angular momentum, allowing them to fall into the black hole rather than just orbit around it. In 2021, the EHT collaboration released new images of M87* (Event Horizon Telescope Collaboration et al., 2021), showing a significant linear polarization due to the synchrotron nature of the emission. This shows that the magnetic field structure in the emitting region is predominantly poloidal, implying that magnetic fields should be dynamically important.

Numerical simulations of supermassive black holes clearly become very important to have a solid validation of such phenomena. In this thesis, we will focus on the above observations by performing numerical simulations of compact-objects dynamics with relative production of GWs, and simulations of plasmas near BHs. In the next Chapter, we introduce some manipulations to Einstein's formalism, which makes the gravitational equations less frightening and more suitable for numerical modeling.

Chapter 2

A new numerical code for the Einstein field equations: `SFINGE`

In this Chapter we will present a new numerical algorithm to solve Einstein's equations, the `SFINGE` code, that solves both spacetimes in vacuum conditions, and with matter distributions. Because of the intrinsic coupling between *space* and *time*, the field equations of general relativity are not suitable – in their original formulation – for numerical approaches. It has become necessary, then, to manipulate the equations in order to facilitate the numerical approach. We start to introduce the "3+1" formalism, in which a *foliation* of the spacetime is employed to decouple "space" and "time", and where it is possible to write new *spatial* variables that evolve in time. After writing down the *ADM* and the *BSSNOK formulation*, we describe our algorithm in detail, presenting the method and main features implemented to improve stability and robustness.

2.1 The foliation of the spacetime

We here introduce the *ADM formalism* (Arnowitt, Deser, and Misner, 2008), a Hamiltonian formulation of general relativity supposing that spacetime is foliated into a family of spacelike surfaces, each of them labeled by their time coordinate t and with coordinates given by x^i. The dynamic variables of this theory are taken to be the metric tensor of three-dimensional spatial slices γ_{ij} and their conjugate momenta π^{ij}. Using these variables it is possible to define a Hamiltonian and thereby write the equations of motion for general relativity in the form of Hamilton's equations. The standard "ADM equations" that we will discuss in this Section, though equivalent, are not identical to the original ones[1]. In fact, in numerical relativity is often used a non-trivial rewriting due to the work by York (York, 1979), where the canonical conjugate momentum π^{ij} is replaced by a new tensor, the *extrinsic curvature* K_{ij}, described in the next Section.

If we denote with $\mathcal{M}$ the 4-dimensional spacetime manifold, we can assume that it can be foliated into a family of nonintersecting spacelike 3-surfaces Σ_t, as shown in figure 2.1. Every hypersurface arises, at least locally, as the level surfaces of a scalar function t that can be interpreted as a global time function (Baumgarte and Shapiro, 2010). At this point it is possible to define a *direction of time* as a vector field $\Omega_\mu = \nabla_\mu t$, with normalization

$$\|\Omega_\mu\|^2 = g^{\mu\nu}\nabla_\mu t \, \nabla_\nu t = -\frac{1}{\alpha^2}.$$

---

[1] The original goal of ADM was to write a Hamiltonian formulation for general relativity that could be used as a basis for quantum gravity and not a system of evolution equations for dynamical simulations.

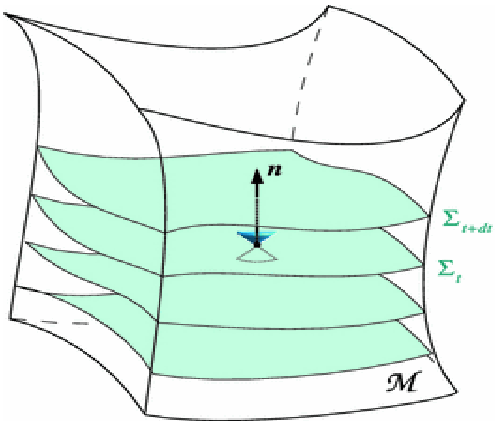

FIGURE 2.1: *Slicing* of spacetime. The hypersurfaces Σ_i are level surfaces of the coordinate time t. Figure from Gourgoulhon, 2012

In the above equation, α is a very important quantity, defined as the *lapse function*. It measures how much proper time elapses between neighboring time slices along the normal vector Ω_μ to the slice. The unit normal $\boldsymbol{n}$ to the slices $\boldsymbol{\Sigma}$ is given by:

$$n_\mu = -\alpha g^{\mu\nu} \Omega_\nu = -\alpha g^{\mu\nu} \nabla_\nu t,$$

where the negative sign has been chosen so that n_μ points in the direction of increasing t. The lapse of proper time $d\tau$ between two hypersurfaces $\boldsymbol{\Sigma}$ measured by an observer moving along the direction normal $\mathbf{n}$ to the hypersurfaces is then

$$d\tau = \alpha(t, x^i)\, dt.$$

If now we contract two normal unit vectors, we obtain:

$$n^\mu n_\mu = \alpha^2 g^{\mu\nu} (\nabla_\mu t)(\nabla_\nu t) = \begin{cases} -1 & \text{for } n_\mu \text{ time-like,} \quad (2.1a) \\ +1 & \text{for } n_\mu \text{ space-like.} \quad (2.1b) \end{cases}$$

The lapse α is assumed nonnegative so that Ω_μ is timelike and the hypersurface $\boldsymbol{\Sigma}$ is spacelike everywhere. Given this decomposition it is useful to introduce a spatial metric $\gamma_{\mu\nu}$ that only acts on slices $\boldsymbol{\Sigma}$. The full 4-metric $g_{\mu\nu}$ and the 3-metric $\gamma_{\mu\nu}$ are related by the following relationship:

$$\gamma_{\mu\nu} = g_{\mu\nu} + n_\mu n_\nu.$$

Since the 3-metric $\gamma_{\mu\nu}$ is purely spatial, $\gamma_{0\nu} = 0, \forall \nu$. There are two useful tensors: the spatial projection operator, and the time-like projection operator, that read respectively

$$\gamma_\mu^{\ \nu} = g_\mu^{\ \nu} + n_\mu n^\nu, \tag{2.2}$$

$$N^\mu_\nu = -n^\mu n_\nu. \tag{2.3}$$

The first projects a generic tensor on the spatial slice $\boldsymbol{\Sigma}$, while the second projects a generic tensor aligned with $\boldsymbol{n}$ and hence orthogonal to $\boldsymbol{\Sigma}$.

Using the above, each tensor $\boldsymbol{T}$ can be decomposed in its *spatial* part and its *normal* part. From equations (2.2)-(2.3) and using the relationship $g_\mu^{\ \nu} = \delta^\nu_\mu$, a first rank tensor T^μ can be decomposed as

$$T^\mu = \delta^\mu_\nu T^\nu = g_\nu^{\ \mu} T^\nu = \underbrace{\gamma_\nu^{\ \mu} T^\nu}_{\text{Spatial proj.}} \underbrace{-n^\mu n_\nu T^\nu}_{\text{Normal proj.}},$$

and for a second rank tensor $T_{\mu\nu}$ we obtain

$$\begin{aligned} T_{\mu\nu} =& g_\mu^{\ \rho} g_\nu^{\ \sigma} T_{\rho\sigma} = (\gamma_\mu^{\ \rho} - n_\mu n^\rho)(\gamma_\nu^{\ \sigma} - n_\nu n^\sigma) T_{\rho\sigma} \\ =& \underbrace{\gamma_\mu^{\ \rho} \gamma_\nu^{\ \sigma} T_{\rho\sigma}}_{\text{Purely Spatial}} \underbrace{- n_\mu n^\rho \gamma_\nu^{\ \sigma} T_{\rho\sigma}}_{\text{Purely Normal}} \underbrace{- n_\nu n^\sigma \gamma_\mu^{\ \rho} T_{\mu\nu} + n_\mu n_\nu n^\rho n^\sigma T_{\rho\sigma}}_{\text{Mixed term}} . \end{aligned}$$

Hortogonality between normal and spatial projections

A spatial projection of a purely normal tensor, and a normal projection of a purely spatial tensor, will give a null result.
As an example, a spatial projection of the normal n_ν reads

$$\gamma_\mu^{\ \nu} n_\nu = g_\mu^{\ \nu} n_\nu + n_\mu n^\nu n_\nu = n_\mu - n_\mu = 0,$$

where we have used the relations $g_\mu^{\ \nu} n_\nu = n_\mu$ and $n^\nu n_\nu = -1$.
The two projectors are obviously orthogonal and holds

$$N^\mu_{\ \nu} \gamma_\mu^{\ \nu} = -n^\mu n_\nu \left(g_\mu^{\ \nu} + n_\mu n^\nu \right) = -n^\mu n_\mu - n^\mu n_\mu n^\nu n_\nu = 0.$$

When considering the spatial hypersurfaces that constitute the foliation of spacetime, it is important to distinguish between the *intrinsic curvature* of those hypersurfaces coming from their internal geometry and the *extrinsic curvature* associated with the way in which those hypersurfaces are immersed in four-dimensional spacetime. The intrinsic curvature is given by the three-dimensional Riemann tensor defined in terms of the 3-metric γ_{ij}. The extrinsic curvature $K_{\mu\nu}$, on the other hand, can be found by projecting gradients of the normal vector into the slice $\boldsymbol{\Sigma}$. In other terms this tensor can be defined as:

$$K_{\mu\nu} = \gamma_\mu^{\ \rho} \gamma_\nu^{\ \sigma} \nabla_\rho n_\sigma. \tag{2.4}$$

The above is know as *Form I* for the extrinsic curvature and in figure 2.2 a geometric representation is shown. Extrinsic curvature $K_{\mu\nu}$ is pure spatial, and it is also a symmetric tensor, i.e. $K_{\mu\nu} = K_{\nu\mu}$.

One can write equation (2.4) expanding the spatial metrics $\gamma_{\mu\nu}$ obtaining

$$K_{\mu\nu} = -\left(g_\mu^{\ \rho} + n_\mu n^\rho \right) \left(g_\nu^{\ \sigma} + n_\nu n^\sigma \right) \nabla_\rho n_\sigma = -\left(g_\mu^{\ \rho} + n_\mu n^\rho \right) \nabla_\rho n_\nu,$$

where we have used that $g_\nu^{\ \sigma} = \delta_\nu^\sigma$ and $n^\sigma \nabla_\rho n^\sigma = 0$. If one identifies $n^\rho \nabla_\rho n_\nu = a_\nu$ as an acceleration, it is possible to write the extrinsic curvature in the so-called, *Form II*:

$$K_{\mu\nu} = -\nabla_\mu n_\nu - n_\mu a_\nu = -\nabla_{(\mu} n_{\nu)} - n_{(\mu} a_{\nu)}. \tag{2.5}$$

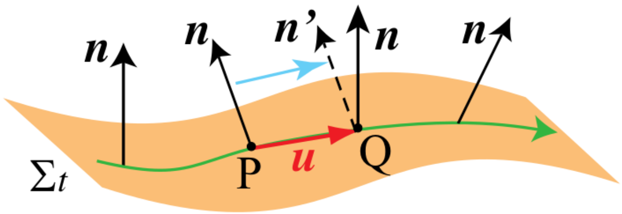

FIGURE 2.2: Concept of the extrinsic curvature. $\boldsymbol{n}$ denotes the timelike unit normal vector field of a spatial hypersurface Σ_t and $\boldsymbol{n}'$ denotes a timelike vector that is obtained by the parallel transportation of $\boldsymbol{n}$ from P to Q along a spatial geodesic (in green) for which the tangent vector is $\boldsymbol{u}$ (in red). The extrinsic curvature denotes the degree of the difference $\boldsymbol{n}' - \boldsymbol{n}$ which does not vanish if the spatial hypersurface is embedded in a bent manner for given spacetime. Figure from Shibata, 2016

Let us now consider the Lie derivative of the $\gamma_{\mu\nu}$ metric along the normal vector $\boldsymbol{n}$, which gives

$$\begin{aligned}\mathcal{L}_{\boldsymbol{n}}\gamma_{\mu\nu} =& n^\rho\nabla_\rho\gamma_{\mu\nu} + \gamma_{\rho\sigma}\nabla_\mu n^\rho + \gamma_{\mu\rho}\nabla_\nu n^\rho\\ =& n^\rho\nabla_\rho\left(g_{\mu\nu} + n_\mu n_\nu\right) + \left(g_{\rho\sigma} + n_\rho n_\sigma\right)\nabla_\mu n^\rho + \left(g_{\mu\rho} + n_\mu n_\rho\right)\nabla_\nu n^\rho\\ =& n_\mu n^\rho\nabla_\rho n_\nu + n_\nu n^\rho\nabla_\rho n_\mu + \nabla_\mu n_\nu + \nabla_\nu n_\mu,\end{aligned}$$

where we have used that $\nabla_\rho g_{\mu\nu} = 0$ and $n_\rho\nabla_\mu n^\rho = 0$. Now, identifying $a_\nu = n^\rho\nabla_\rho n_\nu$ and $a_\mu = n^\rho\nabla_\rho n_\mu$, we get

$$\mathcal{L}_{\mathbf{n}}\gamma_{\mu\nu} = 2\left[\nabla_{(\mu}n_{\nu)} + n_{(\mu}a_{\nu)}\right].$$

Finally, by using Eq. (2.5) one can find the *Form III* for the extrinsic curvature which reads

$$K_{\mu\nu} = -\frac{1}{2}\mathcal{L}_{\boldsymbol{n}}\gamma_{\mu\nu}.$$

The latter will be very important to obtain the evolution equations in the ADM formalism. Interestingly, the extrinsic curvature $K_{\mu\nu}$ and the three-metric $\gamma_{\mu\nu}$ can be considered as the equivalent of velocity and position in classical mechanics: they measure the instantaneous state of the gravitational field. Since they are both spatial tensors, we refer to them often writing K_{ij} and γ_{ij} (Latin subscripts).

To build numerical codes, it is necessary to specify a coordinate basis. Let's choose, as the basis, three space vectors of the type $e^\mu_{(i)}$ and hence tangents to the slice $\boldsymbol{\Sigma}$[2], plus a fourth purely normal vector $e^\mu_{(0)}$. From the properties of orthogonality, one has

$$n_\mu e^\mu_{(i)} = 0, \qquad \gamma^\nu{}_\mu e^\mu_{(0)} = 0.$$

Let's now consider the vector

$$t^\mu = \alpha n^\mu + \beta^\mu, \tag{2.6}$$

where α is the lapse function, and $\boldsymbol{\beta}$ is the spatial shift vector. It will prove useful to choose t^μ to be the congruence along which we propagate the spatial coordinate grid from one time slice Σ_t to the next slice Σ_{t+dt}. In other words, t^μ will connect points

---

[2] An example can be $\left(e^a_{(x)}, e^a_{(y)}, e^a_{(z)}\right)$ in Cartesian coordinates, or $\left(e^a_{(r)}, e^a_{(\theta)}, e^a_{(\phi)}\right)$ in spherical ones.

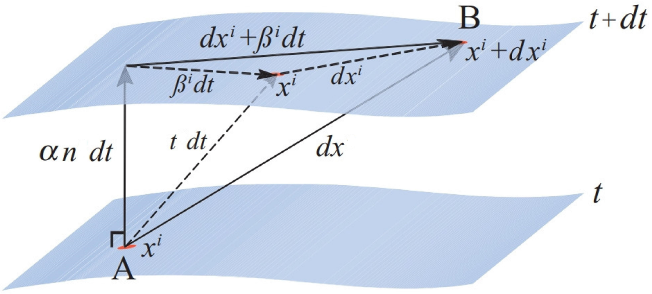

FIGURE 2.3: Schematic representation of the 3+1 decomposition of spacetime. The four-vector $\boldsymbol{t}$ represents the direction of evolution of the time coordinate t and can be split into a timelike component $\alpha\boldsymbol{n}$, where $\boldsymbol{n}$ is a timelike unit normal to the hypersurface, and into a spacelike component, represented by the spacelike four-vector β^i. Figure from Baumgarte and Shapiro, 2010.

with the same spatial coordinates on neighboring time slices. Then the shift vector β^μ will measure the amount by which the spatial coordinates are shifted within a slice concerning to the normal vector $\boldsymbol{n}$, and the lapse function α measures how much proper time elapses between neighboring time slices along the normal vector. Solving equation (2.6) for the normal vector

$$n^\mu = \frac{1}{\alpha}\left(t^\mu - \beta^\mu\right) = \frac{1}{\alpha}\left(1, -\beta^i\right),$$

and using the normalization of n^μ, one gets

$$n_\mu = \left(-\alpha, 0, 0, 0\right), \quad n_\mu n^\mu = n_0 n^0 = \frac{n_0}{\alpha} = -1.$$

Recalling the relation $\gamma_{\mu\nu} = g_{\mu\nu} + n_\mu n_\nu$ one obtains, for the spatial components, $\gamma_{ij} = g_{ij}$. The full covariant 4-metric $g_{\mu\nu}$ can be represented in a matrix form as

$$g_{\mu\nu} = \left(\begin{array}{c|c} -\alpha^2 + \beta_m\beta^m & \beta_i \\ \hline \beta_j & \gamma_{ij} \end{array}\right),$$

as well as its contravariant expression

$$g^{\mu\nu} = \gamma^{\mu\nu} - n^\mu n^\nu = \left(\begin{array}{c|c} -\dfrac{1}{\alpha^2} & \dfrac{\beta^i}{\alpha^2} \\ \hline \dfrac{\beta^j}{\alpha^2} & \gamma^{ij} - \dfrac{\beta^i\beta^j}{\alpha^2} \end{array}\right).$$

Within this 3+1 description, from a slice Σ_t to a neighboring slice Σ_{t+dt}, a generic *event* pass from the point A of coordinates x^i to the point B of coordinates $x^i + dx^i$, as shown in figure 2.3. The change in position of B concerning to the normal projection of A, is given not only by the amount dx^i, but also by the shift between the two slices, namely $\beta^i dt$. The total amount of change is then $\delta^i = \beta^i dt + dx^i$.

The *proper distance* ds^2 between A and B can be found using the Pythagorean theorem in 3+1 spacetime, which reads

$$ds^2 = -\alpha^2 dt^2 + \gamma_{ij}\left(dx^i + \beta^i dt\right)\left(dx^j + \beta^j dt\right).$$

2.2 The ADM equations

In the standard 3+1 decomposition, the Einstein field equations (1.1) are decomposed in a set of two evolution equations and two constraint equations[3]. The set of Partial Differential Equations (PDE) for the evolution of the 3-metric and the extrinsic curvature is given by

$$\begin{cases} \partial_0 \gamma_{ij} = -2\alpha K_{ij}, & \text{(2.7a)} \\ \partial_0 K_{ij} = \alpha\left(R_{ij} - 2K_{ik}K^k_{\ j} + KK_{ij}\right) - D_i D_j \alpha & \\ \qquad -8\pi\alpha\left[S_{ij} - \frac{1}{2}\gamma_{ij}\left(S - \rho\right)\right]. & \text{(2.7b)} \end{cases}$$

Note that $\partial_0 = \partial_t - \mathcal{L}_\beta$, where $\mathcal{L}_\beta$ is the Lie derivative with respect to the shift β^k. The above system of equations has to be solved together with the constraint equations, given by

$$\begin{cases} R + K^2 - K_{ij}K^{ij} = 16\pi\rho, & \text{(2.8a)} \\ D_i\left(K^{ij} - \gamma^{ij}K\right) = 8\pi S^i. & \text{(2.8b)} \end{cases}$$

Equations (2.7) and (2.8) are equivalent to the Einstein's equations (1.1).

Note that we have highlighted the source terms with a lighter color, i.e. in vacuum conditions all the source terms vanish. It is interesting to note that, with this decomposition, only spatial indices appear in the ADM formalism, and space and time have been somehow "detached". Moreover, applying the Lie derivative to a generic tensor T^μ_ν with respect to $t^\sigma = \left(1, 0, 0, 0\right)$, one obtain $\mathcal{L}_t T^\mu_\nu = t^0 \partial_0 T^\mu_\nu = \partial_t T^\mu_\nu$. In other terms, the Lie derivative $\mathcal{L}_t$ becomes a simple derivative ∂_t.

Now we briefly discuss the stability of the ADM equations (2.8) and (2.7). In mathematics, an *hyperbolic* PDE of order n is a PDE that has a well-posed "initial value problem" for the first $n-1$ derivatives. More precisely, *the Cauchy problem* can be locally solved for arbitrary initial data along any non-characteristic hypersurface. The same holds for a system of partial differential equations, so the property of *well-posedness* implies that its solutions depend continuously on the initial data or, in other words, that small changes in the initial data will correspond to small changes in the solution. More formally, if the solution of a system of PDEs is given by a certain function $u(\vec{x}, t)$, this system is called "well-posed" if one can define a norm $||\cdot||$ such that

$$||u(\vec{x}, t)|| \leq Ce^{kt}||u(\vec{x}, 0)||, \quad C,\, k \in \mathbb{R},$$

where C and k are constants that are independent of the initial data. That is, the norm of the solution at time t is at most exponentially larger concerning to the norm of the solution at the initial time $t = 0$. By virtue of this, when the system is hyperbolic the

---

[3] For $n = 3$ dimensions one has 4 scalar constraint equations and 6 scalar evolution equations.

solution will not explode exponentially, if it explodes. It can be shown that the ADM evolution equations (2.8) and (2.7) are only weekly hyperbolic.

Hyperbolicity of ADM equations

We discuss here the hyperbolicity of the ADM equations, where for simplicity we assume that we are in vacuum. This system is first order in time but second order in space. In order to have a purely first order system we introduce the quantities

$$\mathcal{A}_i = \partial_i \ln \alpha, \qquad \mathcal{D}_{ijk} = \frac{1}{2}\partial_i \gamma_{jk}.$$

We consider the lapse α as a dynamical quantity that evolves through an equation of the form $\partial_0 \alpha = -\alpha\Theta$, where Θ denotes the explicit form of the gauge function, while the shift β^i is a know function.
In terms of the $\mathcal{D}_{ijk}$, the "principal part" of the Ricci tensor can be written as

$$R_{ij} \simeq -\partial_k \delta^k{}_{ij} + 2\,\partial_{(i}\delta^k{}_{kj)} - \partial_{(i}\mathcal{D}_{j)k}{}^k.$$

The evolution equations for $\mathcal{A}_i, \mathcal{D}_{ijk}$ and K_{ij} then read

$$\begin{cases} \partial_0 \mathcal{A}_i \simeq -\alpha \partial_i \Theta, & \text{(2.9a)} \\ \partial_0 \mathcal{D}_{ijk} \simeq -\alpha \partial_i K_{jk}, & \text{(2.9b)} \\ \partial_0 K_{ij} \simeq -\alpha \partial_m \Lambda^m{}_{ij}, & \text{(2.9c)} \end{cases}$$

where we define $\Lambda^m{}_{ij} = \mathcal{D}^m{}_{ij} + \delta^k{}_{(i}\left[\mathcal{A}_{j)} + \mathcal{D}_{j)k}{}^k - 2\,\mathcal{D}^k{}_{kj)}\right]$.
The idea is then to find 27 independent eigenfunctions that will allow us to recover the 27 original quantities in (2.9). With eigenfunctions here, we mean linear combinations of the original quantities $u = (\mathcal{A}_i, \mathcal{D}_{ijk}, K_{ij})$ of the form $w_i = \sum_j C_{ij} u_j$, that up to principal part evolve as $\partial_t w_i + \lambda_i \partial_x w_i \simeq 0$, with λ_i the corresponding eigenspeeds. To proceed with the *characteristic* analysis we will choose a specific direction x and ignore derivatives along the other directions, reducing the system to seven fields $\mathcal{A}_x, \mathcal{D}_{xxi}$ and K_{xi}. It is possible to write the evolution equation for $\Lambda^x{}_{xq}$ as

$$\partial_0 \Lambda^x{}_{xq} = \partial_0 \mathcal{D}^x{}_{xq} + \frac{1}{2}\partial_0\left[\mathcal{A}_q + \mathcal{D}_{qk}{}^k - 2\,\mathcal{D}^k{}_{kq}\right] \simeq \alpha\gamma^{xp}\,\partial_x K_{pq},$$

with $p, q \neq x$. In the above equation, we note that while K_{xq} evolves through derivatives of $\Lambda^x{}_{xq}$, the evolution of $\Lambda^x{}_{xq}$ is independent of K_{xq} and only involves derivatives of K_{pq} . This subsystem can therefore not be diagonalized. In particular, if the metric γ_{ij} is diagonal, Λ_{xxq} will remain constant up to the principal part, which implies that K_{xq} will grow linearly unless Λ_{xxq} vanishes initially. This shows that the ADM system is not strongly hyperbolic; it is only weakly hyperbolic as we can show that the eigenvalues of the principal symbol are all real.

Over the past few decades, and particularly since researchers started to work with full three-dimensional evolution codes for numerical relativity, it was realized that the ADM formulation lacked the necessary stability properties to have long-term numerical simulations. It is possible, however, to introduce some changes to the ADM formulation that allow writing the system into a hyperbolic form according to the so-called "BSSNOK formulation". In this thesis we will compare the numerical performances of both ADM and BSSNOK, by developing a new code.

2.3 The BSSNOK equations

In 1987, T. Nakamura, K. Oohara, and Y. Kojima presented a new reformulation of the ADM evolution equations based on a *conformal transformation* that showed improved stability properties when compared to the original ADM formulation (Nakamura, Oohara, and Kojima, 1987). This formulation remained largely unnoticed by the numerical relativity community, until in 1998 T. Baumgarte and S. Shapiro compared it to ADM in a series of spacetimes testbeds, showing that the new formulation had far superior stability properties in all cases considered. It was only at this point that this reformulation became more noticed, and today it is used in different forms by most large three-dimensional codes in the numerical relativity community.

The more common version of this formulation is based on the work of M. Shibata and T. Nakamura (Shibata and Nakamura, 1995), together with the work of T. Baumgarte and S. Shapiro (Baumgarte and Shapiro, 1998), and is commonly known as the *BSSN formulation* (from Baumgarte, Shapiro, Shibata, and Nakamura), or in other cases, as the *BSSNOK* formulation (when adding the Oohara and Kojima contributes).[4]

Instead of evolving the spatial metric γ_{ij} and the extrinsic curvature K_{ij}, the BSSNOK formulation evolves a conformal factor and the trace of the extrinsic curvature separately. So, let's consider first a conformal rescaling of the spatial metric (also called *conformally related metric*) of the form

$$\tilde{\gamma}_{ij} = \psi^{-4}\gamma_{ij},$$

Here ψ is a *conformal factor* that can in principle be chosen in a number of different ways, but in our case, we choose the conformal factor in such a way that the *conformal metric* $\tilde{\gamma}_{ij}$ has unit determinant ($\det[\tilde{\gamma}_{ij}] = \tilde{\gamma} = 1$), that is

$$\psi^4 = \gamma^{1/3} \implies \psi = \gamma^{1/12},$$

with γ the determinant of the physical three-metric γ_{ij}. Usually the conformal factor is taken to be $\phi = \ln\psi = (\ln\gamma)/12$, so that $\tilde{\gamma}_{ij} = e^{-4\phi}\gamma_{ij}$, but it has been suggested by Campanelli et al., 2006 that evolving instead $\chi = 1/\psi^4 = e^{-4\phi}$ is a better alternative when considering black hole spacetimes. In these cases, infact, ψ typically has a $1/r$ singularity (and ϕ has a logarithmic singularity), while χ is a C^4 function at $r = 0$. For regular spacetimes, of course, it should make no difference if one evolves ψ, ϕ or χ, but from here on we will adopt the conformal rescaling $\tilde{\gamma}_{ij} = \chi\gamma_{ij}$.

The BSSN formulation also separates the extrinsic curvature into its trace K and its trace-free part, namely:

$$A_{ij} = K_{ij} - \frac{1}{3}\gamma_{ij}K.$$

---

[4] Throughout this thesis, we will refer to this formalism as BSSN or BSSNOK, indifferently.

We further make a conformal rescaling of the traceless extrinsic curvature (also called *conformally related extrinsic curvature*) of the form

$$\widetilde{A}_{ij} = \psi^{-4} A_{ij}.$$

A crucial point is that BSSN also introduces three auxiliary variables known as the *conformal connection functions* and defined as

$$\widetilde{\Gamma}^i = \widetilde{\gamma}^{jk}\widetilde{\Gamma}^i_{jk} = -\partial_j \widetilde{\gamma}^{ij}, \tag{2.10}$$

where $\widetilde{\Gamma}^i_{jk}$ are the Christoffel symbols associated with the conformal metric and can be expressed in terms of the Γ^i_{jk} as

$$\widetilde{\Gamma}^k_{ij} = \Gamma^k_{ij} + \frac{1}{2\chi}\gamma^{lk}\Big[\gamma_{il}\partial_j\chi + \gamma_{jl}\partial_i\chi - \gamma_{ij}\partial_l\chi\Big].$$

The second equality in Equation (2.10) comes from the definition of the Christoffel symbols in the case of the determinant $\widetilde{\gamma}$ is equal to 1 (which must be true by construction).

Proof of equation (2.10)

The general case of (2.10) reads

$$\widetilde{\gamma}^{jk}\widetilde{\Gamma}^i_{jk} = -\frac{1}{\sqrt{|\widetilde{\gamma}|}}\partial_l\left(\sqrt{|\widetilde{\gamma}|}\;\widetilde{\gamma}^{il}\right). \tag{2.11}$$

We can assume that γ_{ij} has signature $(1,1,1)$, so that we don't need the absolute value for γ. Using the product rule and Jacobi's formula for calculating the derivative of a determinant $\partial_l\widetilde{\gamma} = \widetilde{\gamma}\;\widetilde{\gamma}^{ij}\partial_l\widetilde{\gamma}_{ij}$, one can rewrite the RHS of (2.11) as

$$-\frac{1}{\sqrt{\widetilde{\gamma}}}\partial_l\left(\sqrt{\widetilde{\gamma}}\;\widetilde{\gamma}^{il}\right) = -\partial_l\widetilde{\gamma}^{il} - \frac{1}{\sqrt{\widetilde{\gamma}}}\widetilde{\gamma}^{il}\partial_l\sqrt{\widetilde{\gamma}} = -\partial_l\widetilde{\gamma}^{il} - \frac{1}{2}\widetilde{\gamma}^{il}\widetilde{\gamma}^{jk}\partial_l\widetilde{\gamma}_{jk}. \tag{2.12}$$

On the other hand, one can write explicitly the LHS of (2.11) as

$$\begin{aligned}
\widetilde{\gamma}^{jk}\widetilde{\Gamma}^i_{jk} =& \frac{1}{2}\widetilde{\gamma}^{jk}\widetilde{\gamma}^{is}\left(\partial_j\widetilde{\gamma}_{ks} + \partial_k\widetilde{\gamma}_{js} - \partial_s\widetilde{\gamma}_{jk}\right)\\
=& \frac{1}{2}\widetilde{\gamma}^{jk}\widetilde{\gamma}^{is}\partial_j\widetilde{\gamma}_{ks} + \frac{1}{2}\widetilde{\gamma}^{jk}\widetilde{\gamma}^{is}\partial_k\widetilde{\gamma}_{js} - \frac{1}{2}\widetilde{\gamma}^{jk}\widetilde{\gamma}^{is}\partial_s\widetilde{\gamma}_{jk}\\
=& \widetilde{\gamma}^{jk}\widetilde{\gamma}^{is}\partial_k\widetilde{\gamma}_{js} - \frac{1}{2}\widetilde{\gamma}^{jk}\widetilde{\gamma}^{is}\partial_s\widetilde{\gamma}_{jk}\\
=& \partial_k\widetilde{\gamma}^{ik} - \frac{1}{2}\widetilde{\gamma}^{jk}\widetilde{\gamma}^{is}\partial_s\widetilde{\gamma}_{jk},
\end{aligned} \tag{2.13}$$

where we have played with indices and used $\partial_k\widetilde{\gamma}^{ik} = -\widetilde{\gamma}^{jk}\widetilde{\gamma}^{is}\partial_k\widetilde{\gamma}_{js}$. Matching the results (2.12) and (2.13) we obtain an identity, proving the correctness of Equation (2.11).

In the case of $\widetilde{\gamma} = 1$ and in Cartesian coordinates, we obtain Equation (2.10)

$$\widetilde{\Gamma}^i = \widetilde{\gamma}^{jk}\widetilde{\Gamma}^i_{jk} = -\partial_l\widetilde{\gamma}^{il}.$$

So, instead of the 12 ADM variables γ_{ij} and K_{ij}, the BSSNOK formalism uses the 17 variables ϕ, K, $\tilde{\gamma}_{ij}$, $\tilde{A}_{ij}$ and $\tilde{\Gamma}^i$. We can take the point of view that there are only 15 dynamical variables since $\tilde{A}_{ij}$ is traceless and $\tilde{\gamma}_{ij}$ has unit determinant, but here we will take the point of view that we are freely evolving all components of $\tilde{A}_{ij}$ and $\tilde{\gamma}_{ij}$. However, enforcing the constraint $\tilde{A} = 0$ during a numerical calculation does seem to improve the stability of the simulations significantly, so it has become standard practice in most numerical codes.

The BSSNOK system of evolution equations reads

$$\left\{\begin{aligned}
&\partial_0\tilde{\gamma}_{ij} = -2\alpha\tilde{A}_{ij}, && (2.14a)\\
&\partial_0\chi = \frac{2}{3}\chi\alpha K, && (2.14b)\\
&\partial_0\tilde{A}_{ij} = \alpha\left(K\tilde{A}_{ij} - 2\tilde{A}_{il}\tilde{\gamma}^{ml}\tilde{A}_{mj}\right) + \chi\Big[\alpha R_{ij} - D_iD_j\alpha\Big]^{TF} \\
&\qquad + 4\pi\alpha\chi\Big[\gamma_{ij}(S-\rho) - 2S_{ij}\Big]^{TF}, && (2.14c)\\
&\partial_0 K = -D^kD_k\alpha + \alpha\left(\tilde{A}_{lm}\tilde{A}^{lm} + \frac{1}{3}K^2\right), && (2.14d)\\
&\partial_t\tilde{\Gamma}^i = \tilde{\gamma}^{lm}\partial_l\partial_m\beta^i + \frac{1}{3}\tilde{\gamma}^{il}\partial_l\partial_m\beta^m + \beta^k\partial_k\tilde{\Gamma}^i - \tilde{\Gamma}^k\partial_k\beta^i + \frac{2}{3}\tilde{\Gamma}^i\partial_k\beta^k - 2\tilde{A}^{ik}\partial_k\alpha \\
&\qquad + \alpha\left(2\tilde{\Gamma}^i_{lm}\tilde{A}^{lm} - \frac{3}{\chi}\tilde{A}^{ik}\partial_k\chi - \frac{4}{3}\tilde{\gamma}^{ik}\partial_k K - 16\pi S^i\right), && (2.14e)
\end{aligned}\right.$$

where again we highlighted the source terms with a lighter color, and TF denotes the trace-free part of the expression inside the brackets, i.e.

$$\Big[\alpha R_{ij} - D_iD_j\alpha\Big]^{TF} = \alpha R_{ij} - D_iD_j\alpha - \frac{1}{3}\gamma_{ij}\gamma^{lm}\Big[\alpha R_{lm} - D_lD_m\alpha\Big].$$

In equations (2.14) we have adopted the convention that indices of conformal quantities are raised and lowered with the conformal metric so that, for example, $\tilde{A}_{ij} = \chi^2\gamma_{ik}\gamma_{jm}\tilde{A}^{km}$. It is also important to notice that, in the evolution equation for K, the Hamiltonian constraint

$$R = K_{ij}K^{ij} - K^2 + 16\pi\rho$$

has been used in order to eliminate the Ricci scalar. We must be careful with the fact that, in the BSSNOK formulation, we are computing Lie derivatives with respect to β^k of *tensor densities*, that is tensors multiplied by powers of the determinant of the metric γ. If a given object is a tensor times $\gamma^{\zeta/2}$, then we say that it is a tensor density of *weight* ζ.

Lie derivative of tensor densities

A tensor density is a generalization of the tensor field concept. A tensor density transforms as a tensor field when passing from one coordinate system to another, except that it is additionally multiplied or weighted by a power ζ of the Jacobian determinant of the coordinate transition function or its absolute value. Examples of tensor density are the related metric $\tilde{\gamma}_{ij}$, the conformal trace-free part of the curvature $\tilde{A}_{ij}$, and the conformal factor χ.
The Lie derivative of a generic tensor density T^μ_ν reads

$$\begin{aligned}\mathcal{L}_\beta T^\mu_\nu =& \beta^\rho \nabla_\rho T^\mu_\nu - T^\rho_\nu \nabla_\rho \beta^\mu + T^\mu_\rho \nabla_\nu \beta^\rho + \zeta T^\mu_\nu \nabla_\rho \beta^\rho \\ =& \beta^\rho \partial_\rho T^\mu_\nu - T^\rho_\nu \partial_\rho \beta^\mu + T^\mu_\rho \partial_\nu \beta^\rho + \zeta T^\mu_\nu \partial_\rho \beta^\rho,\end{aligned}$$

where ζ is the weight of the tensor density. We note that the Lie derivative of a tensor density is the same as the Lie derivative of a standard tensor, except for the weight contribution of the tensor density. "Normal" tensors are therefore tensor densities with $\zeta = 0$.
The density weight of the conformal factor $\chi = \gamma^{-1/3}$ is clearly $\zeta = -2/3$. We have the same density weight for the conformal metric $\tilde{\gamma}_{ij} = \chi\gamma_{ij} = \gamma^{-1/3}\gamma_{ij}$ and for the traceless extrinsic curvature $\tilde{A}_{ij}$, but notice that in the contravariant form, both $\tilde{\gamma}^{ij}$ and $\tilde{A}^{ij}$ have weight $\zeta = +2/3$.
The explicit form of the Lie derivative for χ, $\tilde{\gamma}_{ij}$ and $\tilde{A}_{ij}$ is then

$$\begin{cases} \mathcal{L}_\beta \chi = \beta^j \partial_j \chi - \frac{2}{3}\chi \partial_i \beta^i, & \text{(2.15a)} \\ \mathcal{L}_\beta \tilde{\gamma}_{ij} = \beta^k \partial_k \tilde{\gamma}_{ij} + \tilde{\gamma}_{ik}\partial_j \beta^k + \tilde{\gamma}_{jk}\partial_i \beta^k - \frac{2}{3}\tilde{\gamma}_{ij}\partial_k \beta^k, & \text{(2.15b)} \\ \mathcal{L}_\beta \tilde{A}_{ij} = \beta^k \partial_k \tilde{A}_{ij} + \tilde{A}_{ik}\partial_j \beta^k + \tilde{A}_{jk}\partial_i \beta^k - \frac{2}{3}\tilde{A}_{ij}\partial_k \beta^k. & \text{(2.15c)} \end{cases}$$

The Lie derivative of a tensor density of weight ζ is again a tensor density of the same weight.

In the BSSNOK formulation, the Ricci tensor associated with the physical metric is separated into two contributions as $R_{ij} = R^\chi_{ij} + \tilde{R}_{ij}$, where

$$\tilde{R}_{ij} = -\frac{1}{2}\tilde{\gamma}^{lm}\partial_l \partial_m \tilde{\gamma}_{ij} + \tilde{\gamma}_{k(i}\partial_{j)}\tilde{\Gamma}^k + \tilde{\Gamma}^k \tilde{\Gamma}_{(ij)k} + \tilde{\gamma}^{lm}(2\tilde{\Gamma}^k_{l(i}\tilde{\Gamma}_{j)km} + \tilde{\Gamma}^k_{im}\tilde{\Gamma}_{klj})$$

is the Ricci tensor related to the conformal metric and

$$\tilde{R}^\chi_{ij} = \frac{1}{2\chi}\left\{\left[\partial_i \partial_j \chi - \frac{1}{2\chi}\partial_i \chi \partial_j \chi - \tilde{\Gamma}^k_{ij}\partial_k \chi\right] + \tilde{\gamma}_{ij}\tilde{\gamma}^{lm}\left[\partial_l \partial_m \chi - \frac{3}{2\chi}\partial_l \chi \partial_m \chi - \tilde{\Gamma}^k_{lm}\partial_k \chi\right]\right\}$$

denotes the additional term that depends on the conformal factor χ.

In addition to the evolution equations, the BSSN variables must satisfy also the Hamiltonian and the momentum constraints, that are respectively:

$$\begin{cases} \mathcal{H} = R - \widetilde{A}_{lm}\widetilde{A}^{lm} + \frac{2}{3}K^2 = 16\pi\rho, & (2.16a) \\ \mathcal{M}^i = \partial_k \widetilde{A}^{ik} + \widetilde{\Gamma}^i_{lm}\widetilde{A}^{lm} - \frac{3}{2\chi}\widetilde{A}^{ik}\partial_k\chi - \frac{2}{3}\widetilde{\gamma}^{ik}\partial_k K = 8\pi S^i. & (2.16b) \end{cases}$$

In addition to the previous equations, as discussed in (Zlochower et al., 2005; Gundlach and Martin-Garcia, 2006; Brown, 2009), the BSSN variables must satisfy also the constraints

$$\mathcal{G}^i = \widetilde{\Gamma}^i + \partial_j\widetilde{\gamma}^{ij} = 0,$$

$$\widetilde{\gamma} - 1 = 0, \tag{2.17}$$

$$\widetilde{A} = 0. \tag{2.18}$$

During the numerical simulations, we enforce the algebraic constraints in equations (2.17) and (2.18). The remaining constraints, $\mathcal{H}$, $\mathcal{M}^i$ and $\mathcal{G}^i$ are not actively enforced and are used to monitor the accuracy of the numerical solutions (Alcubierre et al., 2004). Note that in all the above equations, $\widetilde{\Gamma}^i$ is replaced by $-\partial_j\widetilde{\gamma}^{ij}$, wherever it is not differentiated (Campanelli et al., 2006).

2.3.1 The Gauge choice

Since the coordinates can be chosen freely, it is natural to expect some degrees of freedom in the choice of some variables. These are the Gauge variables, namely the lapse function α and the shift vector β^i, which determine a foliation of spacetime into space-like hypersurfaces. The Einstein equations say nothing about the choice of the gauge. This allows one to choose the coordinates in a way that either simplifies the evolution equations or makes the solution better behaved.

Here we give the details about the specific gauges used in our simulations. In particular, in the framework of the Bona-Massó formalism (Bona and Massó, 1989), we have used "hyperbolic K-driver slicing conditions" of the form

$$(\partial_t - \mathcal{L}_\beta)\alpha = -\alpha^2 f(\alpha)\,(K - K_0)\,, \tag{2.19}$$

with $f(\alpha) > 0$ (but arbitrary) and $K_0 = K(t = 0)$ (Alcubierre, 2003). In the case in which $f(\alpha) = 1$, the above equation describes the harmonic slicing for the lapse, while by setting $f(\alpha) = n/\alpha$, with n an integer, we recover the generalized "1+log" slicing condition (Bona et al., 1995).

As for the spatial gauge, we use one of the “Gamma-driver” shift conditions proposed in (Campanelli et al., 2006), that essentially act so as to drive the $\widetilde{\Gamma}^i$ to be constant. In this respect, the “Gamma-driver” shift conditions are similar to the “Gamma-freezing” condition $\partial_t\widetilde{\Gamma}^i = 0$, which, in turn, is closely related to the well-known minimal distortion shift condition (Smarr and York, 1978). The differences between these two conditions involve the Christoffel symbols and, while the minimal distortion condition is covariant, the Gamma-freezing condition is not.

One of the most used gauges for the evolution of the shift vector is the hyperbolic Gamma-driver condition, which reads:

$$(\partial_t - \mathcal{L}_\beta)\beta^i = \frac{3}{4}B^i, \quad (2.20)$$

$$(\partial_t - \mathcal{L}_\beta)B^i = \partial_t\widetilde{\Gamma}^i - \beta^j\partial_j\widetilde{\Gamma}^i - \eta B^i, \quad (2.21)$$

where the factor 3/4 is somewhat arbitrary but leads to good numerical results. Note that for the hyperbolic Gamma-driver conditions, it is important to add a dissipation term with coefficient η to avoid strong oscillations in the shift. Experience has shown that by tuning the value of this dissipation coefficient it is possible to almost freeze the evolution of the system at late times (Baumgarte and Shapiro, 1998). In all our simulations we set $\eta = 2.8$ and constant in time.

Hyperbolicity of BSSNOK equations

We discuss here the hyperbolicity of the BSSNOK equations.
This formulation takes as independent variables the conformal metric $\widetilde{\gamma}_{ij}$, the conformal factor $\phi = -1/4\ln\chi$, the trace of the extrinsic curvature K, the conformal tracefree extrinsic curvature $\widetilde{A}_{ij}$, and the contracted conformal Christoffel symbols $\widetilde{\Gamma}^i = \widetilde{\gamma}^{km}\widetilde{\Gamma}^i_{km}$, plus the lapse α and shift vector β^i. In order to study its characteristic structure we will again introduce the spatial derivatives of α, $\widetilde{\gamma}_{ij}$, and ϕ as independent quantities

$$\mathcal{A}_i = \partial_i \ln\alpha, \qquad \widetilde{\mathcal{D}}_{ijk} = \frac{1}{2}\partial_i\widetilde{\gamma}_{jk}, \qquad \Phi_i = \partial_i\phi,$$

and we consider the β^i to be a given function of spacetime.
Note that we have to consider only 30 quantities $u = (\mathcal{A}_i, \Phi_i, \widetilde{\mathcal{D}}_{ijk}, K, \widetilde{A}_{ij}, \widetilde{\Gamma}^i)$, because $\widetilde{A}_{ij}$ is traceless and also $\widetilde{\gamma}^{jk}\widetilde{\mathcal{D}}_{ijk} = 0$, as a consequence that the determinant of the conformal metric is unitary, i.e. $\widetilde{\gamma} = 1$.
From the BSSNOK evolution equations (2.14), we find that up to the principal part, the evolution equations for our dynamical quantities become

$$\begin{cases} \partial_0\mathcal{A}_i \simeq -\alpha\partial_i\Theta, \\ \partial_0\Phi_i \simeq -\frac{1}{6}\alpha\partial_i K, \\ \partial_0\mathcal{D}_{ijk} \simeq -\alpha\partial_i\widetilde{A}_{jk}, \\ \partial_0 K \simeq -\alpha e^{-4\phi}\widetilde{\gamma}^{km}\partial_k\mathcal{A}_m, \\ \partial_0\widetilde{A}_{ij} \simeq -\alpha e^{-4\phi}\partial_m\Lambda^m{}_{ij}, \\ \partial_0\widetilde{\Gamma}^i \simeq -\alpha\partial_k\left[(\zeta-2)\widetilde{A}^{ik} - \frac{2}{3}\zeta\widetilde{\gamma}^{ik}K\right], \end{cases}$$

where we have defined $\widetilde{\Lambda}^m{}_{ij} = \left[\widetilde{\mathcal{D}}^m{}_{ij} + \delta^k{}_{(i}\left(\mathcal{A}_{j)} + \widetilde{\Gamma}_{j)} + 2\Phi_j\right)\right]^{TF}$. Note that standard BSSNOK corresponds to choosing $\zeta = 2$.
(continue)

Hyperbolicity of BSSNOK equations

(continued)
For the hyperbolicity analysis, we again consider only derivatives along the $x-$direction. We immediately find that there are 18 fields that propagate along the time lines with speed $-\beta^x$, namely

$$\mathcal{A}_q,\ \Phi_q,\ \widetilde{\mathcal{D}}_{qij},\ \mathcal{A}_x - 6f\Phi_x,\ \widetilde{\Gamma}^i + (\zeta - 2)\widetilde{\mathcal{D}}_m{}^{mi} - 4\zeta\tilde{\gamma}^{ik}\Phi_k,$$

where we have assumed that we are using a slicing condition of the Bona–Masso family so that $\Theta = fK$, and $q \neq x$.
For our analysis, the only two important characteristic fields represent the trace of the transverse components and are given by

$$e^{2\phi}\sqrt{\tilde{\gamma}^{xx}(2\zeta - 1)}\left[\tilde{A}^{xx} - \frac{2}{3}\tilde{\gamma}^{xx}K\right] \mp \left[\tilde{\Lambda}^{xxx} - \frac{2}{3}\tilde{\gamma}^{xx}\tilde{\mathcal{A}}^{x}\right],$$

where $\tilde{\mathcal{A}}^x = \tilde{\gamma}^{xk}\mathcal{A}_k$. These eigenfields propagate with the characteristic speeds

$$\lambda = -\beta^x + \alpha e^{-2\phi}\sqrt{\tilde{\gamma}^{xx}(2\zeta - 1)/3},$$

which will only be real if $\zeta > \frac{1}{2}$.
We then conclude that the standard BSSNOK system, corresponding to $\zeta = 2$, is strongly hyperbolic.

2.4 A self-consistent BSSNOK model with matter

Relativistic plasmas are important sources of stress-energy in many astrophysical applications. A hydrodynamic description of matter is appropriate whenever the mean free path of a particle due to collisions with neighboring particles is much shorter than the characteristic size or local scale length of the system. Many of the global properties of relativistic stars, like neutron stars, are described by using a fluid approach. In other terms, hydrodynamic (HD) and magnetohydrodynamic (MHD) simulations tell us about the global dynamics of the system. Here we briefly introduce the basic equations of general relativistic hydrodynamics (GRHD), written into forms most suitable for building dynamical spacetimes numerically, i.e., into forms best suited for numerical integration together with the Einstein equations, in 3 + 1 form for the gravitational field.

In nonvacuum spacetimes, the stress-energy tensor $T^{\mu\nu}$ discussed in Chapter 1.1 accounts for all sources of energy-momentum in spacetime, excluding gravity. For brevity, we shall sometimes refer to these sources collectively as the “matter sources” and the terms that they contribute in the 3 + 1 equations as the “matter source terms”. Matter source terms appear in the evolution equations (2.14) and in the constraint equations (2.16), highlighted with a lighter color. The GRHD equations, neglecting for simplicity the terms from electromagnetic fields, can be derived from (Rezzolla and Zanotti, 2013)

$$\begin{cases} \nabla_\nu T^{\mu\nu} = 0, & \text{(2.23a)} \\ \nabla_\mu\left(\rho u^\mu\right) = 0, & \text{(2.23b)} \end{cases}$$

which express the local conservation of the energy-momentum, and the conservation of rest-mass, respectively. In the above $T^{\mu\nu}$ is the stress-energy tensor, ρ is the rest-mass density, and u^{μ} is the fluid 4-velocity. These conservation equations must be solved simultaneously with the 3 + 1 evolution equations for the gravitational field, to determine the entire foliation of spacetime. The resulting equations can be cast in a number of forms, depending on the fluid variables chosen for numerical integration.

One of the most straightforward schemes that readily lends itself to numerical integration is the *Wilson scheme* (Alcubierre, 2008). This scheme was designed to mimic the standard Eulerian equations of hydrodynamics in Newtonian theory and to accomplish this goal, one has to define some auxiliary variables. The final form of the evolution equations reads

$$\begin{cases} \partial_t D = \alpha K D - D_k\left(\alpha D v^k\right) + \beta^k \partial_k D, & (2.24\text{a}) \\ \\ \partial_t S^i - \mathcal{L}_{\vec{\beta}} S^i = -(\mathcal{E} + D) D^i \alpha + \alpha K S^i - D_k\Big[\alpha\left(S^i v^k + \gamma^{ik} p\right)\Big], & (2.24\text{b}) \\ \\ \partial_t \mathcal{E} = (\mathcal{E} + p + D)(\alpha v^m v^n K_{mn} - v^m \partial_m \alpha) + \alpha K(\mathcal{E} + p) - D_k\Big[\alpha v^k (\mathcal{E} + p)\Big] + \beta^k \partial_k \mathcal{E}, & (2.24\text{c}) \end{cases}$$

where the rest mass density $D = \rho W$, the momentum density $S^i = \rho h W^2 v^i$, and the difference between the total energy density to the mass-energy density $\mathcal{E} = \rho h W^2 - p - D$, are the auxiliary variables[5], $W = 1/\sqrt{1 - v_i v^i}$ is the Lorentz factor, $h = 1 + \varepsilon + p/\rho$ is the enthalpy density, $v_i = u_i/W$ is the 3-velocity, ε is the specific internal energy, and p is the pressure. Note that the auxiliary variables are called *conserved* variables, to distinguish from ρ, v and p that are called *primitive* variables. This fluid approach is widely used in the general relativity community, to describe large-scale astrophysical objects, in a number of astrophysical, realistic scenarios.

2.5 The `SFINGE` code

In this Section, we introduce the Spectral FIltered Numerical Gravity codE (`SFINGE`), a numerical algorithm developed by scratch at the University of Calabria (and continuously improved) that solves either the ADM or the BSSNOK equations, discussed above. `SFINGE` solves both spacetimes in vacuum conditions, and recently also with matter, i.e. adding the source terms via the stress-energy tensor. It makes use of a parallel architecture based on MPI directives. In order to solve the gravitational fields equations, we make use of spectral techniques (Canuto, Hussaini, and Quarteroni, 1988; Dutykh, 2016; McCrory and Orszag, 1980; Gottlieb and Orszag, 1977b).

Classical spectral and pseudo-spectral methods are widely used for complex problems that involve strong couplings and nonlinearities, such as Einstein's equations (Grandclément and Novak, 2009). It is worth mentioning, among all, the work of Dimmelmeier et al., 2005, which combines for the first time spectral methods and Godunov-type methods, to study core-collapse supernovae in general relativity. A limitation of this approach is that the gravitational-field equations are approximated within the so-called Conformal-Flatness Condition (CFC), which neglects the GW

---

[5] Note that D, S^i and $\mathcal{E}$ are assumed to be measured in the Eulerian reference frame (the one associated with the observers whose 4-velocity is normal to the spatial hypersurface), which will in general differ from the fluid's frame of reference (the Lagrangian frame).

degrees of freedom. This is an excellent approximation in the case of core collapse, where the amplitude of the emitted gravitational waves is so small to hardly affects the dynamics. The CFC approach has also been extended to full GR in a Fully Constrained Formulation (FCF), in a number of works (Cordero-Carrión, Cerdá-Durán, and Ibáñez, 2012; Cordero-Carrión et al., 2014). Pseudo spectral methods, in full GR, have been also used to model the evolution of neutron star binaries, in harmonic coordinates (Duez et al., 2008).

Currently, the most accurate numerical relativity code in the market, that uses spectral methods, is the SpEC code (Szilágyi, 2014; Gold et al., 2014; Bohn et al., 2015). Their binary black hole merger waveforms are used by all data-analysis groups working on the development of GW approximants (waveform models) to conduct match-filtered searches of compact binary coalescences in LIGO-Virgo-KAGRA (LVK) data (e.g. the NR Surrogate approximants used to analyze discovery events in the third Gravitational-wave Transient Catalog (GWTC-3) are calibrated using SpEC waveforms) and also to perform Bayesian inference and parameter estimation of the sources (Abbott et al., 2016a; Blackman et al., 2017; Huerta et al., 2017; The LIGO Scientific Collaboration et al., 2017; Abbott et al., 2021).

In our code we use the *pseudo-spectral* method, which is a technique characterized by a recurrent switch, back-and-forth, between the physical (real) and the Fourier (complex) space. The rule is quite simple: derivatives are computed in the spectral space while products are computed in the physical space (in order to avoid convolutions). This iterative transformation, as we will see in the next subsection, needs to be regularized via a dealiasing procedure. The main advantage of these techniques relies on the fact that each field and all its derivatives are represented at the collocation points in a very accurate way. This leads to very precise solutions, with an error in the computation of derivatives that is on the order of the machine truncation error. To compute any spatial derivative, imposing periodic boundary conditions in all three spatial dimensions, our code makes use of standard Fast Fourier Transforms (FFTs). More specifically, each field $f(\boldsymbol{x}, t)$ is projected on a 3D spatial box, over a lattice with a number of meshes $\boldsymbol{N} = (N_x, N_y, N_z)$. We decompose the ADM and the BSSN fields as:

$$f_{\boldsymbol{N}}(\boldsymbol{x}, t) = \sum_{k} \widetilde{f}_k(t)\, e^{i\boldsymbol{k}\cdot\boldsymbol{x}}, \tag{2.25}$$

with $f_{\boldsymbol{N}}$ being the fields of the 3+1 foliation (i.e. $\gamma_{ij}, K_{ij}, \chi$ and so on.), at the grid points. As usual, $\widetilde{f}_{\boldsymbol{k}}(t) \in \mathbb{C}$ are the Fourier coefficients and $\boldsymbol{k} = (k_x, k_y, k_z)$ is the k-vector. In each Cartesian direction, $k = 2\pi m / L_0$, L_0 is the box length, $m = 0, \pm 1, \pm 2, \cdots \pm N_k$ with $N_k = N/2$ being the Nyquist mode and N is the number of points along this direction.

Even if pseudo-spectral methods are among the most precise numerical techniques, particularly suitable for solving small-scale complex problems such as wave dynamics, turbulence, and so on, great care must be dedicated to the computation of nonlinear terms. Nonlinearity characterizes gravitation, as in the case of hydrodynamics and plasma-dynamics (although in these cases the level of nonlinearity is certainly lower, as we shall discuss later.) In the spectral methods representation, the nonlinear terms become a convolution and there are several transform-based techniques for evaluating it efficiently (Canuto, Hussaini, and Quarteroni, 1988; Boyle et al., 2007; Cooley and Tukey, 1965). Numerical problems might arise from the so-called aliasing instabilities (Hossain, Matthaeus, and Ghosh, 1992), since any product among fields creates new k-components (spectral leakage).

In discrete Fourier transforms, *alias* happens when the size N_k of sampled Fourier modes is less than the effective size of modes. In such cases, due to the cyclic assumption in discrete Fourier transform, a Fourier mode with a wavenumber out of the size-range is aliased to another wavenumber in the domain. In a time-evolving system, this aliasing creates numerical instabilities. The importance of eliminating the aliasing error (dealiasing) has been studied since pioneering works by Orszag et al. (Orszag, 1971). As follows, we briefly mention this problem, well-known in hydrodynamics, and propose a similar "cure" to this numerical instability in the case of gravitational dynamics.

2.5.1 The dealiasing filters

Let's consider the simplest possible nonlinearity, i.e. the product of two functions $f(x)$ and $g(x)$ in a 1D, periodic domain (the 3D extension is straightforward). The truncated Fourier series with a set of $\{N_k\}$ modes are, respectively

$$f_N(x) = \sum_{p\in\{N_k\}} \widetilde{f}_p\, e^{ipx}, \qquad g_N(x) = \sum_{q\in\{N_k\}}^{m} \widetilde{g}_q\, e^{iqx},$$

where $\widetilde{f}_p$ and $\widetilde{g}_q$ are the complex Fourier coefficients, as defined in (2.25). The product of the above two functions $Q(x) = f(x)g(x)$ becomes a convolution product in Fourier space, namely

$$\widetilde{Q}_k = \int \sum_p \sum_q \widetilde{f}_p\, \widetilde{g}_q\, e^{i(p+q-k)x} dx = \sum_{k=p+q} \widetilde{f}_p\, \widetilde{g}_q, \tag{2.26}$$

where the last sum is the convolution on all the possible modes p and q of the set $\{N_k\}$ that satisfies the resonance $k = p + q$. It can be seen that the product (2.26) generates high-order harmonics concerning the Fourier series truncated at N_k. They will contribute to the well-known *aliasing error* (Boyd, 2001b). The dealiasing technique consists of making the maximum number of Fourier modes k^* in the above centered convolution free of aliasing, by extending the vector on both sides by zeros, to a larger vector of size N_k (zero padding). Analogously, it is easy to demonstrate that the full dealiasing can be achieved by defining a k^* in such a way that all coefficients with $p, q, ... > k^*$ are zero. For a quadratic nonlinearity like in equation (2.26), it has been demonstrated that is sufficient to filter out modes with $k > k^* = 2N_k/3 = N/3$. This fully eliminates the aliasing instability (Canuto, Hussaini, and Quarteroni, 1988) and is often called the "2/3 *rule*", since the number of dealiased modes is 2/3 of the total number of modes.

Compared to the most widely inspected cases, such as the Burgers equations and Navier-Stokes, gravitational equations involve high-order products and derivatives. In particular, from a quick analysis of the ADM equations, it is clear that one has products of order $p = 4$, or more. The nonlinearity is not completely well-defined because of contravariant tensors which complicate the degree of the nonlinearity, involving inverse computation of the metric. In these cases, it is still possible to suppress the aliasing instability by finding an accurate truncation (Hossain, Matthaeus, and Ghosh, 1992), which establishes a direct comparison between spectral methods and a full Galerking truncation. The above quadratic dealiasing described before can be extended to simple polynomial nonlinear terms of order p, by setting $k^* = N/(1 + p)$, therefore reducing the number of degrees of freedom in the Fourier space.

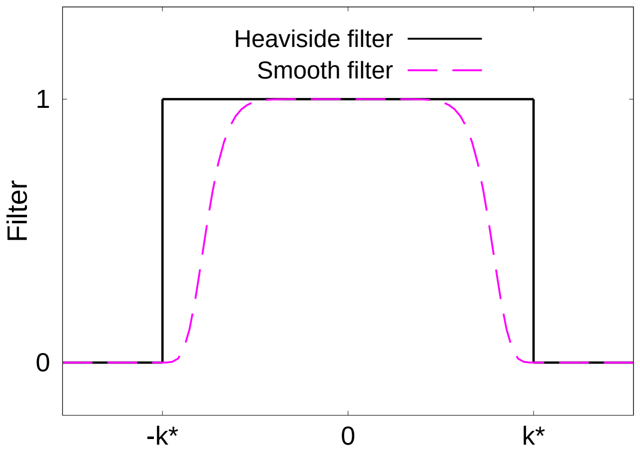

FIGURE 2.4: Comparison of the two anti-aliasing filters described by equations (2.28) and (2.29). The figure shows a section of the Fourier space, where all the $|k| \geq k^*$ are truncated. The Heaviside filter is a unit step-function, while the smooth filter goes from 0 to 1 more gently. In the example, it has been used $a = 10$ to emphasize the smoothness of this filter. In all our simulations we set $a = 20$.

In this work, we will inspect the role of the aliasing truncation and also the shape of the filter (Frisch et al., 2008; Shu et al., 2005). The technique is very simple to implement: on the final product, it is enough to set $\widetilde{Q}_k = 0$ for $k > k^\star$. In the case of the Einstein field equations, it is important to consider the very high nonlinearity of the system, where one has products of the type:

$$\partial_t \widetilde{A}_{ij} \sim \cdots + \alpha \chi^3 \gamma_{ik} \gamma^{mk} \gamma_{mj} K^2 + \ldots .$$

The above quantity corresponds to a challenging convolution in the Fourier space. Moreover, other complications come from the contravariant tensors, which involve further products. It is easy to envision a process in which the above products produce immediately high-order harmonics and therefore a pronounced aliasing instability. In order to suppress the above numerical pathology, different values of k^* have been chosen, depending on the difficulty of the simulation and on the initial data. Generally, by filtering high Fourier modes, the price to pay is the loss of effective resolution (information). However, by suppressing these high-k's couplings, the codes become more stable and accurate.

Apart from the mobile cutoff at k^*, in this paper we propose two different shapes of the spectral filter, described as follows. For each representation, we define

$$f_N(\boldsymbol{x}, t) = \sum_{\boldsymbol{k}} \widetilde{f}_{\boldsymbol{k}}(t)\, e^{i\boldsymbol{k}\cdot\boldsymbol{x}} \Phi_{k^*}(\boldsymbol{k}), \tag{2.27}$$

where $\Phi_{k^*}(\boldsymbol{k})$ is the spectral anti-aliasing filter. The first type, is the classical spherical truncation technique, namely a "Heaviside" filter (H) defined as:

$$\Phi^H_{k^*}(\boldsymbol{k}) = \begin{cases} 1 & \text{for } |\boldsymbol{k}| \leq k^*, \\ 0 & \text{for } |\boldsymbol{k}| > k^*. \end{cases} \tag{2.28}$$

A second smooth filter (S), usually adopted for treating discontinuities and singularity formation (Shu et al., 2005; Lele, 1992), is given by

$$\Phi^S_{k^*}(\vec{k}) = \exp[-a(|\vec{k}|/k^*)^a], \tag{2.29}$$

where a is a free parameter. It's clear that in the limit $a \to \infty$, the two filters become identical. A cartoon of the two filters is represented in figure 2.4. Generally, in our numerical experiments, we will use $k^* = \infty$ (no-filter), $k^* = N/2$ (grid-size), $k^* = N/3$ (typical quadratic nonlinearities), $N/4$ and so on. For the smooth filters $\Phi^S_{k^*}(k)$ in equation (2.29), we set $a = 20$. A more detailed study of the aliasing error propagation in the ADM and BSSN simulations, will be discussed in Section 3.2.

The main challenge with using spectral methods for numerical relativity is the fact that they require sufficiently smooth solutions. A spectral decomposition can provide derivative evaluations with exponential accuracy (that is, higher than any polynomial power of the grid spacing) only if the data being represented is C_∞. When derivatives are continuous at some lower order, then the error might rise too much. The filtering techniques might help to suppress the above problem. However, the accuracy of the method needs to be verified via a convergence analysis, especially when evolving non-smooth solutions. These numerical tests are reported in Appendix 3.1.10.

Note that even flux-conservative, Godunov-type schemes, although they formally solve the ideal equations, retain a considerable amount of artificial dissipation in the flux-reconstruction scheme (Anderson, Thomas, and Van Leer, 1986; Choi et al., 2018). The dissipation of these space filters is sometimes difficult to quantify. In our much simple pseudo-spectral approach, the algorithm is stabilized by definite spectral kernels, that act only at very small scales, over a controlled and limited bandwidth of modes.

2.5.2 The time integration

The above pseudo-spectral technique, used for the products and the spatial derivatives, has been associated with a simple second-order Runge–Kutta[6] method for the time integration (Press et al., 2007). At each time discretization n, the function f is advanced in time by using

$$f^{n+1} = f^n + \Delta t\, F\left[t^n + \frac{\Delta t}{2}, f^n + \frac{\Delta t}{2} F(t^n, f^n)\right], \tag{2.30}$$

where $f^n \equiv f(x, y, z, t^n)$ is any of the gravitational fields at the time $t^n = n\Delta t$, F is the time-derivative defined by the 3+1 governing equations, and Δt is the time-step, chosen to be sufficiently small. It is worth saying that second-order evolution might be too dissipative, especially in very stressful conditions such as the inspiraling of binary systems, while it might still manifest a good "convergence". In Appendix 3.1.9, we report on the adaptation of the current method to fourth-order Runge-Kutta, which is surely more precise but is more numerically expensive. Moreover, in a pseudo-spectral algorithm, where the number of allocated arrays is large, memory-saving becomes a challenge. Hereafter, we will therefore show the main results for the second-order scheme, which has the advantage of being simpler, more dissipative for the highest frequencies, and adaptable to other algorithms such as the implicit Crank-Nicholson.

---

[6] In the `SFINGE` code, also a fourth-order Runge-Kutta method is implemented.

In numerical methods, the Courant-Friedrichs-Lewy (CFL) condition is a necessary stability condition for the solution of certain partial differential equations problems (Courant, Friedrichs, and Lewy, 1928). In the simplest case of the motion of a wave traveling through a discrete spatial grid with speed v, the CFL condition imposes $\Delta t < C\Delta x/v$, namely a condition on the characteristic time of integration. In the above condition, C is the Courant number and is in general a number smaller than one. Numerical simulations of purely hyperbolic systems must satisfy this condition. The case of numerical relativity is more complicated because of the strong nonlinear couplings and because of the low level of hyperbolicity of the $3+1$ models (the strictly–hyperbolic nature of $3+1$ models is still an open issue (Radice and Rezzolla, 2012)). The above complications might lead to stability conditions that are more restrictive than a simple CFL. A general criterion for the determination of the time-step integration Δt is therefore necessary in order to have a good balance between the time-efficiency of the integration and avoidance of nonphysical solutions. Here we re-elaborate the CFL idea, in a more general sense, as follows.

For any ADM or BSSN dynamic field f, one can estimate a global characteristic time as

$$\mathcal{T}_f = \frac{\delta f}{\sqrt{\left\langle \left(\frac{\partial f}{\partial t}\right)^2 \right\rangle}}, \tag{2.31}$$

where $\delta f = \sqrt{\langle (f - \langle f \rangle)^2 \rangle}$ is the *rms* of the field and $\langle \dots \rangle$ indicates a volume average. The above quantity can be interpreted as a typical dynamical time of f, evaluated as the ratio between the level of fluctuations and its typical time-derivative, similar to plasma characteristic times in turbulence (De Giorgio, Servidio, and Veltri, 2017). The characteristic time in equation (2.31) is defined at any given time of the foliation and does not involve any complicated computation in explicit time-integration schemes. For any dynamical field f, one has $\frac{\partial f}{\partial t} \simeq \frac{\Delta f}{\Delta t}$ which, from the time discretization in equation (2.30), corresponds to $F\left[t^n + \frac{\Delta t}{2}, f^n + \frac{\Delta t}{2} F(t^n, f^n)\right]$. From the latter approximation, at the intermediate step, for example, one can estimate the dynamical time in the equation (2.31). Note that one can also build local versions of this time, or can measure the minimum time by finding the maximum of the denominator.

In analogy with the CFL condition, it is possible to use the characteristic time $\mathcal{T}_f$ for guessing an appropriate Δt. If the system undergoes fast evolution, $\mathcal{T}_f$ will drop off and the algorithm can self-adjust Δt. This might indicate a "precursor" of a simulation blow-up, as we shall see in our numerical experiments. Throughout this work, we will introduce the *Running Stability-Check* (RSC), which is a method that consists of a continuous adjustment of the Runge-Kutta time-step, based on the measure of $\mathcal{T}_f$ in equation (2.31), such that

$$\Delta t < C \min_f \{\mathcal{T}_f\}. \tag{2.32}$$

Here C is similar to the Courant number. The method simply corresponds to a *adaptive time-refinement*, typical of many schemes such as the leapfrog integration, except here is constrained with the minimum characteristic time given by (2.31). This strategy is very similar to the adaptive stepsize control for Runge-Kutta, described in standard numerical textbooks (Press et al., 2007). The general purpose of these classical methods is the achievement of some predetermined accuracy in the solution, with minimum computational effort. Here we re-elaborate this technique, but instead of establishing a desired error, we define a global time $\mathcal{T}_f$ for the system and keep the integration step always smaller than this dynamical time. Note also that the above technique might provide a general condition not only in the case of Runge-Kutta methods but in any explicit time-integration scheme.

2.5.3 The implicit hyperviscous boundary method

In this Section, we propose a new method in order to treat the boundary conditions with our pseudo-spectral, periodic code, based on the use of absorbing hyperviscous boundaries. As demonstrated in Meringolo, Servidio, and Veltri, 2021, our pseudo-spectral technique, together with an appropriate choice of the dealiasing and the time-step, is able to handle all the classical numerical testbeds. The main advantage of the pseudo-spectral code is of being relatively fast (since it stems from FFTs) and incredibly precise (since it relies on an exact decomposition). It would be hard to beat the precision of such methods with finite difference or finite volume/elements techniques, at a given resolution (Orszag, 1971). On the other hand, it is evident that the main weakness of the method relies on the boundary conditions that need to be periodic for this particular spectral decomposition. Periodic boundaries are not always a good choice for general relativity problems, for example in the case of compact object mergers. Here we present an additional algorithm that helps to overcome this limitation, which is based on the use of dissipating boundaries, combined with implicit time integration. This Implicit Hyperviscous Boundary (IHB) method has been tested with gravitational waves and compact object dynamics. The method is relatively easy-to-implement and efficient.

The following IHB method has been inspired by works in hydrodynamics and magnetohydrodynamics, with applications to turbulence and to the stellar dynamo. It is indeed possible to use Cartesian geometries in order to simulate spherical domains, using for example volume penalization methods (Schneider and Farge, 2005; Dobler, Stix, and Brandenburg, 2006), or by using hyperviscous forces (Servidio et al., 2007), starting from a given distance from the center of the Cartesian lattice. In this way it is possible, for example, to embed a spherical domain inside a cube, by dissipating the regions close to the corners, with a radial envelope. Here we re-elaborate this idea and apply it to numerical relativity, in a pretty straightforward way.

Hyperviscoscous terms of the type $\nu_n \nabla^n f$, with ν_n a numerical coefficient, are able to dissipate quickly ripples and numerical artifacts, but they might reduce dramatically time-step since they involve high-order derivatives and fast diffusion. The method presented here shows results with fourth-order dissipation (but the technique can be extended to any order.) We make use of a technique for the hyperviscous terms based on the implicit, second-order Crank-Nicholson method (Smith, 1985). We will apply this technique only to the BSSN code, which is a stable method for solving problems such as binary mergers and black hole dynamics.

For any variable of the BSSN method, we advance in time the solution $f^{\{ideal\}}(\boldsymbol{x}, t)$ by using the second-order Runge-Kutta described in equation (2.30). Simultaneously, we evolve in time an accompanying, twin field $f^{\{H\}}(\boldsymbol{x}, t)$ which obeys the same BSSN equation but is also subject to hyperviscous dissipation, being therefore highly damped. We advance in time this hyperviscous field $f^{\{H\}}(\boldsymbol{x}, t)$ by using a Crank–Nicolson (CN), semi-implicit method. The CN integration can be easily matched with the Runge–Kutta method and it is numerically very stable with respect to viscous dynamics. For any BSSN hyper-dissipated variable we have an evolution equation of the type

$$\frac{\partial f^{\{H\}}(\boldsymbol{x},t)}{\partial t} = N(\boldsymbol{x},t) - \nu_4 \nabla^4 f^{\{H\}}(\boldsymbol{x},t), \tag{2.33}$$

where N indicates the BSSN evolution equation and ν_4 is the hyper-viscous coefficient. In the case of the "ideal" BSSN set of equation, $\nu_4 = 0$ and taking the Fourier transform, from the typical Runge-Kutta 2-steps method one gets

$$\frac{\widetilde{f}_{\boldsymbol{k}}^{\{ideal\}}(t^* + \Delta t) - \widetilde{f}_{\boldsymbol{k}}^{\{ideal\}}(t^*)}{\Delta t} = \widetilde{N}_{\boldsymbol{k}} \left(t^* + \frac{\Delta t}{2} \right),$$

at a given time t^*, for any Fourier coefficient $\widetilde{f}_{\boldsymbol{k}}^{\{ideal\}}$, at a given wavenumber $\boldsymbol{k}$. At each time t^* we start with $f^{\{H\}}(\boldsymbol{x},t) = f^{\{ideal\}}(\boldsymbol{x},t)$. Proceeding in a similar way for the hyper-viscous accompanying field $f^{\{H\}}$, and making implicit the linear hyper-viscous term on the *rhs*, one obtains

$$\frac{\widetilde{f}_{\boldsymbol{k}}^{\{H\}}(t^* + \Delta t) - \widetilde{f}_{\boldsymbol{k}}^{\{H\}}(t^*)}{\Delta t} = \widetilde{N}_{\boldsymbol{k}} \left(t^* + \frac{\Delta t}{2} \right) - \frac{\nu_4 k^4}{2} \left[\widetilde{f}_{\boldsymbol{k}}^{\{H\}}(t^* + \Delta t) + \widetilde{f}_{\boldsymbol{k}}^{\{H\}}(t^*) \right].$$

At this point, for any damped field, it is easy to get the time-splitting, second-order CN formula,

$$\widetilde{f}_{\boldsymbol{k}}^{\{H\}}(t^* + \Delta t) = \left[\frac{1 - \frac{\nu_4 k^4}{2} \Delta t}{1 + \frac{\nu_4 k^4}{2} \Delta t} \right] \widetilde{f}_{\boldsymbol{k}}^{\{H\}}(t^*) + \left[\frac{\Delta t}{1 + \frac{\nu_4 k^4}{2} \Delta t} \right] \widetilde{N}_{\boldsymbol{k}} \left(t^* + \frac{\Delta t}{2} \right), \tag{2.34}$$

which is stable and particularly easy to implement in pseudo-spectral codes. For all the BSSN variables, we advance in time equation (2.34) for both the ideal fields $\widetilde{f}_{\boldsymbol{k}}^{\{ideal\}}$ ($\nu_4 = 0$) and the hyperviscous counterparts $\widetilde{f}_{\boldsymbol{k}}^{\{H\}}$ ($\nu_4 \neq 0$). By taking the inverse transform now one has both fields $f^{\{ideal\}}(\boldsymbol{x}, t + \Delta t)$ and $f^{\{H\}}(\boldsymbol{x}, t + \Delta t)$ and then has to deal with the solutions match. The scope is to suppress spurious effects only at the boundaries, therefore we interpolate between the two solutions gradually (or in a Heaviside way) going towards the borders, only in a region close to the boundaries. With this procedure, we retain the pure, ideal dynamics of the BSSN formalism in the center of the box. Overall, the price to pay for the IHB is that we have to double the time of integration, slowing down the computation. On the other hand, the method gives clear benefits on the stability and the goodness to the solutions, as we shall see in the next subsections.

The `SFINGE` code has been presented in a series of recent works (Meringolo, Servidio, and Veltri, 2021; Meringolo and Servidio, 2021; Meringolo and Servidio, 2022; Imbrogno, Meringolo, and Servidio, 2022). In the next Chapter, we will discuss, more in detail, some main results obtained with our code.

Chapter 3

Numerical simulations of the spacetime: from standard testbeds to multiple black holes dynamics

In this Chapter, we perform direct numerical simulations, by evolving both the ADM (2.7) and the BSSN equations (2.14), in vacuum conditions and a number of different configurations. We split our campaign of simulations into three parts.

In the first Section (3.1) we start via standard gravitational testbeds, revealing that the filtered pseudo-spectral technique is among the most accurate approaches. After these typical, fundamental tests, we propose a new possible initial data that leads to stationary, large amplitude, nonlinear waves. Then, we stress our code via a single Schwarzschild black hole and the head-on collision of two black holes.

In the second Section (3.2) we discuss, in more detail, the aliasing problem, that can afflict the spectral methods. In particular, we inspect the emergence of numerical artifacts, in a variety of conditions. By monitoring the highest $k-$modes of the dynamical fields, we identify the culprits of the aliasing and propose procedures that cure such instabilities, based on the suppression of the aliased wavelengths.

Finally, in Section (3.3), we evolve the full 3D dynamics of different singular spacetimes. Here we abandon the ADM formalism in favor of the BSSNOK. In particular, we describe the binary system of black holes, and three black hole collisions, using different initial configurations. We then analyze the gravitational emission using the *Newman-Penrose* formalism, performing a refined analysis of the signals via Fourier and Shannon wavelet spectra. The analysis reveals net differences between the 2- and the 3-BHs cases, revealing, in the latter, multiple frequencies produced during the evolution. All the simulations have been performed by using a parallel architecture based on MPI directives, at the Newton HPPC Computing Facility at the University of Calabria. In this work, no commercial or external codes have been used.

3.1 Standard numerical testbeds

In this Section we perform direct numerical simulations in order to validate our numerical procedure, starting via standard gravitational testbeds (Alcubierre et al., 2004; Dumbser et al., 2018; Alic et al., 2012; Cook, 2000a). For each initial data, we check the accuracy by inspecting the conservation of several quantities, for both the ADM and BSSN formalism. Regarding the spatial integration, we show how to stabilize the pseudo-spectral code by varying our dealiasing filter in the projection (2.27), by changing both the k^* and the filter shape. For the time integration, in each test, we apply the RSC by monitoring the characteristic times in (2.31). After these typical, fundamental tests, we show a new possible initial data that leads to stationary, large amplitude, nonlinear waves. These waves bounce with growing amplitude and therefore represent another good test for numerical relativity. We will then move to more stressful conditions, such as the Gowdy spacetime (both forward and backward in time) and the Schwarzschild equilibria. All the simulations performed are summarized in table 3.1, where we report all the main parameters used, such as the type of the initial condition, the number of points of the spatial grid, the k^* of anti-aliasing filter, the type of filter, the formalism adopted, and so on. In the last column, for the reader's convenience, we also report the stability of the run.

3.1.1 The gauge wave test

The gauge wave test is based on a gauge transformation of the Minkowski spacetime. As suggested by (Alcubierre et al., 2004), the metric is given by

$$ds^2 = -H(x,t)\,dt^2 + H(x,t)\,dx^2 + dy^2 + dz^2, \tag{3.1}$$

where $H(x,t) = 1 - A\ \sin\left[2\pi(x-t)\right]$ describes a sinusoidal modulation of amplitude A, propagating along the x-axis. Since derivatives are zero in the y and z directions, the problem is essentially 1D. The metric in equation (3.1) implies $\beta^i = 0$, and $K_{xx} = -\partial_t \gamma_{xx}/2\alpha$. For the spatial metric γ_{ij} one gets

$$\gamma_{ij} = \begin{pmatrix} 1 - A\ \sin[2\pi(x-t)] & 0 & 0 \\ 0 & 1 & 0 \\ 0 & 0 & 1 \end{pmatrix},$$

while the only nontrivial component of the extrinsic curvature is

$$K_{xx} = -A\pi \frac{\cos[2\pi(x-t)]}{\sqrt{1 - A\ \sin[2\pi(x-t)]}}.$$

It is easy to demonstrate that the above fields satisfy the initial data constraints in equations (2.8).

In order to stress the stability of our new code, we solved the ADM equations (2.7) and the slicing (2.19), with both small- and large-amplitude initial conditions (Dumbser et al., 2018). We chose a spatial domain $x \in [0,1]$ with a number of meshes $N_x = 64$. The initial time-step is $\Delta t = 5 \times 10^{-3}$ and, according to the literature, we used the harmonic slicing, namely $f(\alpha) = 1$ in equation (2.19). For the first run, Run 1 in table 3.1, we impose $A = 10^{-2}$ and for the numerical technique, we choose the filtering mode $k^* = N_x/3$, with the smooth filter described by equation (2.29). In order to test the RSC method described in Section 2.5.2, the run was performed twice: with a fixed time-step (Run 1) and with an adaptive-time-refinement suggested by the RSC method (Run 2). Figure 3.1 (a) shows the evolution of the characteristic times given by equation (2.31). Note that only the characteristic times associated with the non-null fields have been reported, namely $\mathcal{T}_{K_{xx}}$, $\mathcal{T}_{\gamma_{xx}}$ and $\mathcal{T}_{\alpha}$. The full (black) line represents the time-step Δt of the simulation. One can immediately see that when a dynamical time $\mathcal{T}_f$ becomes on the order of the time-step, instabilities arise and the code crashes. In the second test, reported in panel (b) of the same figure, we repeated the experiment with the RSC switched on. In particular, we set the adaptive time refinement in equation (2.32) with $C = 1/6$, and the time-step has

TABLE 3.1: Table of simulations. From left to right: the run number, the initial condition, the mesh points, the k^* of the filter, the filter type, the RSC status, the IBH status, the formalism used and, finally, the stability of the simulation. Here "✓" stands for on, and "×" for off.

Run	IC	N	k^*	Filter	RSC	IBH	Formalism	Stable
1	Gauge wave	64	$N/3$	S	×	×	ADM	no
2	Gauge wave	64	$N/3$	S	✓	×	ADM	yes
3	Gauge wave	128	∞	/	✓	×	ADM	no
4	Gauge wave	128	$N/3$	S	✓	×	ADM	yes
5	Gauge wave	128	$N/2.5$	H	✓	×	ADM	yes
6	Gauge wave	128	$N/2.5$	S	✓	×	ADM	yes
7	Gauge wave	128	$N/3$	S	✓	×	BSSN	yes
8	Gauge wave	128	$N/3$	S	✓	×	BSSN	yes
9	Robust stab. (n = 1)	64	∞	/	×	×	ADM	no
10	Robust stab. (n = 2)	128	∞	/	×	×	ADM	no
11	Robust stab. (n = 4)	256	∞	/	×	×	ADM	no
12	Robust stab. (n = 1)	64	$N/4$	H	×	×	ADM	no
13	Robust stab. (n = 1)	64	$N/4$	S	×	×	ADM	yes
14	Robust stab. (n = 1)	64	$N/4$	H	×	×	BSSN	no
15	Robust stab. (n = 1)	64	$N/4$	S	×	×	BSSN	yes
16	Robust stab. (n = 1)	64	$N/4$	H	✓	×	BSSN	yes
17	Robust stab. (n = 1)	64	$N/4$	S	✓	×	BSSN	yes
18	Standing wave	64	∞	/	✓	×	ADM	no
19	Standing wave	64	$N/3$	S	✓	×	ADM	yes
20	Standing wave	64	$N/3$	H	✓	×	ADM	no
21	Standing wave	64	$N/3$	S	✓	×	ADM	yes
22	Gravitational wave	64	$N/4$	S	×	×	ADM	yes
23	Gravitational wave	128	$N/8$	S	×	×	BSSN	yes
24	Gowdy forw. (n = 1)	64	$N/5$	S	✓	×	BSSN	yes
25	Gowdy forw. (n = 2)	128	$N/5$	S	✓	×	BSSN	yes
26	Gowdy forw. (n = 4)	256	$N/5$	S	✓	×	BSSN	yes
27	Gowdy backward	64	$N/5$	S	✓	×	ADM	yes
28	Gowdy backward	64	$N/5$	S	✓	×	BSSN	yes
29	Schwarzschild BH	64^3	$N/2$	H	✓	×	ADM	no
30	Schwarzschild BH	64^3	$N/2$	S	✓	×	ADM	no
31	Schwarzschild BH	64^3	$N/2$	H	✓	×	BSSN	no
32	Schwarzschild BH	64^3	$N/2$	S	✓	×	BSSN	yes
33	GW absorbtion	128	$N/4$	S	✓	✓	BSSN	yes
34	Head on collision	128^3	$N/2$	S	✓	×	BSSN	no
35	Head on collision	128^3	$N/2$	S	✓	✓	BSSN	yes

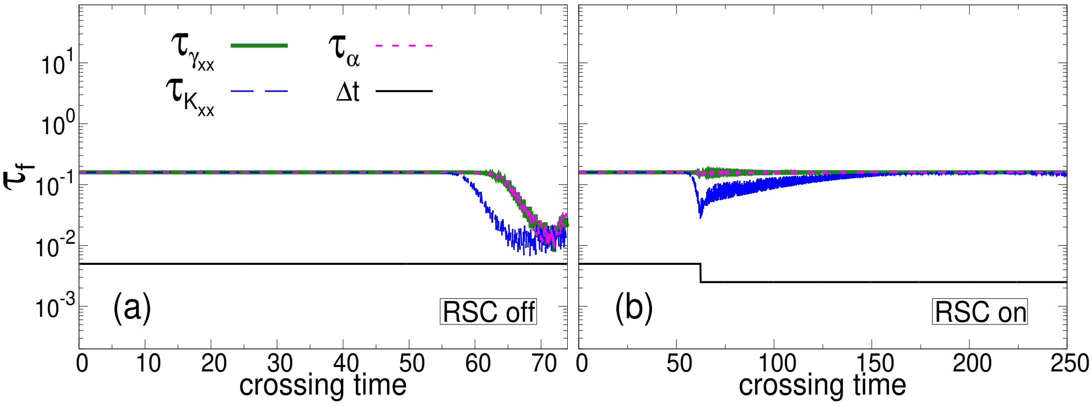

FIGURE 3.1: Small amplitude gauge wave test for the ADM code. Left: RSC conditions without adaptive time refinement (Run 1). The code crashes at $t \simeq 75$. Right: RSC conditions with $C = 1/6$ (Run 2): the simulation remains stable. The full black line represents the time-step.

been halved any time that the condition is violated. The run is therefore stabilized and carried out until 250 crossing times. This simulation is reported as Run 2 in table 3.1. Similar behavior has been obtained for other initial data (not shown here).

For the large-amplitude regime of the gauge-wave test, we have chosen $A = 0.9$ and $A = 0.96$, with a spatial grid along the x-axis of $N_x = 128$ points and $\Delta t = 10^{-3}$. The other parameters are the same as in the small amplitude case, including the slicing gauge. Again we have performed two experiments: first without anti-aliasing filter (Run 3) and second with a $k^* = N/3$ smooth filter (Run 4), defined in equation (2.29). A comparison between the waveforms of the extrinsic curvature trace K, in both cases, has been represented in the top-row of figure 3.2. As can be seen, there is a net improvement with the anti-aliasing filter. One can observe, overall, an excellent agreement between the exact and the numerical solutions. In the unfiltered case, numerical instabilities arise, as can be seen in panel (a). The analogous filtered simulation is reported in (b).

A second, more challenging test has been performed, with a larger perturbation, i. e. $A = 0.96$. We found that now a stable solution can be achieved even with $k^* = N/2.5$. In order to test the different anti-aliasing filters we performed the test twice: Run 5 uses the Heaviside filter defined in equation (2.28) while Run 6 adopts the smooth filter (2.29). The panel (d) of figure 3.2 shows the L_2 errors of the $x-$momentum constraint, where L_2 norm is given by

$$\|\ldots\|_2 = \sqrt{\frac{\int_\Omega (\ldots)^2 \, d\Omega \sqrt{|\gamma|}}{\int_\Omega d\Omega \sqrt{|\gamma|}}}, \tag{3.2}$$

where $d\Omega \sqrt{|\gamma|}$ is the volume element. The smooth filter again stabilizes the code. In figure 3.2 (c) we report the waveform of K at time $t = 10$, which is in very good agreement with the exact solution. It is important to emphasize that the last set of runs, where $A = 0.96$, is considered to be a very strong stress for codes, as discussed in (Dumbser et al., 2018).

For this testbed, we obtained similar results for the BSSN code. Our conformal model follows the approach by Zlochower et al., 2005. We used $A = 10^{-2}$ (Run 7) and $A = 10^{-1}$ (Run 8), a spatial grid with $N_x = 128$ mesh points and a time-step

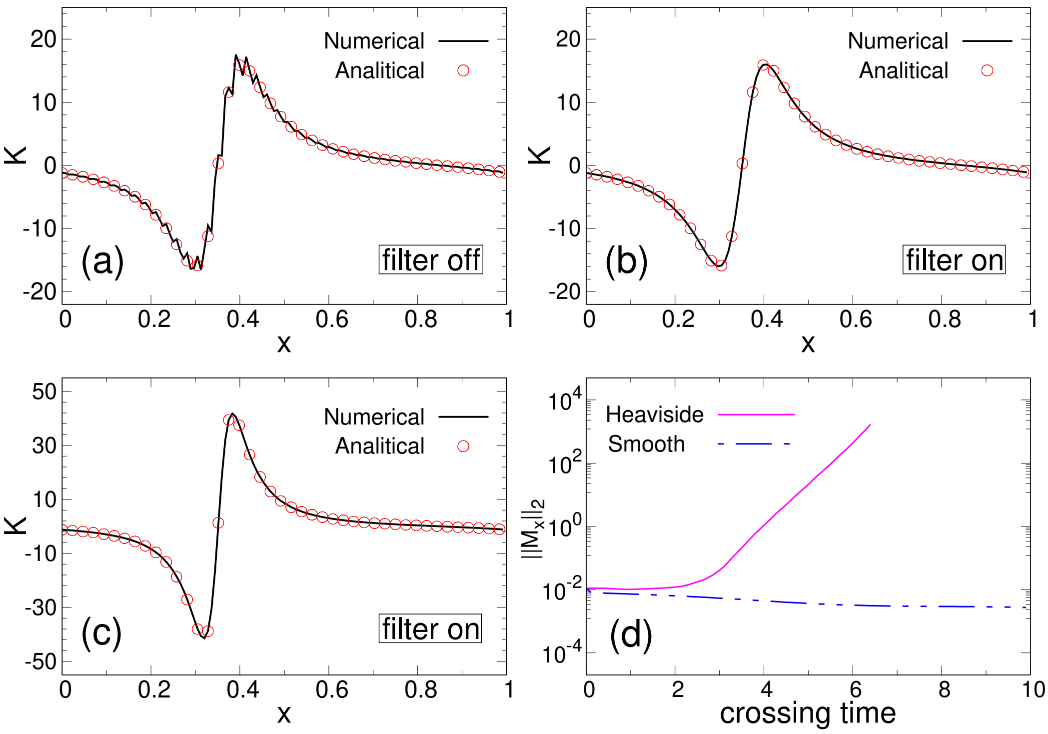

FIGURE 3.2: Gauge wave test with the ADM formulation. (a) Run 3, the trace of the extrinsic curvature K in a nonlinear regime ($A = 0.9$), without filter, at $t = 1.2$ (full black line). The exact solution is reported with (red) circles. (b) Run 4, same as Run 3 but with a smooth filter at $k^* = N_x/3$. The anti-aliasing filter leads to an improved waveform. (c) Run 6, K for the case with very high amplitude $A = 0.96$, at $t = 10$, using the smooth filter. (d) Evolution of $x-$momentum constraint for the very high amplitude case, using Heaviside (Run 5) and smooth (Run 6) filter.

$\Delta t = 5 \times 10^{-4}$. The harmonic gauge in equation (2.19) has been used. In order to better stabilize the simulation, a smooth filter with $k^* = N/3$ has been chosen, for both amplitudes, similar to the ADM cases. The left panel of figure 3.3 shows the L_2 errors of the Hamiltonian for the two amplitudes, while in the right panel, we compare the wave-form of γ_{xx}, at $t = 500$. At this time, the norm of the Hamiltonian violation $||H||_2$ is about 0.1% of A, for the case with $A = 10^{-2}$. The run shows an excellent agreement between numerical and exact solutions.

In agreement with the existing literature (see for example Jansen, Bruegmann, and Tichy, 2006), we found that generally, the BSSN formalism is less able to handle gauge waves compared to the ADM [1]. The present results are also in agreement with the simulations in Zlochower et al., 2005; Daverio, Dirian, and Mitsou, 2018, although the Hamiltonian error shown here is at least one order of magnitude smaller than the one presented in the above works. This good performance is evidently due to the precision of the spectral representation, accompanied by the RSC and the dealiasing filters.

---

[1] This difference is mainly due to truncation and roundoff error propagation. The BSSN formalism involves a higher number of products than the ADM. Just as an example, by using double precision (that we use throughout the paper), even the initial Hamiltonian is already $\sim 10^{-16}$. We checked that by switching to quadruple precision the errors reduces to $H \sim 10^{-32}$.

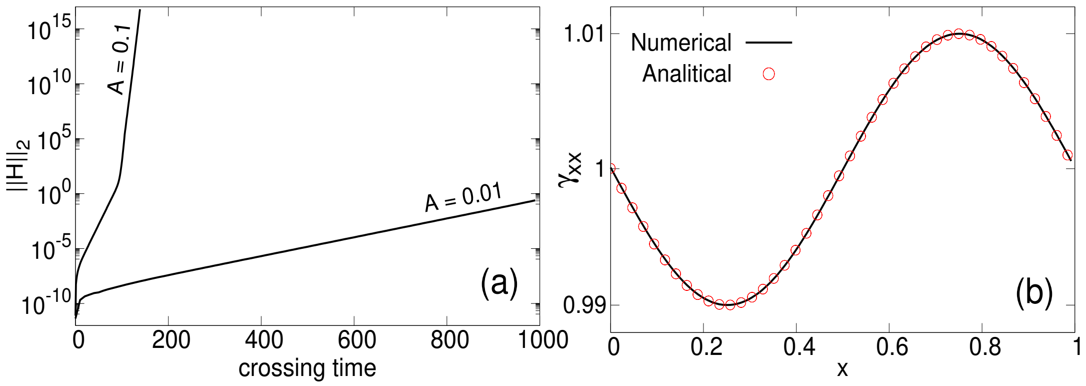

FIGURE 3.3: (a) Hamiltonian violation $||H||_2$ for the gauge wave, for the BSSN simulations Run 7 ($A = 0.01$) and Run 8 ($A = 0.1$). These results are in good agreement with Zlochower et al., 2005; Daverio, Dirian, and Mitsou, 2018. (b) γ_{xx} at $t = 500$, for Run 7 (line) and analytical (circles).

3.1.2 The robust stability test

The robust stability test is a classical initial condition for numerical relativity, particularly stressful from the numerical point of view, that makes use of random, small perturbations in the initial data. This testbed is able to initiate numerical instabilities that might exponentially grow in time, arising from small scales and propagating back to larger structures. These growing modes are quite dangerous since they might be confused with physical mechanisms. It is therefore important to inspect these numerical instabilities in order to prevent numerical artifacts.

The initial configuration consists of small random perturbations to the Minkowski space, where $ds^2 = -dt^2 + dx^2 + dy^2 + dz^2$, with the unperturbed metric η_{ij}. The numerical noise is distributed among every field. Since we base our numerical algorithm on the use of FFTs, we vary several resolutions, keeping the number of meshes as a power of 2. In order to follow the same configuration of (Alcubierre et al., 2004), we chose a spatial domain $x, y, z \in [0, 1]$, a number of grid points $N_x = 50\rho_n$, where the mesh size is therefore $\Delta x = 1/(50\rho_n)$ and the initial time-step is $\Delta t = 0.01/\rho_n$. Here we vary $\rho_n = 64n/50$, with $n = 1, 2, 4$. To speed up calculations, we use only four grid points in the y and z directions. We solve the equations by using the harmonic gauge, i.e. $f(\alpha) = 1$ in the slicing equation (2.19). In the ADM tests, the initial conditions are given by

$$\gamma_{ij} = \eta_{ij} + \varepsilon_{\gamma_{ij}}\,, \quad K_{ij} = \varepsilon_{K_{ij}}, \quad \alpha = 1 + \varepsilon_\alpha, \tag{3.3}$$

where ε_f are random independent perturbations with

$$\varepsilon_f \in \left[-10^{-10}/\rho_n^2, 10^{-10}/\rho_n^2\right]. \tag{3.4}$$

In our robust stability tests, we vary the resolution (n), the type of the dealiasing filter (Heavyside or smooth), and we vary from fixed time-step to the RSC. The goodness of our numerics has been monitored by looking at the evolution of the constraints in time, such as the L_2-norm of the Hamiltonian constraint.

In figure 3.4 (a) we report the Hamiltonian error, for different resolutions, namely for $n = 1, 2, 4$. No anti-aliasing filters have been used for the runs in this panel. As can be seen, the code becomes suddenly unstable. These runs are reported in

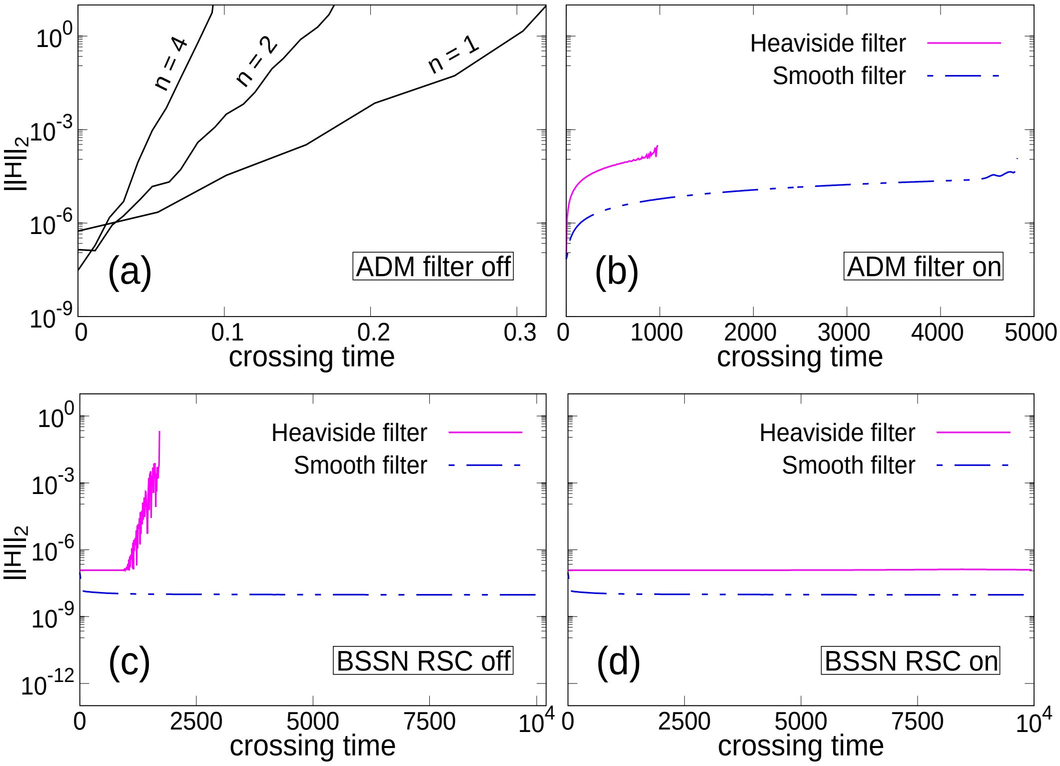

FIGURE 3.4: Hamiltonian constraints $||H||_2$ for the robust stability test. (a) Results for the ADM code, with $n = 1$ (Run 9), $n = 2$ (Run 10), and $n = 4$ (Run 11). No RSC and no anti-aliasing filters have been used. (b) Same ADM simulations, with filters at $k^* = N/4$, as described by equations (2.28)-(2.29), $\Delta t = 10^{-3}$ (fixed, no RSC) and $n = 1$. These runs are labeled as Run 12 and Run 13. (c) Results from the BSSN code, using filters and no RSC with $\Delta t = 10^{-3}$ (Run 14 and Run 15). (d) Same simulations, for the BSSN, with the RSC (Run 16 and Run 17). Numerical stability has been achieved with the combined use of filters and time-step conditioning.

table 3.1 , labeled as Run 9–Run 11. In order to show the benefit of the anti-aliasing filters and the robustness of the code, a second set of tests has been performed, by using filters at $k^* = N/4$, but without RSC. A time-step of $\Delta t = 10^{-3}$ and $n = 1$ has been chosen. The L_2-norms of the Hamiltonian constraint are shown for these cases in figure 3.4 (b). The simulations show that, with the “Heaviside” filter in (2.28), the code becomes now stable until $t \sim 1000$, while is even more stable using the smooth filter. These runs are reported in table 3.1 , as Run 12 and Run 13.

We complete the robust stability test campaign with the BSSN approach and finally introduce the RSC condition. The parameters are the same as the ADM previous tests. For the slicing condition, we used the harmonic and hyperbolic Gamma-driver slicing in equations (2.20) and (2.21). The tests are carried out for $t = 10^4$ crossing times, at most. First, we compare the two filters described by equations (2.28)-(2.29), but keeping a fixed time-step of integration. In the bottom left panel of figure 3.4, we show the $||H||_2$ for the two filters. Note that using the Heaviside filter the code crashes at $t \sim 2000$ crossing times (Run 14) while using the smooth version it remains more stable (Run 15). In panel (d), finally, we show the same tests with the RSC, by using an adaptive time refinement with $C = 1/4$, as described in Section 2.5.2. In this case, the full algorithm stabilizes the simulation until $t = 10^4$ crossing times (Run 16–Run 17). The stability of the run has been achieved with the

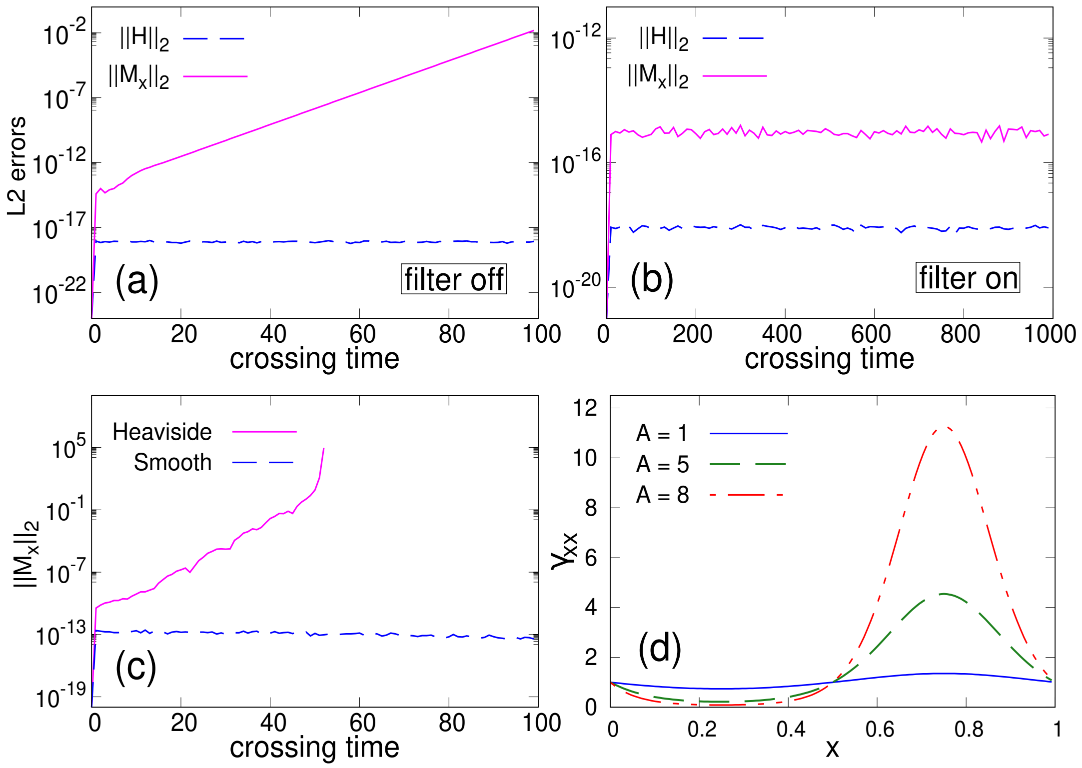

FIGURE 3.5: (a) L_2 norm of Hamiltonian and $x-$momentum violation for the standing waves (Run 18). Without an anti-aliasing filter, the Hamiltonian constraint remains constant while the $x-$momentum constraint grows exponentially. The evolution is carried out for $t = 100$ crossing times. (b) Same simulations but with a smooth filter at $k^* = N/3$: both constraints remain negligible (Run 19). (c) The $x-$momentum constraint for the nonlinear test ($A = 8$), using both anti-aliasing filters at $k^* = N_x/3$ (Run 20 and Run 21). The comparison emphasizes again the goodness of the smooth filter. (d) γ_{xx} for the standing wave test, for different amplitudes. As the amplitude increases, the wave becomes more asymmetric.

combined use of filters and adaptive time-integration.

3.1.3 New initial data: the standing waves

Here we propose a very simple, 1D, initial set of data that satisfies equations (2.8) and that can be used to test codes in numerical relativity, with various amplitudes. This initial condition consists of simple initial data for the extrinsic curvature only, on an initial flat metric, that suddenly produces some non-propagating, oscillatory modes. The physical pattern consists of a “bouncing metric”. This solution to the constraint conditions is not supposed to have an immediate physical application, as in many of the other testbeds, but only for testing purposes. However, it might have some applications and similarities with cosmological models of inflation. For this regard, see for example Adamek et al., 2020.

The initial spatial metric γ_{ij} obeys Minkowski flat space, which means zero curvature and where Ricci tensor vanishes ($R = 0$). In this case, the Hamiltonian and the momenta constraints reduce to

$$K^2 - K_{ij}K^{ij} = 0, \tag{3.5}$$

$$D_i(K^{ij} - \gamma^{ij}K) = 0, \tag{3.6}$$

respectively. We now chose an initial perturbation only for the extrinsic curvature K_{ij}, with a Minkowski flat initial metric. With this choice, one has:

$$\gamma_{ij} = \eta_{ij}\,, \qquad K_{xx} = A\ \sin(2\pi x),$$

and $K_{ij} = 0$ otherwise, which satisfies constraints in equation (3.5). Unlike the previous case of gauge waves, this condition does not lead to wave propagation in space but to standing waves of the metric. One can stress the code by increasing the amplitude of the extrinsic curvature perturbation A, as follows.

In figure 3.5 we report the time evolution of the metric, for several ADM tests. For Run 18, a small amplitude $A = 10^{-1}$ and no anti-aliasing filter have been used. We chose a spatial domain with $x \in [0, 1]$ and a spatial grid $N_x = 64$. The time-step is $\Delta t = 10^{-3}$ and the harmonic slicing $[f(\alpha) = 1]$ has been chosen. The simulation has been carried out until 100 crossing times. We have carried out a second test (Run 19) with the same parameters but choosing a smooth filter with $k^* = N_x/3$, as reported in figure 3.5 (b). It is evident that the filter improves the stability, in fact, this run is carried out until 1000 crossing times. The top panels of figure 3.5 show that the Hamiltonian constraint remains constant in both cases, but the $x-$momentum constraint (for the symmetry of the problem the $y-$momentum and z-momentum are zero) grows without filter and remains constant with $k^* = N/3$.

In order to test a more nonlinear case, a second, high-amplitude condition has been used, where we chose $A = 8$, a spatial grid with $N_x = 128$ points, and a $k^* = N/3$ filter. All the other parameters have been chosen as in the previous tests, as summarized in the table . The higher amplitude of A now induces asymmetry in the standing wave. The metric starts to bounce and becomes asymmetric. Again, this test has been performed twice: a first test (Run 20) using the standard truncated filter described by equation (2.28) and a second one (Run 21) with the filter in equation (2.29). The time-evolution of L_2 norm of $x-$momentum constraint, computed using the definition in equation (3.2), is shown in the panel (c) of figure 3.5, for both cases. It is clear that the smooth filter works better than the Heaviside filter.

We ran the same tests for the BSSN code (not shown), setting $A = 10^{-1}$, a spatial grid with $N_x = 64$ points, a time-step $\Delta t = 10^{-4}$ and the “1 + log” slicing (i.e. $f(\alpha) = 2/\alpha$ in equation (2.19) and $\beta^i = \partial_t \beta^i = 0$). The tests are carried out until 100 crossing times. Similarly, as in the previous ADM tests, the smooth filter better stabilizes the code.

3.1.4 The gravitational wave test

In this subsection, we test the `SFINGE` code with both the ADM and the BSSN formalisms, via linear gravitational waves. In particular, we check whether they are able to retain accuracy, for long spacetime travels, by comparing amplitudes and phases with the well-known analytical solution. This solution to the linearized Einstein field equation can be written as

$$ds^2 = -dt^2 + dx^2 + (1 + b)\, dy^2 + (1 - b)\, dz^2, \tag{3.7}$$

where $b = A\ \sin[2\pi(x-t)/d]$ and $d = 1$ is the linear size of the propagation domain. The wave amplitude is small, in order to satisfy the linear regime conditions. The metric in equation (3.7) represents the transverse-traceless gauge in which the wave amplitudes are purely spatial, with null trace and transverse to the propagation direction. It describes a wave propagating along the x axis, with the polarization aligned with the y and z axes (Anninos et al., 1997). This metric is written in Gauss coordinates, that is $\alpha = 1$ and $\beta^i = 0$. Using this metric, the extrinsic curvature reduces to $K_{ij} = -\partial_t \gamma_{ij}/(2\alpha)$, so that the nontrivial components reduce to $K_{yy} = \frac{1}{2}\partial_t b$ and $K_{zz} = -\frac{1}{2}\partial_t b$. Since this wave propagates along the x-axis and all derivatives are zero in the y and z directions, the problem is essentially 1D. We chose a spatial domain $x \in [0,1]$ on a spatial grid with $N_x = 64$, with an initial $\Delta t = 10^{-3}$ and the harmonic slicing. We use a very small amplitude, namely $A = 10^{-8}$, in order to satisfy the linearity of the simulation (Dumbser et al., 2018). The evolution is carried out up to $t = 1000$ and a smooth filter, described by equation (2.29), with $k^* = N/4$, has been used.

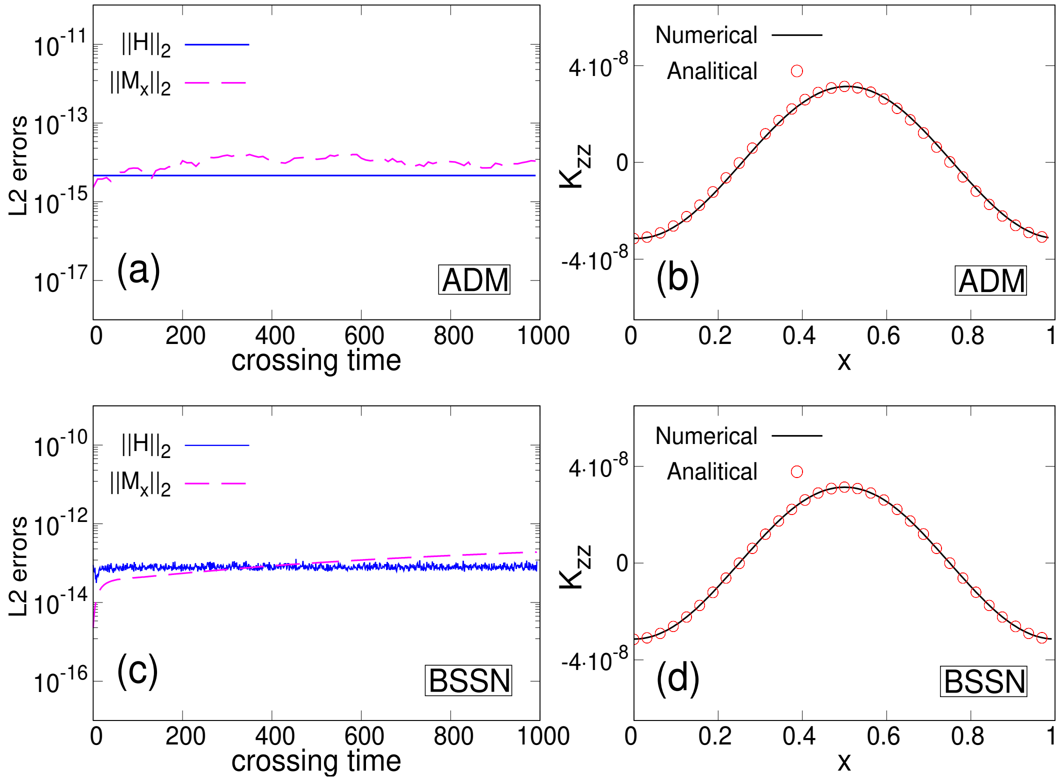

FIGURE 3.6: Gravitational wave test. (a) L_2 norm of ADM constraints (Run 22). A smooth filter with $k^* = N_x/4$ has been used. (b) Comparison of K_{zz} and its exact solution, at $t = 1000$ for the same run. (c) Constraints for the BSSN simulation (Run 23). (d) Comparison of the waveform of K_{zz} with the exact solution at $t = 1000$, for the same run. A smooth filter with $k^* = N_x/8$ has been used for this simulation.

Figure 3.6 (a) represents the time evolution of the L_2 norm of ADM constraints. The errors are well bounded. In panel (b) we compare the wave-form of K_{zz} at the final time, i.e. at $t = 1000$, showing overall an excellent agreement between numerical and exact solutions. This run is reported in table 3.1 as Run 22. We performed an analogous test with the BSSN formalism, choosing $N_x = 128$, $\Delta t = 5 \times 10^{-5}$, with the harmonic slicing and the "Gamma-driver" shift condition. The evolution is carried out again for a time of $t = 1000$ and the smooth filter with $k^* = N_x/8$ has been used. This run is labeled in table 3.1 as Run 23. The bottom left panel of figure 3.6 shows the L_2 Norm of the Hamiltonian, and the bottom right panel of the same figure shows the excellent agreement with the analytical solution for the waveform of K_{zz}, at the final time. It is important to stress that, in the BSSN runs, the choice of a stronger dealiasing filter has been used in order to obtain a longer time, stable and accurate simulation. We also point out that here we used a finer grid so that the simulation corresponds essentially to the ADM runs. More points are now needed since the BSSN is less accurate. As discussed in previous Sections, this is related to the fact that BSSN is a more elaborated formalism, where a larger number of products leads to higher truncation errors and therefore to less precise solutions (Alcubierre et al., 2004).

In summary, the gravitational wave test, therefore, is well solved via both algorithms, the smooth filter stabilizes the code for very long times, giving a very good representation of the solution.

3.1.5 The Gowdy spacetime

All the tests described so far considered perturbations to the flat metric. In this Section, we deal with a genuinely curved exact solution, known as the polarized Gowdy spacetime (Daverio, Dirian, and Mitsou, 2018; Zlochower et al., 2005). The Gowdy waves are vacuum cosmological models used to test codes in a strong field context and present a serious challenge for numerical relativity. These particular solutions of the vacuum Einstein equations on the 3-torus describe an expanding/collapsing universe, containing plane-polarized gravitational waves where

$$ds^2 = -\frac{e^{\lambda/2}}{\sqrt{t}}dt^2 + \frac{e^{\lambda/2}}{\sqrt{t}}dz^2 + te^P dx^2 + te^{-P}dy^2. \tag{3.8}$$

Here λ and P are functions of z and t only. The time coordinate t is chosen such that time increases as the universe expands. The metric is singular at $t = 0$ which corresponds to the cosmological singularity. We will carry out our tests in both time directions, i.e. in the collapsing and expanding dynamics.

With the metric described by (3.8), the Einstein equations lead to (Alcubierre et al., 2004; New et al., 1998)

$$P(z,t) = J_0(2\pi t)\,\cos(2\pi z), \tag{3.9}$$

$$\begin{aligned}\lambda(z,t) = {} & -2\pi J_0(2\pi t)\,J_1(2\pi t)\,cos^2(2\pi z) + 2\pi^2 t^2\left[J_0^2(2\pi t) + J_1^2(2\pi t)\right] \\ & -\frac{1}{2}\left[4\pi^2\left[J_0^2(2\pi) + J_1^2(2\pi)\right] - 2\pi J_0(2\pi) + J_1(2\pi)\right],\end{aligned} \tag{3.10}$$

where J_0 and J_1 are Bessel functions. Equations (3.9) and (3.10) yields a diagonal spatial metric of the type

$$\gamma_{xx} = te^P\ , \quad \gamma_{yy} = te^{-P}\ , \quad \gamma_{zz} = \frac{e^{\lambda/2}}{\sqrt{t}}.$$

To complete the initial data conditions, the extrinsic curvature is obtained as a time derivative of the metric. Since the metric (3.8) depends only on the $z-$direction, the spatial evolution is 1D. We chose a spatial domain $z \in [0,1]$, with $N_z = 50\rho_n$,

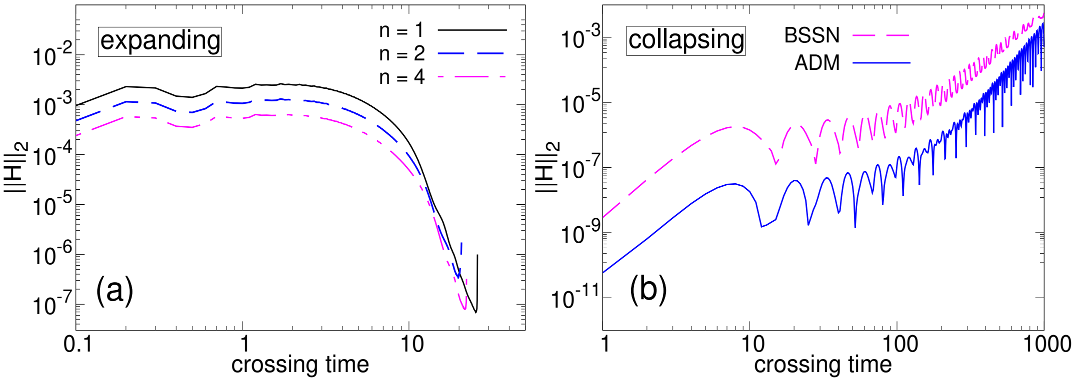

FIGURE 3.7: (a) Constraint violation $||H||_2$ for the BSSN pseudo-spectral code, for the expanding Gowdy spacetime, at different resolutions (Run 24–Run 26). (b) Same, for both ADM (Run 27) and BSSN (Run 28), for the collapsing spacetime and $n = 1$.

$\Delta z = 1/(50\rho_n)$ (see before), and a $\Delta t = 5 \times 10^{-4}/\rho_n$. In all the Gowdy tests, we used a $k^* = N_z/5$, smooth, anti-aliasing filter.

In the expanding form, the time coordinate t increases during the evolution of the simulation, P approaches zero asymptotically and λ increases linearly. Since the metric is singular at $t = 0$, we set the initial data from the exact solution at $t = 1$ and proceed forward in time. Due to the exponential growth, such evolution may crash rather soon but it will test the accuracy of a code in a rather harsh situation. In figure 3.7 (a) we report the L_2 norm of the Hamiltonian, for the three resolutions $n = 1, 2, 4$ (Run 24–Run 26). The errors are bounded in all the tests and our results are in good agreement with the basic literature (Babiuc et al., 2008; Clough et al., 2015). Similar results have been found for the ADM simulation.

In the collapsing version, the time coordinate in the Gowdy metric can be transformed so that the initial singularity is approached asymptotically, and backwards. The new time coordinate τ is defined by $\tau = \frac{1}{c}\ln(t/k)$. In other terms, we replace $t \to ke^{c\tau}$, and the time-step $\Delta\tau$ is chosen to be negative. We choose a particular value of t_0 such that the initial slice is far from the cosmological singularity and, following the standard approach (Alcubierre et al., 2004), we chose the twentieth zero of the Bessel function, so that $J_0(2\pi t_0) = 0$. Finally we get $c \sim 2 \times 10^{-3}$ and $k \sim 9.6 \times 10^{13}$. In panel (b) of figure 3.7, we present a comparison between the ADM (Run 27) and BSSN (Run 28) runs, for the collapsing direction. The ADM code shows a smaller error on the Hamiltonian constraint, but both schemes proceed until 1000 crossing times ($\tau = -1000$). This evolution is less challenging than the expanding case since the lapse function is essentially exponential in τ so that the spacetime is becoming less dynamic. On the other hand, the value of the physical metric γ_{zz} at $t = t_0$ is of the order of 10^3. Overall, as it can be seen, also in this more challenging test, the pseudo-spectral code is able to handle the numerical evolution, with violation errors that are comparable (or smaller) than in the existing literature (Alcubierre et al., 2004).

3.1.6 The Schwarzschild Black Hole

In this classical test, we consider the stability of an isolated, Schwarzschild black hole (BH), in a fully 3D spatial geometry. The Schwarzschild metric is used as initial data to test the ability of the code to evolve BH spacetimes within the puncture approach (Campanelli et al., 2006; Hannam et al., 2007; Montero and Cordero-Carrión, 2012; Ruchlin et al., 2017). The metric in isotropic coordinates can be written as (Baumgarte and Shapiro, 2010)

$$ds^2 = \left(\frac{1 - m/(2r)}{1 + m/(2r)}\right)^2 dt^2 + \psi^4 \left(dr^2 + r^2 d\Omega^2\right),$$

where r is the isotropic radius, m is the mass of the black hole and

$$\psi = 1 + \frac{m}{2r}$$

is the conformal factor. The initial spatial metric and the extrinsic curvature become

$$\tilde{\gamma}_{ij} = \psi^{-4}\gamma_{ij} = \chi\, \gamma_{ij}, \qquad K_{ij} = 0,$$

respectively. The lapse is initially set to one and the shift is vanishing everywhere. For a Schwarzschild black hole both the linear momentum and the dimensionless spin are set to zero (Bowen and York, 1980).

We set the puncture mass $m = 1.0M$ and the runs are carried out until $t = 1000M$, corresponding to 1000 crossing times, unless the code becomes unstable. The spatial domain is $x, y, z \in [0, 300]$, with an isotropic spatial grid $N = 64^3$ and a time-step $\Delta t = 10^{-1}$. The 1 + log gauge condition is now used [i.e. $f(\alpha) = 2/\alpha$ in equation (2.19) and $\beta^i = \partial_t \beta^i = 0$], for both the ADM and BSSN tests.

In order to handle Schwarzschild equilibrium, since the puncture limits the differentiability of the solution, we shifted the position of the singularity by half grid-step, namely $\Delta/2$, for each Cartesian direction. In this regard, it is worth saying that exact spectral projections always allow us to obtain the field in the continuum via a simple phase-shift of the Fourier coefficients (Shallcross, Fox, and Capecelatro, 2020).

In panel (a) of figure 3.8 we report the evolution of the Hamiltonian error $||H||_2$, for the ADM (Run 29 and Run 30) and the BSSN tests (Run 31 and Run 32), with and without the smooth dealiasing filter. Here we found that $k^* = N/2$ is enough to stabilize the simulation. As expected, and as well known in the literature (Baumgarte and Shapiro, 2010; Alcubierre, 2008), the ADM formalism is not well suited for the simulations of singular objects such as BH's. Even if the ADM "beats" the BSSN formalism in several numerical challenges (see previous testbeds) regarding the precision, the BSSN remains one of the most stable numerical approaches for massive stars dynamics.

In figure 3.8 (b) we report the conformal factor $\chi = \psi^{-4}$ for a simulation with the same parameters of Run 32 but with higher resolution (128^3). We report a 1D cut through the center of the domain. The simulation shows slightly higher non-conservation (probably due to the choice of the time step), but it is extremely more precise, as we shall discuss later in the convergence tests of the Appendix. For this version of the algorithm, namely the filtered BSSN, the simulation is stable (due to the constraint propagation properties of BSSN), accurate and convergent.

As is clear from figure 3.8, the BSSN is able to simulate black hole dynamics, accurately, for long times. Even with very small dealising filters, with $k^* = N/2$, the BSSN retains the black hole shape and keeps a very small error on the constraints. However, the small violation of the periodicity, together with the high accuracy of the spectral code, might produce wiggles that propagate from the discontinuous

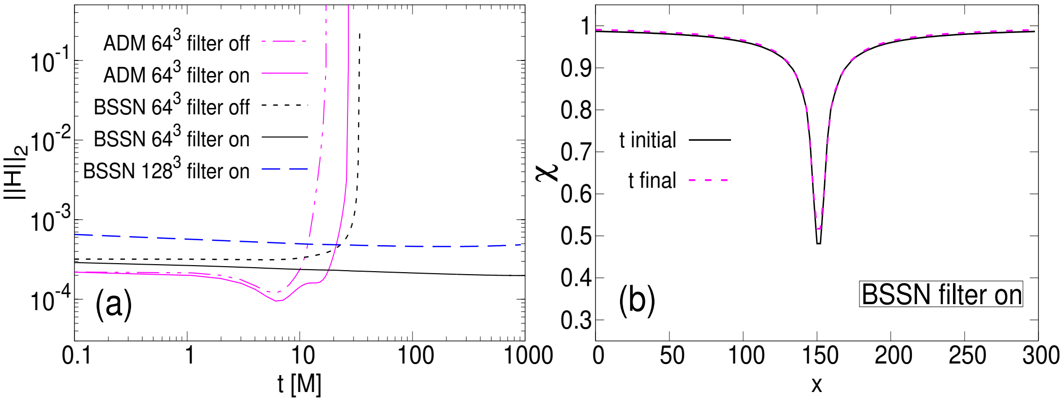

FIGURE 3.8: Simulations of the Schwarzschild black hole. (a) Comparison of the time history of the error $||H||_2$, between the ADM and the BSSN codes (Run 29 - Run 32). Note the log scale of the $x-$axis. (b) Conformal factor $\chi = \psi^{-4}$, at different times of the BSSN simulation, with the same parameters as Run 32, but higher resolution 128^3. A smooth filter $k^* = N/2$ has been used.

boundary. In the next Section, we will deal with these effects and cure this pathology by using our IBH method, described in Section 2.5.3.

3.1.7 Gravitational wavepacket absorption

In order to test the IHB method, we check whether the algorithm is able to absorb fluctuations that move outward, from the center of the domain toward the boundaries. At the initial time, we build a gravitational wavepacket, namely a windowing of the gravitational wave at the center of the domain via a Gaussian-shaped filter, as shown in figure 3.9-(a). As in the linearized gravitational wave test (see Section 3.1.4), the metric is given by equation (3.7). We initialize the perturbation $b(x, t = 0)$ as a wavepacket that propagates along the $x-$axis, with a Gaussian window of the type $\exp[-(\frac{x-x_0}{\sigma})^2]$. We set an amplitude of $A = 10^{-5}$, the wavenumber $k = 40$, and the width of the window $\sigma = 0.05$ is small enough in order to localize the waves in the center, namely $x_0 = L_0/2 = 1/2$, where $L_0 = 1$ is the domain.

In order to match the two solutions $f^{\{ideal\}}(\mathbf{x}, t)$ and $f^{\{H\}}(\mathbf{x}, t)$ in the IHB technique, we chose a linear matching when distance approaches the borders. In particular, at the end of each time step, we impose the BSSN variables

$$f(\boldsymbol{x}, t) = \begin{cases} f^{\{ideal\}}(\boldsymbol{x}, t) & \text{for } |\boldsymbol{x} - \boldsymbol{x}_0| \leq \lambda, \\ f^{\{ideal\}}(\boldsymbol{x}, t)\left[2 - \frac{|x-x_0|}{\lambda}\right] + f^{\{H\}}(\mathbf{x}, t)\left[\frac{|x-x_0|}{\lambda} - 1\right] & \text{otherwise.} \end{cases} \tag{3.11}$$

In the above matching-condition, we chose $\lambda = L_0/4$, namely one-quarter of the box. In this test, we set the hyperviscous coefficient $\nu_4 = 10^{-7}$. This test is labeled as Run 33 in table

With our IHB approach, when the packet is far from the boundaries, the BSSN evolution equation $f^{\{ideal\}}(\mathbf{x}, t)$ dominates in equation (3.11) – all the field equations evolve in the standard way. Otherwise, when the waves approach the boundaries, the hyperviscous terms of the type $\nu_4 \nabla^4 f$ dominate and the wavepacket is totally absorbed. The time history of the propagating gravitational wave is reported in figure 3.9. As it can be seen, the modulation moves coherently from the center of

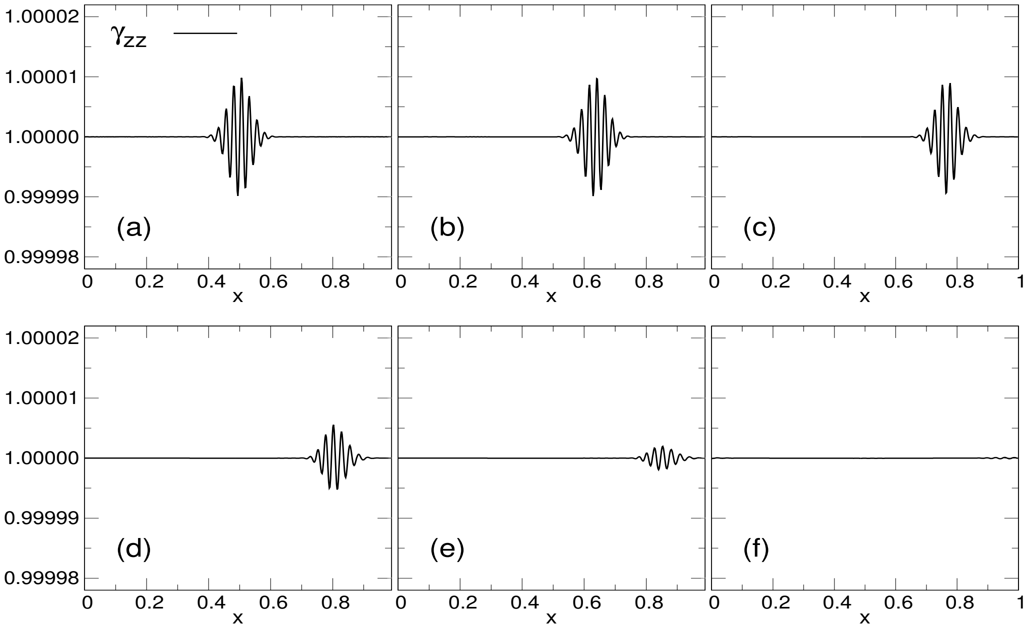

FIGURE 3.9: Absorption of a 1D wavepacket of gravitational waves using our Implicit Hyperviscous Boundary (IHB) method, for the Run 33. The panels show the section of the physical metric γ_{zz} at different times, i.e. $t = 0, 0.14, 0.26, 0.32, 0.37, 0.48$.

the domain, toward $L_0 = 1$. When the wavepacket enters the region of the viscous boundary, at $x = \frac{3}{4}L_0$, it starts to "feel" the hyperviscous damping in equation (2.33). Before approaching the borders, the wave is totally absorbed. Similar results (not shown here) have been obtained with other matching conditions, discussed in the next subsection. The method can be easily exported to 3D gravitational dynamics, in order to suppress boundary effects, as we will see in the next experiment.

3.1.8 Head-on collision of two Black Holes

In this last Section, we test the IHB technique via the head-on collisions of two equal-mass Misner-Wheeler-Brill-Lindquist (MWBL) black holes (Brill and Lindquist, 1963; Misner and Wheeler, 1957). The MWBL data represent conformally flat slices of multiple black holes space-times with n punctures. We test this black hole crash only via the most numerically stable approach, namely the BSSN spectral code, with a smooth filter in equation (2.29) and with the RSC active.

The parameters of the initial conditions are the following. The three-dimensional computational domain is $x, y, z \in [0, 25]$ and flat Minkowski spacetime is imposed as a boundary condition everywhere. We chose two identical black holes with masses $m_1 = m_2 = 0.5M$, $\mathbf{C_1} = \{10.5, 12.5, 12.5\}$ and $\mathbf{C_2} = \{14.5, 12.5, 12.5\}$, where the $\mathbf{C}_j$ are the locations of the two punctures. These parameters correspond to an initial separation of the BHs a little larger than that of an approximate innermost stable circular orbit (ISCO), as determined in (Baumgarte, 2000). The two punctures consist of two Schwarzschild solutions with initially zero linear momentum and spin, as described in Section 3.1.6.

As suggested by (Dumbser et al., 2018), the lapse is initially set to:

$$\alpha = \frac{1}{2}\left(\frac{1 - \frac{1}{2}(m_1/r_1^*) - \frac{1}{2}(m_2/r_2^*)}{1 + \frac{1}{2}(m_1/r_1^*) + \frac{1}{2}(m_2/r_2^*)} + 1\right)$$

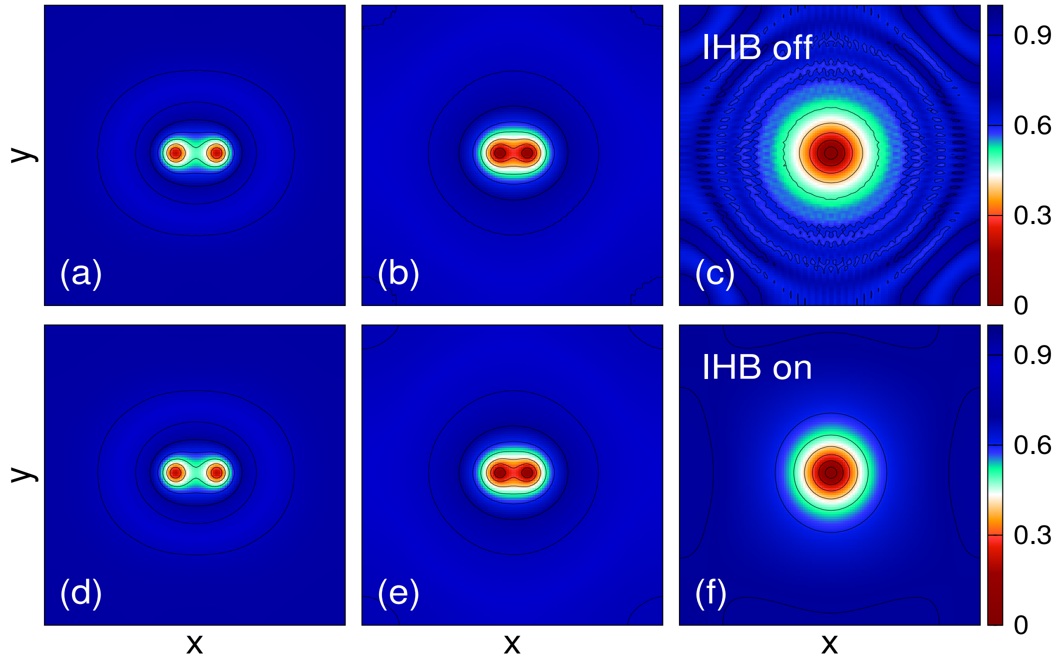

FIGURE 3.10: Time evolution of the contour surfaces of the lapse α for the head-on collision of two puncture black holes of equal mass $m_1 = m_2 = 0.5M$ at times $t = 1, 13$ and $25M$ (from left to right). Top row: without implicit hyperviscous boundaries (IBH), Run 34. Bottom row: with IHB, Run 35.

where $r^* \overset{d}{=} \left(r^4 + 10^{-24}\right)^{\frac{1}{4}}$ and r is the coordinate distance of a grid point from the puncture. We present two types of runs for head-on collisions. We evolved a first simulation (Run 34) without the IHB method. We carried out the simulation until the code crashed, that is a few times after the collision. The evolution of the contour surfaces of the lapse α are reported in the top row of figure 3.10. The panels (a), (b) and (c) show the $x - y$ section of the 3D domain, at $z = L_0/2$, i.e. at the middle of the $z-$domain, at times $t = 1$, 13 and $25M$, respectively. As can be seen, after the BH's collision, spurious harmonics develop and grow in time. These numerical disturbances are related to gravitational fluctuations, generated at the central collision region, that propagate away and interact at the periodic borders. This non-physical interference is also amplified by the violation of the mean gravitational profile of the black holes at the border, which eventually leads the simulation to crash at $t \sim 30$.

In order to stabilize the spectral algorithm, a second simulation (Run 35) has been carried out by switching-on the IHB technique. In order to quickly truncate noise that periodically travels through the periodic boundaries, we match the two solutions, $f^{\{ideal\}}(\boldsymbol{x}, t)$ and $f^{\{H\}}(\boldsymbol{x}, t)$, with a rigid condition

$$f(\boldsymbol{x}, t) = \begin{cases} f^{\{ideal\}}(\boldsymbol{x}, t) & for |\boldsymbol{x} - \boldsymbol{x}_0| \leq \lambda, \\ f^{\{H\}}(\boldsymbol{x}, t) & for |\boldsymbol{x} - \boldsymbol{x}_0| > \lambda, \end{cases}$$

where $\mathbf{x}_0$ is set at the center of the 3D spatial domain, and $\lambda = \frac{3}{8} L_0$. In the bottom row of figure 3.10 we represent the contour surfaces of the lapse [panels (d), (e) and (f)], at the same times of the previous run. The simulation has been noticeably improved, thanks to the diffusive boundaries that absorb the spurious periodic effects, as well as the out-propagating gravitational fluctuations. The line contours reveal a very

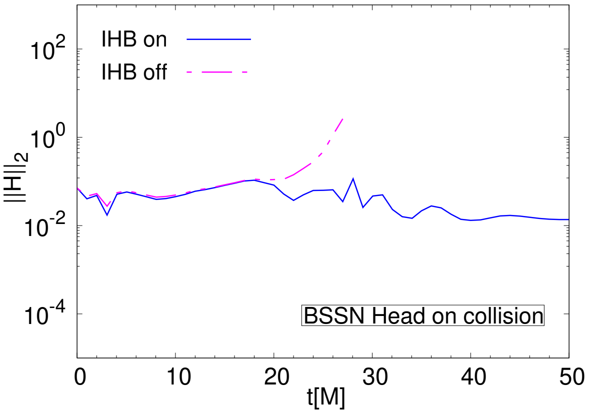

FIGURE 3.11: L2 errors of the Hamiltonian constraint for the BH's collision. The dash-dotted line represents the violation for the simulation without IHB (Run 34). The code crashes at $t \sim 30M$. The solid line represents the same test with IHB (Run 35). The Hamiltonian is well bounded and the simulation is carried out until $t = 50M$.

smooth and well-behaved profile of the final (merged) black hole, confirming that dealiased pseudo-spectral methods can represent a good numerical strategy for the simulation of compact object dynamics.

Finally, we compare the violation of the Hamiltonian constraints for the two runs (with and without IHB), as reported in figure 3.11. As can be seen, the run with the viscous boundaries is much more stable, manifesting also a lower violation of the constraints. This is due to the fact that the boundary ripples have been absorbed and the method prevents the contamination of these wiggles in the central ideal part of the domain, where the merger occurs. A similar strategy can be used for a variety of studies, including the inspiring binaries and the multiple black hole systems (Pretorius, 2006; Matzner, Huq, and Shoemaker, 1999; Lousto and Zlochower, 2008).

There are other techniques able to handle black hole dynamics, as in the SpEC code (Scheel et al., 2006; Szilágyi, 2014), where the method imposes a large infrastructure able to handle the singularity. The method presented here is different and simpler than the above (more refined) strategy. In the case of massive objects, we base our numerical approach on (1) a simple grid-shift of the black hole (in the case of the static Schwarzschild), (2) the use of filtering/dealiasing techniques that retain the differentiability of the solution and (3) the use of hyperviscous boundaries which absorb perturbations.

3.1.9 Appendix A: The time integration scheme

The most commonly used methods to integrate in time systems of coupled partial differential equations are the well-known Runge-Kutta (RK) schemes. Several classifications of these methods can be done, according to their convergence order, the number of stages, or their explicit/implicit structure. Low-order RK methods have the advantage of simplicity and the relatively low need for memory allocation. This is surely a good point for numerical relativity, especially in the BSSN formalism, where the number of tensors proliferates compared to the ADM approach. However, low-order RK, such as the second-order method (RK2) are quite dissipative, causing a departure (in time) from exact solutions (when these are known). Some of these accuracy problems are partially solved by using higher-order, such as the popular fourth-order RK4 [2].

In this brief subsection of the Appendix, we compare the accuracy of both RK2 and RK4, in the case of our pseudo-spectral filtered method. The RK2 has been described in Section 2.5.1, by equation (2.30). Analogously, for the RK4 one gets

$$f^{n+1} = f^n + \frac{\Delta t}{6}\left[F_1 + 2F_2 + 2F_3 + F_4\right], \tag{3.12}$$

where $F_1 = F(f^n)$, $F_2 = F(f^n + \frac{\Delta t}{2}F_1)$, $F_3 = F(f^n + \frac{\Delta t}{2}F_2)$ and $F_4 = F(f^n + \Delta t F_3)$.

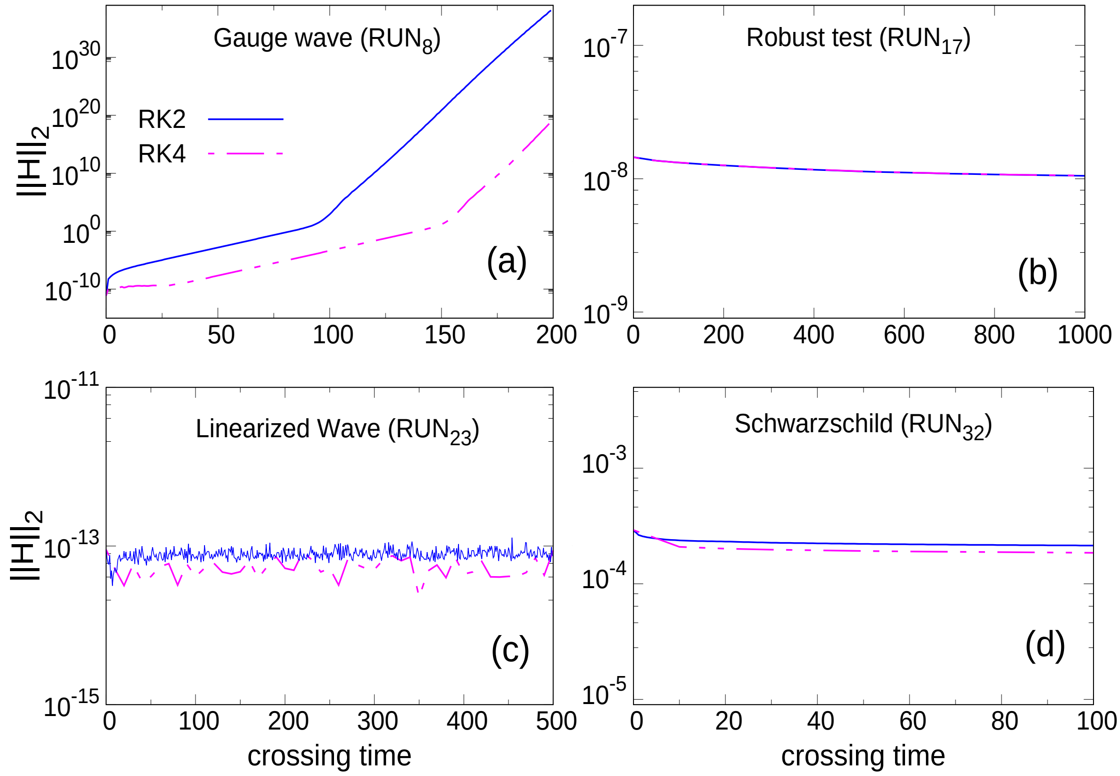

FIGURE 3.12: Hamiltonian constraint for different initial data, for both second-order (full) and fourth-order (dot-dot-full) Runge-Kutta. The performances of the runs are summarized in table 3.2.

In figure 3.12 we show the Hamiltonian error $||H||_2$, for the most stable runs shown in table 3.1. For the sake of simplicity, we show only a few testbeds, namely: the large amplitude Gauge wave (Run 8), robust stability test (Run 17), the gravitational wave test (Run 23) and the Schwarzschild black hole (Run 32). In all the cases, the RK4 has always a smaller violation error, as expected.

In table 3.2 we report the difference between the simulated profile of the field χ and its analytical solution. In particular, we computed the L_2 norm of the error

$$\Delta_a \chi = \chi^{RK\#} - \chi^{analytical}, \tag{3.13}$$

---

[2] Alternatively, explicit (e.g. Adams-Bashford) or implicit (Adams-Moulton) linear multi-step methods improve the stability properties, albeit at the expense in increasing the complexity of the algorithm.

TABLE 3.2: Convergence table for different integration schemes. The numerical values in the table refers to the discrepancy $||\Delta_a \chi||_2$, defined in equation (3.13), evaluated for the second (# = 2) and the fourth (# = 4) order Runge-Kutta. The gauge waves have been compared at $t = 100$, the gravitational waves at $t = 500$, and the Schwarzschild BH at $t = 100$.

Algorithm	gauge wave	linearized wave	Schwarzschild
RK2	9.6×10^{-1}	2.4×10^{-12}	1.1×10^{-3}
RK4	2.4×10^{-2}	2.3×10^{-12}	1.1×10^{-3}

TABLE 3.3: Convergence table for the Schwarzschild black hole. The errors have been quantified as the L_2 norm of the discrepancy from the analytical solution, similarly to equation (3.13).

Resolution	32^3	64^3	128^3	256^3
$\|\|\Delta_a \chi\|\|_2$	1.5×10^{-3}	1.2×10^{-3}	1.1×10^{-3}	8.9×10^{-4}

for both the second (#=2) and the fourth (#=4) order. As can be seen, the RK4 is more accurate, although it requires extra computational time and memory. In future works, a combination of high-order time-integration schemes with the IHB will be presented, coupling alternative techniques with implicit diffusion for the boundaries.

3.1.10 Appendix B: Convergence tests for singular Spacetimes

In this second Appendix, we present the convergence tests at different resolutions N, for the filtered BSSN algorithm. It is important to remark that our spectral method is different from typical spectral elements methods, where the convergence depends upon the number of modes in the local projection basis (Dumbser et al., 2018). In the classical pseudospectral algorithms, the error on the derivative depends on the properties of the function. For purely periodic, regular, and smooth functions, the error is essentially close to the machine precision or, to be more precise, is due to the noise-floor of the FFT algorithm. Different is the case of non–periodic and discontinuous functions, where the spectrum cannot be entirely described within the limited spectral projection. Even if the Fourier transform of a given discontinuous function quickly converges to zero for wavenumbers $k \to \infty$, the discrepancy with exact solutions is no more negligible (Canuto et al., 1988; Boyd, 2001b). This last class of functions comprehends the Schwarzschild solutions and the error, which is always smaller than (or on the order of) high-order finite differences methods, converges only weakly. We will therefore inspect the convergence for black hole simulations.

We start with the Schwarzschild black hole, discussed in subsection 3.1.6, by varying the resolution from very-low ($N = 32^3$) to moderate resolution ($N = 256^3$). For this set of runs, we used the same parameters as for Run 32 (see table 3.1) and by shifting the puncture position in between mesh-nodes, as described before.

In order to quantify accuracy, for each resolution we computed the difference between a profile at the end of the simulation and its analytical solution, as in equation (3.13), where now $\Delta_a \chi = \chi^N - \chi^{analytical}$ and χ^N is the conformal factor for the simulation at a given resolution N. This norm can be computed for any variable but

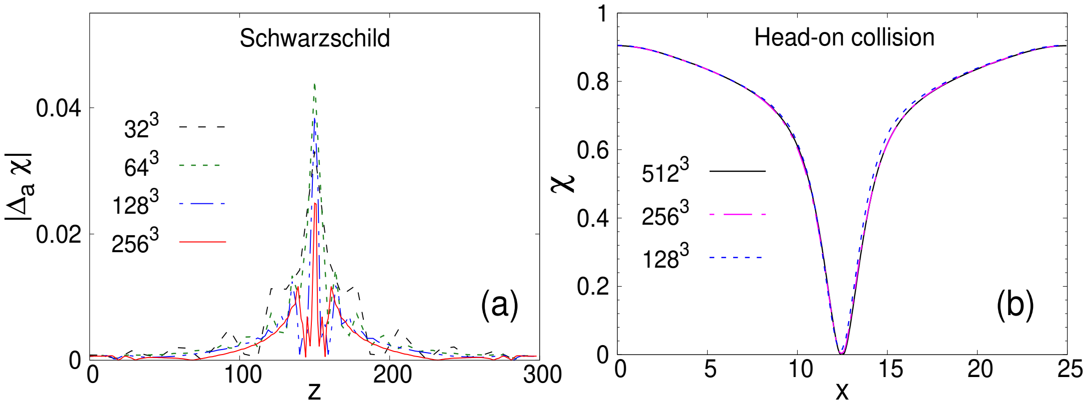

FIGURE 3.13: (a) One-dimensional cut of the discrepancy between the simulation and the analytical results $|\Delta_a \chi|$ (see text), for different resolutions summarized in table 3.3. (b) Head-on collision, final profile, for different resolutions.

here we report results for χ (other fields give similar results, not shown). In figure 3.13 (a) we show this discrepancy, for different numerical resolutions, at the end of the Schwarzschild simulations ($t = 100$). As can be seen (and as expected) the error diminishes with increasing resolution. To quantify the convergence, we computed the L_2 norm of this error, as reported in table 3.3. The global error, going from low to high resolutions, slightly diminishes. In particular, this convergence study reveals that $||\Delta_a \chi||_2$ decreases with the mesh size almost linearly (not shown). However, at these typical resolutions, the values of the errors are smaller than (or comparable to) similar experiments reported in previous works (Campanelli et al., 2006; Montero and Cordero-Carrión, 2012; Dumbser et al., 2018).

As a final set of convergence tests, we repeated the head-on collision of black holes, discussed in subsection 3.1.8. In particular, we performed Run 35, going from 128^3 up to the moderately-high resolution, with $N = 512^3$ mesh points. We compared the simulations just after the collision of the BHs, at $t = 22$, reported in panel (b) of figure 3.13. This sequence of runs suggests that the solution is well described within our typical resolutions, for $N \geq 128^3$. In particular, the profiles are very similar, although the highest resolutions reveal a more singular and accurate profile. After the merger, the filter, together with the good differentiability properties of the BSSN formalism (Zlochower et al., 2005), is able to handle the final singularity at the location of the puncture, which typically is expected to cause problems for spectral codes. To quantify the level of convergence here, we computed the error $\Delta_N \chi = \chi^{N_1} - \chi^{N_2}$, for neighboring spectral resolutions N_1 and N_2. In order to perform these direct measurements, we computed the difference only on the coarser grid and we used for all the simulations the same time-step, constrained by the 512^3 run. We obtained $||\chi^{256} - \chi^{128}||_2 = 3.3 \times 10^{-3}$ and $||\chi^{512} - \chi^{256}||_2 = 9.7 \times 10^{-4}$. This further confirms that the solution is accurate and convergent.

3.2 Aliasing instabilities in the ADM and BSSN formalism

We have seen with the previous tests that spectral methods are very performing techniques for numerical relativity. However, as we already mentioned in Section 2.5, the nonlinear terms become convolutions in the complex (Fourier) space (Boyd, 2001a), and numerical problems might arise from the so-called aliasing instabilities

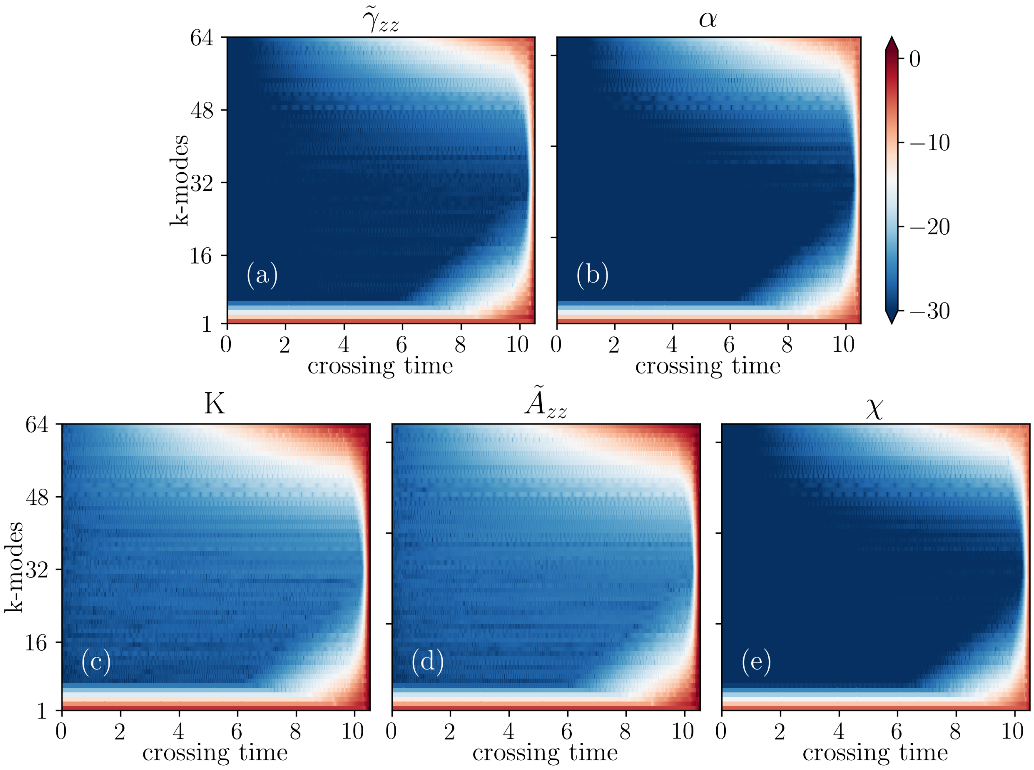

FIGURE 3.14: Energy spectra of the main BSSN dynamical variables, as a function of time and k, for the small amplitude gauge wave test (Run 1). No anti-aliasing filter has been used and the code becomes unstable at $t \sim 10.4$. From panel (a) to (e) we show $\widetilde{\gamma}_{zz}$, α, K, $\widetilde{A}_{zz}$ and χ, respectively.

(Orszag, 1971; Gottlieb and Orszag, 1977a). These instabilities generally start from the higher Fourier-modes and propagate back to smaller $k-$vectors (larger scales) during the simulation. This transfer of information is a purely numerical artifact, with no physical meaning and the numerical simulation generally loses accuracy, with a consequent blow-up of the solution. The dealiasing procedure plays a crucial role, as we shall see.

In this Section, we investigate the role of artificial instabilities, by monitoring the behavior of the isotropic spectra of the dynamical variables and, in particular, the evolution of the highest modes in the Fourier space - the modes close to the Nyquist wavenumber. We show that these modes rapidly grow up during the simulation, leading to the inaccuracy of the results. We propose a way to prevent these numerical problems, based on the dealiasing of high-order products. In practice, we remove these aliasing instabilities and improve the numerical simulations by constructing dealiasing filters (Hou and Li, 2007). In this way, the BSSN code becomes stable and very accurate, with an excellent agreement with analytical solutions - whenever they are available. Such a technique can be used also in compact object simulations.

We perform some of the standard gravitational testbeds already discussed in the previous Section, summarized in Table 3.4. For each initial data, we follow the evolution of the spectral power of the fields, highlighting the hints of the aliasing instabilities, that usually manifest as an exponential pile-up of energy at small scales. We check the accuracy of the simulation (1) by matching the numerical result with the analytical one (where it is possible), (2) by inspecting the BSSN constraints, and (3) via the computation of power spectra.

TABLE 3.4: Table of simulations. From left to right: the run number, the initial condition, the number of points, k^* of the filter, the filter status, the RSC status, the IBH status, and finally, the stability of the simulation. Here "✓" stands for on, and "×" for off.

Run	IC type	N	k^*	Filter	RSC	IHB	Stable
36	Gauge wave	128	∞	×	×	×	no
37	Gauge wave	128	$N/3$	✓	×	×	yes
38	Robust stability	128	∞	×	×	×	no
39	Robust stability	128	$N/3$	✓	×	×	yes
40	Gowdy wave	64	∞	×	×	×	no
41	Gowdy wave	64	$N/4$	✓	✓	×	yes
42	Head on collision	256^3	∞	×	×	×	no
43	Head on collision	256^3	$N/2$	✓	×	×	no
44	Head on collision	256^3	$N/2$	✓	✓	✓	yes

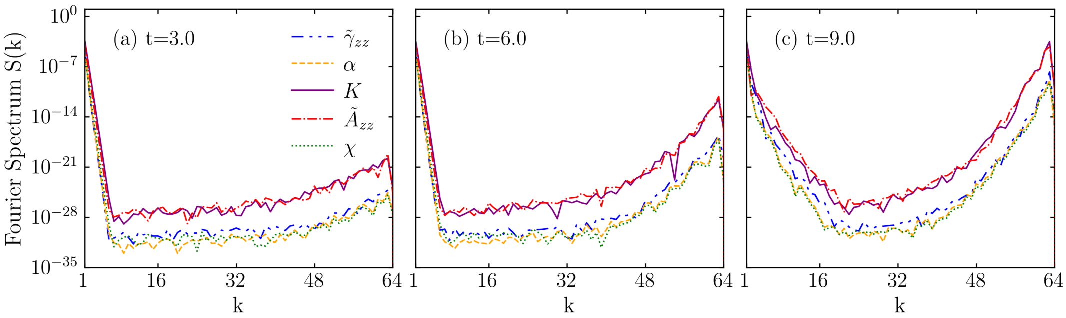

FIGURE 3.15: Spectra of $\widetilde{\gamma}_{zz}, \alpha, K, \widetilde{A}_{zz}$ and χ, for Run 1, at different times of the simulation.

For the first numerical test, the gauge wave test described in Section 3.1.1, we chose a spatial domain $x \in [0,1]$ with a number of meshes $N_z = 128$, where the metric is given by

$$ds^2 = -H(z,t)\,dt^2 + dx^2 + dy^2 + H(z,t)\,dz^2. \tag{3.14}$$

The Runge-Kutta time-step is $\Delta t = 10^{-3}$ and, according to the literature, we use the harmonic slicing in Eq. (2.19), without shift evolution ($\beta^k = \partial_t \beta^k = 0$) (Baumgarte and Shapiro, 2010). The amplitude of the perturbation is $A = 10^{-2}$. For the first run, Run 36, no anti-aliasing filter ($k^* = \infty$) and no adaptive time refinement (RSC) have been used. The code crashes very quickly, at 10.4 crossing times.

In order to better understand where the numerical instabilities arise from, we monitor the Fourier spectra of the main BSSN variables. In figure 3.14, we report the Fourier spectrum for the BSSN variables, as a function of both time and wavenumber k. In particular, we show $\widetilde{\gamma}_{zz}$, α, K, $\widetilde{A}_{zz}$, and χ, until the code crashes. Notice that a logarithmic scale has been used. From the above Figure, one can appreciate that the first hint of instability seems to come from the extrinsic curvature (the conformal trace-free part $\widetilde{A}_{zz}$ (panel (d)) and its trace K (panel (c)). Then these instabilities gradually contaminate all the other dynamical variables until the code becomes unstable and blows up, at about $t \sim 10.4$.

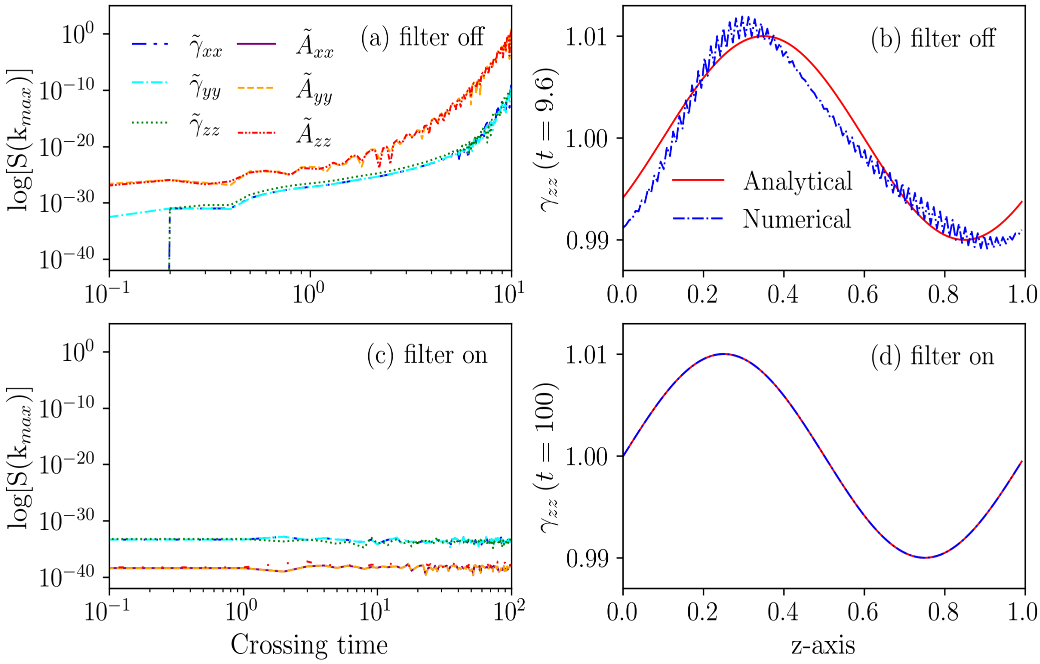

FIGURE 3.16: Top row: small amplitude gauge wave test, without filters (Run 36). In panel (a) we show the evolution in time of the $k = k_{max}$ Fourier mode of the diagonal elements for the conformal $\tilde{\gamma}_{ij}$ and $\tilde{A}_{ij}$. The aliasing instability leads to an exponential growth of such modes. In (b) we report a comparison between the physical metric γ_{zz} at $t = 9.6$ and the exact solution of the wave-form. Bottom row: same for the filtered Run 37, where the solution becomes very stable and accurate.

In figure 3.15 we show the energy spectra of the same dynamical variables, at $t = 3.0$, 6.0, and 9.0. Note that nonphysical "energy" contaminates first the higher Fourier modes, and then diffuses back to the whole spectrum. The major contribution comes from the extrinsic curvature.

It is interesting now to follow in time the modes. In figure 3.16-(a) we show the evolution of $k_{max} \sim N/2$, for the diagonal elements of the conformal metric and the conformal trace-free part of the curvature. The exponential growth in time is evident. This *spectral check* shows clearly that aliasing errors arise first in the trace-free part of the extrinsic curvature and then in the metric components. The consequences of such instabilities are visible in figure 3.16 (b), where we show a section of the physical three-metric γ_{zz} at $t = 9.6$, compared with the analytical solution. It is interesting to note not only the appearance of wiggles but also a strong deformation of the largest wavelength (initial) mode.

In order to avoid these instabilities and stabilize the algorithm, in the second run (Run 37) we use our smooth anti-aliasing filter described by equations (2.27)-(2.29), using $k^* = N_z/3$ (the other parameters are the same as the previous run.) In figure 3.16-(c) we show the evolution of the $k = k_{max}$ Fourier-mode. The filter suppresses the non-physical energy in all the highest harmonics and the simulation remains stable for a long time. The advantage is evident from panel (d), where we show a section of the γ_{zz} component at $t = 100$ crossing time, compared with the exact solution. Finally, in figure 3.17, we show the evolution in time of the spectra of the main BSSN variables, for Run 37. One can see that, in contrast with the previous test, the smooth filter suppresses higher Fourier modes and the code remains very stable.

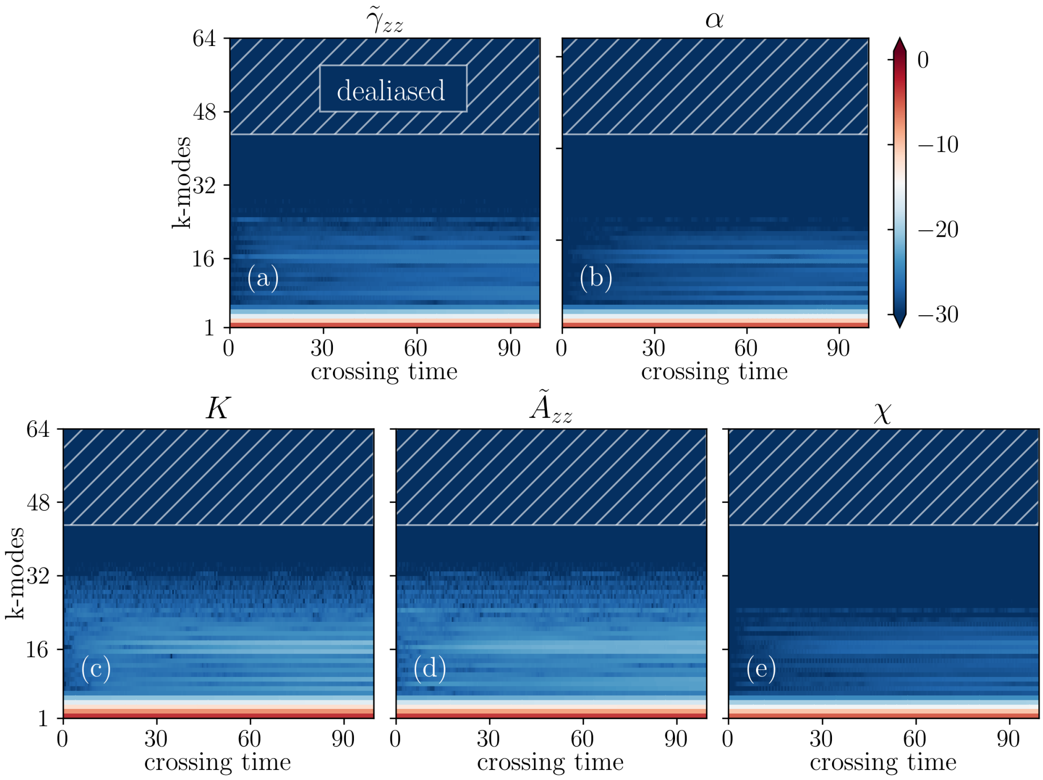

FIGURE 3.17: Energy spectra of the main BSSN dynamical variables as a function of k and t, for Run 37. A smooth filter with $k^* = N_z/3$ has been used. The code remains stable for long time.

The second experiment is the robust stability test. The numerical noise is distributed among every BSSN dynamical field, let's say $f = f_0 + \varepsilon_f$, with f_0 being the unperturbed field. The perturbation is chosen to be $\varepsilon(f) \in [-10^{-10}, 10^{-10}]$. We chose a spatial domain $x, y, z \in [0, 1]$, a number of grid points $N_z = 128$, where the mesh size along z is therefore $\Delta z = 1/128$ and the time-step is $\Delta t = 10^{-3}$. To speed up calculations, we use only four grid points in the x and y directions. According to the literature, we use the harmonic slicing to evolve the lapse, namely $f(\alpha) = 1$ in equation (2.19). We use the "Gamma driver" condition to evolve the shift (Cao, Yo, and Yu, 2008). For the first test (Run 38) no anti-aliasing filter has been used, and the code crashes at $t \sim 5.7$ crossing times. In figure 3.18 the energy spectra of the main BSSN dynamical variables are reported as a function of time. From this Figure is clear that aliasing instabilities, once again, come first from the extrinsic curvature (the trace and the traceless part) and then contaminate all the other dynamical fields, until the code crashes. In figure 3.19, we report the whole energy spectra at time $t = 0$, 2 and 5, for the same fields.

The BSSN formalism involves a large number of auxiliary variables. It is instructive, in this regard, to monitor the more physical ADM fields, i.e. the metric γ_{ij}, the extrinsic curvature K_{ij}, and the lapse α. In table 3.5, we report in detail the various terms of the ADM evolution equations, together with the corresponding order of the products. The number of products varies from quadratic (for example the time evolution of the metric), to very high nonlinearity (5^{th} order products), as for the Ricci component of the extrinsic curvature. In order to inspect which is the main candidate for the numerical instability, for each of these terms, we computed the energy spectra. Figure 3.20 shows the evolution in time of the $k = k_{max}$ Fourier mode, on a

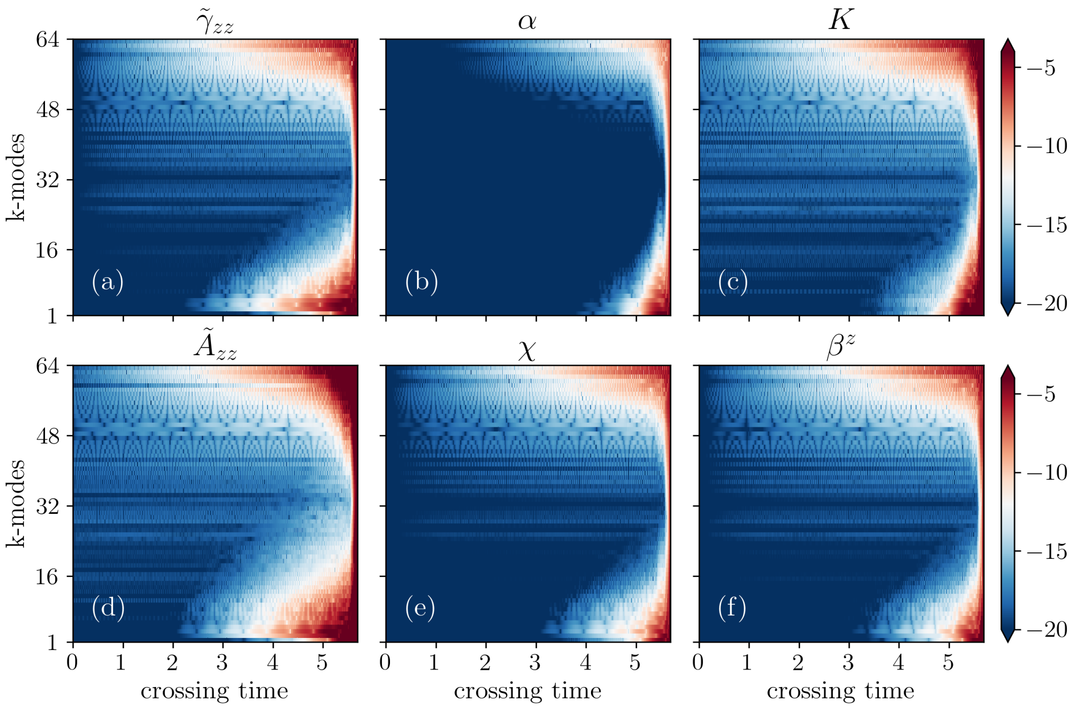

FIGURE 3.18: The isotropic energy spectra *vs.* k and t, for the robust stability test (Run 38), without anti-aliasing filter. The code becomes unstable due to the aliasing error and the simulation crashes at $t \sim 5.7$. From (a) to (f), we show $\widetilde{\gamma}_{zz}$, α, K, $\widetilde{A}_{zz}$, χ, and β^z.

log-log scale. This analysis shows that the (non-physical) energy due to the aliasing phenomenon grows rapidly until the code crashes. Different terms have different amplitudes and growth rates.

At this point, it is then useful to inspect the very initial stages, in order to reveal the precursor of such instability. The inset shows the earlier times of the simulation. As expected, the $K[1]$ term is higher in energy since the initial time-steps, and remains always one of the most aliased during the simulation. Even in the end, this term keeps growing faster and reaching higher values. This behavior is due to the fact that $K[1]$ is proportional to the Ricci tensor R_{ij} which involves more complex convolutions in the Fourier space, as discussed in Table 3.5. In order to show the benefit of the anti-aliasing filter and the robustness of the code, a second test (Run 39) has been performed, by using our smooth filter at $k^* = N_z/3$, with the same parameters as Run 38. The code remains stable for a long time and the Fourier spectra are well bounded (see for example Meringolo, Servidio, and Veltri, 2021).

We now analyze the aliasing instability via the Gowdy spacetime, discussed in Section 3.1.5. The Gowdy wave test evolves a strongly curved spacetime, representing a vacuum cosmological model and therefore used to test codes in a strong field context. Such vacuum solutions describe an expanding/collapsing universe, and it contains plane-polarized gravitational waves. For this test, we will carry out our simulations in the collapsing direction, i.e. backward in time. We chose a spatial domain $z \in [0,1]$, with $N_z = 64$, $\Delta t = 5 \times 10^{-4}$ and the harmonic slicing. This is an important challenge for a numerical code because there is both a small effect (the dynamics in γ_{xx} and γ_{yy}) and a larger effect (dynamics in γ_{zz}) in the metric components.

As usual, the first run (Run 40) is carried out without the anti-aliasing filter. The

TABLE 3.5: Table of ADM terms, together with the corresponding order of the products. The highest nonlinearity is due to the $K[1]$ term, which is proportional to the Ricci tensor R_{ij}.

term	explicit form	# products
$\gamma\,[1]$	$-2\alpha K_{ij}$	2
$\gamma\,[2]$	$\beta^k \partial_k \gamma_{ij}$	2
$\gamma\,[3]$	$\gamma_{ik}\partial_j \beta^k$	2
$K\,[1]$	$\alpha R_{ij} \sim \alpha[\gamma^{**}\partial_* \gamma_{**}][\gamma^{**}\partial_* \gamma_{**}]$	5
$K\,[2]$	$-2\alpha K_{im} K^m_j \sim \alpha K_{**}\gamma^{**}K_{**}$	4
$K\,[3]$	$-2\alpha K K_{ij}$	3
$K\,[4]$	$-D_i D_j \alpha \sim [\gamma^{**}\partial_* \gamma_{**}]\partial_* \alpha$	3
$K\,[5]$	$\beta^k \partial_k K_{ij}$	2
$K\,[6]$	$K_{ik}\partial_j \beta^k$	2
α	$-\alpha^2 K$	3

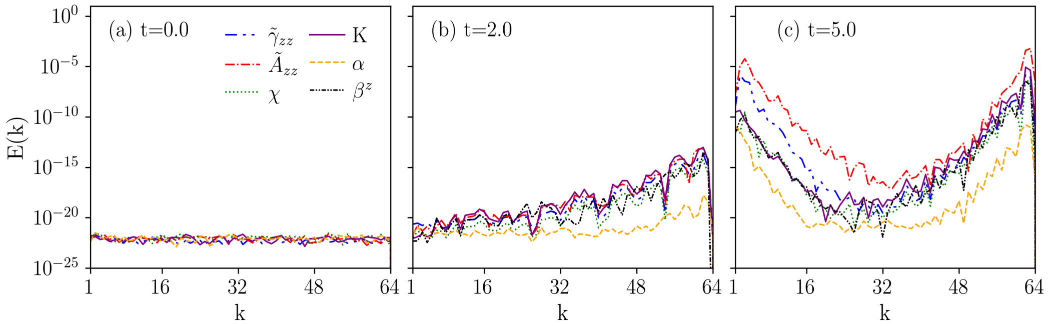

FIGURE 3.19: Robust stability test for Run 38. The energy spectra are shown as a function of k, for $\tilde{\gamma}_{zz}, \tilde{A}_{zz}, \chi, K, \alpha$ and β^z, at 3 different times.

code becomes unstable and crashes at $t \sim 240$ crossing times. In panel (a) of figure 3.21, the time evolution of the spectrum of $\tilde{A}_{xx}$ is shown. Note that with our choice of parameters, $k_{max} = N_z/2 = 32$. The instabilities arise, again, from small wavelengths and propagate backward to larger scales. In order to stabilize the simulation, in Run 41, we set our smooth filter to $k^* = N_z/4$, together with the RSC condition. In this way, the evolution becomes well-behaved until $t = 1000$, as can be seen from figure 3.21 (right).

In figure 3.22 we show the largest modes of $\tilde{\gamma}_{xx}$ and $\tilde{A}_{xx}$, for both the unfiltered (Run 40) and the dealiased Gowdy test (Run 41). To check the consistency of the results, we computed the L_2 norm of the Hamiltonian constraints. This quantity, which should be null in the ADM representation of the Einstein field equations, is very small, as can be seen from Figure 3.22 (right). However, the solution becomes suddenly unstable in the unfiltered case, while it keeps more reasonable low values in the filtered case, for longer times. In both cases, as expected in this kind of very difficult initial data, the solution inexorably blows up, in agreement with previous works (Clough et al., 2015). Overall, as it can be seen, also in this more challenging test our pseudo-spectral code is able to handle the numerical evolution and is stable

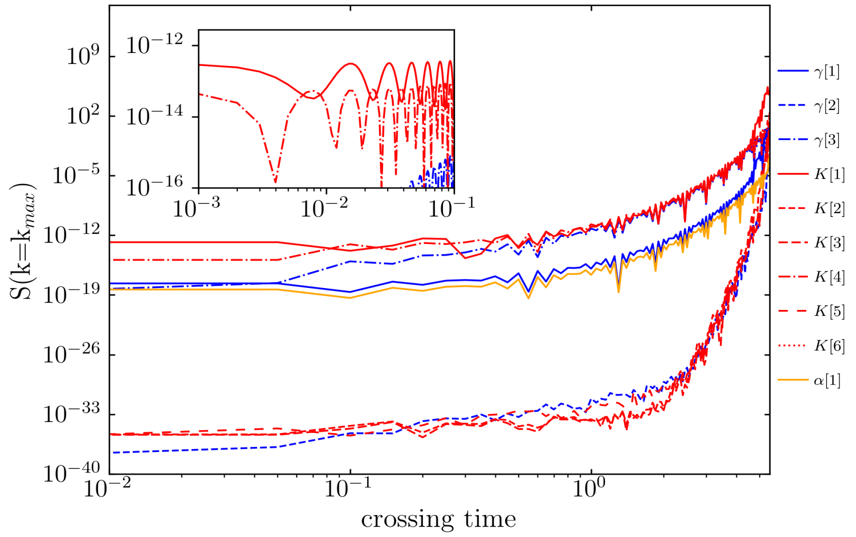

FIGURE 3.20: Energy of the maximum mode, as a function of time, for the robust stability test with no anti-aliasing filter (Run 38). In the inset, we show the initial stages, with the $K[1]$ term ($\propto R_{ij}$) being the dominant growing term. This term remains the most aliased, until the code crashes.

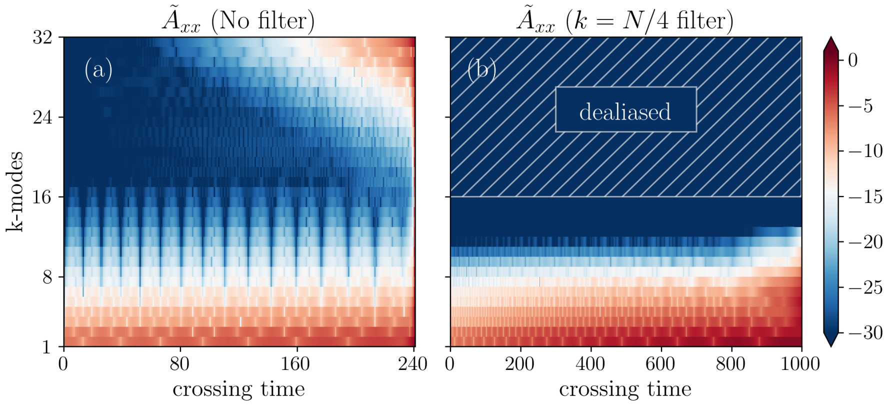

FIGURE 3.21: Energy spectrum of $\tilde{A}_{xx}$ as a function of time, for the Gowdy test (a) without anti-aliasing filter (Run 40) and (b) with a $k^* = N_z/4$ filter (Run 41).

for the full 1000 crossing times, with violation errors that are comparable (or smaller) than in previous works (Alcubierre et al., 2004).

As a final test, we present results about the head-on collisions of two equal-mass MWBL black holes. Each black hole is parametrized by m_j and $\mathbf{r}_j$, namely the mass parameter and the position of the $j-th$ black hole, respectively. For the head-on test, the ADM mass is given by the sum of m_j. Both the ADM linear and angular momentum are set to zero, this means that the black holes start without boost and spin. The extrinsic curvature is set initially to zero, with $\tilde{A}_{ij} = K = 0$, and with a conformal factor that is

$$\chi = \left[1 + \frac{m_1}{2|\mathbf{r}-\mathbf{r}_1|} + \frac{m_2}{2|\mathbf{r}-\mathbf{r}_2|}\right]^{-4}.$$

In this case the 3D computational domain extends over $x, y, z \in [0, 25]$ We set the mass parameters and the initial location of the $j-th$ puncture to be $m_j = 0.5$ and

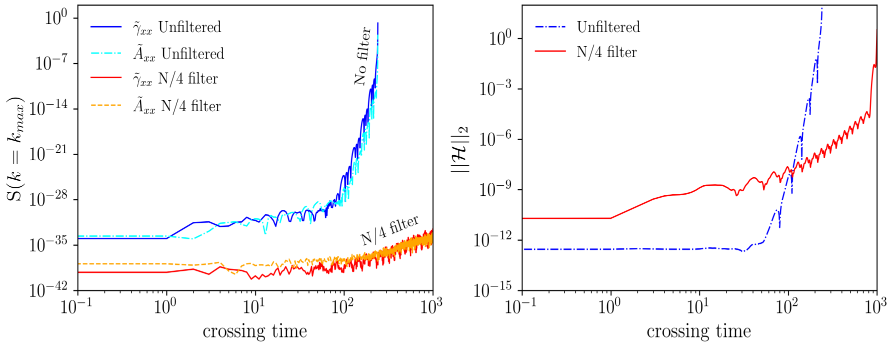

FIGURE 3.22: Gowdy spacetime. Left: the evolution of the $k = 32$ Fourier mode for the conformal metric $\widetilde{\gamma}_{xx}$ and the trace-free part of the extrinsic curvature $\widetilde{A}_{xx}$, with no filter (Run 40) and with a smooth $k^* = N_z/4$ filter (Run 41). Right: The evolution of the L_2 norm of the Hamiltonian, for both runs.

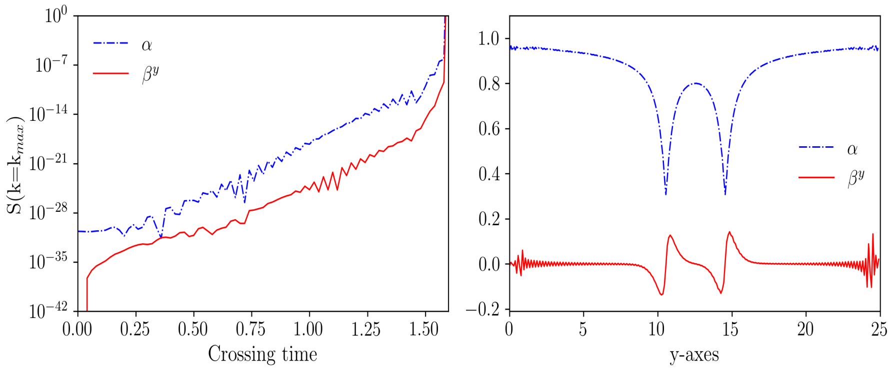

FIGURE 3.23: The head-on collision test (Run 42). Left: the time-growth of the mode $k = k_{max}$, for both the lapse and the shift. The code crashes at $t \sim 1.6$. Right: 1D section in the $y-$direction for both fields, at $t = 1.5$, just before the code crashes. Note that the instabilities arise from the boundaries and propagate into the domain.

$\mathbf{C_j} = \{12.5, 12.5 \pm 2, 12.5\}$, respectively. We use the harmonic slicing to evolve the lapse, and the "Gamma driver" condition to evolve the shift (Cao, Yo, and Yu, 2008).

For the first run, we stress the code without an anti-aliasing filter (Run 42). As expected, such a heavy test quickly induces aliasing instabilities and the code suddenly crashes. Since this is a simulation with a 3D mesh, with $N = 256$ grid points for each Cartesian direction, the maximum mode is at about $N_k = \frac{1}{2}\sqrt{3N^2} \sim 222$. In figure 3.23 (left) we show the evolution of the $k = k_{max}$ mode for the lapse α and the shift β^y. In the right panel, a 1D cut of the same fields is shown, at $t = 1.5$, just before the code blows up. For the symmetry of the problem, the cut is along the y-axis, at $N_x/2$ and $N_z/2$. One can see the growth of ripples at the boundary regions, due to the propagation of internal waves and their interference related to periodicity. These non-physical fluctuations grow up exponentially in time and lead to unstable solutions. A second simulation (Run 43) has been carried out by using a smooth filter with $k^* = N/2$. The filter surely improves the stability of the simulation, but the code crashes later than Run 42, namely at $t \sim 4.2$. This indicates that the boundary might be now the cause of the aliasing problems.

In order to definitively stabilize the code, we carried out a third simulation (Run 44) with the viscous approach, switching on the IHB technique described in Meringolo,

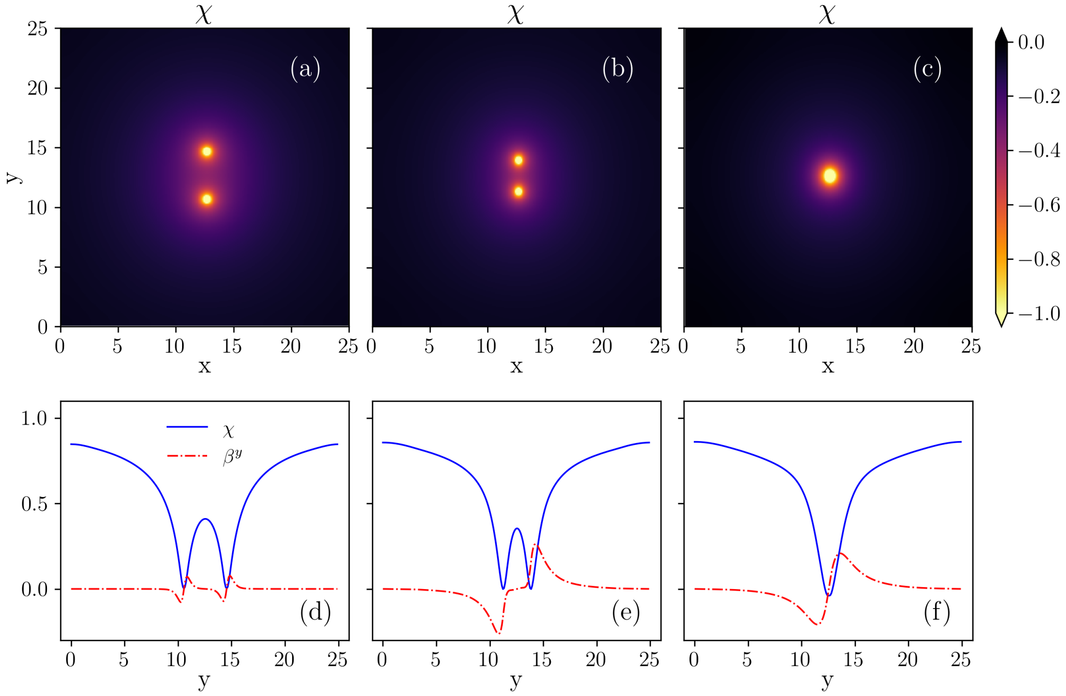

FIGURE 3.24: Head-on collision with a stabilizing procedure (Run 43). A smooth filter with $k^* = N/2$ and the IHB has been used. Top row: $xy-$plane at time $t = 1, t = 13$ and $t = 26$ for the conformal factor χ. Bottom row: 1D cut in the $y-$direction for χ and β^y, at same times. The field remains well-behaved at the boundaries. The merger occurs at $t \sim 21$ and the simulation is carried out until $t = 50$.

Servidio, and Veltri, 2021. We carried out the simulation several times after the merging of the two black holes. In the top row of figure 3.24 is reported a section in the $xy-$plane (at $N_z/2$) of the conformal factor χ, at three times, namely $t = 1, 13$ and 26. The merging occurs at $t \sim 21$, even though the simulation is carried out until $t = 50$. In the bottom-row, we show, at the same times, 1D cuts in the $y-$direction (at the middle of the lattice) of χ and β^y. The numerical artifacts in figure 3.23 have been suppressed thanks to the combination of filtering and the IHB technique. For completeness, we monitor the evolution in time of all the BSSN constraints during the simulation, for the three head-on collision tests. In figure 3.25 we report the L_2 norm of the Hamiltonian constraint, described by Eq. (3.2), for the Run 42–Run 44. As it can be seen, the run with the hyperviscous boundaries is stable long after the collision, manifesting also a lower violation of the constraints.

The `SFINGE` code, with the above filtering and boundary treatments, is able to handle such difficult gravitational dynamics. A similar strategy can be used for a variety of studies, including the inspiring binaries and the multiple black hole systems (Pretorius, 2006; Lousto and Zlochower, 2008), with the consequent analysis of the gravitational signal. This will be discussed in the next Section.

3.3 Gravitational waves from black holes collisions

In this Section, we will focus on GWs, a perturbation of spacetime that propagates with an undulatory character at the speed of light, and one of the most important

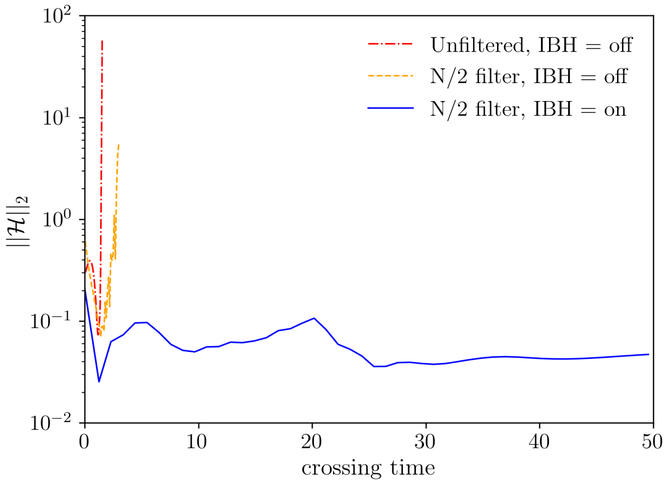

FIGURE 3.25: L_2 norm of the Hamiltonian constraint, for the head-on collision of two equal masses black holes. The merger occurs at $t \sim 21$. The solid line represents the test with IHB on and a smooth filter with $k^* = N/2$ (Run 44), while the dashed (Run 42) and the dot-dashed (Run 43) represent the unstable runs.

predictions of general relativity. Gravitational radiation can carry energy and momentum away from an isolated system, and it encodes information about the physical properties of the system itself. GWs are one of the most important physical phenomena associated with the presence of strong and dynamic gravitational fields, and they are of great interest in numerical relativity. Predicting the GW signal coming from real astrophysical systems has been one of the main themes in numerical relativity over the years since such predictions can be used as templates that can significantly improve the possibility of detection.

Our campaign of simulations consists of six different configurations. First, we evolve a binary system of two inspiraling equal masses BHs. The other configurations consist of the more complex dynamics of three compact objects, spanning different initial conditions. For each of them, we capture the corresponding gravitational signal, and we perform more detailed analyses via Fourier and wavelet spectra.

3.3.1 The Newman-Penrose formalism and the Weyl scalars

In numerical relativity, GWs are extracted via the traceless Weyl tensor with respect to a frame of null vectors, using what is known as the *Newman–Penrose formalism* (Newman and Penrose, 1962). The Newman-Penrose formalism is a set of notations developed to treat general relativity in terms of spinor notation, which introduces complex forms of the usual variables and where the tensors are projected onto a complete vector basis at each point in spacetime. Usually, this vector basis is chosen to reflect some symmetry of the spacetime, leading to simplified expressions for physical observables. In the case of the Newman-Penrose formalism, the vector basis chosen is a null tetrad: a set of four null vectors-two real, and a complex-conjugate pair (Alcubierre et al., 2004). The two real vectors asymptotically point radially inward and radially outward, and the formalism is well adapted to the treatment of the propagation of radiation in curved spacetime.

As we have seen, the Weyl tensor, for $n = 4$, has 10 independent components. In the Newman–Penrose formalism those components can be conveniently represented by five complex scalar quantities known as the *Weyl scalars*, defined as[3]

$$\begin{aligned}
\Psi_0 &= C_{\mu\nu\rho\sigma} l^\mu m^\nu l^\rho m^\sigma, \\
\Psi_1 &= C_{\mu\nu\rho\sigma} l^\mu k^\nu l^\rho m^\sigma, \\
\Psi_2 &= C_{\mu\nu\rho\sigma} l^\mu m^\nu \widetilde{m}^\rho k^\sigma, \\
\Psi_3 &= C_{\mu\nu\rho\sigma} l^\mu k^\nu \widetilde{m}^\rho k^\sigma, \\
\Psi_4 &= C_{\mu\nu\rho\sigma} k^\mu \widetilde{m}^\nu k^\rho \widetilde{m}^\sigma,
\end{aligned} \tag{3.15}$$

where $l^\mu, m^\mu, \widetilde{m}^\mu$ and k^μ represent the null tetrad. Notice that, as with all other Newman–Penrose quantities, the Ψ_μ are scalars with respect to coordinate transformations, but they clearly depend on the choice of the null tetrad. These five complex scalars are enough to specify all 10 independent components of the Weyl tensor. The symmetries of the Weyl tensor imply that all other possible contractions of $C_{\mu\nu\rho\sigma}$ with combinations of the tetrad vectors either vanish or can be expressed as combinations of the Ψ_μ.

It is possible to interpret the scalars Ψ_0 and Ψ_4 as measures of the ingoing and outgoing gravitational radiation. For obvious reasons, we are interested in Ψ_4, which encodes in a single complex field everything about outgoing gravitational waves, as well as the radiated energy and linear momentum. Furthermore, this quantity can be interpreted as the relativistic analog of the Poynting vector S^i, which expresses the energy flow outgoing from a surface containing a certain volume V, projected along the radial direction $\hat{r}$.

A very important property of the Ψ_4 scalar is that in the asymptotic limit, it completely describes the outgoing gravitational radiation field: far from a source, a gravitational wave is locally plane and Ψ_4 is directly related to the metric perturbation in the so-called *TT gauge*:

$$\Psi_4 = \partial_t^2 (h_+ - i h_\times), \tag{3.16}$$

where h_+ and $h_\times$ are the amplitudes of the two independent components with linear polarization of the wave solution (Baumgarte and Shapiro, 1998). Another useful expression of the Ψ_4 scalar is given by:

$$\Psi_4 = (E_{ij} - i B_{ij}) \widetilde{m}^i \widetilde{m}^j, \tag{3.17}$$

where we define the *electric tensor* E_{ij} and *magnetic tensor* B_{ij} as:

$$\begin{cases}
E_{ij} = R_{ij} + \gamma^{mn}(K_{ij}K_{mn} - K_{im}K_{jn}), & \text{(3.18a)} \\
B_{ij} = \gamma_{ik}\epsilon^{kmn} D_m K_{nj}, \quad \epsilon^{kmn} = \epsilon_{kmn}, & \text{(3.18b)}
\end{cases}$$

or equivalently (Reisswig et al., 2011):

$$\Psi_4 = \frac{1}{2}\left[E_{ij}(w^i w^j - v^i v^j) - B_{ij}(w^i v^j + v^i w^j)\right] - \frac{i}{2}\left[E_{ij}(w^i v^j + v^i w^j) + B_{ij}(w^i w^j - v^i v^j)\right]. \tag{3.19}$$

It is convenient to project Ψ_4 onto the sphere and describe its angular dependence in terms of the *spin-weighted spherical harmonics* $Y_{lm}^{(s)}(\theta, \varphi)$. The contributions of the individual modes l, m are obtained from projecting Ψ_4 onto the spherical harmonics

---

[3] The sign convention in these definitions is by no means universal and is frequently reversed

$Y^{(s)}_{lm}(\theta, \varphi)$ of spin weight $s = -2$. Using the orthogonality relation between spin-weighted spherical harmonics

$$\int d\Omega\, \bar{Y}^{(-2)}_{lm}(\theta, \varphi) Y^{(-2)}_{l'm'}(\theta, \varphi) = \int_0^{2\pi} \int_0^{\pi} \bar{Y}^{(-2)}_{lm}(\theta, \varphi) Y^{(-2)}_{l'm'}(\theta, \varphi) \sin\theta \, d\theta \, d\varphi = \delta_{ll'}\delta_{mm'}, \tag{3.20}$$

these projections are encoded by A_{lm}, defined in terms of the scalar product

$$A_{lm} = < Y^{(-2)}_{lm}, \Psi_4 > = \int_0^{2\pi} \int_0^{\pi} \Psi_4 \bar{Y}^{(-2)}_{lm} sin\theta \, d\theta \, d\varphi. \tag{3.21}$$

The spin-weighted spherical harmonics $Y^{(-s)}_{lm}$ can be defined in terms of the Wigner d-functions as

$$Y^{(s)}_{lm}(\theta, \varphi) = (-1)^s \sqrt{\frac{2l+1}{4\pi}} d^l_{m(-s)}(\theta) e^{im\varphi}, \tag{3.22}$$

where

$$d^l_{ms}(\theta) = \sum_{t=C_1}^{C_2} \frac{(-1)^t[(l+m)!(l-m)!(l+s)!(l-s)!]^{1/2}}{(l+m-t)!(l-s-t)!t!(t+s-m)!} \left[\cos\frac{\theta}{2}\right]^{2l+m-s-2t} \left[\sin\frac{\theta}{2}\right]^{2t+s-m} \tag{3.23}$$

with $C_1 = \max(0, m - s)$ and $C_2 = \min(l + m, l - s)$. It can be shown that more than 98% of the energy is radiated in the form of the dominant $l = 2, m = \pm 2$ modes (Wiaux, Jacques, and Vandergheynst, 2007). This is the reason why is commonly used the projection Ψ_4 along the spin-weighted spherical harmonic $Y^{(-2)}_{22}(\theta, \varphi)$ to obtain the final waveform:

$$A_{22} = < Y^{(-2)}_{22}, \Psi_4 > = \int_0^{2\pi} \int_0^{\pi} \Psi_4 \bar{Y}^{(-2)}_{22} sin\theta \, d\theta \, d\varphi. \tag{3.24}$$

3.3.2 Multiple Black Hole dynamics

The `SFINGE` code also includes modules to build initial data for a variety of problems, in a self-consistent way. We implement an iterative algorithm based on the same pseudo-spectral structure of the main code, to impose a set of well-posed initial conditions at some initial instant of time. Apart from the head-on collision of two black holes discussed above, the initial conditions for a generic configuration in general relativistic simulations contain non-zero velocities. Therefore, the initial values for the extrinsic curvature K_{ij} will depend on both the linear and angular momentum of the black holes.

In such cases, the momentum constraints do not vanish trivially and the conformal factor takes the following form (Brandt and Brügmann, 1997)

$$\psi = 1 + \sum_k \frac{M_k}{2r_k} + u \ = 1 + \psi_0 + u, \tag{3.25}$$

where M_k and r_k are respectively the mass parameter and the distance from the k^{th} black hole from the origin of coordinates, and u is a corrective term. To build the initial condition for multiple black holes with certain boost and spin, we follow the *Bowen-York* approach. This method consists to solve the momentum constraints analytically and the Hamiltonian constraint numerically (Alcubierre, 2008; Cook, 2000b), where we used an iterative Newton-based technique.

TABLE 3.6: Parameters of the BSSN simulations, reported in geometrical units. Note that all the configurations have $z/M = v_z/M = 0$, omitted for the reason of space. The last line indicates the initial Arnowitt-Deser-Misner mass, evaluated as suggested by Baumgarte, 2000.

Run	45	46	47	48	49	50
# of BHs	2	3	3	3	3	3
M_1	0.450	0.250	0.333	0.250	0.250	0.250
M_2	0.450	0.333	0.333	0.333	0.333	0.333
M_3	//	0.417	0.333	0.417	0.417	0.417
$\boldsymbol{r}_1/M$	(0, 1.15)	(0.93, 2.70)	(0.67, 1.86)	(2.55, -0.17)	(-1.87, 0.86)	(-1.87, 0.86)
$\boldsymbol{r}_2/M$	(0, -1.15)	(-1.54, -0.93)	(-0.93, -0.24)	(-2.56, 0.38)	(-1.35, -1.05)	(-1.35, -1.05)
$\boldsymbol{r}_3/M$	//	(0.68, -0.87)	(0.26, -0.61)	(0.51, -0.20)	(2.21, 0.32)	(2.21, 0.32)
$\boldsymbol{v}_1/M$	(0.33, 0)	(-0.04, -0.04)	(-0.12, -0.36)	(-0.30, -0.13)	(0.04, -0.38)	(0.04, -0.38)
$\boldsymbol{v}_2/M$	(-0.33, 0)	(0.25, 0.04)	(-0.34, 0.23)	(0.03, -0.07)	(-0.06, -0.03)	(-0.06, -0.03)
$\boldsymbol{v}_3/M$	//	(-0.18, 0.07)	(0.45, 0.13)	(0.15, 0.13)	(0.02, 0.26)	(0.02, 0.26)
$\boldsymbol{J}_1/M^2$	(0, 0, 0)	(0, 0, 0)	(0, 0, 0)	(0, 0, 0)	(0, 0, 0)	(0, 0, 0.100)
$\boldsymbol{J}_2/M^2$	(0, 0, 0)	(0, 0, 0)	(0, 0, 0)	(0, 0, 0)	(0, 0, 0)	(0, 0, -0.05)
$\boldsymbol{J}_3/M^2$	(0, 0, 0)	(0, 0, 0)	(0, 0, 0)	(0, 0, 0)	(0, 0, 0)	(0, 0, -0.05)
M_{ADM}	0.904	1.001	1.003	1.004	1.008	1.007

To do this, we assume that the conformal metric is flat ($\tilde{\gamma}_{ij} = \delta_{ij}$), the physical metric is asymptotically flat ($\lim_{r\to\infty} \psi = 1$), and the trace of the extrinsic curvature is identically zero (maximal slicing, $K = 0$) so that the momentum constraints reduce to a simple tensorial equation that can be solved analytically (Baumgarte and Shapiro, 2010). The conformal trace-free part of the extrinsic curvature can be expressed as

$$\begin{aligned}
\tilde{A}_{ij} &= \sum_{k=1}^{N} \psi^{-6} \bar{A}_{ij}^{(k)} \\
&= \sum_{k=1}^{N} \psi^{-6} \frac{3}{2(r^{(k)})^2} \Big[P_i^{(k)} n_j^{(k)} + P_j^{(k)} n_i^{(k)} - \left(\delta_{ij} - n_i^{(k)} n_j^{(k)} \right) P^{l\,(k)} n_l^{(k)} \\
&+ \frac{2}{r} \left(\varepsilon_{ilm} S^{l\,(k)} n^{m\,(k)} n_j^{(k)} + \varepsilon_{jlm} S^{l\,(k)} n^{m\,(k)} n_i^{(k)} \right) \Big],
\end{aligned}$$

where the over-bar notation indicates a further conformal transformation, $n_i^{(k)} = x_i^{(k)} / \sqrt{\left[(x^{(k)}\right]^2 + \left[y^{(k)}\right]^2 + \left[z^{(k)}\right]^2}$ is the unit normal vector pointing away from the k^{th} black hole's center in the flat conformal space, $P^i = (P^x, P^y, P^z)$ and $S^i = (S^x, S^y, S^z)$ are constant vectors, standing for the linear and the angular momentum, respectively, and ε_{ijl} is the completely antisymmetric Levi-Civita tensor in three dimensions.

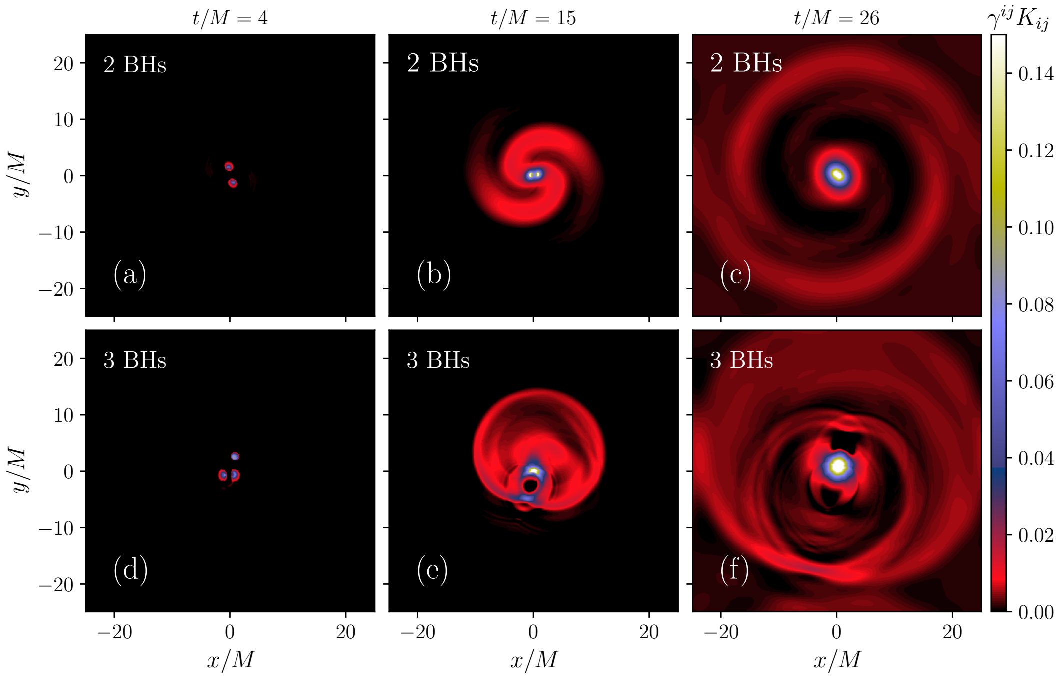

FIGURE 3.26: Shaded contours of the extrinsic curvature K for the two black holes (Run 45, top row) and the three black holes (Run 46, bottom row), at three different times of the evolution, that is before, during, and after the merger.

We then solve numerically the Hamiltonian constraint, which reduces to an elliptic equation for u (Alcubierre, 2008):

$$D^2u + \frac{1}{8}\psi_0^{-7}\bar{A}_{ij}\bar{A}^{ij}\left[1+\frac{u}{\psi_0}\right]^{-7} = 0, \tag{3.26}$$

where we have enforced the fact that $K = 0$ and that the spatial metric is conformally flat so that $\bar{R} = 0$. To solve such an elliptic equation, we have used an iterative Gauss-Seidel algorithm (Albu and Kwan, 2004), starting from an initial guess, as specified in Cao, Yo, and Yu, 2008.

The initial data for multiple black holes contain more conditions and a longer convergence time for the iterative algorithm. In particular, these calculations might take several CPU hours by using the above Gauss-Seidel technique. To accelerate the convergence, we propose a different technique. We start on a low-resolution initial cube (64^3 mesh points), solving the Hamiltonian constraint relatively quickly. Then, to interpolate on a finer lattice (i.e. reducing the grid spacing), we first move on the Fourier space by increasing the number of $k-$vectors via zero-padding, and then we obtain the physical fields performing an inverse FFT. This allows us to have a better initial guess on the higher-resolution box, with a much faster converge rate. By iterating this technique, adapting recursively (by interpolation) the solution to finer grids, we finally get the initial data. In this campaign of numerical simulations, the domain is represented by a cube of side $L_0/M = 50$, with 512^3 mesh points. The time step is initially chosen to be $\Delta t = 8 \times 10^{-3}$. Furthermore, we check, for each case, that the Hamiltonian and the momentum constraints are well satisfied.

We first start our numerical experiments via two-body inspiralling black holes, which will provide us with the classical waveform (Baker, 2002; Campanelli et al., 2006). The numerical experiment describes the evolution of two compact objects of

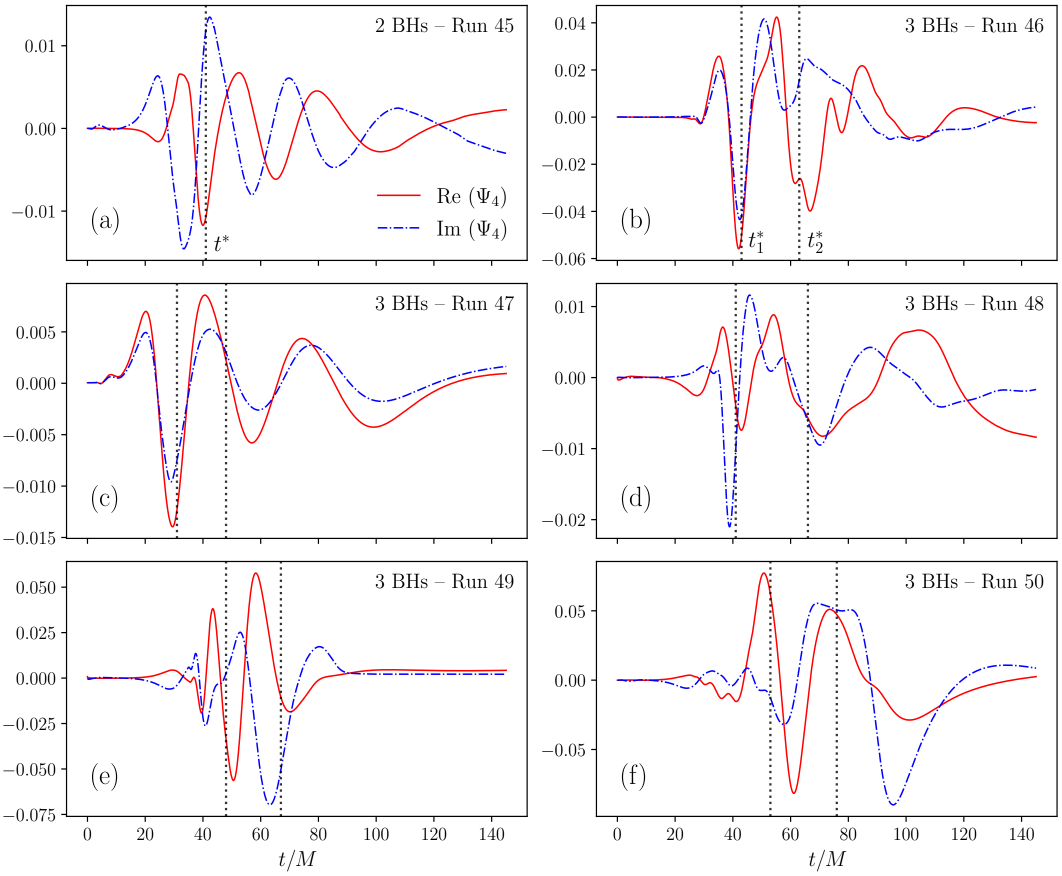

FIGURE 3.27: Reconstruction of the gravitational wave signal for (a) the binary black hole system and (b)–(f) the three-black holes systems. Figures (a)–(f) refer respectively to Runs 45–50 listed in Table 3.6. The solid (dash-dotted) lines represent the real (imaginary) part of the spherical projection of Ψ_4; the vertical dotted black lines represent the merging time(s) of the black holes (t^* is related to the 2-BHs merger, while t_1^* and t_2^* are related to the 3-BHs mergers), defined as in Baker et al., 2006; Buonanno, Cook, and Pretorius, 2007. All the simulations are performed up to $t/M = 145$. The three-black hole cases reveal a more structured and nonlinear behavior.

equal masses that are initially placed symmetrically with respect to the x-axis. They have a small initial velocity which is the same for both bodies but in opposite directions, and the properties of such “2 BHs” configuration are summarized in Table 3.6 as Run 45. A simple, fast way to identify a gravitational disturbance is to look at a scalar measure of the value of the extrinsic curvature, especially in the ecliptic plane. As can be seen from panels (a)–(c) of figure 3.26, small amplitude waves are generated during the merger. After that, a large amplitude modulation propagates away, and several disturbances of smaller amplitude begin to propagate until the system converges into a Kerr-type black hole.

Then we perform five new simulations, describing the evolution of 3-BHs, referred to as Run 46–50 in Table 3.6 In particular, the three compact objects have different separation, boost, and spin.[4] With this strategy, by using spectral methods, we can concentrate on events that might be energetically relevant, and hence detectable by experiments. Focusing on the overview of K reported in figure 3.26 (d)–(f), one can see how, compared to the 2-BHs, the patterns are more distorted,

---

[4] In Imbrogno, Meringolo, and Servidio, 2022 Runs 46–50 are named: "Classical Burrau", "equal masses", "normalized masses", "spinning Burrau" and "intrinsic spinning", respectively.

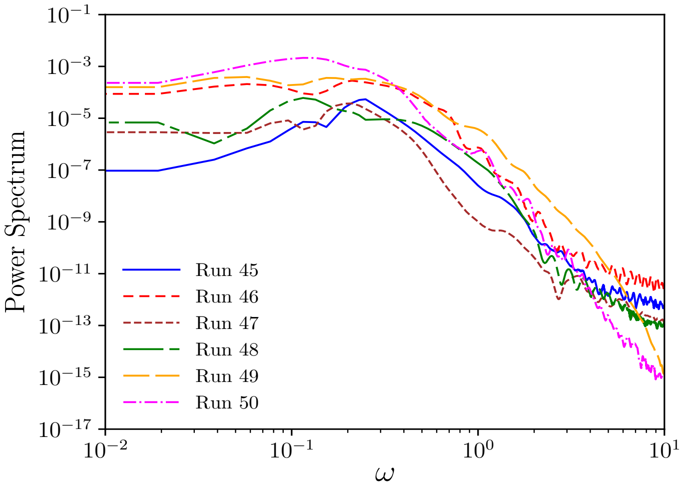

FIGURE 3.28: Power spectrum of the waveforms in figure 3.27. The spectrum represents an average over the power spectra of the two signals (real and imaginary part of the projection of the Newman-Penrose scalar Ψ_4).

with finer scales. In the post-merging phase, after the system has been allowed to "relax", it is possible to see a different pattern for the extrinsic curvature, suggesting a different kind of asymptotic solution for the final black hole.

To get more insight into the multi-black hole dynamics, we analyze the waveform by computing the projection of the Newman-Penrose scalar Ψ_4, which quantifies the radiation from a source of gravitational waves (Alcubierre, 2008). After we computed this scalar by following the procedure described in Brügmann et al., 2008 we interpolated Ψ_4 from a Cartesian to a spherical grid, on which we calculated the outgoing radiation via the spin-weighted spherical harmonic $Y_{22}^{(-2)}(\theta, \varphi)$. This projection extracts the dominant contribution of the emitted waves, which comes from the quadrupole mode ($l = 2, m = 2$).

We compared all the signals coming from these multiple black hole interactions, by looking at the outgoing radiation as measured away from the sources. We evaluated the above projection at a given distance from the center of the box, namely at $r^{\star} = 20M$, as a function of time, while the disturbances fly through the virtual detector. The signals are depicted in figure 3.27, revealing net differences among the cases. First, contrary to the case of the binary [panel (a)], the real and imaginary parts of the waveform of some of the 3-BHs cases are almost in phase. Second, while for the 2-BHs only one peak can be observed (corresponding to the single merger), in the other cases multiple-scale disturbances are present, due to the subsequent mergers. Third, the signal from the three-body problem is much more irregular and unpredictable, revealing the presence of higher-order nonlinearities (Anninos et al., 1995; Zlochower et al., 2005; Centrella et al., 2010). These more structured signals demand a deeper statistical investigation, performed as follows. We also defined the merging time t^{*} as the moment when a single connected isosurface of the lapse $\alpha = 0.3$ forms around two approaching black holes (Baker et al., 2006; Buonanno, Cook, and Pretorius, 2007). All these times have been reported in figure 3.27 employing vertical dotted black lines.

To further highlight the differences among the configurations, and identifying possible peculiarities of the 3-BHs interaction, we performed a spectral analysis of the metric disturbances shown in figure 3.27. As a first step, we smoothed the boundaries via a *generalized normal window*, then we computed the Fourier transform

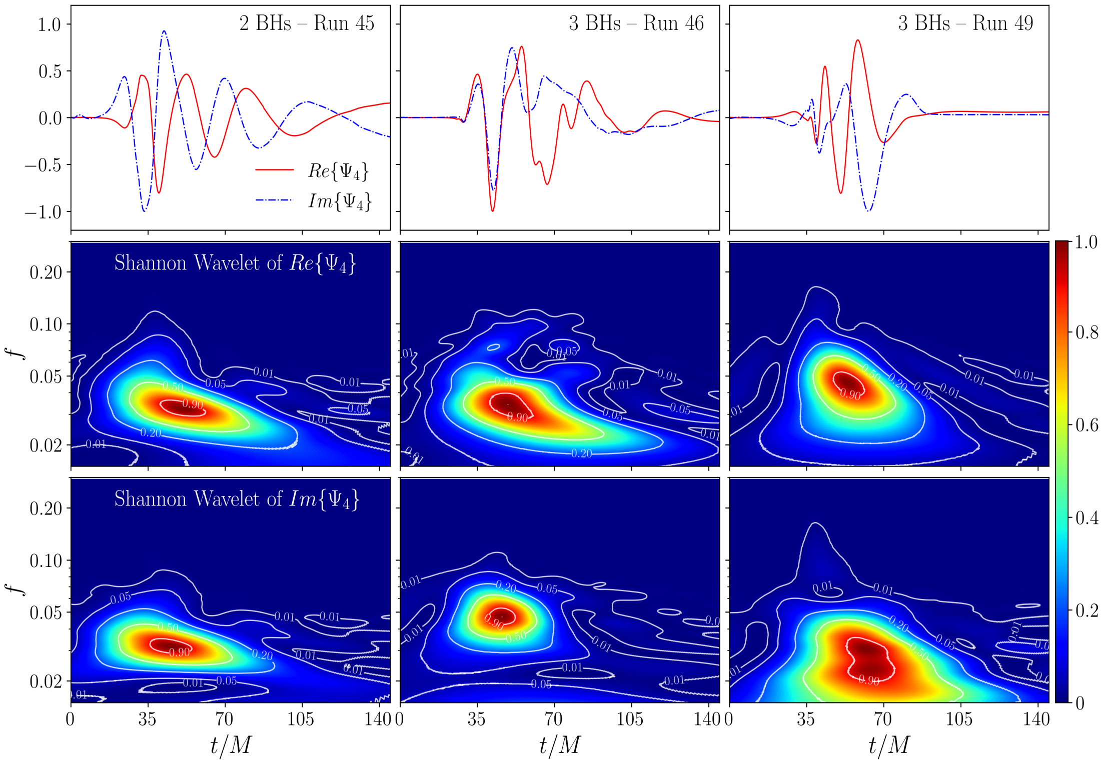

FIGURE 3.29: Spectrogram of the Shannon wavelet (second and third row) for three different waveforms (first row), namely for Run 45 (left), Run 46 (center), and Run 49 (right). In the middle and bottom row, we report the wavelet analysis for the real and the imaginary part of Ψ_4, respectively. The signals and the spectra have been normalized here to one to favor the comparison.

and hence the power spectrum. We cross-checked the spectrum with an analogous procedure, by using the Blackman-Tukey technique (Blackman and Tukey, 1958), transforming the windowed auto-correlation function of the signal. The spectrum has been computed for both the real and the imaginary parts of the projection appearing in figure 3.27. Finally, to decrease statistical uncertainties, we produced an average of the powers. As can be noticed from these averaged power spectra in figure 3.28, the 3-BHs cases (Runs 46–50) produce in general a broader distribution of frequencies. The excess of high frequencies reflects the small-scale features observed in the vicinity of the three-body system, already noticed in figure 3.26. The narrower spectrum is observed for the binary system and for Run 47, in which the head-on of the smallest black holes did not produce enough nonlinearity. On the other hand, our Run 49 produces the smallest scales of our campaign of simulations.

It is worth noticing that in the three-body case, the spectrum manifests a power-law behavior for $0.6 < \omega < 3$, stimulating interesting speculations about the possibility of a *gravitational turbulent cascade*. However, the classical one-dimensional Fourier spectrum alone cannot say too much about the nature of the dynamics, since the processes are highly non-stationary. In this regard, we shall proceed with a refined analysis, described hereafter.

Because of the non-stationarity of the signal, we analyze the wavefront by employing a wavelet decomposition. The main feature of wavelets is their natural splitting of fluctuations into different scale components according to the multiscale resolution analysis (Daubechies, 1992), being therefore a powerful tool of investigation for multi-body coalescence events. Among the several choices, all of them qualitatively consistent with each other, the clearest results are here obtained for the Shannon generating function (Unser, 2000). This reconstruction makes use of the "sinc function", which is very localized and rapidly decaying to zero – very adequate for the presence of discrete frequencies although less performant for time-localization (Cattani, 2008).

Such a typical wavelet spectrogram is reported in figure 3.29, where we take into consideration three characteristic cases: Run 45, 46, and 49. The 2-BHs case manifests a clear single peak in frequency, corresponding to the merging event. A rise-up in frequency can be seen for $5 < t < 40$, typical of the inspiral phase (Campanelli et al., 2006; Centrella et al., 2010). Real and imaginary signals of the scalar have very similar behavior. At a later time, the system shows the typical low-frequency modulation of the resultant, perturbed black hole.

Very different is the behavior of the 3-BHs. In the Classical Burrau, by looking at $Re\{\Psi_4\}$, apart from the main frequency similar to the 2-BHs due to the first head-on merger, there are secondary peaks. There is a secondary peak at $t \sim 70$ and $f \sim 0.08$, due to the follow-up disturbance that propagates from the secondary merger, when the larger BH *eats* the remaining one. This corresponds to a disturbance coming from large mass ratio coalescence. Finally, we performed the same analysis for the case with the broadest Fourier spectrum in figure 3.28, namely for Run 49. In this case, indeed, the BHs are confined by the large global angular momentum. This constraint forces the two mergings to happen at about the same time, with multiple nonlinear effects. This highly nonlinear interaction can be observed as a net broadening of the wavelet spectrum. In this case, the outgoing gravitational waves are carrying away from the final event horizon the reminiscence of such extreme interaction.

With the analysis of multiple black hole coalescence and the relative gravitational signals, we conclude our campaign of simulations in vacuum spacetimes. In the next Section, we present a preliminary GRHD test by using our `SFINGE` algorithm. Our scope is to model the dynamics of a shock wave in a nonlinear regime, using a hyperviscous technique to suppress numerical artifacts and stabilize the simulation.

3.4 Matter dynamics in `SFINGE`: preliminar tests

Our algorithm also implements the GRHD equations (2.24), together with a *Newton Raphson* scheme, to obtain the primitive variables from the evolved conservative ones. In this Section, we aim to test our `SFINGE` code via a simple, GRHD simulation, by modeling the propagation of a classical 1D sound wave, in strong nonlinear regimes. We initialize, in a Minkowsky spacetime ($\gamma_{ij} = \eta_{ij}$), the $x-$component of the 3-velocity in the form of a monochromatic sound wave, namely

$$v_x\left(x,t\right) = A\, c_s \sin\left(kx - \omega t\right),$$

where $A = 0.5$ is the amplitude, $k = 2\pi/L_x$, and $L_x = 1$ is the box size. In the above, c_s is the phase velocity equal to the classical sound speed ($c_s \ll c$), given by

$$c_s = \omega/k = \sqrt{\frac{\Gamma P_0}{\rho_0}} = 10^{-2},$$

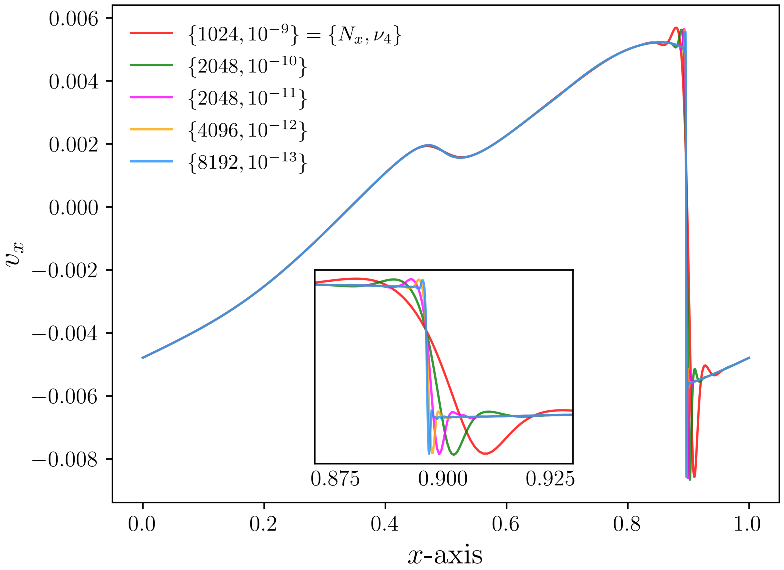

FIGURE 3.30: High amplitude shock wave at $t^* = 40$, for different resolutions and dissipative coefficients ν_4. Our Crank-Nicolson scheme can handle the shock, despite the strong gradients. The inset shows a magnification, at $x \sim 0.9$, of the shock region. For this test has been used the `SFINGE` code.

with $\rho_0 = 1$ and $P_0 = 10^{-4}/\Gamma$ unperturbed quantities and $\Gamma = 4/3$ the adiabatic index. The mass density and the pressure are initialized, respectively, by

$$\rho(x,t) = \rho_0 \left[1 + A\, c_s \sin(kx - \omega t)\right],$$
$$P(x,t) = P_0 \left[1 + A\, c_s \sin(kx - \omega t)\right].$$

The aim is to evolve a clean shock wave, without the presence of ripples, and making sure that the simulation doesn't explode. To this scope, we add in the fluid evolution equations a hyperviscous term of the form $\nu_4 \nabla^4 f(x, t)$, with $f(x, t) = D$, S^i, $\mathcal{E}$ the fluid fields and ν_4 a numerical dissipative coefficient. After doing this, we integrate them over time through a Crank-Nicolson scheme, described in Section 2.5.3.

Figure 3.30 shows the numerically simulated wave velocity $v_x(x, t^*)$ at time $t^* = 40$. We have changed the resolution of the grid, increasing the number of points from $N_x = 1024$ to $N_x = 8192$, passing through $N_x = 2048$ and $N_x = 4096$, and setting the dissipation coefficient gradually from $\nu_4 = 10^{-9}$ to $\nu_4 = 10^{-13}$. We found that by systematically increasing the dissipation coefficient ν_4, the numerically simulated wave velocity $v_x(x, t^*)$ tends to converge to a smooth and steep shock wave, as can be seen for $N_x = 8192$ and $\nu_4 = 10^{-13}$ (the blue line in the plot). In the same figure, we also report a magnification in the x-axis of the shock region, revealing more clearly the differences between configuratons. Our tests also show that a simple increase in the resolution does not involve any change in the wave profile (not shown here). For higher values of the dissipative coefficient, however, the wave is dampened too much, while for lower values the ripples are not completely eliminated. The anti-aliasing smooth filter used in the above simulations is always characterized by $k^* = N_x/6.0$, in fact, by varying the latter we have verified that the shock wave remains the same.

With the sound wave, we conclude the first part of the thesis. In the next Chapter, we move to a more realistic and exciting scenario, modeling a GRMHD simulation of plasma surrounding a rotating Kerr black hole, and making use of the Black Hole Accretion Code (`BHAC`) (Porth et al., 2017). Finally, performing direct kinetic simulations, we will focus on the behavior of the plasma in locally flat spacetimes and turbulent regimes, such as accretion disks and relativistic jets near compact objects.

Chapter 4

Plasma turbulence near compact objects

Relativistic plasmas play a not negligible role in the observation and the dynamics of supermassive compact objects. Matter surrounding black holes can orbit in the turbulent accretion disk, or be ejected in the form of relativistic jets of particles that are accelerated to velocities near the speed of light. These highly energetic phenomena lead to very complex, unpredictable, and highly turbulent dynamics. It becomes important, then, to build a solid numerical model to describe the relativistic plasma surrounding black holes. In this Chapter we aim to cope with this, by performing a campaign of direct simulations, using two different numerical codes. We start realizing a GRMHD simulation making use of the Black Hole Accretion Code (`BHAC`) (Porth et al., 2017). In particular, we aim to evolve a toroidal structure immersed in the equatorial plane of a rotating Kerr black hole, in a 2D (r, θ) geometry.

GRMHD simulations are widely used to describe astrophysical compact objects, in a number of realistic scenarios, but leave completely undetermined the microproperties of the non-thermal plasma. It becomes necessary, then, to support global fluid simulations by local, *kinetic* approaches, to capture microphysical plasma dynamics otherwise not modeled. To this scope, by introducing one of the main novelties of our work, we show results from a campaign of large-scale Particle-In-Cell (PIC) simulations, by using the `Zeltron` code (Cerutti et al., 2013). After a brief overview of the kinetic methods, in Section 4.3, we present important relationships between microphysical and macrophysical properties of relativistic plasmas surrounding black holes.

The accreting BH torus simulation has been performed at the Newton HPPC Computing Facility at the University of Calabria. The PIC simulations have been performed on HPE Apollo HAWK at the High Performance Computing Center Stuttgart (HLRS) under the grant BNSMIC, and on the SuperMUC cluster at the Leibniz Supercomputing Centre (LRZ) in Garching.

4.1 Evolution of accreting BH torus

To describe a realistic astrophysical system – such as rotating compact objects immersed in a relativistic plasma – one has to take into account both the curvature of spacetime and the matter that surrounds the object. Considerable effort has been dedicated over the last years to the modeling via general-relativistic simulations of plasma accreting onto supermassive black holes (Giacomazzo and Rezzolla, 2007; Font, 2008; Montero, Font, and Shibata, 2010; Ripperda et al., 2019; Nathanail et al., 2020; Del Zanna et al., 2020; Younsi et al., 2020).

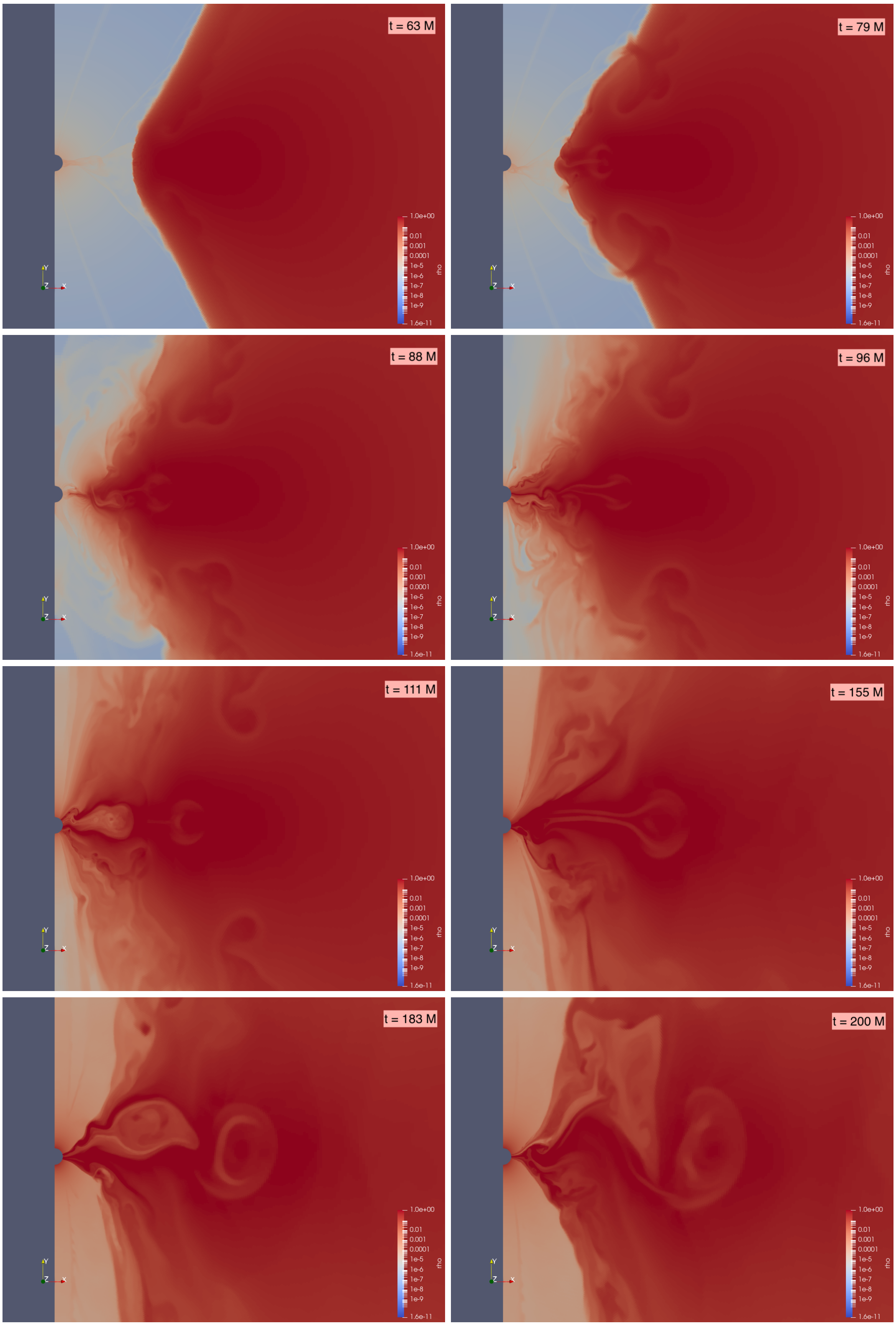

FIGURE 4.1: Evolution of the density ρ in the accreting torus evolution. One can see that, from $t/M \gtrsim 63$ (upper left panel), the instability triggers, and at $t/M = 79$ (upper right panel) vortexes are visible, where probably some local Kelvin-Helmholz instabilities are initiated. The simulation ends at $t/M = 200$ (bottom right panel) when the torus structure is destroyed. For this test the `BHAC` code has been used (Porth et al., 2017).

In this Section, we aim to model the evolution of accreting BH torus, by using the `BHAC` code. As is common in GRMHD numerical simulations, we will use the Fishbone and Moncrief (FM) accretion torus as the initial toroidal configuration (Fishbone and Moncrief, 1976). The particular solution is an equilibrium torus with constant angular momentum, presented in Kerr-Schild coordinates (Baumgarte and Shapiro, 2010), and threaded by a weak magnetic field loop. Here the spacetime is a stationary, rotating BH, with dimensionless spin parameter $a_\star = 15/16$, in the so-called *test fluid approximation*. In this theoretical context, the gravitational field of the fluid is negligible in comparison with that of the compact object, and the fluid is considered to be a perfect conductor.

The inner radius of the torus is set to $r_{\rm in}/M = 6$ and the maximum density is located at $r_{\rm max}/M = 12$, where the radial positions refer to Boyer-Lindquist (BL) coordinates. We adopt also an ideal-gas equation of state, with an adiabatic index of $\gamma^{\rm EoS} = 5/3$, and the initial entropy is $h = 10^{-3}$. The electron Γ_e and proton Γ_p adiabatic indices are fixed, respectively to 4/3 and 5/3. We set the plasma-β, namely the ratio between the plasma pressure to the magnetic pressure, to be

$$\beta = \frac{8\pi n k_B T_\alpha}{B^2} = 10^2, \tag{4.1}$$

where n and T are the number density and the temperature of the plasma, respectively, k_B is the Boltzmann constant, and $\boldsymbol{B}$ is the magnetic-field vector in the ambient plasma. The minimum density scale is $\rho_{\rm min} = 10^{-5}$ and the minimum pressure parameter is $P_{\rm min} = 0.3 \times 10^{-7}$. In our configuration, we adopt the number of grid points to be $N_r = 1024$ and $N_\theta = 512$, but the resolution is variable for the adaptive mesh refinement (AMR) technique.

We carried out the simulation up to $t/M = 200$. In figure 4.1 we report the evolution of the density ρ, for different time evolutions, namely $t/M = 63$, 79, 88, 96, 111, 155, 183, and 200 (from upper left to bottom right panel). At the beginning of the evolution, the torus is stable, but as soon as the simulation proceeds, the instability triggers. Some evident vortexes begin to evolve and it is possible to see some little, local Kelvin-Helmholz features until the instability is enough to destroy the torus structure. Large vortexes are then produced that dominate the intermittent and turbulent dynamic of the plasma in the vicinity of the black hole.

While essential to make theoretical progress on these scenarios, these GRMHD simulations can only describe the dynamically important part of the fluid, the protons (or "ions" as they are sometimes referred to), leaving completely undetermined the physical properties – such as the energy distribution, the number densities, and the temperatures – of the "lighter" part of the fluid, namely, the electrons. This represents a serious limitation for two different reasons. First, in hot, ionized plasma jets around black holes, the Coulomb coupling between electrons and protons is inefficient, so that protons and electrons are likely to have distinct temperatures, as it happens in the solar wind (Tu and Marsch, 1997; van der Holst et al., 2010; Howes, 2010; Dihingia et al., 2022). Second, proper knowledge of the the electron energy distribution is essential in order to obtain accurate imaging of supermassive black holes and hence compare with the observations (Davelaar et al., 2019; Mizuno et al., 2021; Cruz-Osorio et al., 2022). To cope with this problem, a number of phenomenological prescriptions have been suggested in the literature to relate the electron temperature to the simulated proton temperature.

In this context, a very commonly employed approach is the so-called $R-\beta$ model

(Mościbrodzka, Falcke, and Shiokawa, 2016), where the electron temperature is related to the protons temperature in terms of the plasma-β parameter, and of two free parameters, R_{low} and R_{high} (see also Anantua, Ressler, and Quataert, 2020, for a critical-β model, where two additional parameters are introduced). The plasma-β for the species $\alpha = e, p$ for electrons and protons, is defined by $\beta_\alpha = 8\pi n_\alpha k_B T_\alpha / B_0^2$, where $\boldsymbol{B}_0 = (0, 0, B_0)$ is the magnetic-field vector in the ambient plasma ($B_0 =$ const.).

The $R-\beta$ approach has been widely used by the Event Horizon Telescope (EHT) Collaboration to reconstruct theoretically the first images of supermassive black holes M87* (Event Horizon Telescope Collaboration et al., 2019a), and Sgr A* (Event Horizon Telescope Collaboration et al., 2022a) [see figure 1.3] . These investigations, in particular, have resorted to a simplified version of the $R-\beta$ approach in which $R_{\text{low}} = 1$ and spanning different values of R_{high} (Event Horizon Telescope Collaboration et al., 2019b; Event Horizon Telescope Collaboration et al., 2022b). Taking into account a more realistic description of the plasma parameters using self-consistent kinetic models have shown that finer details of the image can appear, but also that the $R-\beta$ approach is remarkably robust (Mizuno et al., 2021). Clearly, it is essential to connect the microphysical properties of the plasma with the macrophysical ones β and σ, where hybrid-kinetic models might have some limitations (Arzamasskiy et al., 2019; Valentini et al., 2014; Cerri, Servidio, and Califano, 2017). In the above, the magnetization σ is the ratio between the magnetic energy density to enthalpy density defined as

$$\sigma = \frac{B_0^2}{4\pi w}, \tag{4.2}$$

where w is the enthalpy density of the plasma $w := (\rho_e + \rho_p)c^2 + \Gamma_e \epsilon_e + \Gamma_p \epsilon_p$, with $\rho_{e,p}$, and $\epsilon_{e,p}$ being, respectively, the rest-mass densities, and the internal energy densities of electrons and protons when following an ideal-fluid equation of state (Rezzolla and Zanotti, 2013).

To gain a deeper understanding of the plasma microphysical properties, and to model also the dynamics of relativistic electrons, we have performed a campaign of large-scale PIC simulations of special-relativistic plasma in the so-called "trans-relativistic regime", that is when the plasma magnetization σ is of order unity (Ripperda et al., 2019; Mizuno et al., 2021; Bandyopadhyay, 2022; Janssen et al., 2021), and covering four orders of magnitude in the plasma-β parameter. The ranges of σ and β considered in this work are motivated by previous studies (Ball, Sironi, and Özel, 2018) and state-of-the-art GRMHD simulations with radiative transfer calculations (Cruz-Osorio et al., 2022). More specifically, the typical values for the plasma-β are $\beta \sim 0.1 - 1.0$ on the surface of accretion discs, and $\beta \sim 10^{-3} - 10^{-1}$ in the relativistic jet sheaths, while magnetization is in the range $\sigma \sim 10^{-3} - 10^{-2}$ on the surface of accretion discs, and $\sigma \sim 10^{-1} - 3$ in the jet sheaths.

In the next Section, we introduce the method adopted, and we briefly describe the code used.

4.2 A kinetic approach to plasmas: the `Zeltron` code

The classical or relativistic kinetic description of a physical system is based on describing the interaction of elements of matter via force fields, and PIC methods have been one of the most successful. In this method, the plasma is treated as an ensemble of computational particles. The system is composed of charged particles (for example negative electrons and positive ions) interacting via the Lorentz force.

The usage of PIC simulations started in the 1950s, and the development of codes worldwide is continuously increasing. Nowadays, computational resources increase exponentially, and although in general, PIC simulations require very large memory, many extensive 3D PIC simulations have been performed. A number of PIC codes have been developed in the last years, by different groups and using different techniques. They are worth mentioning, among all, `TRISTAN` (TRIdimensional STANford) (Buneman, 1993), `VPIC` (Vector Particle-In-Cell) (Bowers et al., 2008), `iPIC3D` (Markidis, Lapenta, et al., 2010), `Zeltron` (Cerutti et al., 2013), `PHOTON-PLASMA` (Haugbølle, Frederiksen, and Nordlund, 2013), `PIConGPU` Bussmann et al., 2013, `PICCANTE` (Sgattoni et al., 2015), `FBPIC` (Lehe et al., 2016), and many others.

Also, hybrid models have been developed to retain some aspects of collisionless plasma physics, while gaining orders of magnitude in resolution or in the duration of the simulation by adding some fluid description. In the hybrid-PIC method, for instance, electrons are considered massless, so they constitute a perfectly conducting fluid (Winske and Omidi, 1991; Fife, 1998). An MHD-PIC approach has also been developed to treat kinetically one species (e.g., cosmic rays), and study the interaction between this collisionless plasma and a thermal plasma (Bai et al., 2015).

Relativistic fully kinetic approaches, in which both electrons and ions are treated as particles, are widely used by the astrophysics community, to simulate plasmas in turbulent regimes, and modeling acceleration processes (Duţan et al., 2017; Sironi and Cerutti, 2017; Comisso and Sironi, 2018; Comisso et al., 2018; Comisso and Sironi, 2019). Recently, has been also presented `GRZeltron` (Parfrey, Philippov, and Cerutti, 2019), the first PIC code that considers spacetime curvatures in full GR fashion, and uses a modified $3+1$ formulation of equations. The authors provide a first-principles model for the magnetosphere and for the corona around supermassive, rotating BHs. (Crinquand, 2021; Crinquand et al., 2022; El Mellah et al., 2022).

The idea at the basis of PIC codes is to solve *indirectly* the Vlasov equation

$$\partial_t f_\alpha + \boldsymbol{v}\cdot\nabla_{\boldsymbol{x}} f_\alpha + q_\alpha\left[\boldsymbol{E}+\frac{\boldsymbol{v}}{c}\times\boldsymbol{B}\right]\cdot\nabla_{\boldsymbol{p}} f_\alpha = 0, \tag{4.3}$$

where $f_\alpha = f_\alpha(\boldsymbol{x},\boldsymbol{p},t)$ is the distribution function for the species α that characterize the palsma, $\boldsymbol{p} = \gamma m_\alpha \boldsymbol{v}$ is the momentum of the particle, $\boldsymbol{v}$ is the 3-velocity of the particles, $\gamma = 1/\sqrt{1-(v/c)^2}$ is the Lorentz factor[1], q_α and m_α are the charge and the mass of the species α.

In the particle approximation each particle does not represent a single electron (or ion), but an *ensamble* of particles, for this reason, we often refer to particles as *macro-particles*. A macro-particle in a PIC code can be seen as a small portion of the phase space distribution of the system. Such choice is physically consistent with the representation of many particles in a constant-sized macro-particle since particles with the same momentum remain close in the phase space. It is possible to show that, integrating the discrete particle trajectories, is equivalent to solving the full kinetic collisionless Vlasov equation along characteristic curves.

In this approach, the distribution function for N macroparticles is approximated by

$$f_\alpha(\boldsymbol{x},\boldsymbol{p},t) = \sum_{j=1}^{N} w_j\,\delta(\boldsymbol{r}-\boldsymbol{r}_j(t))\,\delta(\boldsymbol{p}-\boldsymbol{p}_j(t)), \tag{4.4}$$

---

[1] According to the literature, troughout this Chapter we will refer to the Lorentz factor as γ instead of W, used in the previous Chapter.

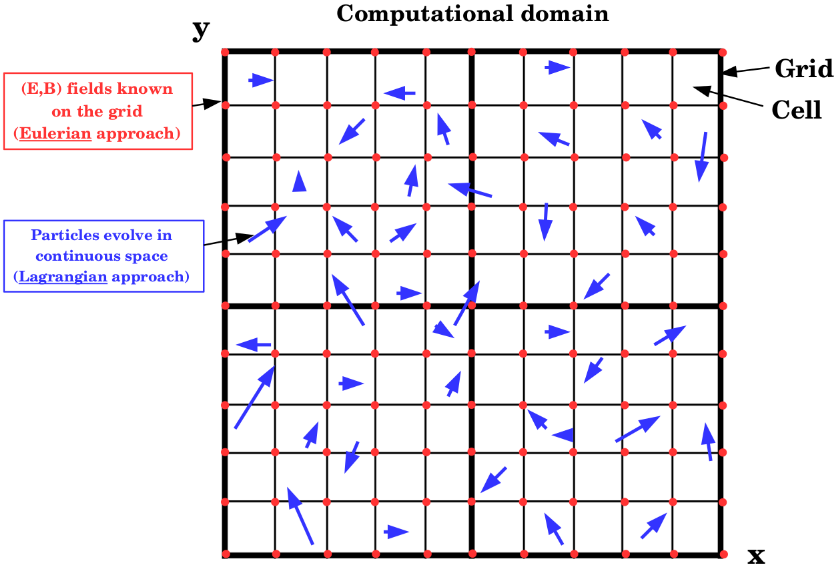

FIGURE 4.2: Schematic representation of the computational domain in PIC methods. The electromagnetic fields are known and evolved on the grid points (red dots), while the particles evolve in continuous space (blue arrows). Each cell is delimited by 4 neighboring grid points. Figure from https://ipag.osug.fr/ ceruttbe/Zeltron/index.html.

with $\boldsymbol{r}_j(t)$ and $\boldsymbol{p}_j(t)$ the position and the momenta of the $j-$th particle, and w_j is a coefficient called the *weight* of the $j-$th particle. In PIC simulations the dynamics of particles are driven by collective processes, operating through the electromagnetic fields, rather than by individual collisions which are not resolved by the PIC method. Plasma physics is only relevant at scales larger than the Debye length, defined as

$$\lambda_D = \sqrt{\frac{k_B T_e}{4\pi n e^2}}, \tag{4.5}$$

where e is the electron charge. In PIC simulations, resolving the microscopic kinetic scales is necessary.

A PIC code must solve self-consistently Newton's equations for the particles, and Maxwell's equations for the electric and magnetic fields. The computational macroparticles move on a grid (Lagrangian approach) on which their charge and current density are weighted at every time iteration Δt. The fields are then computed from Maxwell equations on the grid (Eulerian approach) starting from the interpolated sources and finally, the force on every particle is extrapolated from the grid, allowing to advance in time their position and momenta. The force acting on the particles is computed from the electric and magnetic fields evaluated at the particle position, while the electric and magnetic fields are themselves modified by the particles in the system. A schematic picture of this approach is shown in figure 4.2, where the grid nodes are marked with red dots, while the blue arrows represent the positions and the particle's velocities. This sequence of operations is repeated at each time-step in a self-consistent way, evolving the particles and the electromagnetic field states. In figure 4.3 is reported the procedure of a single time-step Δt.

In our campaign of relativistic kinetic simulations, we made use of the publicly available `Zeltron` code (Cerutti et al., 2013), an explicit relativistic electromagnetic PIC code, ideally suited for modeling particle acceleration in astrophysical plasmas. Here we briefly describe the method. In `Zeltron` code, the equations of motion are

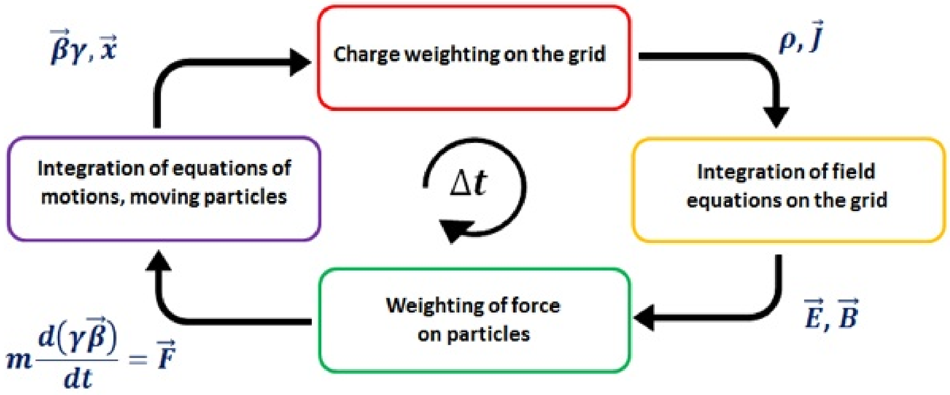

FIGURE 4.3: Typical computational procedure of PIC algorithm per time step. Yellow box: $\vec{E}$ and $\vec{B}$ fields are evolved via Maxwell's equation; Green box: the Lorentz force acting on the particles is computed with updated fields and evaluated at the particle position; Purple box: the equation of motion for particles is obtained using the Lorentz force; Red box: charge and current densities are deposited on the grid point, where $\vec{E}$ and $\vec{B}$ can be updated. Figure from http://gaps.ing2.uniroma1.it/alberto/alberto/PIC.html.

solved at each time step Δt for every of the N particles in the simulation, with $N \gtrsim 10^9$. For this reason in choosing the integration scheme for the particles, there must be a compromise between efficiency, accuracy, and computer storage capacity. The `Zeltron` code uses a *leapfrog* algorithm to evolve macroparticles in time, described here for a simple 1D case. In this approach, position and velocities are staggered on the time axis by half a timestep $\Delta t/2$, in such a way positions are defined at $t_n = n\Delta t$, while velocities are defined at $t_{n+1/2} = (n+1/2)\Delta t$. At the time step n, the basic integration formula for the leapfrog algorithm is

$$\begin{cases} x^{n+1} = x^n + \dfrac{\Delta t}{m_\alpha} p^{n+1/2}, & (4.6a) \\[2ex] p^{n+3/2} = p^{n+1/2} + \Delta t\, F(x^{n+1}), & (4.6b) \end{cases}$$

where $F(x)$ is the velocity-independent force that acts on the particles. The initialization of the scheme seems problematic, as for a given initial position and momentum, one must compute $p^{1/2}$. This induces a first-order error, but this does not matter since it only has to be done once. As a result, one can prove by a Taylor expansion in time that this scheme is accurate to the second order. Unlike the second-order Runge-Kutta method, it requires only one evaluation of the function F per time step. Note that the finite difference scheme in Equations (4.6) is time-centered, so it is time-reversal invariant. However, a minor issue of this scheme is that positions and velocities are never known at the same time step, which might be inconvenient for a variety of diagnostics.

The main upside of the leapfrog algorithm is its symplecticity, which implies a global stability of the algorithm. This means that there one can not have a secular trend, and global conserved quantities (energy, angular momentum) are usually bounded (Springel, 2016; Hairer et al., 2006). Such trends can instead be observed on long time scales even in very accurate non-symplectic schemes, such as the fourth order Runge-Kutta scheme. The equation of motion of a single macro-particle is

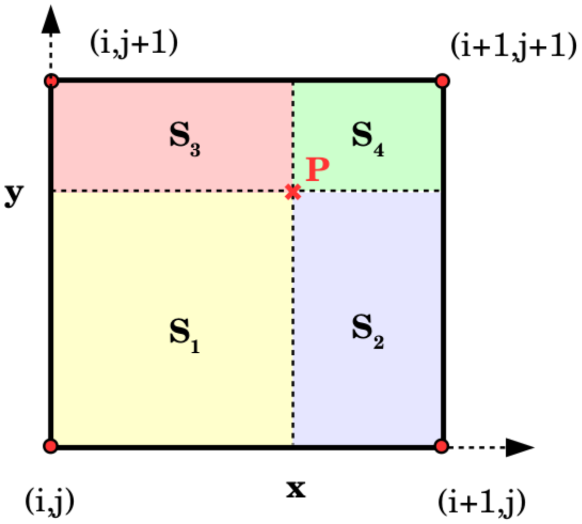

FIGURE 4.4: Area-weighting procedure on the case of a 2D Cartesian grid. The fractional charge of a particle at the point P is deposited on the four surrounding nodes in proportion to the colored shaded areas. Figure from https://ipag.osug.fr/ ceruttbe/Zeltron/index.html.

given by the Lorentz–Abraham–Dirac equation (Landau, 2013)

$$\begin{cases} \dfrac{d\boldsymbol{r}}{dt} = \dfrac{c\boldsymbol{u}}{\gamma}, & (4.7a) \\[2ex] \dfrac{d\boldsymbol{u}}{dt} = \dfrac{q_\alpha}{m_\alpha c}\left[\boldsymbol{E} + \dfrac{\boldsymbol{u}}{c} \times \boldsymbol{B}\right]. & (4.7b) \end{cases}$$

The above is the special relativistic version of Newton's equations for a macroparticle with 3-velocity $\boldsymbol{v}$ and normalized momentum $\boldsymbol{u} = \gamma \boldsymbol{v}/c$.[2]. Moreover, the fields appearing in these equations are evaluated at the particle's position. A linear interpolation from the grid to the particle's position works fine for this purpose.

A practical implementation of the particle mover is the *Boris push* (Boris and Shanny, 1973), which splits the effects of the electric and magnetic force, and can be used to evolve the momentum under the action of the Lorentz force. This method allows us to write the momentum discretized equation as

$$\begin{cases} \dfrac{\boldsymbol{u}^{+} - \boldsymbol{u}^{-}}{\Delta t} = \dfrac{q_\alpha}{2 m_\alpha c \gamma}\left[\boldsymbol{u}^{+} - \boldsymbol{u}^{-}\right] \times \boldsymbol{B}, & (4.8a) \\[2ex] \boldsymbol{u}^{\pm} = \boldsymbol{u}^{n \pm 1/2} \mp \dfrac{q_\alpha \Delta t}{2 c m_\alpha}\boldsymbol{E}_n. & (4.8b) \end{cases}$$

The Lorentz force is evaluated at integer steps (see figure 4.5), so the mean velocity $\boldsymbol{u}^n \simeq \left(\boldsymbol{u}^{n+1/2} + \boldsymbol{u}^{n-1/2}\right)/2$ is employed.

In order to solve the time-dependent Maxwell's equations, the source terms are yet to be computed. The charge density and current density are determined by the

---

[2] The `Zeltron` code also includes the radiation reaction force if synchrotron radiation is included in the simulation, not taken into account in our simulations.

particle contributions:

$$\begin{cases} \rho(\boldsymbol{r}) = \sum_{j=1}^{N} q_j \, w_j \, \delta(\boldsymbol{r} - \boldsymbol{r}_j), & \text{(4.9a)} \\ \boldsymbol{j}(\boldsymbol{r}) = \sum_{j=1}^{N} q_j \, w_j \, \boldsymbol{v}_j \, \delta(\boldsymbol{r} - \boldsymbol{r}_j). & \text{(4.9b)} \end{cases}$$

The values of the source terms must be deposited on the grid nodes, so they can be injected on the spatially discretized Maxwell's equations. The `Zeltron` code uses linear interpolation to deposit the charges and currents generated by each particle at the nodes of the computational grid (see figure 4.4). The code also assigns variable weights to the macro-particles to model particle density gradients. `Zeltron` successfully scaled on thousands of cores on the Kraken supercomputer and on the University of Colorado Janus and Verus supercomputers (Cerutti et al., 2013).

When the source terms have been updated and deposited on the grid nodes, the last step consists in evolving the fields equations. The code uses the Yee algorithm (Yee, 1966) to solve the time-dependent Maxwell's equations:

$$\begin{cases} \partial_t \boldsymbol{B} = -c \nabla \times \boldsymbol{E}, & \text{(4.10a)} \\ \partial_t \boldsymbol{E} = c \nabla \times \boldsymbol{B} - 4\pi \boldsymbol{J}, & \text{(4.10b)} \end{cases}$$

where $\boldsymbol{B}$ is magnetic field, $\boldsymbol{E}$ is the electric field, and $\boldsymbol{J}$ is the current density. The key idea of the Yee algorithm is to stagger the different components of the fields on different nodes of the grid[3]. It is instructive, for instance, to show the discretized Faraday's law (4.10a) in this fashion, which reads

$$\begin{cases} (B_x)^{n+1/2}_{i,j+1/2} - (B_x)^{n-1/2}_{i,j+1/2} = -\frac{c\Delta t}{\Delta y} \left[(E_x)^n_{i,j+1} - (E_x)^n_{i,j} \right], & \text{(4.11a)} \\ (B_y)^{n+1/2}_{i+1/2,j} - (B_y)^{n-1/2}_{i+1/2,j} = \frac{c\Delta t}{\Delta x} \left[(E_z)^n_{i+1,j} - (E_z)^n_{i,j} \right], & \text{(4.11b)} \\ (B_z)^{n+1/2}_{i+1/2,j+1/2} - (B_z)^{n-1/2}_{i+1/2,j+1/2} = c\Delta t \Big\{ -\frac{1}{\Delta x} \left[(E_y)^n_{i+1,j+1/2} - (E_y)^n_{i,j+1/2} \right] & \\ \qquad + \frac{1}{\Delta y} \left[(E_x)^n_{i+1/2,j+1} - (E_x)^n_{i+1/2,j} \right] \Big\}. & \text{(4.11c)} \end{cases}$$

In the above, the upper index denotes the time step and the lower index denotes the spatial position on the Yee grid. A schematic representation of the electromagnetic fields staggered on a 2D Cartesian grid is shown in figure 4.6.

To advance the particles, the electric and magnetic fields must be known at the same time. The magnetic field is first advanced only by half a time step $\Delta t/2$, so the particle motion can be computed. Then, the magnetic field is once again advanced by $\Delta t/2$. Assuming $\boldsymbol{E}^n$ and $\boldsymbol{B}^n$ are initially known, there are five steps to update, in

---

[3] Yee's idea was extended to numerical MHD by Brecht et al., 1981, and implemented by Evans and Hawley, 1988 in their code, coining the term *constrained transport*.

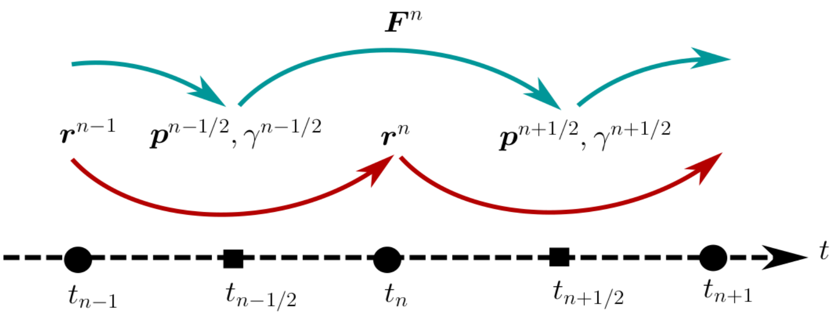

FIGURE 4.5: Representative diagram of the leapfrog scheme for the particles. The positions are defined at integer time steps, whereas the velocities are defined at half-integer time steps. Figure from Crinquand, 2021.

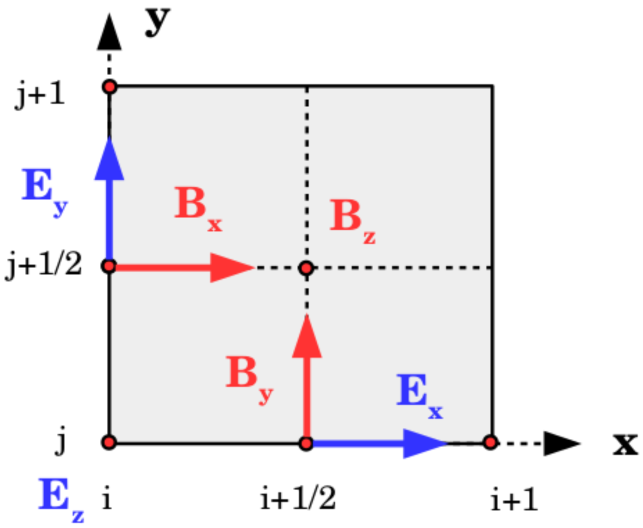

FIGURE 4.6: Graphic representation of a 2D Cartesian Yee grid. The blue arrows denote the components of the electric fields, the red ones denote the magnetic fields. The positions on the mesh are labelled by the indices i in the x direction and j in the y direction. Note that the two fields are staggered in space. Figure from https://ipag.osug.fr/ ceruttbe/Zeltron/index.html.

order:

$$\begin{aligned}
&(1)\ \ \boldsymbol{u}^{n-1/2} \longrightarrow \boldsymbol{u}^{n+1/2};\\
&(2)\ \ \boldsymbol{r}^{n} \longrightarrow \boldsymbol{r}^{n+1};\\
&(3)\ \ \boldsymbol{B}^{n+1/2} \longrightarrow \boldsymbol{B}^{n} - \frac{c\Delta t}{2}\left[\nabla \times \boldsymbol{E}\right]^{n};\\
&(4)\ \ \boldsymbol{E}^{n+1} \longrightarrow \boldsymbol{E}^{n} - c\Delta t\left[\nabla \times \boldsymbol{B}\right]^{n+1/2} - 4\pi\Delta t \boldsymbol{J}^{n+1/2};\\
&(5)\ \ \boldsymbol{B}^{n+1} \longrightarrow \boldsymbol{B}^{n+1/2} - \frac{c\Delta t}{2}\left[\nabla \times \boldsymbol{E}\right]^{n+1};
\end{aligned} \tag{4.12}$$

where the current density $\boldsymbol{J}^{n+1/2}$ is computed as the average between $\boldsymbol{J}(\boldsymbol{r}^n, \boldsymbol{u}^{n+1/2})$ and $\boldsymbol{J}(\boldsymbol{r}^{n+1/2}, \boldsymbol{u}^{n+1/2})$. Note that in step (1) the electric field $\boldsymbol{E}^n$ and the magnetic field $\boldsymbol{B}^n$ are used to update the momentum, while in step (2) the position uses the momentum $\boldsymbol{u}^{n+1/2}$.

The `Zeltron` code does not satisfy the Maxwell-Gauss constraint $\nabla \cdot \boldsymbol{E} = 4\pi\rho$ exactly, where ρ is the charge density, and the electric charge deposited on the grid is not exactly conserved. If this happens, small errors can accumulate and lead to unphysical charge densities. Therefore, the electric field has to be corrected every time step by the small amount $\delta \boldsymbol{E}$, obtained by solving the following Poisson equation

$$\nabla^2(\delta\phi) = \nabla \cdot \boldsymbol{E} - 4\pi\rho, \tag{4.13}$$

with $\delta \boldsymbol{E} = -\nabla(\delta\phi)$. This method is called *divergence cleaning* (Birdsall and Langdon, 2018). `Zeltron` has a second-order error in space and time and ensures that the magnetic constraint $\nabla \cdot \boldsymbol{B} = 0$ is satisfied at any instant of the simulation. In fact, one of the major benefits of employing the Yee grid is that the divergence of the magnetic field is automatically satisfied to machine roundoff precision provided this constraint is satisfied at the initial time.

Proof that $\nabla \cdot \boldsymbol{B} = 0$

We show here that using the Yee grid, the constraint $\nabla \cdot \boldsymbol{B} = 0$ is satisfied automatically.
One can write the discretized divergence of $\boldsymbol{B}$ as:

$$(\nabla \cdot \boldsymbol{B})^{n+1/2}_{i+1/2,j+1/2} = \frac{(B_z)^{n+1/2}_{i+1,j+1/2} - (B_z)^{n+1/2}_{i,j+1/2}}{\Delta x} + \frac{(B_z)^{n+1/2}_{i+1,j+1/2} - (B_z)^{n+1/2}_{i,j+1/2}}{\Delta y}. \tag{4.14}$$

If the divergence of the magnetic field remains constant, this means that the variation $\delta(\nabla \cdot \boldsymbol{B}) = (\nabla \cdot \boldsymbol{B})^{n+1/2}_{i+1/2,j+1/2} - (\nabla \cdot \boldsymbol{B})^{n-1/2}_{i+1/2,j+1/2} = 0$. Using the discretization reported in Equations (4.11) one has

$$\begin{aligned}
\delta(\nabla \cdot \boldsymbol{B}) =& \frac{1}{\Delta x}\left\{ \left[(B_x)^{n+1/2}_{i+1,j+1/2} - (B_x)^{n-1/2}_{i+1,j+1/2}\right] - \left[(B_x)^{n+1/2}_{i,j+1/2} - (B_x)^{n-1/2}_{i,j+1/2}\right] \right\} \\
&+ \frac{1}{\Delta y}\left\{ \left[(B_y)^{n+1/2}_{i+1/2,j+1} - (B_y)^{n-1/2}_{i+1/2,j+1}\right] - \left[(B_y)^{n+1/2}_{i+1/2,j} - (B_y)^{n-1/2}_{i+1/2,j}\right] \right\} \\
=& \frac{c\Delta t}{\Delta x \Delta y}\Big[- (E_z)^n_{i+1,j+1} + (E_z)^n_{i+1,j} + (E_z)^n_{i,j+1} - (E_z)^n_{i,j} \\
&+ (E_z)^n_{i+1,j+1} - (E_z)^n_{i,j+1} - (E_z)^n_{i+1,j} + (E_z)^n_{i,j} \Big] \\
=& 0.
\end{aligned} \tag{4.15}$$

As a result we obtain $\nabla \cdot \boldsymbol{B} = \text{const}$. It remains zero if it is initialized at zero.

4.3 A kinetic study of special-relativistic plasma turbulence

In this Section, we present a very comprehensive campaign of two-dimensional PIC simulations of special-relativistic turbulence to investigate systematically the microphysical properties of the plasma in the trans-relativistic regime. In all the simulations, we employ a physical proton-to-electron mass ratio (see Rowan, Sironi, and Narayan, 2017, for the importance of using a realistic mass ratio), and analyze the most important microphysical properties of the turbulent plasma, namely, the spectral index of the electron energy distributions κ, the efficiency in the production of nonthermal particles $\mathcal{E}$, and the temperature ratio $\mathcal{T} := T_e/T_p$.

For each of these quantities, we provide two-dimensional fitting functions that describe their behavior in the relevant space of parameters, thus connecting the microphysical properties of the plasma with the macrophysical ones β and σ. The parameter ranges explored here overlap and extend those considered in previous and influential works of astrophysical kinetic turbulence (Zhdankin et al., 2019; Zhdankin, 2021; Kawazura, Barnes, and Schekochihin, 2019; Kawazura et al., 2020). Exploiting this large coverage of the space of parameters, we can model the behavior of all of these quantities, providing a convenient tool to introduce kinetic effects in global GRMHD simulations.

Our results can find application in a wide range of astrophysical scenarios, including the accretion and the jet emission onto supermassive black holes, such as M87* and Sgr A*, thus improving the existing modeling of accretion flows (Porth et al., 2019; Cruz-Osorio et al., 2022; Chatterjee et al., 2021; Ripperda et al., 2022; Event Horizon Telescope Collaboration et al., 2022b) The physical and numerical parameters of our simulations are summarized in Tables 4.1, and 4.2. Each of the large-scale simulations has been performed via parallel MPI directives on 32, 768 cores, using a total of $\sim$ 20 M CPU hours.

4.3.1 Simulation setup

To carry out our investigation and to simulate the full development of relativistic turbulence in kinetic plasmas, we employ a two-dimensional (2D) geometry in Cartesian coordinates retaining, as in any fully consistent plasma model, the three-dimensional components of the magnetic and electric fields, of the current density, and of the pressure tensor. We initialize all of our simulations with the same number density for electrons and protons in a computational domain that is a Cartesian box of side $L_x = L_y = L = 16384\,dx$, where $dx = d_e/3$ is the cell resolution and $d_e := c/\omega_{pe}$ is the electron-skin depth. In the above, c is the speed of light and

$$\omega_{pe} = \sqrt{\frac{4\pi n_e e^2}{m_e}}\left[1 + \frac{\theta_e}{\Gamma_e - 1}\right]^{-1/2} \tag{4.16}$$

is the electron plasma frequency, m_e the electron mass, Γ_e the electron adiabatic index, and $\theta_e = k_B T_e/(m_e c^2)$ the dimensionless electron temperature. We have also carried out three more simulations with a smaller box, $L = 2730\,d_e$, and resolution of $(8192)^2$, $(16384)^2$, and $(32768)^2$ points (see Appendix for details). Furthermore, we set up our computational box so that it is periodic in the x- and in the y-directions. Finally, in all our simulations, each computational cell is initialized with 10 particles per cell (i.e. 5 electrons and 5 protons). As a result, during our evolutions, we follow the dynamics of $\sim 2.7 \times 10^9$ particles per simulation.

We initialize our system as done in typical simulations of plasma turbulence (see, e.g. Servidio et al., 2012). The initial conditions consist of a relativistic plasma perturbed by a 2D spectrum of Fourier modes for the magnetic field. To avoid any compressive activity, neither density perturbations nor parallel variances (i.e. with components out of plane) are imposed at $t = 0$. In practice, we start from expressing the z-component of the vector potential in Fourier modes as $A_z(x, y) := \sum_{k_x,k_y} A_k \exp\left[i(\boldsymbol{k} \cdot \boldsymbol{x} + \phi_{\boldsymbol{k}})\right]$, where $\boldsymbol{k} = (k_x, k_y)$ is the wavevector with modulus $k = |\boldsymbol{k}| = (2\pi/L)m$ (m is the dimensionless wavenumber), and $\phi_{\boldsymbol{k}}$ are randomly chosen

TABLE 4.1: Summary of the physical parameters of our main simulations, which are all performed with the real electron-to-proton mass ratio, equal electron and proton initial temperatures, a resolution of three cells per electron-skin depth ($d_e/dx = 3$), and a box of size $\sim 5461\, d_e$ in both directions. From top to bottom we report: the number of the Run, the magnetization σ, the plasma β, the dimensionless temperatures $\theta_{p,e}$ for protons and electrons respectively, and the Debye length λ_D in units of d_e.

Run	σ	β	θ_p	θ_e	λ_D
1	0.1	10^{-4}	5×10^{-6}	9.2×10^{-3}	9.6×10^{-2}
2	0.1	3×10^{-4}	1.5×10^{-5}	2.7×10^{-2}	0.16
3	0.1	10^{-3}	5×10^{-5}	9.2×10^{-2}	0.3
4	0.1	3×10^{-3}	1.5×10^{-4}	0.27	0.52
5	0.1	10^{-2}	5×10^{-4}	0.92	0.96
6	0.1	2×10^{-2}	10^{-3}	1.84	1.36
7	0.1	0.1	5×10^{-3}	9.18	3.02
8	0.1	0.3	2×10^{-2}	36.7	6.05
9	0.1	0.7	4.5×10^{-2}	82.6	9.08
10	0.1	1.0	6.8×10^{-2}	124.8	11.2
11	0.1	1.5	0.1	183.6	13.5
12	0.3	10^{-4}	1.5×10^{-5}	2.7×10^{-2}	0.16
13	0.3	3×10^{-4}	5×10^{-5}	9.2×10^{-2}	0.3
14	0.3	10^{-3}	1.5×10^{-4}	0.27	0.52
15	0.3	3×10^{-3}	5×10^{-4}	0.92	0.96
16	0.3	10^{-2}	1.5×10^{-3}	2.75	1.66
17	0.3	3×10^{-2}	5×10^{-3}	9.18	3.02
18	0.3	0.11	2×10^{-2}	36.7	6.06
19	0.3	0.34	8×10^{-2}	146.9	12.1
20	0.3	0.55	0.2	367,2	19.6
21	1.0	10^{-4}	5×10^{-5}	9.2×10^{-2}	0.3
22	1.0	3×10^{-4}	1.5×10^{-4}	0.27	0.52
23	1.0	10^{-3}	5×10^{-4}	0.92	0.96
24	1.0	3×10^{-3}	1.5×10^{-3}	2.75	1.66
25	1.0	10^{-2}	5×10^{-3}	9.18	3.02
26	1.0	3×10^{-2}	1.5×10^{-2}	27.5	5.24
27	1.0	10^{-2}	5×10^{-2}	91.8	9.58
28	1.0	0.16	0.2	367.2	19.2
29	3.0	10^{-4}	1.5×10^{-4}	0.27	0.52
30	3.0	3×10^{-4}	5×10^{-4}	0.92	0.96
31	3.0	10^{-3}	1.5×10^{-3}	2.75	1.66
32	3.0	3×10^{-3}	5×10^{-3}	9.18	3.02
33	3.0	10^{-2}	1.5×10^{-2}	27.5	5.24
34	3.0	2.6×10^{-2}	5×10^{-2}	91.8	9.58
35	3.0	5.5×10^{-2}	0.2	367.2	19.2

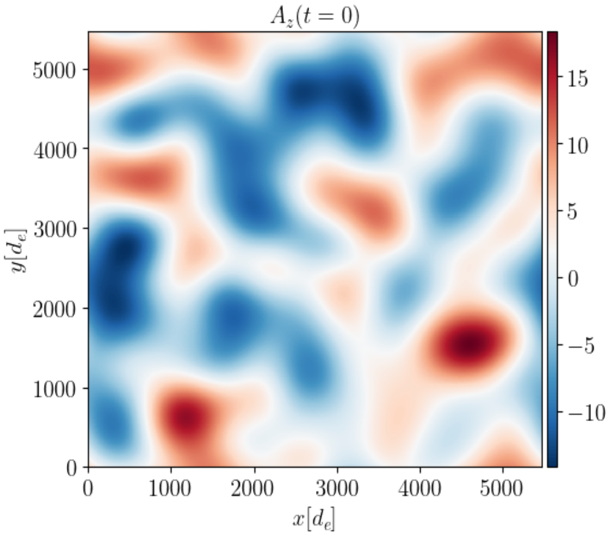

FIGURE 4.7: Out-of-plane component for the vector potential at initial time, for a representative PIC simulations. The field is initialized perturbing the Fourier spectrum with random modes.

phases. The amplitude of the modes is set as

$$A_k = \left[1 + \left(\frac{k}{k_0}\right)^{15/3}\right]^{-1},$$

such that it is peaked at $k_0 = (2\pi/L)m_0$ with $m_0 = 4$. The spectrum is set to zero at $m > 7$ in order to construct initial conditions consistent with random large-scale structures. In figure 4.7 we report the initial out-of-plane component of the vector potential, for a representative configuration. The magnetic-field components B_x and B_y are then computed by straightforward derivatives. Finally, in order to mimic a highly turbulent regime, we fix the amplitude of the fluctuations to be $\langle B_\perp \rangle / B_0 \sim 1$, where $\langle B_\perp \rangle$ is the root-mean-square value of the in-plane fluctuations. Note that, to satisfy the above condition, different value of the initial A_z are employed for different simulations. We also define the Alfvén crossing time as $t_A := L/v_A$, where $v_A := c\sqrt{\sigma/(1+\sigma)}$ is the Alfvén speed.

As the simulation proceeds, turbulent magnetic reconnection takes place, leading to a nonlinear change in magnetic topology and converting magnetic energy into kinetic and internal energy (Servidio et al., 2009; Servidio et al., 2012). This process strongly affects the dynamics of the plasma on all the scales we could reproduce with our simulations. This highly dynamical system evolves with magnetic flux ropes moving, colliding, and sometimes repelling each other depending on the magnetic-field polarity. This dynamics proceeds till a stationary state is achieved after about an Alfvén crossing time (see also the top panels of figure 4.9 and the Appendix for a detailed discussion).

4.3.2 Relativistic plasma turbulence

At the initial time, after fixing β and σ for each simulation, we set the temperatures, which are uniform for both species. In particular, we first specify the proton-β_p parameter and then obtain the electron temperature so as to have a specific initial temperature ratio $\mathcal{T}_0 := T_{e,0}/T_{p,0}$. At any time during the simulation we measure

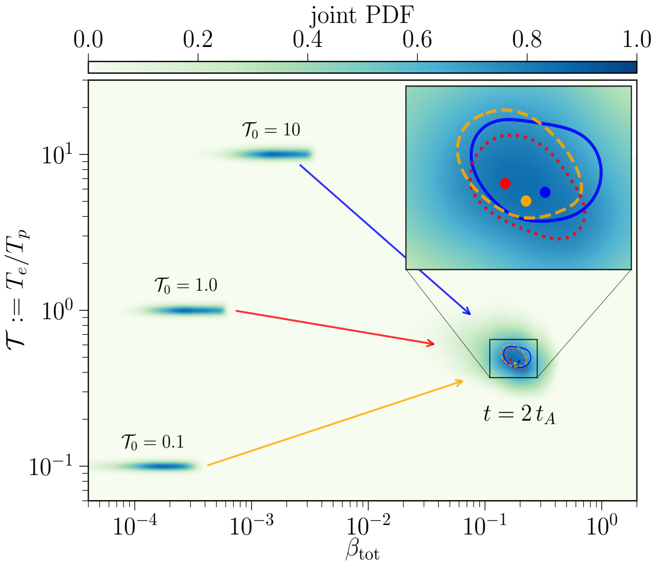

FIGURE 4.8: Initial and final values at time $t = 2\,t_A$ of the normalized joint PDFs of the temperature ratio $\mathcal{T}$ and of the total β parameter, $\beta_{\rm tot} := \beta_e + \beta_p$. The data refers to three representative simulations with initial temperature ratio $\mathcal{T}_0 = 0.1, 1.0$ and 10. The inset shows the 90% contour lines of the joint PDFs, while the circles mark the maxima of each PDF. Note that all PDFs converge to the same final area in the $(\mathcal{T}, \beta_{\rm tot})$ plane despite the very different initial data

the spatial distributions in the (x, y) plane of $\beta_{\rm tot} := \beta_e + \beta_p$ and $\mathcal{T}$, from which we compute the joint PDFs for the two quantities, namely, $(\beta_{\rm tot}, \mathcal{T})$. The temperature for each species is computed from $T_\alpha := p_\alpha / n_\alpha k_B$, where p_α is the isotropic pressure, i.e. $p_\alpha := \frac{1}{3}(p^{xx}_\alpha + p^{yy}_\alpha + p^{zz}_\alpha)$ and p^{ij}_α is the pressure tensor.

This is shown in figure 4.8, where we report the joint PDFs at the initial ($t = 0$) and final ($t = 2\,t_A$) times for three representative simulations initialized respectively with $\mathcal{T}_0 = 0.1, 1.0$, and 10. Clearly, the three initial setups have different joint PDFs narrowly distributed around the three initial values of the temperature ratio $\mathcal{T}_0$. Interestingly, however, at the final time they have all converged to the same equilibrium distribution, irrespective of the initial data. This can be best appreciated in the inset, which reports a zoom-in of the central region of the final distributions, with the color-coded contour reporting the 90%-value for each simulation, while the circles represent the maximum of each joint PDF. This convergence has been verified to take place for four different values of the initial temperature ratio ($\mathcal{T}_0 = 0.01, 0.1, 1.0$ and 10.0), while keeping $\sigma = 0.3$ and $\beta = 3 \times 10^{-4}$. The behaviour in figure 4.8 induces us to conjecture that the choice of the initial temperature $\mathcal{T}_0$ is effectively unimportant at least in the ranges explored here[4] as its memory is lost by the time the system has reached a steady state. In view of this, we set $\mathcal{T}_0 = 1.0$ for the 35 simulations performed varying σ and β (note that with such initial temperature ratio, the plasma-β parameter is the same for electrons and protons, i.e. $\beta_e = \beta_p =: \beta$). The ranges of σ and β explored are compatible with previous kinetic studies, state-of-the-art GRMHD simulations, and radiative-transfer calculations (Ball, Sironi, and Özel, 2018; Cruz-Osorio et al., 2022; Fromm et al., 2022). As also noted by Pecora

---

[4] A word of caution: we have shown the initial temperature to be irrelevant once turbulence is developed for a specific set of initial values of β and σ. Given the physical arguments given above, extending this conclusion to different initial values is a conjecture that is reasonable but challenging to prove, especially for $\beta \sim 1$.

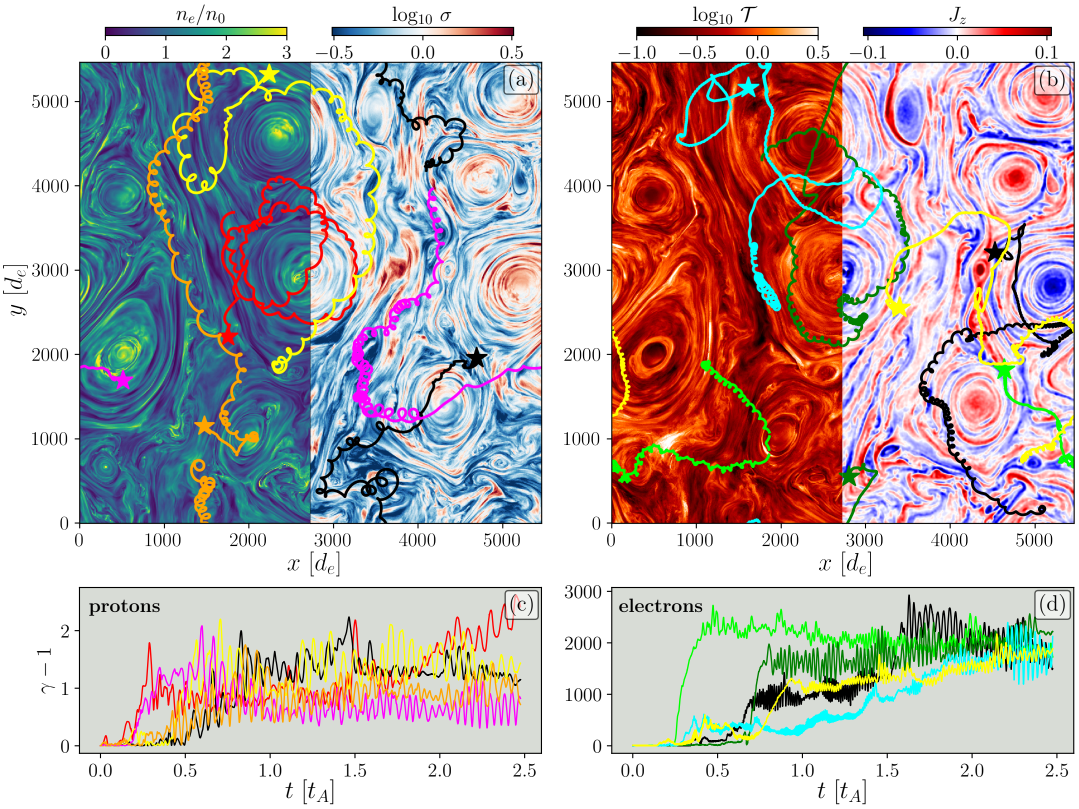

FIGURE 4.9: Representative quantities in a fully developed 2D turbulence at $t = 1.5\,t_A$ for a representative simulation with $\sigma = 1$ and $\beta = 3\times10^{-3}$. The top panels offer a dual view of: the electron number density normalized to the initial value n_e/n_0 and of the magnetization σ [panel (a)], and of temperature ratio $\mathcal{T}$ and of the total current density J_z [panel (b)]. Also overplotted with different colors are representative particle trajectories, with protons on the left and electrons on the right of each panel (the initial position of each particle is marked with a star). The lower panels [(c) and (d)] report instead the evolution of the Lorentz factor for the same particles marked above.

et al. (2019), higher values of β would require a much higher number of particles to counter the statistical noise, making purely PIC calculations of this type computationally expensive with modern resources.

Figure 4.9 provides a very compact but powerful overview of the fully developed turbulent state for a simulation with $\sigma = 1.0$ and $\beta = 3\times10^{-3}$ (Run 24 in Table 4.1), at time $t = 1.5\,t_A$. Each upper panel is split into two regions reporting different plasma properties. Panel (a) shows the electron number density n_e normalized to the initial number of particles per cell n_0 (left), and the magnetization σ (right). Panel (b), instead, reports temperature ratio $\mathcal{T}$ (left) and the out-of-plane electric-current density J_z (right). Note how in analogy to nonrelativistic kinetic simulations, vortex-like and sheet-like structures corresponding to magnetic flux tubes are present at all the scales that are resolved in the simulation (Servidio et al., 2012; Comisso and Sironi, 2018; Parashar, Matthaeus, and Shay, 2018; Pecora et al., 2019). High number-densities "magnetic islands" can be found in large-scale flux tubes, and in general, the density is larger in these coherent quasi-circular structures.

At the same time, the largest temperatures (ratios) are not achieved at the center of the islands, which are instead comparatively cooler. This is because the temperature is higher between flux tubes, where reconnection layers lead to the formation of plasmoids within narrow current sheets (Servidio et al., 2009; Comisso and

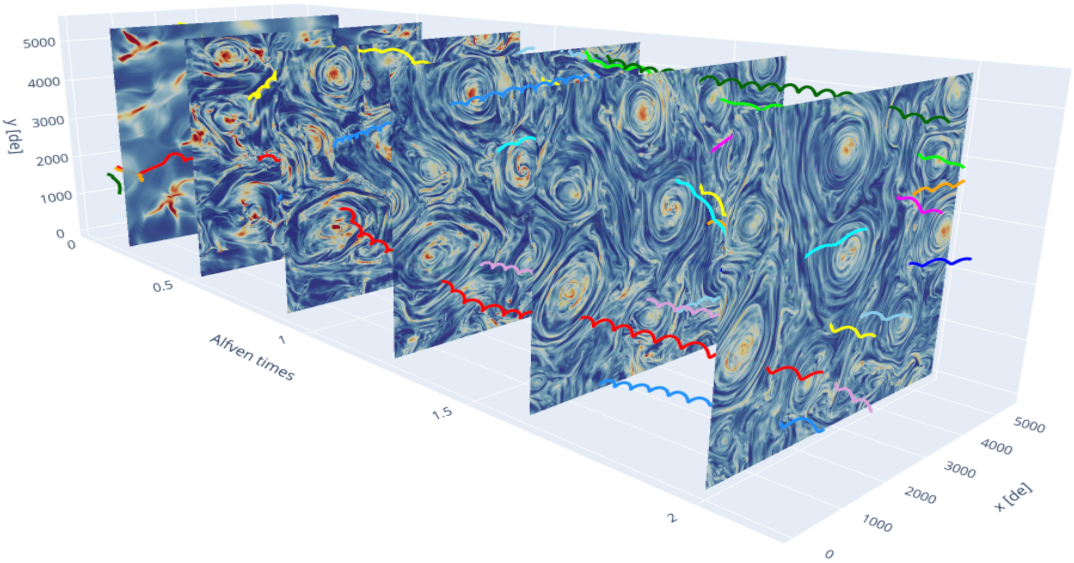

FIGURE 4.10: 3D visualization for the electron density field and for some macroparticles (protons) trajectories, for the Run 24 (see Table 4.1). Note that the trajectories move on a periodic boundary box.

Sironi, 2018; Pezzi et al., 2021). Elongated unstable current sheets tend to fragment into chains of plasmoids and small-size current sheets appear on a wide range of scales (Hellinger et al., 2015; Dong et al., 2018; Huang and Bhattacharjee, 2016). Notice also that the out-of-plane electric-current density J_z shows a variety of current sheets of different sizes. Some of these current layers break into smaller plasmoids and these regions are important for the heating of the plasma and the acceleration of the particles.

The various quantities shown in figure 4.9 are overlaid with the trajectories of some of the most energized particles that we tracked (protons in the left panels and electrons in the right ones). In particular, we track a sample of 500 electrons and 500 protons during the whole simulation, both randomly chosen. The starting position of each particle is marked with a star. Note how, quite generically, and in addition to the basic gyrations at the corresponding Larmor radii, there are particles that have closed orbits as they are trapped in a flux rope, while others experience turnovers that suddenly bend the trajectory, similarly to what observed in nonrelativistic turbulence simulations (Pecora et al., 2018)[5]. Overall, when a particle experiences a reconnection process and is accelerated, it increases abruptly its Larmor radius, but also its Lorentz factor γ, and kinetic energy.

In the lower panels (c) and (d) of figure 4.9 we show the evolution of the Lorentz factor of the particles tracked in the upper panels (a) and (b), with protons being reported in panel (c) and electrons in panel (d). As expected, and shown by the different vertical scales of panels (c) and (d), electrons experience considerably larger accelerations when compared to protons. This is simply due to the different masses of the two species: electrons, which have a smaller Larmor radius, are more efficiently accelerated by the thin current sheets where magnetic reconnection takes place. This stochastic acceleration mechanism of multi-reconnection events is very efficient and

---

[5] When the turbulence is fully developed, the velocity distribution of the electrons is highly nonthermal and their Larmor radius is significantly larger as a result of the large accelerations, and this effectively increases our resolution.

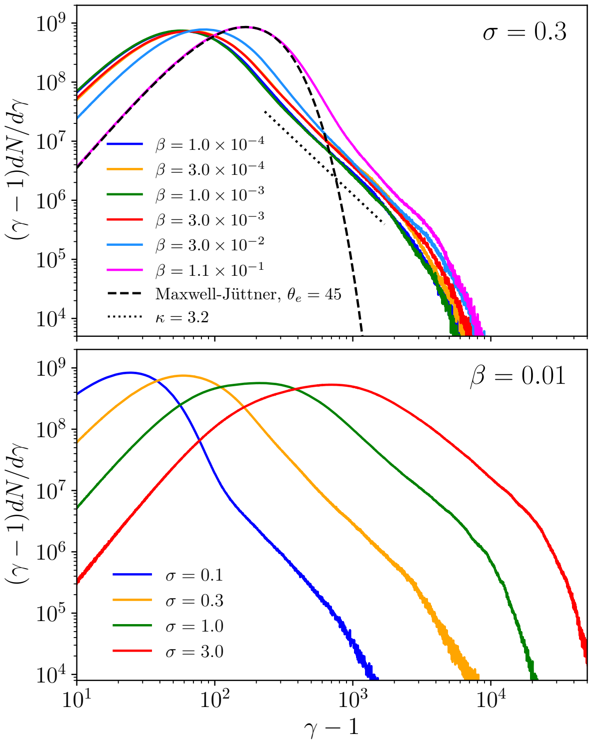

FIGURE 4.11: *Top panel:* electron-energy spectra at $t = 2\,t_A$ for simulations with $\sigma = 0.3$ and different values of β; indicated with a dashed line is the a Maxwell-Jüttner distribution for $\beta \simeq 0.1$, while the dotted line indicates the almost constant spectral index $\kappa \simeq 3.2$. *Bottom panel:* Same as above, but for simulations with $\beta = 0.01$ and different values of σ.

commonly observed in astrophysical plasma turbulence (Drake et al., 2009; Haynes, Burgess, and Camporeale, 2014).

The tracked particles start from $\gamma \gtrsim 1$, and most of them experience a sudden acceleration episode, and then a sequence of second-order Fermi-like processes of acceleration (Comisso and Sironi, 2018; Comisso and Sironi, 2019). Particles trapped in magnetic islands show a Lorentz factor increasing in time (e.g. the red proton in the left panels). Other particles, instead gain energy only once and then reach a quasi-steady state as is typical for particles entering the magnetic island only for a short time and then bounced in a stochastic manner between different structures. In figure 4.10 is shown the same simulation in a 3D fashion, showing the turbulent electron density field in time. Also, the trajectories of macro-particles (protons) are reported and highlighted with different colors. One can notice that particles move in a periodic world, appearing through one side when they overstepped the opposite side.

Relativistic hydrodynamical turbulence naturally provides a landscape of intermittency and large spatial variance because the compressibility is enhanced by relativistic effects (Radice and Rezzolla, 2013); in addition, relativistic magnetohydrodynamical turbulence provides the natural conditions to produce extreme-acceleration events and generate a large population of particles – electrons in particular – with energy distributions that differ significantly from a thermal one (see, e.g. Zhdankin et al., 2017). This is summarized in figure 4.11, which reports the electron energy-distribution functions (spectra) $(\gamma - 1)dN/d\gamma$ at $t = 2\,t_A$ as a function of the Lorentz factor $\gamma - 1$, for some representative simulations. More specifically, the upper panel shows the electron spectra from simulations with $\sigma = 0.3$ and for a wide range of values of β; the black dashed line is a Maxwell-Jüttner distribution where the value of the dimensionless electron temperature $\theta_e := k_B T_e/(m_e c^2) = 45$ is chosen to reproduce the low-energy part of the spectrum for the case $\beta = 0.11$ and is obviously different for each simulation. Note that the high-energy part of the spectra is well approximated by a power-law $dN/d\gamma \propto \gamma^{-\kappa+1}$ (Davelaar et al., 2019; Fromm et al., 2021), whose index $\kappa \simeq 3.2$ is quite insensitive to the value of the plasma-β parameter in the range $\beta \lesssim 3 \times 10^{-3}$ (see black dotted line). For very large values of β, however, a single power law does not represent the distribution accurately, and only the very high-energy part of the spectrum maintains an index $\kappa \simeq 3.8$.

In the bottom panel of figure 4.11, we instead explore how the electron-energy spectra change when varying σ while keeping $\beta = 0.01$. Note that as the magnetization increases, the amount of magnetic energy available for dissipation increases, leading to a systematic shift towards progressively larger energies of the spectra. Furthermore, the high-energy part of the spectra is well approximated by power laws with indexes $\kappa \simeq 3 - 4$, while the highest regions of the spectra terminate with increasingly harder slopes. Overall, and in agreement with several previous works (Comisso and Sironi, 2018) – some of which even have different initial conditions (Werner et al., 2018; Ball, Sironi, and Özel, 2018) – our results clearly indicate that turbulence promotes the particle acceleration, producing energy distributions that contain a considerable fraction of very energetic (suprathermal) particles.

We provide evidence that the computed electron-energy spectra reach a steady state after $t/t_A \gtrsim 1.8 - 2.0$, so that the extraction of the spectral index κ and of the efficiency $\mathcal{E}$ is both accurate and robust. Figure 4.16 shows four representative simulations having different values of σ (see Runs 7, 18, 27, and 31 in Table 4.1). In each case, we plot the electron-energy spectra at different times during the evolution as indicated by the colormap on the right of each of the four panels. Furthermore, marked with black vertical lines of various types are three different values of the Lorentz factor $\gamma - 1$ and the corresponding evolutions are shown in the bottom panels for each of the four simulations considered. Clearly, all cases show that by $t/t_A \sim 2.0$ the simulations have reached stationarity with relative time variations that are $\lesssim 1.5\%$, so that κ and $\mathcal{E}$ can be extracted reliably.

Given the kinetic behavior of the plasmas described so far, it is essential to be able to express their properties via analytic fitting functions and in terms of the basic parameters of the plasma, namely, β, σ, so that the resulting expressions can then be employed directly in the GRMHD modeling of astrophysical plasma. A summary of this analytical modeling is presented in figure 4.12, where in the top row we show as a function of β and σ, respectively, the electron spectral index κ, the nonthermal energy efficiency $\mathcal{E}$, and the temperature ratio $\mathcal{T}$. Note that the data reported in the first two columns refers to simulations at $t = 2\,t_A$, while that in the right column is averaged over the time window $1.7 < t/t_A < 2.3$ to avoid the oscillations introduced by the stochastic behavior of turbulence. Similarly, the bottom row of figure 4.12 reports one-dimensional cuts of the same quantities, but at fixed values of the magnetization ($\sigma = 0.1 - 3.0$), where each circle refers to a distinct simulation of our set. Note that for any fixed value of σ we explored plasma parameters up to the maximum one $\beta_{\max} \sim 1/(4\sigma)$ (Ball, Sironi, and Özel, 2018), where our estimates are inevitably less accurate.

Exploiting the large set of simulations performed, we can now construct analytical 2D fits to the various quantities, starting with the electron spectral index $\kappa(\beta, \sigma)$, which can be expressed as

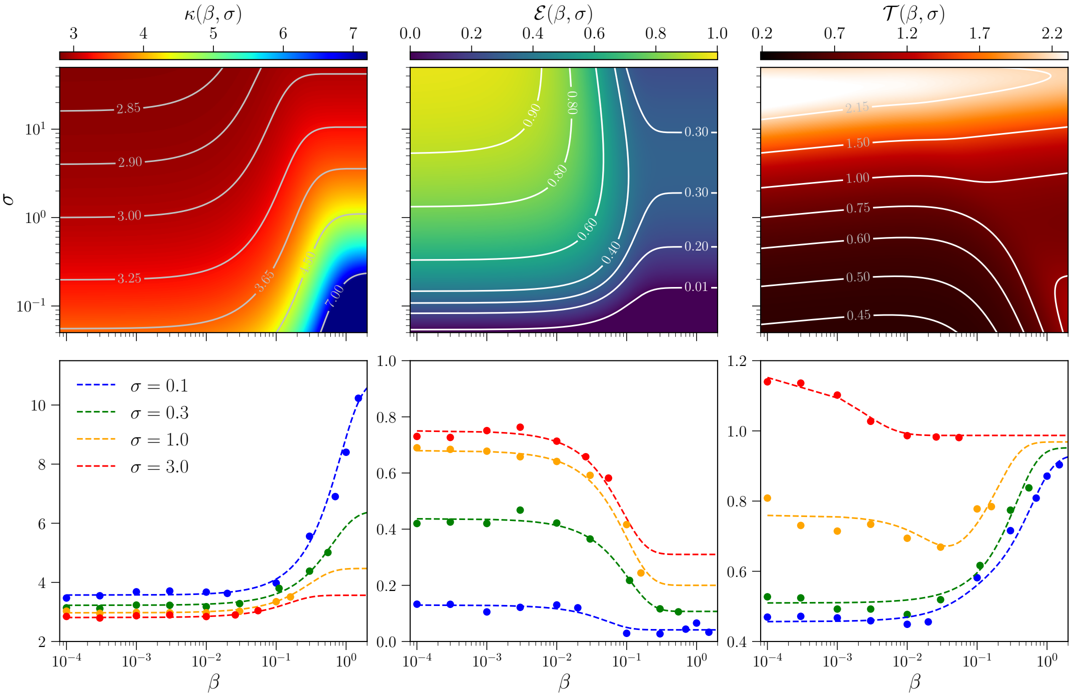

FIGURE 4.12: *Top panels:* from the left to right are reported as a function of β and σ: the electron spectral index κ, the energy efficiency $\mathcal{E}$, and the temperature ratio $\mathcal{T}$, respectively [see Eqs.(4.17)–(4.20)]. *Bottom panels:* Same as above, but at fixed values of the magnetization ($\sigma = 0.1 - 3.0$); each circle refers to a distinct simulation.

$$\kappa(\beta,\sigma) = k_0 + \frac{k_1}{\sqrt{\sigma}} + k_2\,\sigma^{-6/10}\tanh\left[k_3\,\beta\,\sigma^{1/3}\right]\,, \tag{4.17}$$

where $k_0 = 2.8$, $k_1 = 0.2$, $k_2 = 1.6$ and $k_3 = 2.25$ (see top-left panel of figure 4.12). Note that Zhdankin et al. (2017) have proposed a similar but simpler fitting expression that depends on σ only and thus does not account for variations in the plasma β. Overall, the spectral index shows two main features. First, at fixed σ, the spectral index is essentially independent of β, for $\beta \lesssim 10^{-2}$, but it increases at larger values of β, approaching a very steep tail. Second, at fixed β, the index becomes generally smaller for increasing values of σ.

Next, we quantify the efficiency in the production of particles with nonthermal energies in terms of the weighted average of the excess over a Maxwell-Jüttner distribution (Ball, Sironi, and Özel, 2018), namely

$$\mathcal{E} := \frac{\int_{\gamma_0}^{\infty}\left[dN/d\gamma - f_{\rm MJ}(\gamma,\theta)\right](\gamma-1)\,d\gamma}{\int_{\gamma_0}^{\infty}(dN/d\gamma)(\gamma-1)\,d\gamma}\,, \tag{4.18}$$

where γ_0 denotes the peak of the spectrum, $f_{\rm MJ} := \gamma^2 v/[c\,\theta_e K_2(1/\theta_e)]e^{-\gamma/\theta_e}$, with v the velocity and K_2 the modified Bessel function of the second kind. The corresponding 2D fit of the data can then be expressed as

$$\mathcal{E}(\beta,\sigma) = e_0 + \frac{e_1}{\sqrt{\sigma}} + e_2\,\sigma^{1/10}\tanh\left[e_3\,\beta\,\sigma^{1/10}\right]\,, \tag{4.19}$$

where $e_0 = 1.0$, $e_1 = -0.23$, $e_2 = 0.5$ and $e_3 = -10.18$ (see top-middle panel of figure 4.12). Also in this case, the energy efficiency shows three main features. First,

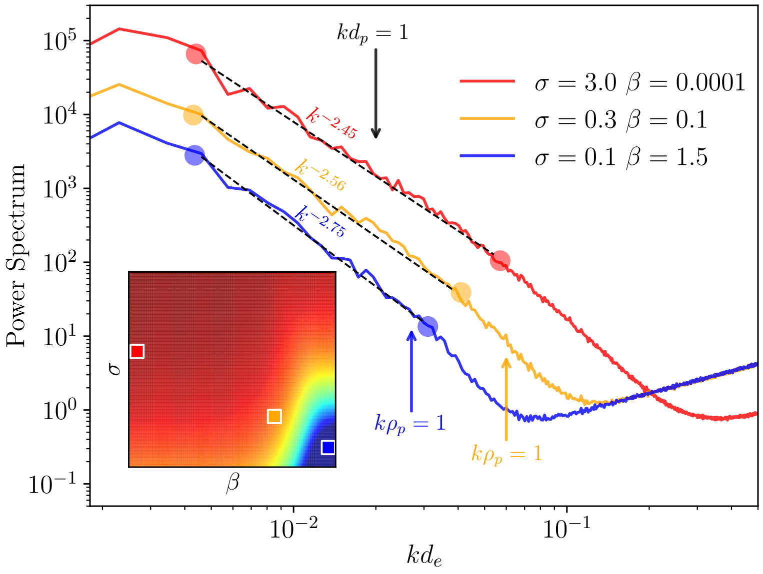

FIGURE 4.13: Magnetic-field power spectra for three simulations sampling important locations in the (β, σ) space of parameters. Each simulation is marked with a different color and the corresponding location is shown in the inset, which reports also the electron spectral index. Black dashed lines indicate the turbulent power laws, while the circles delimit the boundaries of each turbulent range, which we define as the limits of the power-law scaling; the arrows mark the wavevectors associated to the proton-skin depth ($kd_p = 1$) and to the proton Larmor radius ($k\rho_p = 1$), which is outside the horizontal scale for the red line.

for $\beta \lesssim 10^{-2}$ the efficiency saturates at a value that is independent of β, but systematically larger for higher values of σ. Second, for high values of β and low values of σ, it approaches $\mathcal{E} \sim 0$, because the electron spectrum becomes significantly softer. Third, for higher values of σ, the efficiency is the largest, since the spectra widen to larger electron energies.

Finally, we consider what is arguably the most important quantity modeled in our simulations, namely, the dependence of the temperature ratio on the plasma properties. The corresponding 2D fit is given by

$$\mathcal{T}(\beta, \sigma) = t_0 + t_1 \sigma^{\tau_1} \tanh\left[t_2\, \beta\, \sigma^{\tau_2}\right] + t_2\, \sigma^{\tau_3} \tanh\left[t_3\, \beta^{\tau_4}\, \sigma\right] \,, \tag{4.20}$$

where $t_0 = 0.4$, $t_1 = 0.25$, $t_2 = 5.75$, $t_3 = 0.037$, and $\tau_1 = -0.5$, $\tau_2 = 0.95$, $\tau_3 = -0.3$, $\tau_4 = -0.05$ (see top-right panel of figure 4.12). Overall, it is easy to see that for low magnetizations, i.e $\sigma \in [0.1, 0.3]$, and small values of the β parameter, i.e. $\beta \lesssim 0.01$, the temperature ratio is essentially constant and then starts to grow to values as large as $\mathcal{T} \simeq 1$ for $\beta \lesssim 1.0$. On the other hand, for high values of the magnetization, i.e. $\sigma \simeq 3.0$, the behavior is quite the opposite, the values of $\mathcal{T}$ are higher for lower β and decrease when increasing β. For intermediate values of the magnetization, i.e. $\sigma = 1.0$, the behavior is a combination of the two described above, showing a nonmonotonic dependence for $\beta \in [0.01, 0.1]$. Interestingly, in all cases, $\mathcal{T} \sim 1.0$ for $\beta \simeq 1$, independently of the value of σ, thus highlighting that, under these conditions, electrons and protons are fully coupled and have roughly the same temperature. Conversely, for $\beta \lesssim 10^{-4}$, the temperature ratio will depend on the plasma magnetization, being larger for larger magnetizations, as expected for regimes where electrons can be accelerated to suprathermal energies at reconnection

TABLE 4.2: Table of simulation in which we varied different parameters. Runs A1-A3 have different initial $\mathcal{T} = T_p/T_e$ (and hence different β_e and θ_e), while all other parameters ($\sigma, \beta_p, \theta_p, d_e/dx, L/d_e$) are the same. Runs B1-B3 have different values of the electron-skin depth per dx and use a smaller physical box of $2730\,d_e$. From top to bottom we report: the number of the Run, the magnetization σ, the proton and electron plasma β, the proton and electron dimensionless temperatures $\theta_{p,e}$, the initial temperature ratio $\mathcal{T}_0$, the number of cells per electron-skin depth (d_e/dx), and the physical box size in terms of electron-skin depth.

Run	A1	A2	A3	B1	B2	B3
σ	0.3	0.3	0.3	0.3	0.3	0.3
β_p	3×10^{-4}	3×10^{-4}	3×10^{-4}	3×10^{-4}	3×10^{-4}	3×10^{-4}
β_e	3×10^{-2}	3×10^{-3}	3×10^{-5}	3×10^{-4}	3×10^{-4}	3×10^{-4}
θ_p	5×10^{-5}	5×10^{-5}	5×10^{-5}	5×10^{-5}	5×10^{-5}	5×10^{-5}
θ_e	9.18	0.92	9.2×10^{-3}	9.2×10^{-2}	9.2×10^{-3}	9.2×10^{-3}
$\mathcal{T}_0$	10^{-2}	0.1	10.0	1.0	1.0	1.0
d_e/dx	3.0	3.0	3.0	3.0	6.0	12.0
L/d_e	5461.3	5461.3	5461.3	2730.6	2730.6	2730.6

sites. More importantly, expression (4.20) provides a compact and microphysically consistent description of the electron temperatures that can be employed in modern GRMHD codes of accretion flows onto black holes.

We conclude the discussion of our results by returning to the behavior of the electron spectral index κ. As shown in the top-left panel of figure 4.12 and summarized in Eq. (4.17), electron acceleration is higher in low-β and high-σ turbulent plasmas. As suggested already by Drake et al. (2009), this behaviour may be due to the interaction of the electron orbits with small-sized current sheets; such a mechanism can then extract particles from the thermal population and bring them to very high energies via primary and secondary Fermi-like mechanisms (Pecora et al., 2018; Comisso and Sironi, 2018). In fully developed GRMHD turbulence, accelerating islands and current sheets are present on all scales and these could therefore provide the natural site for the accelerating mechanism.

In this simple picture, it is natural to expect that the larger the spectrum of fluctuations at small scales, the more efficient the accelerating mechanism (Haynes, Burgess, and Camporeale, 2014). To validate whether this applies also to trans-relativistic plasmas, we have computed the (not normalized) isotropic power spectrum of the magnetic field for three representative simulations and reported them in figure 4.13 as a function of the dimensionless kd_e [the inset shows with colored squares the location in the $(\sigma,\ \beta)$ plane of the three configurations, while the arrows mark the wavevectors associated to the proton-skin depth ($kd_p = 1$) and to the proton Larmor radius ($k\rho_p = 1$)] and over a downsampled grid of $(1024)^2$ (see Appendix for a discussion). In essence, after assuming the turbulence to be isotropic and homogeneous, we integrate the 2D Fourier transforms $\widetilde{B}_i$ over concentric shells (in this sense, the power spectrum is isotropic) to obtain one-dimensional spectra, whose sum we plot in figure 4.13 [note that the growth of the power spectrum at large wavenumbers is a typical noise effect of PIC simulations due to a finite number of particles, (see, e.g. Karimabadi et al., 2013)].

In general, figure 4.13 reveals a number of interesting features, moving in the

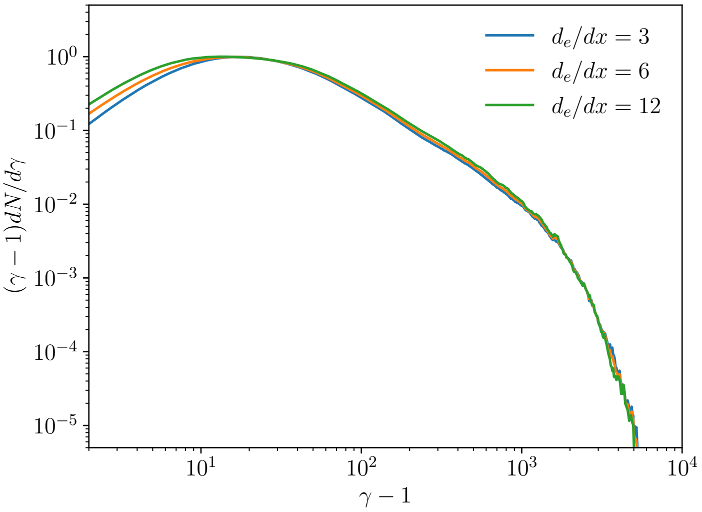

FIGURE 4.14: Electron-energy spectra with $\sigma = 0.3$ and $\beta = 3 \times 10^{-4}$ for three different resolutions $d_e/dx = 3, 6$ and 12, using a physical box size of $L/d_e = 2730$. The spectra are computed at $t/t_A = 2.0$ and clearly show to be nearly insensitive to the increased resolution.

parameter space from (low-β, high-σ) to (high-β, low-σ). First, the power spectrum is clearly higher in the case of the low-β, high-σ simulation, confirming a more efficient cascade process (Franci et al., 2016). Second, the spectrum is shallower in the sub-ion inertial range (Sahraoui et al., 2009) indicating a more developed turbulence. Finally, and more interestingly, the turbulent cascades terminate at much smaller scales for (low-β, high-σ) simulations, suggesting the existence of thinner current sheets at subproton scales that accelerate particles more efficiently (Pecora et al., 2018). Figure 4.13 then confirms the suggestion that plasmas with low β and large σ naturally lead to broad turbulent scenarios and are the most efficient in extracting particles from the thermal population and accelerating them (Pecora et al., 2018; Comisso and Sironi, 2018).

As these simulations represent one of the most systematic PIC explorations of trans-relativistic turbulence, can be employed in a wide range of astrophysical systems, such as jets and accretion disks around supermassive black holes, and, of course, their imaging (see, e.g. Event Horizon Telescope Collaboration et al., 2019b; Event Horizon Telescope Collaboration et al., 2022b). In particular expressions (4.17), (4.18), and (4.20) provide compact and reasonably accurate descriptions of the behavior of these microphysical plasma properties and can be employed in a number of scenarios involving compact objects and described by macrophysical plasma characteristics. Importantly, since they have been derived from first-principle calculations, they represent a considerable improvement over the rather crude and purely empirical expressions employed at the moment in GRMHD simulations. The formulas provided in this work can be improved by extending the present two-dimensional treatment to three dimensions and thus assessing the role played by dimensionality in studies of this type.

4.4 Appendix A: additional simulations

Apart from the 35 large-scale simulations reported in Table 4.1, we performed 6 additional configurations varying different parameters, as reported in Table 4.2. As a

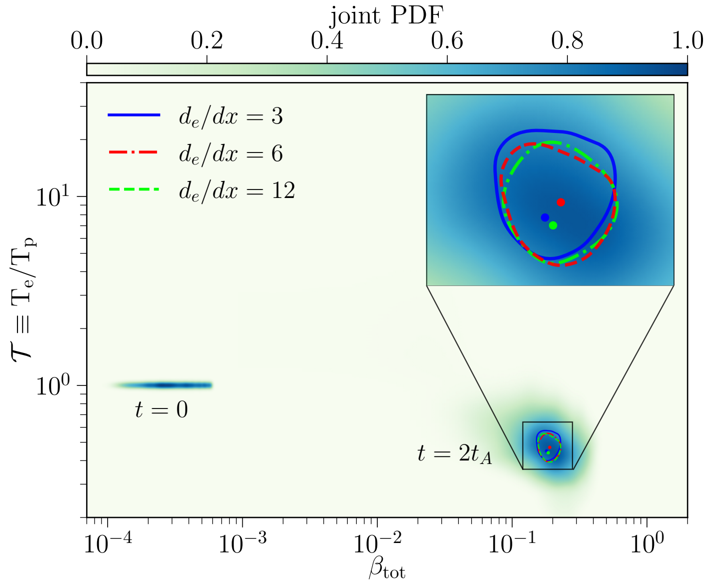

FIGURE 4.15: Initial and final values at time $t = 2\,t_A$ of the normalized joint PDFs of the temperature ratio $\mathcal{T}$ and of the total plasma β (see figure 1), using three different resolutions, namely $d_e/dx = 3, 6$, and 12. The inset shows the 90% contour lines of the joint PDFs, while the circle mark the maxima of each distribution. Note that all PDFs converge to the same final area in the $(\mathcal{T}, \beta_{\rm tot})$ plane.

first test, to show that our final configuration is independent of the initial electron-to-proton temperature, we have varied $\mathcal{T}_0$ spanning in the range $[0.001 - 10.0]$ (see Runs A1-A3 in Table 4.2). Results of these simulations are reported in Fig. 4.8, where we show that final joint PDFs are independent of the choice of $\mathcal{T}_0$. Note that for these configurations, the initial plasma β is different for electrons and protons.

4.4.1 Resolution tests

We have also verified that our results are insensitive to the choice of different (higher) resolutions in terms of d_e/dx. In particular, we have performed three simulations using an increasing number of cells per electron skin depth, from $d_e/dx = 3$ up to $d_e/dx = 12$ (see Runs B1-B3 in Table 4.2). In the latter case, we have used a physical box of $L/d_e = 2730$ in both directions and varied the number of mesh points from $(8192)^2$ up to $(32768)^2$. In this last high-resolution configuration, we have followed the dynamics of $\sim 1.1 \times 10^{11}$ particles.

Figure 4.14 compares the electron-energy spectra for a case with $\sigma = 0.3$ and $\beta = 3 \times 10^{-4}$ when varying the number of electron-skin depths per cell, i.e. $d_e/dx = 3 - 12$. Clearly, the main features of the electron-energy spectra and in particular the slope are very similar for the three different resolutions. Indeed, the relative differences between the three spectra are $\lesssim 6.0\%$ and thus even smaller than the variations due to the stochastic nature of turbulence, which can cause variation in κ up to $\sim 10.0\%$ (Ball, Sironi, and Özel, 2018).

In figure 4.15 we show the joint PDFs for the ratio of temperatures $\mathcal{T}$ and the plasma $\beta_{\rm tot} = \beta_e + \beta_p$ for the same runs. In the inset we report a zoom-in of the central region of the PDFs at the final time of $t = 2\,t_A$. The color-coded contour report the 90%-value for each distribution, while the circle represent the maximum of each joint PDF. One can see that for the three different resolutions we obtain similar final distributions, with a variation in $\mathcal{T} \lesssim 5.0\%$.

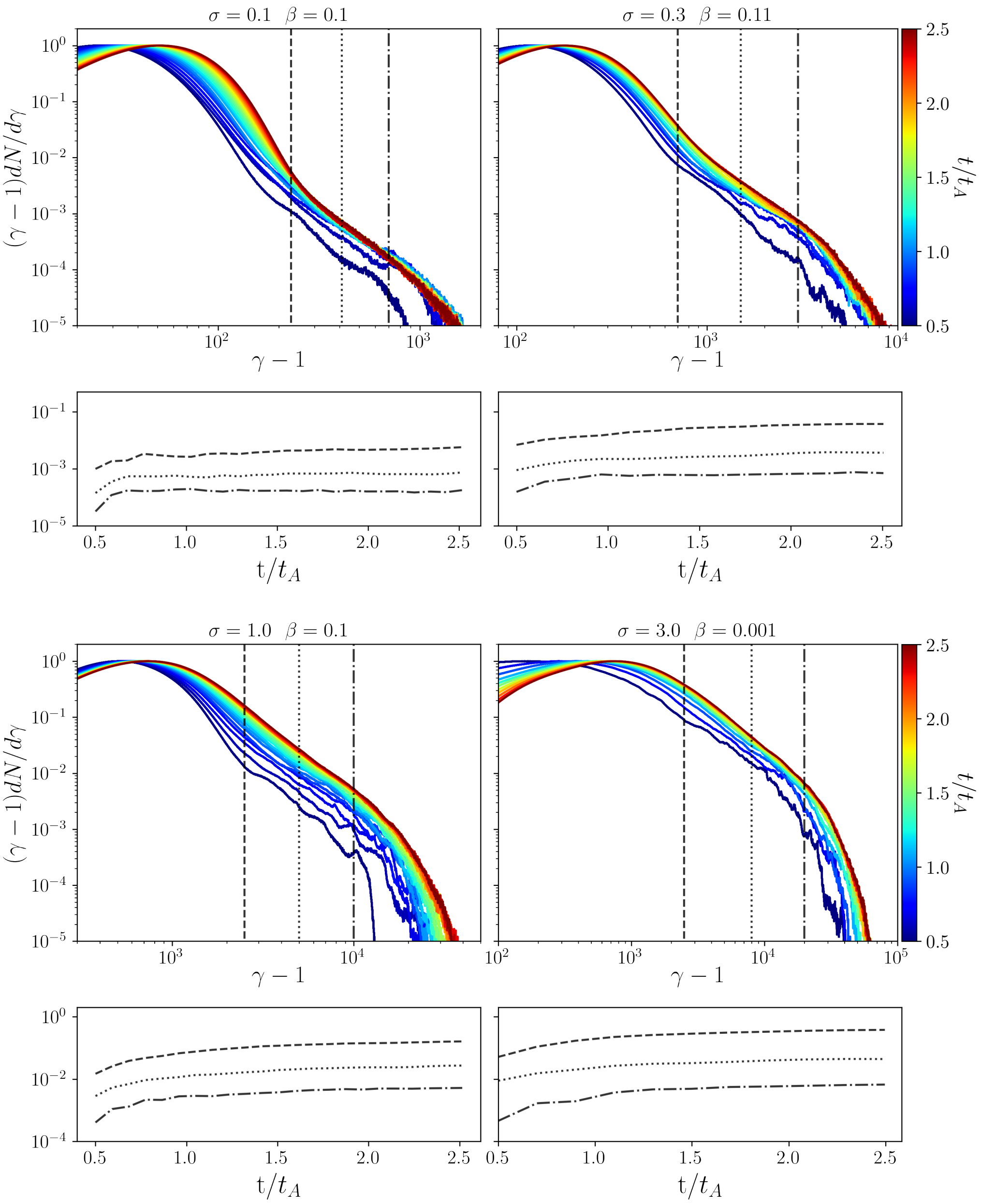

FIGURE 4.16: Four representative simulations in which we show the stationarity of the electron-energy spectra (see Runs 7, 18, 27, and 31 in Table 4.2). For each simulation, we report the spectra at different times during the evolution as indicated by the colormap on the right of each of the four panels. Marked with black vertical lines of various type are three different values of the Lorentz factor $\gamma - 1$ and the corresponding evolutions are shown in the bottom panels for each of the four simulations considered. Clearly, all cases show that by $t/t_A \sim 2.0$ the simulations have reached stationarity.

As a concluding remark, we note that the power spectrum in Fig. 4.13 has been computed on a down-sampled grid of $(1024)^2$ points and not on the full-resolution data of $(16348)^2$ points. This coarse-graining operation is routinely done in such expensive simulations, and for two distinct reasons. First, the large particle noise due to the high temperatures reached essentially blurs out the smallest scales, so that using the full resolution does not really provide any additional information. Second, the downsampling allows us to reduce by a factor of $16^2 \sim 250$ the space needed for the ouput (we recall that we save data for 38 fields at very high cadence).

As a result, while the simulation maximum wavenumber is $k_{\max}\, d_e = 9.4$ and is not shown in the spectrum in Fig. 4.13, the maximum wavenumber in the downsampled spectrum is $k_{\max}\, d_e = 0.6$ and is well-captured.

4.4.2 Stationarity of spectra

Finally, we provide evidence that the computed electron-energy spectra reach a steady state after $t/t_A \gtrsim 1.8 - 2.0$, so that the extraction of the spectral index κ and of the efficiency $\mathcal{E}$ is both accurate and robust. Figure 4.16 shows four representative simulations having different values of σ (see Runs 7, 18, 27, and 31 in Table 4.1). In each case, we plot the electron-energy spectra at different times during the evolution as indicated by the colormap on the right of each of the four panels. Furthermore, marked with black vertical lines of various type are three different values of the Lorentz factor $\gamma - 1$ and the corresponding evolutions are shown in the bottom panels for each of the four simulations considered. Clearly, all cases show that by $t/t_A \sim 2.0$ the simulations have reached stationarity with relative time variations that are $\lesssim 1.5\%$, so that κ and $\mathcal{E}$ can be extracted reliably.

4.5 The role of kinetic turbulence for black hole images reconstruction: preliminary tests

We here report preliminary results of the impact of our self-consistent prescriptions (4.17), (4.18), and (4.20) on the structure and morphology of the M87 jet. In particular, we performed long-term, high-resolution, three-dimensional GRMHD simulations of magnetically arrested (MADs) disks around rotating BHs with a fixed spin value of Kerr black hole, $a_\star = 15/16$, which is the best model found in Cruz-Osorio et al., 2022.

We initialize our state-of-the-art three-dimensional GRMHD simulations with a magnetized torus seeded with weak poloidal magnetic field in hydrodynamical equilibrium, using the numerical code `BHAC` (Porth et al., 2017). During the simulation, the development of the magnetorotational instability triggers accretion and leads to a fully turbulent flow and jet launching.

The further step consists of the calculation of the radiative signatures and, to this scope, the general-relativistic radiative transfer (GRRT) calculations are performed with the `BHOSS` code (Younsi et al., 2020). The code needs to be tuned by fixing the mass of the M87* as $M = 6.5 \times 10^9 M_\odot$, and the distance to $D = 16.8$ Mpc. An essential aspect of such GRRT modeling consists in the use of a non-thermal energy distribution for the electrons, that we model as (Fromm et al., 2022)

$$\frac{dN_e}{d\gamma_e} = N_0 \gamma_e \sqrt{\gamma_e^2 - 1}\left[1 + \frac{\gamma_e - 1}{\kappa w}\right]^{-(\kappa+1)}, \tag{4.21}$$

where N_e is the electron number density, γ_e is the electron Lorentz factor and N_0 is a normalization parameter. In the above expression, the "kappa" distribution κ is taken from our self-consistent model, using equation (4.17). The weighted temperature w is defined as

$$w = \frac{\kappa - 3}{\kappa}\theta_e + \frac{\epsilon}{2}\left[1 + \tanh(r - r_{\rm inj})\right]\frac{\kappa - 3}{6\kappa}\frac{m_p}{m_e}\sigma, \tag{4.22}$$

where $r_{\rm inj}$ is the injection position in terms of gravitational radii r_g, and ϵ is a tunable parameter between zero and one, that accounts for the fraction of magnetic energy

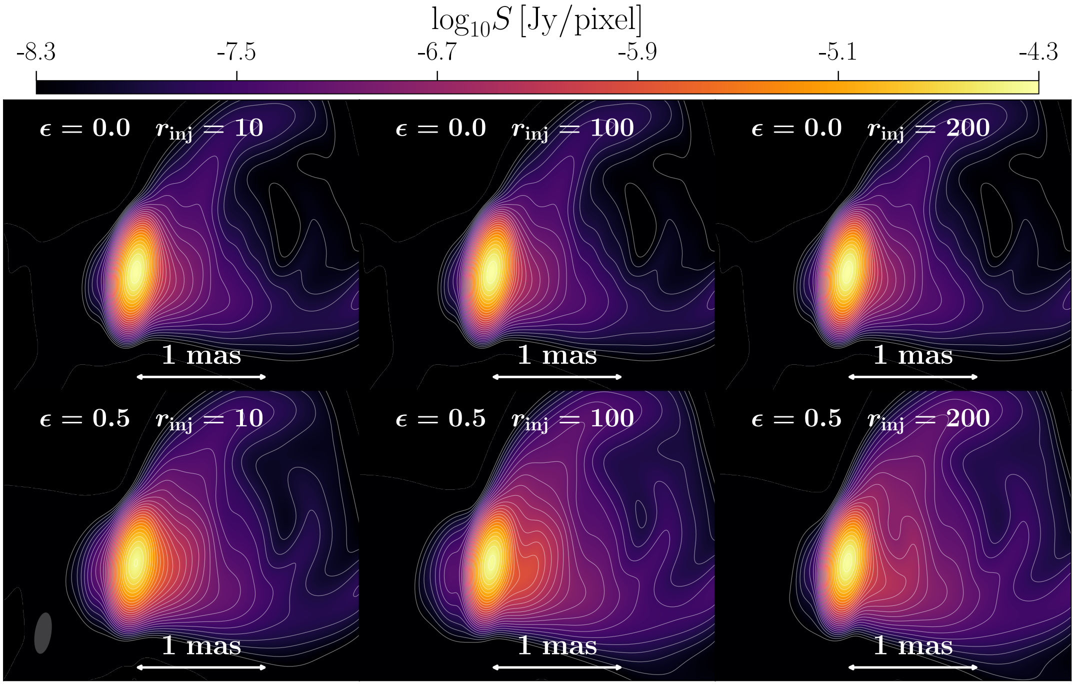

FIGURE 4.17: Convolved GRRT images for thermal and nonthermal emission models at 86 GHz for our MADs models of M87. Notice the different $r_{\rm inj}$ values (columns) and different ε (rows), while the parameter spin is fixed at $a_\star = 15/16$.

contributing to the heating of the radiating electrons. As we already mentioned, the GRMHD simulations only model the dynamics of the non-radiating ions. To close the system and to relate the temperature of the latter to the temperature of the radiating electrons, we use our prescription $\mathcal{T}(\beta, \sigma)$ (4.20).

We only consider results of the simulations in the time interval between $t/M \in [13,000 - 15,000]$ for our GRRT analysis, to ensure a stable mass accretion rate $\dot{M}$ and well-developed turbulence. We also scale $\dot{M}$ in order to match the observed compact flux density of 1.0 janskys (Jy) at 86 GHz (3 mm) (Mościbrodzka et al., 2014) and to fit the broad-band spectrum of the flux density S in the range of frequencies $\nu \in [10^{10}\ \mathrm{Hz} - 10^{16}\ \mathrm{Hz}]$. Our simulations can reproduce the morphology of the M87 jet with high accuracy up to distances $r \sim 1$ milliarcsecond (mas) from the core, as deduced from the Global mm Very Long Baseline Interferometry Array (GMVA) observation in February 2014 (Narayan et al., 2012). In figure 4.17 we present the 86 GHz convolved images from our model of M87 for different $r_{\rm inj}$ values (columns) and different ε (rows). In particular ϵ assumes values 0.0 and 0.5, while $r_{\rm inj} = 10, 100, 200$. We present the best-fit images, deduced from the normalized cross-correlation coefficient, computed between the GRRT images and the GMVA observations.

The overall structure of the 86 GHz images can be described by a bright innermost region and a broader, weak jet. The innermost emission (r < 0.1 mas) is mainly generated in the disk region and is nearly independent of the choice of ε. The jet emission could be understood as a radiation generated in the jet sheath and disk wind. These two regions are characterized by plasma$-\beta \simeq 0.1$ (Fromm et al., 2022). As a comparison, in figure 4.18 we report the 86 GHz GMVA observation in February 2014 for M87* (Kim et al., 2018). Note the overall good matching between our

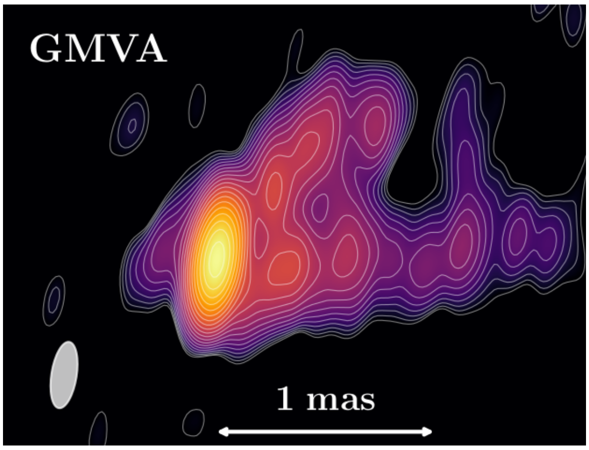

FIGURE 4.18: 86 GHz GMVA observation in February 2014, for M87*. Figure from Kim et al., 2018

.

six models reported in figure 4.17, and the GMVA analysis. However, for larger distances, i.e., for $r \gtrsim 1$ mas, we find that the jet widths are in good agreement with the observations for our model $\epsilon = 0.5$.

In figure 4.19 we report the large-scale morphology, time and azimuthally averaged in $t/M = [13,000 - 15,000]$. In particular, each panel is split into two subpanels, showing the normalized $\rho/\rho_{\max}$ density (left side) and the plasma magnetization σ (right side), for our MAD model of M87*. The two panels represent the same simulations, but with different length-scales. Note, also, that the quantities are reported on a logarithmic scale. The morphology of our simulations can be divided into two distinct regions: the jet and the disk. The jet region can be further divided into a jet spine and a jet sheath region. The former is characterized by a high magnetization $\sigma > \sigma_{\rm cut}$ and low plasma beta ($\beta \ll 1$).

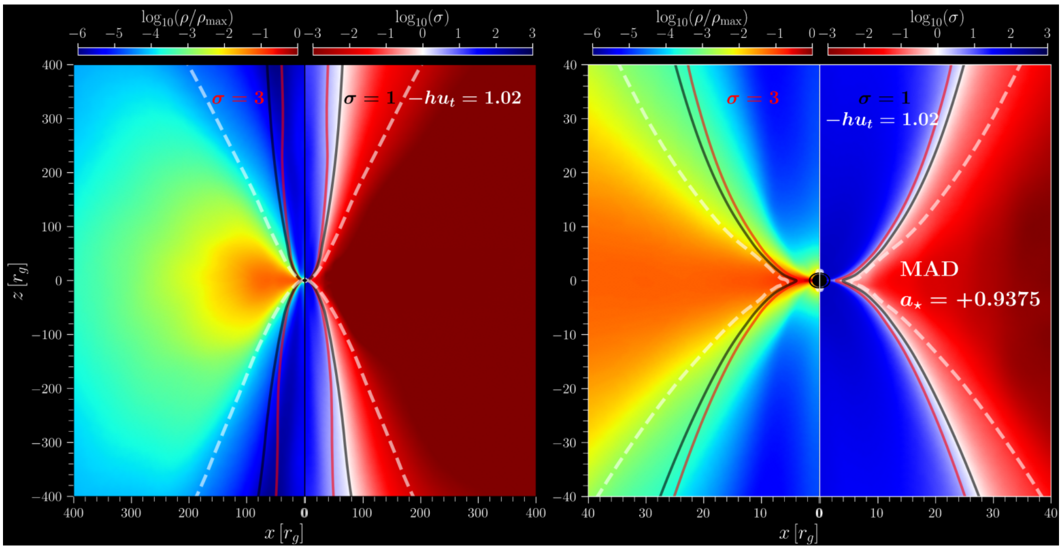

FIGURE 4.19: Normalized $\rho/\rho_{\max}$ density (left side) and plasma magnetization σ (right side), for our MAD model of M87*. The two panels refer to the same simulations and differ only for the length-scales. Note that the quantities are reported in a log-scale.

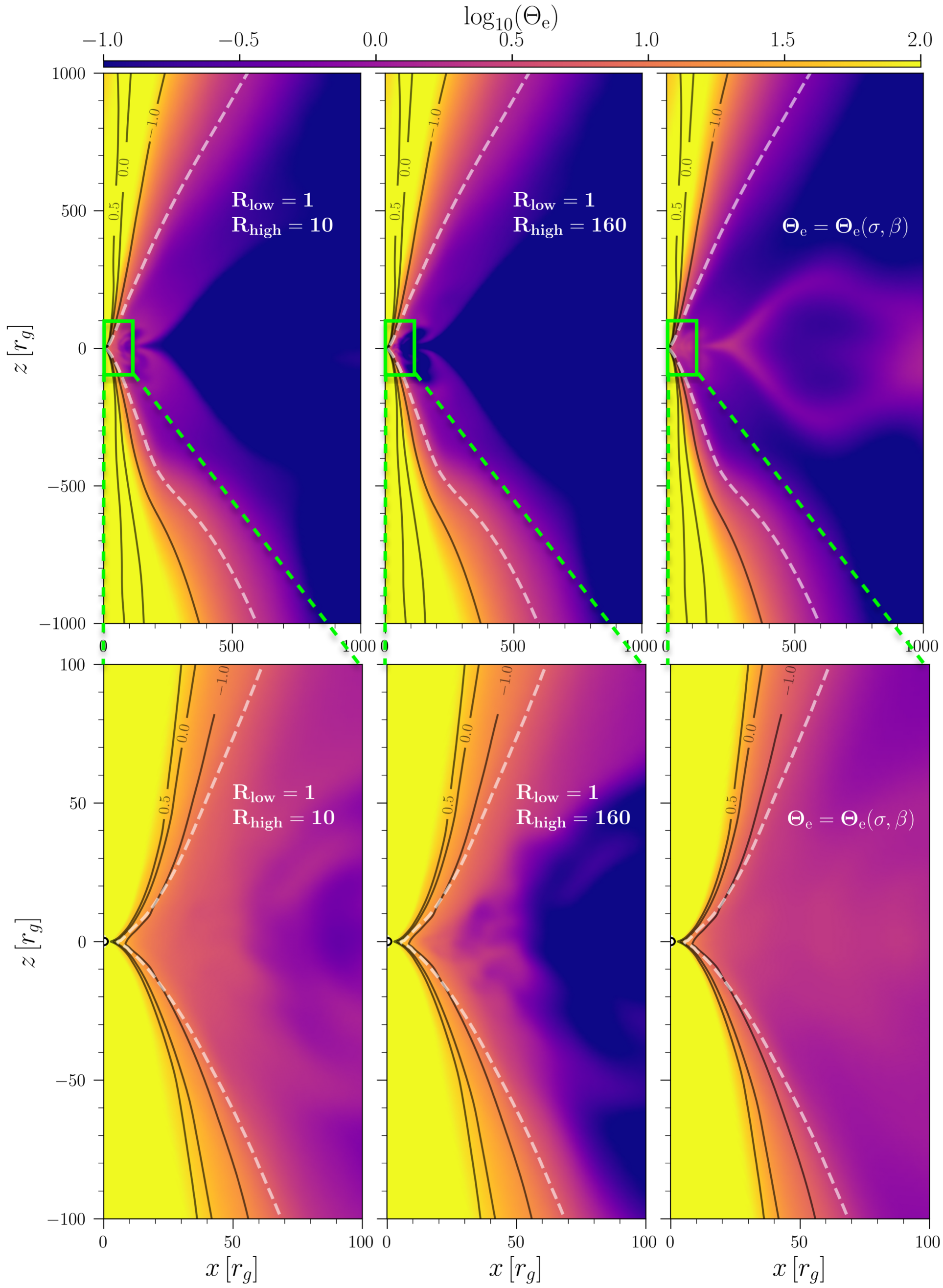

FIGURE 4.20: Logarithm of the electron temperature θ_e for our model of M87, using different R_{high} and R_{low} values (left and center column). In the right column we used our self-consistent model $\theta_e = \theta_e(\sigma, \beta)$. In the bottom row is reported a magnification of the green box, near the black hole.

We report two different σ_{cut} isocontours, namely $\sigma_{\text{cut}} = 3$ (red line) and $\sigma_{\text{cut}} = 1$ black line. The white dashed line marks the boundary between bounded (Be < 1.02) and unbounded (Be > 1.02) material, where in the latter case one has out-flowing of plasma. In the above, $\text{Be} = -hu_0$ is the Bernoulli parameter, h is the specific enthalpy, and u_0 is the time-component of the fluid four-velocity.

Finally, in figure 4.20 we show the distribution of the electron temperature θ_e, for different models. In particular, in the first two columns we used the $R - \beta$ prescription (Mościbrodzka, Falcke, and Shiokawa, 2016), by fixing $R_{\text{low}} = 1$, and we set $R_{\text{high}} = 10$ (left column), and $R_{\text{high}} = 160$ (middle column). In the left column, instead, we employ our self-consistent model $\theta_e = \theta_e(\sigma, \beta)$. Again, we report with a dashed white line the Bernoulli parameter Be $= 1.02$, indicating out-flowing plasma for regions outside it. In the same figure, the black lines show the most important contours of the logarithm of the magnetization, $\log_{10}\sigma = -1.0, 0.0$, and 0.5. Note that, in the bottom row, is shown a magnification of the central region x/r_g and $z/r_g \in [0 - 100]$, highlighted by a green box in the first row.

From the distribution of electron temperatures shown in the figure, it is clear that the highest thermal energies will be located in the jet region, for all of the models. One can appreciate net differences between the $R - \beta$ models and our self-consistent $\theta_e(\sigma, \beta)$ model. First, at large scales (top row), the jet is confined in a narrower region, resulting in a more collimate flux for our model. Second, at lower latitudes, a more structured shape can be appreciated, revealing higher temperatures in the plasma composing the surface of the accretion disk. This is in accord with VLBI observations, where the plasma surrounding the black hole is emitting. Third, in the regions closer to the black hole (bottom row) it is evident higher temperatures in the equatorial plane.

The above are only preliminary results, and of course, a more detailed study is needed to obtain a consistent description of the physics near supermassive compact objects. However, these first analyses are very encouraging and stimulating. These results will be published (with other additional analyses) in a future manuscript.

Conclusions

The last years have seen a number of breakthroughs in general relativity. We witnessed both the first direct observation of GWs (Abbott et al., 2016b) and the first images of supermassive BHs (Event Horizon Telescope Collaboration et al., 2019b; Event Horizon Telescope Collaboration et al., 2022b). Numerical models play, now more than ever, a fundamental role to accompany and understand these extraordinary observations.

In this thesis, we have presented a journey that starts from Einstein's laws of general relativity and finishes with the small-size dynamics of particles near black holes. With equations in hand, we presented the `SFINGE` code, a novel algorithm based on a filtered pseudo-spectral scheme. We based our algorithm on pioneering works on spectral methods, applying them to numerical relativity. We have studied the evolution of gravitational fields by solving numerically the Einstein field equations, in vacuum, with two different approaches, namely the ADM and the BSSNOK formalism. In our pseudo-spectral technique, we compute spatial derivatives via simple and efficient Fast Fourier Transforms.

We presented a new technique that improves the stability of the simulations, which monitors the strength of the time derivatives, providing an optimal timestep. The code shows a very low violation of the constraints, due to the precision of standard spectral methods, which are high-order accurate. We have found that the filter type and the cutoff wavenumber are crucial for the evolution of the gravitational equations, with very stable and accurate solutions. We show that `SFINGE` can handle even more difficult gravitational problems, by solving BH equilibria and the dynamics of binary systems. In this regard, we did overcome the typical limitations of periodicity, which is needed for such pseudo-spectral, FTT-based methods. Our strategy, borrowed from fluid and plasma dynamics, is able to suppress spurious boundary effects. We matched the ideal solution in the center of the domain, based on the pseudo-spectral solution of the BSSNOK system of equations, with a semi-implicit, second-order Crank-Nicholson technique at the boundaries, where we added hyper-viscous diffusion. This strategy has been successfully tested via a simple gravitational wavepacket absorption, as well as more challenging singular dynamical spacetimes.

A detailed analysis of the aliasing instabilities has been presented, both for the AMD and BSSNOK variables. We monitored the Fourier spectra of the dynamical variables, showing how the numerical noise due to the aliasing error affects the highest Fourier modes, propagating eventually to the whole spectrum, and proliferating over all the fields. We presented a strategy that mitigates such instabilities. Two types of anti-aliasing filters have been used in order to suppress numerical artifacts that are due to the intrinsic nonlinear nature of the governing equations. Our analysis confirms that spectral codes are very accurate for numerical relativity, suggesting however that great care must be taken about the numerical computation of highly nonlinear terms, where the aliasing effect is more pronounced.

As a more realistic and challenging test, we built a gravitational model to study the dynamics of multiple BHs collisions. In view of those tests, we abandoned the ADM formalism and finally optimized our `SFINGE` code on the BSSNOK model. We considered the problem of the binary, and the three black hole collisions, in a number of different initial configurations By using a spherical interpolation, and following the Newman-Penrose formalism, we measured the outgoing gravitational waves, as classically done for compact objects simulations. We compared the binary merger and the strong three-body interaction, by computing the power spectra of the signals for all the cases. We found net differences, essentially at high frequencies, where the 3-BHs system exhibits a broader distribution of power. The spectrum seems consistent with a power-law distribution which might suggest that gravitation, similarly to hydrodynamics, is subject to a turbulent cascade.

To get more insight into the outcome of the multi-BH radiation, we performed a refined analysis of the signals. In particular, to detect the main differences among the cases, we made use of a Shannon wavelet. This analysis reveals net differences between the 2- and the 3-BHs cases. While in the former the projection evidences a single dominating frequency, in the 3-BHs the wavelets suggest that there are multiple frequencies produced during the evolution. Finally, in the case in which there is a global angular momentum that confines the BHs, there is a net broadening of the wavelet power, typical of nonlinear phenomena. While the 2-BHs inspiral has been largely investigated in literature (Campanelli et al., 2006; Brügmann et al., 2008; Tichy, 2009; Sperhake, 2015), there is much less documentation about 3-BHs, and, at the present, there is no observational evidence. These results could be of interest for future observational campaigns, since we expect that, with modern technologies, one can achieve better signal-to-noise sensibility, investigating whether such spectacular events might sometimes occur in the Universe. Once we have discussed spacetimes dynamics in vacuum conditions, we moved towards simulations in which the matter is taken into account. In particular, by using our `SFINGE` algorithm, we simulated the propagation of a 1D sound wave in a nonlinear regime, employing an implicit Crank-Nicolson method to suppress numerical artifacts.

In the second part, we moved to more realistic and spectacular scenarios, evolving a toroidal structure immersed in the equatorial plane of a rotating Kerr black hole. To this scope, we made use of the `BHAC` code, employing a 2D (r, θ) geometry. As the simulation proceeds, local Kelvin-Helmholz features can be observed and large-scale vortexes are then produced, dominating the turbulent dynamics of the plasma in the vicinity of the black hole. Such fluid approaches only describe the global dynamics of the plasma, leaving completely undetermined micro-properties of the plasma. To gain a deeper understanding of the microphysical properties of accreting black holes, we have employed the PIC `Zeltron` code to carry out a large campaign of 2D simulations of special-relativistic, decaying plasma turbulence. Particularly important in our analysis is the use of a physical mass ratio between electrons and protons and the exploration of a wide range of values in the plasma-β parameter ($\beta = 10^{-4} - 1.5$) and in the magnetization σ ($\sigma = 0.1 - 3.0$).

Having simulated such a large portion of the space of parameters encountered in astrophysical plasmas has allowed us to derive analytical fitting functions for the behavior of a number of important plasma quantities as a function of β and σ. More specifically, we have presented 2D fitting functions of the electron spectral index $\kappa(\beta, \sigma)$, of the efficiency in generating nonthermal particles $\mathcal{E}(\beta, \sigma)$, and of the ratio between the electron and proton temperatures $\mathcal{T}(\beta, \sigma)$. These expressions provide compact and reasonably accurate descriptions of the behavior of these microphysical plasma properties and can be employed in a number of scenarios involving compact objects and described by macrophysical plasma characteristics. Importantly, since they have been derived from first-principle calculations, they represent a considerable improvement over the rather crude and purely empirical $R - \beta$ prescription, employed at the moment in GRMHD simulations. Finally, we have confirmed the suggestion that plasmas with low β and large σ naturally lead to broad turbulent scenarios and are the most efficient in extracting particles from the thermal population and accelerating them (Pecora et al., 2018; Comisso and Sironi, 2018).

As these simulations represent one of the most systematic PIC explorations of trans-relativistic turbulence can be employed in a wide range of astrophysical systems, such as jets and accretion disks around supermassive black holes, and, of course, their imaging (see, e.g. Event Horizon Telescope Collaboration et al., 2019b; Event Horizon Telescope Collaboration et al., 2022b). In light of this, in the last Section 4.5 we presented our new, preliminary results by performing direct GRMHD simulations of the structure and morphology of M87 jet, using the `BHAC` and the `BHOSS` numerical codes. The novelty of the approach is that we employed our self-consistent prescriptions, directly from our PIC campaign of simulations. The results of such preliminary analysis will be improved, extended, and will be material for future publications.

List of Publications

Here I report a list of papers developed (some of them still in preparation) during my Ph.D. period at the University of Calabria. I spent also six months in the Institute of Theoretical Physics at the Goethe University of Frankfurt, as a visiting under the supervision of Prof. Luciano Rezzolla.

Published:

- *Microphysical plasma relations from kinetic modelling of special-relativistic turbulence* (2023)
  C. Meringolo, A. Cruz-Osorio, L. Rezzolla, S. Servidio ApJ 944 (122) 10.3847/1538-4357/acaefe
- *Extreme gravitational interactions in the problem of three black holes in general relativity* (2023)
  M. Imbrogno, **C. Meringolo**, S. Servidio, Classical and Quantum Gravity 40 (7) 10.1088/1361-6382/acb881
- *A spectral method algorithm for numerical simulations of gravitational fields* (2021)
  C. Meringolo, S. Servidio, P. Veltri, Classical and Quantum Gravity 38 (7) 10.1088/1361-6382/abdd0b
- *Aliasing instabilities in the numerical evolution of the Einstein field equations* (2022)
  C. Meringolo, S. Servidio, General Relativity and Gravitation 53 (10), 1-21 10.1007/s10714-021-02865-5
- *A pseudo-spectral numerical approach to solve the Einstein field equations* (2022)
  C Meringolo, S Servidio, Il Nuovo Cimento C 148 10.1393/ncc/i2022-22148-x
- *Wireless at its origin* (2022)
  P. Riccardi, G. Prete, F. Chiappetta, **C. Meringolo**, Physics Education 10.1088/1361-6552/aca313
- *The impact of the "Third Mission" of Universities and Research Institutions on Physics Education in Secondary Schools* (2022)
  P. Riccardi, G. Prete, F. Chiappetta, **C. Meringolo**, Proceedings of International Conference on Social and Education Sciences, 181-187 978-1-952092-39-8
- *History of Physics and Trust in Science* (2022)
  P. Riccardi, G. Prete, F. Chiappetta, **C. Meringolo**, Proceedings of International Conference on Social and Education Sciences, 282-288 978-1-952092-39-8

In Press:

- *Microphysical aspects of binary neutron star mergers* (2022)
  M. Chabanov, A Cruz-Osorio, C. Ecker, **C. Meringolo**, C. Musolino, L. Rezzolla, S. Tootle, K. Topolski (Accepted to be published in High Performance Computing in Science and Engineering, Springer, Cham)

In Preparation:

- *Multi-wavelength emission from M87 jet with self-consistent electron temperature.*
  A. Cruz-Osorio, **C. Meringolo**, C. Fromm, Y. Mizuno, S. Servidio, L. Rezzolla.
  To be submitted to Astrophysical Journal Letters

- *Analytical modeling of relativistic kinetic equilibria.*
  M. Imbrogno, **C. Meringolo**, A. Cruz-Osorio, L. Rezzolla, F. Pegoraro, S. Servidio
  To be submitted to Physical Review Letters

- *Chaotic advection of fluid particles at different Reynolds numbers: Two-dimensional Smoothed Particle Hydrodynamics.*
  D. D. Meringolo, S. Servidio, V. Carbone, **C. Meringolo**, F. Aristodemo, P. Veltri, P. Filianoti
  To be submitted to Physics of Fluids

- *Supernovae shocks in turbulent plasmas.*
  G. Prete, **C. Meringolo**, L. Primavera, S. Servidio, S. Perri
  To be submitted to Astrophysical Journal Supplement Series

Bibliography

Abbott, B. P. et al. (Sept. 2016a). "Directly comparing GW150914 with numerical solutions of Einstein's equations for binary black hole coalescence". In: 94.6, 064035, p. 064035. DOI: `10.1103/PhysRevD.94.064035`. arXiv: `1606.01262 [gr-qc]`.

Abbott, B. P. et al. (Feb. 2016b). "Observation of Gravitational Waves from a Binary Black Hole Merger". In: *Phys. Rev. Lett.* 116.6, 061102, p. 061102. DOI: `10.1103/PhysRevLett.116.061102`. arXiv: `1602.03837 [gr-qc]`.

Abbott, R et al. (2021). "GWTC-3: compact binary coalescences observed by LIGO and Virgo during the second part of the third observing run". In: *arXiv preprint arXiv:2111.03606*.

Adamek, Julian et al. (2020). "Numerical solutions to Einstein's equations in a shearing-dust universe: a code comparison". In: *Classical and quantum gravity* 37.15, p. 154001.

Albu, Felix and Hon Keung Kwan (2004). "Combined echo and noise cancellation based on Gauss-Seidel pseudo affine projection algorithm". In: *2004 IEEE International Symposium on Circuits and Systems (IEEE Cat. No. 04CH37512)*. Vol. 3. IEEE, pp. III–505.

Alcubierre, Miguel (2003). "Hyperbolic slicings of spacetime: singularity avoidance and gauge shocks". In: *Class. Quantum Grav.* 20.4, pp. 607–624. eprint: `gr-qc/0210050`.

— (Apr. 2006). "Introduction to 3+1 Numerical Relativity". In: *Introduction to 3+1 Numerical Relativity*. DOI: `10.1093/acprof:oso/9780199205677.001.0001`.

— (2008). *Introduction to* $3+1$ *Numerical Relativity*. Oxford, UK: Oxford University Press. DOI: `10.1093/acprof:oso/9780199205677.001.0001`.

Alcubierre, Miguel et al. (2004). "Towards standard testbeds for numerical relativity". In: *Class. Quantum Grav.* 21.2, pp. 589–613. eprint: `gr-qc/0305023`.

Alic, Daniela et al. (2012). "Conformal and covariant formulation of the Z4 system with constraint-violation damping". In: *Physical Review D* 85.6, p. 064040.

Anantua, Richard, Sean Ressler, and Eliot Quataert (Mar. 2020). "On the comparison of AGN with GRMHD simulations: I. Sgr A*". In: *Mon. Not. R. Astron. Soc.* 493.1, pp. 1404–1418. DOI: `10.1093/mnras/staa318`. arXiv: `2001.11556 [astro-ph.HE]`.

Anderson, W Kyle, James L Thomas, and Bram Van Leer (1986). "Comparison of finite volume flux vector splittings for the Euler equations". In: *AIAA journal* 24.9, pp. 1453–1460.

Anninos, Peter et al. (1995). "Three-dimensional numerical relativity: The evolution of black holes". In: *Physical Review D* 52.4, p. 2059.

Anninos, Peter et al. (1997). "Dynamics of Gravitational Waves in 3D: Formulations, Methods, and Tests". In: *Phys. Rev. D* 56, p. 842.

Arnowitt, R., S. Deser, and C. W. Misner (Sept. 2008). "Republication of: The dynamics of general relativity". In: *General Relativity and Gravitation* 40, pp. 1997–2027. DOI: `10.1007/s10714-008-0661-1`. eprint: `gr-qc/0405109`.

Arzamasskiy, Lev et al. (July 2019). "Hybrid-kinetic Simulations of Ion Heating in Alfvénic Turbulence". In: 879.1, 53, p. 53. DOI: `10.3847/1538-4357/ab20cc`. arXiv: `1901.11028 [astro-ph.HE]`.

Babiuc, Maria C et al. (2008). “Implementation of standard testbeds for numerical relativity”. In: *Classical and Quantum Gravity* 25.12, p. 125012.

Bai, Xue-Ning et al. (2015). “Magnetohydrodynamic-particle-in-cell method for coupling cosmic rays with a thermal plasma: application to non-relativistic shocks”. In: *The Astrophysical Journal* 809.1, p. 55.

Baker, B. D. (2002). “Binary Black Holes in Quasi-Stationary Circular Orbits”. In: eprint: `gr-qc/0205082`.

Baker, John G. et al. (2006). “Binary black hole late inspiral: Simulations for gravitational wave observations”. In: gr-qc/0612117. eprint: `gr-qc/0612117`.

Ball, David, Lorenzo Sironi, and Feryal Özel (July 2018). “Electron and Proton Acceleration in Trans-relativistic Magnetic Reconnection: Dependence on Plasma Beta and Magnetization”. In: *Astrophys. J.* 862.1, 80, p. 80. DOI: `10.3847/1538-4357/aac820`. arXiv: `1803.05556 [astro-ph.HE]`.

Bandyopadhyay, Bidisha (Jan. 2022). “Jet launching of M87”. In: *Nature Astronomy* 6, pp. 14–15. DOI: `10.1038/s41550-021-01535-5`.

Baumgarte, Thomas W. (2000). “Innermost stable circular orbit of binary black holes”. In: *Phys. Rev. D* 62, p. 024018. eprint: `gr-qc/0004050`.

Baumgarte, Thomas W and Stuart L Shapiro (1998). “Numerical integration of Einstein’s field equations”. In: *Physical Review D* 59.2, p. 024007.

— (2010). *Numerical relativity: solving Einstein’s equations on the computer*. Cambridge University Press.

Birdsall, Charles K and A Bruce Langdon (2018). *Plasma physics via computer simulation*. CRC press.

Blackman, Jonathan et al. (May 2017). “A Surrogate model of gravitational waveforms from numerical relativity simulations of precessing binary black hole mergers”. In: 95.10, 104023, p. 104023. DOI: `10.1103/PhysRevD.95.104023`. arXiv: `1701.00550 [gr-qc]`.

Blackman, Ralph Beebe and John Wilder Tukey (1958). “The measurement of power spectra from the point of view of communications engineering—Part I”. In: *Bell System Technical Journal* 37.1, pp. 185–282.

Bohn, A. et al. (Mar. 2015). “What does a binary black hole merger look like?” In: *Classical and Quantum Gravity* 32.6, 065002, p. 065002. DOI: `10.1088/0264-9381/32/6/065002`. arXiv: `1410.7775 [gr-qc]`.

Bona, Carles and Joan Massó (1989). “Einstein’s evolution equations as a system of balance laws”. In: *Physical Review D* 40.4, p. 1022.

Bona, Carles et al. (1995). “New formalism for numerical relativity”. In: *Physical Review Letters* 75.4, p. 600.

Boris, Jay P and Ramy A Shanny (1973). *Proceedings*. Naval Research Laboratory.

Bowen, Jeffrey M. and James W. York (1980). “Time-Asymmetric Initial Data for Black Holes and Black Hole Collisions”. In: *Phys. Rev. D* 21.8, pp. 2047–2056.

Bowers, Kevin J et al. (2008). “Ultrahigh performance three-dimensional electromagnetic relativistic kinetic plasma simulation”. In: *Physics of Plasmas* 15.5, p. 055703.

Boyd, John P (2001a). *Chebyshev and Fourier spectral methods*. Courier Corporation.

Boyd, John P. (2001b). *Chebyshev and Fourier Spectral Methods (Second Edition, Revised)*. New York: Dover Publications. ISBN: 0-486-41183-4.

Boyle, Michael et al. (2007). “Testing the accuracy and stability of spectral methods in numerical relativity”. In: *Physical Review D* 75.2, p. 024006.

Brandt, S. and B. Brügmann (1997). “A Simple Construction of Initial Data for Multiple Black Holes”. In: *Phys. Rev. Lett.* 78.19, pp. 3606–3609. eprint: `gr-qc/9703066`.

Brecht, SH et al. (1981). “A simulation study of east-west IMF effects on the magnetosphere”. In: *Geophysical Research Letters* 8.4, pp. 397–400.

Brill, Dieter S. and Richard W. Lindquist (1963). “Interaction Energy in Geometrostatics”. In: *Phys. Rev.* 131.1, pp. 471–476.

Brown, David J. (May 2009). “Covariant formulations of Baumgarte, Shapiro, Shibata, and Nakamura and the standard gauge”. In: *Phys. Rev. D* 79.10, p. 104029. DOI: `10.1103/PhysRevD.79.104029`.

Brügmann, B. et al. (Jan. 2008). “Calibration of moving puncture simulations”. In: *Phys. Rev. D* 77.2, 024027, p. 024027. DOI: `10.1103/PhysRevD.77.024027`. eprint: `gr-qc/0610128`.

Buneman, Oscar (1993). “TRISTAN: the 3-D, EM particle code”. In: *Computer Space Plasma Physics: Simulation Techniques and Software*.

Buonanno, Alessandra, Gregory B Cook, and Frans Pretorius (2007). “Inspiral, merger, and ring-down of equal-mass black-hole binaries”. In: *Physical Review D* 75.12, p. 124018.

Bussmann, Michael et al. (2013). “Radiative signatures of the relativistic Kelvin-Helmholtz instability”. In: *Proceedings of the International Conference on High Performance Computing, Networking, Storage and Analysis*, pp. 1–12.

Campanelli, M. et al. (Mar. 2006). “Accurate Evolutions of Orbiting Black-Hole Binaries without Excision”. In: *Phys. Rev. Lett.* 96.11, p. 111101. DOI: `10.1103/PhysRevLett.96.111101`.

Campanelli, Manuela et al. (2006). “Accurate evolutions of orbiting black-hole binaries without excision”. In: *Phys. Rev. Lett.* 96, p. 111101. eprint: `gr-qc/0511048`.

Canuto, Claudio, MY Hussaini, and Alfio Quarteroni (1988). “TA Zang Spectral Methods in Fluid Dynamics”. In: *Series in Computational Physics*.

Canuto, Claudio et al. (1988). *Spectral Methods in Fluid Dynamics*. 2nd Printing. New York and Berlin: Springer-Verlag. ISBN: 3-540-52205-0 (Berlin), 0-387-52205-0 (New York).

Cao, Zhoujian, Hwei-Jang Yo, and Jui-Ping Yu (2008). “Reinvestigation of moving punctured black holes with a new code”. In: *Physical Review D* 78.12, p. 124011.

Cattani, Carlo (2008). “Shannon wavelets theory”. In: *Mathematical Problems in Engineering* 2008.

Centrella, J. et al. (Oct. 2010). “Black-hole binaries, gravitational waves, and numerical relativity”. In: *Reviews of Modern Physics* 82, pp. 3069–3119. DOI: `10.1103/RevModPhys.82.3069`. arXiv: `1010.5260 [gr-qc]`.

Cerri, Silvio Sergio, Sergio Servidio, and Francesco Califano (Sept. 2017). “Kinetic Cascade in Solar-wind Turbulence: 3D3V Hybrid-kinetic Simulations with Electron Inertia”. In: 846.2, L18, p. L18. DOI: `10.3847/2041-8213/aa87b0`. arXiv: `1707.08429 [physics.plasm-ph]`.

Cerutti, Benoit et al. (2013). “Simulations of particle acceleration beyond the classical synchrotron burnoff limit in magnetic reconnection: an explanation of the Crab flares”. In: *The Astrophysical Journal* 770.2, p. 147.

Chatterjee, K. et al. (Nov. 2021). “General relativistic MHD simulations of non-thermal flaring in Sagittarius A*”. In: *Mon. Not. R. Astron. Soc.* 507.4, pp. 5281–5302. DOI: `10.1093/mnras/stab2466`. arXiv: `2011.08904 [astro-ph.HE]`.

Choi, Young-Kwang et al. (2018). “Performance of various shock-capturing-type reconstruction schemes in the Boussinesq wave model, FUNWAVE-TVD”. In: *Ocean Modelling* 131, pp. 86–100.

Clough, Katy et al. (2015). “GRChombo: numerical relativity with adaptive mesh refinement”. In: *Classical and Quantum Gravity* 32.24, p. 245011.

Comisso, L. et al. (Feb. 2018). “Magnetohydrodynamic Turbulence in the Plasmoid-mediated Regime”. In: *Astrophys. J.* 854.2, 103, p. 103. DOI: `10.3847/1538-4357/aaac83`. arXiv: `1802.02256 [physics.plasm-ph]`.

Comisso, Luca and Lorenzo Sironi (Dec. 2018). “Particle Acceleration in Relativistic Plasma Turbulence”. In: *Phys. Rev. Lett.* 121.25, 255101, p. 255101. DOI: `10.1103/PhysRevLett.121.255101`. arXiv: `1809.01168 [astro-ph.HE]`.

— (Dec. 2019). “The Interplay of Magnetically Dominated Turbulence and Magnetic Reconnection in Producing Nonthermal Particles”. In: 886.2, 122, p. 122. DOI: `10.3847/1538-4357/ab4c33`. arXiv: `1909.01420 [astro-ph.HE]`.

Cook, Gregory B. (2000a). “Initial Data for Numerical Relativity”. In: *Living Rev. Relativ.* 3, p. 5.

— (2000b). “Initial Data for Numerical Relativity”. In: *Living Rev. Relativ.* 3, p. 5.

Cooley, James W and John W Tukey (1965). “An algorithm for the machine calculation of complex Fourier series”. In: *Mathematics of computation* 19.90, pp. 297–301.

Cordero-Carrión, Isabel, Pablo Cerdá-Durán, and José María Ibáñez (Feb. 2012). “Gravitational waves in dynamical spacetimes with matter content in the fully constrained formulation”. In: 85.4, 044023, p. 044023. DOI: `10.1103/PhysRevD.85.044023`. arXiv: `1108.0571 [gr-qc]`.

Cordero-Carrión, Isabel et al. (Aug. 2014). “Excision scheme for black holes in constrained evolution formulations: Spherically symmetric case”. In: 90.4, 044062, p. 044062. DOI: `10.1103/PhysRevD.90.044062`. arXiv: `1306.5976 [gr-qc]`.

Courant, R., K. Friedrichs, and H. Lewy (1928). “Über die partiellen Differenzengleichungen der mathematischen Physik”. In: *Mathematische Annalen* 100, pp. 32–74. DOI: `10.1007/BF01448839`.

Crinquand, Benjamin (2021). “Particle acceleration in Kerr black-hole magnetospheres”. PhD thesis. Université Grenoble-Alpes.

Crinquand, Benjamin et al. (2022). “Synthetic Images of Magnetospheric Reconnection-Powered Radiation around Supermassive Black Holes”. In: *Physical Review Letters* 129.20, p. 205101.

Cruz-Osorio, Alejandro et al. (Jan. 2022). “State-of-the-art energetic and morphological modelling of the launching site of the M87 jet”. In: *Nature Astronomy* 6, pp. 103–108. DOI: `10.1038/s41550-021-01506-w`. arXiv: `2111.02517 [astro-ph.HE]`.

Daubechies, Ingrid (1992). *Ten lectures on wavelets*. SIAM.

Davelaar, Jordy et al. (Dec. 2019). “Modeling non-thermal emission from the jet-launching region of M 87 with adaptive mesh refinement”. In: *Astron. Astrophys.* 632, A2, A2. DOI: `10.1051/0004-6361/201936150`. arXiv: `1906.10065 [astro-ph.HE]`.

Daverio, David, Yves Dirian, and Ermis Mitsou (Oct. 2018). “Apples with Apples comparison of 3+1 conformal numerical relativity schemes”. In: *arXiv e-prints*, arXiv:1810.12346, arXiv:1810.12346. arXiv: `1810.12346 [gr-qc]`.

De Giorgio, Elisa, Sergio Servidio, and Pierluigi Veltri (2017). “Coherent structure formation through nonlinear interactions in 2d magnetohydrodynamic turbulence”. In: *Scientific Reports* 7.1, pp. 1–9.

Del Zanna, L. et al. (Sept. 2020). “Creation and dissipation of magnetic fields in non-ideal GRMHD simulations”. In: *Journal of Physics Conference Series*. Vol. 1623. Journal of Physics Conference Series, 012004, p. 012004. DOI: `10.1088/1742-6596/1623/1/012004`.

Dihingia, Indu K. et al. (June 2022). “Temperature properties in magnetised and radiatively cooled two-temperature accretion flows onto a black hole”. In: *arXiv e-prints*, arXiv:2206.13184, arXiv:2206.13184. arXiv: `2206.13184 [astro-ph.HE]`.

Dimmelmeier, H. et al. (Mar. 2005). “Combining spectral and shock-capturing methods: A new numerical approach for 3D relativistic core collapse simulations”. In:

Phys. Rev. D 71.6, p. 064023. DOI: 10.1103/PhysRevD.71.064023. eprint: arXiv:astro-ph/0407174.

Dobler, Wolfgang, Michael Stix, and Axel Brandenburg (2006). "Magnetic field generation in fully convective rotating spheres". In: *The Astrophysical Journal* 638.1, p. 336.

Dong, Chuanfei et al. (Oct. 2018). "Role of the Plasmoid Instability in Magnetohydrodynamic Turbulence". In: *Phys. Rev. Lett.* 121.16, 165101, p. 165101. DOI: 10.1103/PhysRevLett.121.165101. arXiv: 1804.07361 [physics.plasm-ph].

Drake, J. F. et al. (July 2009). "A Magnetic Reconnection Mechanism for Ion Acceleration and Abundance Enhancements in Impulsive Flares". In: *Astrophys. J. Lett.* 700.1, pp. L16–L20. DOI: 10.1088/0004-637X/700/1/L16.

Duţan, Ioana et al. (Jan. 2017). "Particle-in-cell Simulations of Global Relativistic Jets with Helical Magnetic Fields". In: *New Frontiers in Black Hole Astrophysics*. Ed. by Andreja Gomboc. Vol. 324, pp. 199–202. DOI: 10.1017/S1743921316012722. arXiv: 1611.02882 [astro-ph.HE].

Duez, Matthew D. et al. (2008). "Evolving black hole-neutron star binaries in general relativity using pseudospectral and finite difference methods". In: *Phys. Rev. D* 78, p. 104015. DOI: 10.1103/PhysRevD.78.104015. arXiv: 0809.0002 [gr-qc].

Dumbser, Michael et al. (2018). "Conformal and covariant Z4 formulation of the Einstein equations: strongly hyperbolic first-order reduction and solution with discontinuous Galerkin schemes". In: *Physical Review D* 97.8, p. 084053.

Dutykh, Denys (2016). "A brief introduction to pseudo-spectral methods: application to diffusion problems". In: *arXiv preprint arXiv:1606.05432*.

El Mellah, I et al. (2022). "Spinning black holes magnetically connected to a Keplerian disk-Magnetosphere, reconnection sheet, particle acceleration, and coronal heating". In: *Astronomy & Astrophysics* 663, A169.

Etienne, Z. B. et al. (Sept. 2015). "IllinoisGRMHD: an open-source, user-friendly GRMHD code for dynamical spacetimes". In: *Class. Quantum Grav.* 32.17, 175009, p. 175009. DOI: 10.1088/0264-9381/32/17/175009. arXiv: 1501.07276 [astro-ph.HE].

Evans, Charles R and John F Hawley (1988). "Simulation of magnetohydrodynamic flows-A constrained transport method". In: *The Astrophysical Journal* 332, pp. 659–677.

Event Horizon Telescope Collaboration et al. (Apr. 2019a). "First M87 Event Horizon Telescope Results. I. The Shadow of the Supermassive Black Hole". In: *Astrophys. J. Lett.* 875, L1, p. L1. DOI: 10.3847/2041-8213/ab0ec7.

— (Apr. 2019b). "First M87 Event Horizon Telescope Results. V. Physical Origin of the Asymmetric Ring". In: *Astrophys. J. Lett.* 875, L5, p. L5. DOI: 10.3847/2041-8213/ab0f43.

Event Horizon Telescope Collaboration et al. (Mar. 2021). "First M87 Event Horizon Telescope Results. VIII. Magnetic Field Structure near The Event Horizon". In: *Astrophys. J. Lett.* 910.1, L13, p. L13. DOI: 10.3847/2041-8213/abe4de. arXiv: 2105.01173 [astro-ph.HE].

Event Horizon Telescope Collaboration et al. (May 2022a). "First Sagittarius A* Event Horizon Telescope Results. I. The Shadow of the Supermassive Black Hole in the Center of the Milky Way". In: *Astrophys. J. Lett.* 930.2, L12, p. L12. DOI: 10.3847/2041-8213/ac6674.

Event Horizon Telescope Collaboration et al. (May 2022b). "First Sagittarius A* Event Horizon Telescope Results. V. Testing Astrophysical Models of the Galactic Center Black Hole". In: *Astrophys. J. Lett.* 930.2, L16, p. L16. DOI: 10.3847/2041-8213/ac6672.

Fife, John Michael (1998). “Hybrid-PIC modeling and electrostatic probe survey of Hall thrusters”. PhD thesis. Massachusetts Institute of Technology.

Fishbone, L. G. and V. Moncrief (Aug. 1976). “Relativistic fluid disks in orbit around Kerr black holes”. In: *Astrophys. J.* 207, pp. 962–976.

Font, J. A. (2008). “Numerical Hydrodynamics and Magnetohydrodynamics in General Relativity”. In: *Living Rev. Relativ.* 6, 4; http://www.livingreviews.org/lrr–2008–7. eprint: `0704.2608.`. URL: `http://www.livingreviews.org/lrr-2008-7`.

Franci, Luca et al. (Dec. 2016). “Plasma Beta Dependence of the Ion-scale Spectral Break of Solar Wind Turbulence: High-resolution 2D Hybrid Simulations”. In: *Astrophys. J.* 833.1, 91, p. 91. DOI: `10.3847/1538-4357/833/1/91`. arXiv: `1610.05158 [physics.space-ph]`.

Frisch, Uriel et al. (2008). “Hyperviscosity, Galerkin truncation, and bottlenecks in turbulence”. In: *Physical review letters* 101.14, p. 144501.

Fromm, C. M. et al. (May 2021). “Using space-VLBI to probe gravity around Sgr A*”. In: *Astron. Astrophys.* 649, A116, A116. DOI: `10.1051/0004-6361/201937335`. arXiv: `2101.08618 [astro-ph.HE]`.

Fromm, Christian M. et al. (Apr. 2022). “Impact of non-thermal particles on the spectral and structural properties of M87”. In: 660, A107, A107. DOI: `10.1051/0004-6361/202142295`. arXiv: `2111.02518 [astro-ph.HE]`.

Gammie, Charles F., Jonathan C. McKinney, and Gábor Tóth (May 2003). “HARM: A Numerical Scheme for General Relativistic Magnetohydrodynamics”. In: *Astrophys. J.* 589.1, pp. 444–457. DOI: `10.1086/374594`. arXiv: `astro-ph/0301509 [astro-ph]`.

Giacomazzo, B. and L. Rezzolla (June 2007). “WhiskyMHD: a new numerical code for general relativistic magnetohydrodynamics”. In: *Class. Quantum Grav.* 24, p. 235. DOI: `10.1088/0264-9381/24/12/S16`. eprint: `gr-qc/0701109`.

Gold, R. et al. (Mar. 2014). “Accretion disks around binary black holes of unequal mass: General relativistic magnetohydrodynamic simulations near decoupling”. In: *Phys. Rev. D* 89.6, 064060, p. 064060. DOI: `10.1103/PhysRevD.89.064060`. arXiv: `1312.0600 [astro-ph.HE]`.

Gottlieb, David and Steven A. Orszag (1977a). *Numerical Analysis of Spectral Methods*. Vol. 26. CMBS-NSF Regional Conference Series in Applied Mathematics. Philadelphia: Society for Industrial and Applied Mathematics. ISBN: 0-89871-023-5 (paperback).

Gottlieb, David and Steven A Orszag (1977b). *Numerical analysis of spectral methods: theory and applications*. SIAM.

Gourgoulhon, Eric (2012). *3+1 Formalism in General Relativity*. Vol. 846. Lecture Notes in Physics, Berlin Springer Verlag. Springer. DOI: `10.1007/978-3-642-24525-1`.

Grandclément, Philippe and Jérôme Novak (2009). “Spectral methods for numerical relativity”. In: *Living Reviews in Relativity* 12.1, pp. 1–103.

Gundlach, Carsten and Jose M. Martin-Garcia (2006). “Well-posedness of formulations of the Einstein equations with dynamical lapse and shift conditions”. In: *Phys. Rev. D* 74, p. 024016. eprint: `gr-qc/0604035`.

Hairer, Ernst et al. (2006). “Geometric numerical integration”. In: *Oberwolfach Reports* 3.1, pp. 805–882.

Hannam, Mark et al. (2007). “Where do moving punctures go?” In: *Journal of Physics: Conference series*. Vol. 66. 1. IOP Publishing, p. 012047.

Haugbølle, Troels, Jacob Trier Frederiksen, and Åke Nordlund (2013). “photon-plasma: A modern high-order particle-in-cell code”. In: *Physics of Plasmas* 20.6, p. 062904.

Haynes, C. T., D. Burgess, and E. Camporeale (Mar. 2014). "Reconnection and Electron Temperature Anisotropy in Sub-proton Scale Plasma Turbulence". In: *Astrophys. J.* 783.1, 38, p. 38. DOI: `10.1088/0004-637X/783/1/38`. arXiv: `1304.1444 [physics.space-ph]`.

Hellinger, Petr et al. (Oct. 2015). "Plasma Turbulence and Kinetic Instabilities at Ion Scales in the Expanding Solar Wind". In: *Astrophys. J. Lett.* 811.2, L32, p. L32. DOI: `10.1088/2041-8205/811/2/L32`. arXiv: `1508.03159 [physics.space-ph]`.

Hossain, Murshed, William H Matthaeus, and Sanjoy Ghosh (1992). "On computing high order Galerkin products". In: *Computer physics communications* 69.1, pp. 1–6.

Hou, Thomas Y and Ruo Li (2007). "Computing nearly singular solutions using pseudo-spectral methods". In: *Journal of Computational Physics* 226.1, pp. 379–397.

Howes, G. G. (Nov. 2010). "A prescription for the turbulent heating of astrophysical plasmas". In: *Mon. Not. R. Astron. Soc.* 409.1, pp. L104–L108. DOI: `10.1111/j.1745-3933.2010.00958.x`. arXiv: `1009.4212 [astro-ph.HE]`.

Huang, Yi-Min and A. Bhattacharjee (Feb. 2016). "Turbulent Magnetohydrodynamic Reconnection Mediated by the Plasmoid Instability". In: *Astrophys. J.* 818.1, 20, p. 20. DOI: `10.3847/0004-637X/818/1/20`. arXiv: `1512.01520 [physics.plasm-ph]`.

Huerta, E. A. et al. (Jan. 2017). "Complete waveform model for compact binaries on eccentric orbits". In: 95.2, 024038, p. 024038. DOI: `10.1103/PhysRevD.95.024038`. arXiv: `1609.05933 [gr-qc]`.

Imbrogno, Mario, Claudio Meringolo, and Sergio Servidio (2022). "Strong Interactions in the Three Black Holes Problem". In: *arXiv preprint arXiv:2108.01392*.

Jansen, Nina, Bernd Bruegmann, and Wolfgang Tichy (2006). "Numerical stability of the Alekseenko-Arnold evolution system compared to the ADM and BSSN systems". In: *Physical Review D* 74.8, p. 084022.

Janssen, Michael et al. (July 2021). "Event Horizon Telescope observations of the jet launching and collimation in Centaurus A". In: *Nature Astronomy* 5, pp. 1017–1028. DOI: `10.1038/s41550-021-01417-w`. arXiv: `2111.03356 [astro-ph.GA]`.

Karimabadi, H. et al. (2013). "Coherent structures, intermittent turbulence, and dissipation in high-temperature plasmas". In: *Physics of Plasmas* 20.1, p. 012303. DOI: `10.1063/1.4773205`. eprint: `https://doi.org/10.1063/1.4773205`. URL: `https://doi.org/10.1063/1.4773205`.

Kawazura, Y. et al. (Apr. 2020). "Ion versus electron heating in compressively driven astrophysical gyrokinetic turbulence". In: *arXiv e-prints*, arXiv:2004.04922, arXiv:2004.04922. arXiv: `2004.04922 [physics.plasm-ph]`.

Kawazura, Yohei, Michael Barnes, and Alexander A. Schekochihin (Jan. 2019). "Thermal disequilibration of ions and electrons by collisionless plasma turbulence". In: *Proceedings of the National Academy of Science* 116.3, pp. 771–776. DOI: `10.1073/pnas.1812491116`. arXiv: `1807.07702 [physics.plasm-ph]`.

Kerr, R. P. (1963). "Gravitational field of a spinning mass as an example of algebraically special metrics". In: *Phys. Rev. Lett.* 11, pp. 237–238.

Kim, Jae-Young et al. (2018). "Long-term millimeter VLBI monitoring of M 87 with KVN at milliarcsecond resolution: nuclear spectrum". In: *Astronomy & Astrophysics* 610, p. L5.

Landau, Lev Davidovich (2013). *The classical theory of fields*. Vol. 2. Elsevier.

Lehe, Rémi et al. (2016). "A spectral, quasi-cylindrical and dispersion-free Particle-In-Cell algorithm". In: *Computer Physics Communications* 203, pp. 66–82.

Lele, Sanjiva K. (1992). "Compact Finite Difference Schemes with Spectral-like Resolution". In: *J. Comput. Phys.* 103, pp. 16–42.

Londrillo, P. and L. Del Zanna (Feb. 2000). “High-Order Upwind Schemes for Multidimensional Magnetohydrodynamics”. In: *Astrophys. J.* 530, pp. 508–524. DOI: `10.1086/308344`. eprint: `arXiv:astro-ph/9910086`.

Lora-Clavijo, F. D., A. Cruz-Osorio, and F. S. Guzmán (June 2015). “CAFE: A New Relativistic MHD Code”. In: *Astrophys. J., Supp.* 218, 24, p. 24. DOI: `10.1088/0067-0049/218/2/24`. arXiv: `1408.5846 [gr-qc]`.

Lousto, Carlos O and Yosef Zlochower (2008). “Foundations of multiple-black-hole evolutions”. In: *Physical Review D* 77.2, p. 024034.

Markidis, Stefano, Giovanni Lapenta, et al. (2010). “Multi-scale simulations of plasma with iPIC3D”. In: *Mathematics and Computers in Simulation* 80.7, pp. 1509–1519.

Matzner, Richard A., Mijan F. Huq, and Deirdre Shoemaker (1999). “Initial Data and Coordinates for Multiple Black Hole Systems”. In: *Phys. Rev. D* 59, p. 024015.

McCrory, Robert L and Steven A Orszag (1980). “Spectral methods for multi-dimensional diffusion problems”. In: *Journal of Computational Physics* 37.1, pp. 93–112.

Meringolo, C and S Servidio (2022). “A pseudo-spectral numerical approach to solve the Einstein field equations”. In: *Il nuovo cimento C* 45.5, pp. 1–4.

Meringolo, C., S. Servidio, and P. Veltri (Apr. 2021). “A spectral method algorithm for numerical simulations of gravitational fields”. In: *Classical and Quantum Gravity* 38.7, 075027, p. 075027. DOI: `10.1088/1361-6382/abdd0b`. arXiv: `2011.10354 [gr-qc]`.

Meringolo, Claudio and Sergio Servidio (2021). “Aliasing instabilities in the numerical evolution of the Einstein field equations”. In: *General Relativity and Gravitation* 53.10, pp. 1–21.

Misner, C. and J. Wheeler (1957). “Classical Physics as Geometry”. In: *Ann. Phys. (N.Y.)* 2, pp. 525–603.

Misner, Charles W., Kip S. Thorne, and John A. Wheeler (1973). *Gravitation*. San Francisco: W. H. Freeman.

Mizuno, Yosuke et al. (Sept. 2021). “Comparison of the ion-to-electron temperature ratio prescription: GRMHD simulations with electron thermodynamics”. In: 506.1, pp. 741–758. DOI: `10.1093/mnras/stab1753`. arXiv: `2106.09272 [astro-ph.HE]`.

Montero, P. J., J. A. Font, and M. Shibata (May 2010). “Influence of Self-Gravity on the Runaway Instability of Black-Hole-Torus Systems”. In: *Phys. Rev. Lett.* 104.19, 191101, p. 191101. DOI: `10.1103/PhysRevLett.104.191101`. arXiv: `1004.3102 [gr-qc]`.

Montero, Pedro J and Isabel Cordero-Carrión (2012). “BSSN equations in spherical coordinates without regularization: Vacuum and nonvacuum spherically symmetric spacetimes”. In: *Physical Review D* 85.12, p. 124037.

Mościbrodzka, M., H. Falcke, and H. Shiokawa (Feb. 2016). “General relativistic magnetohydrodynamical simulations of the jet in M 87”. In: *Astron. Astrophys.* 586, A38, A38. DOI: `10.1051/0004-6361/201526630`. arXiv: `1510.07243 [astro-ph.HE]`.

Mościbrodzka, M. et al. (Oct. 2014). “Observational appearance of inefficient accretion flows and jets in 3D GRMHD simulations: Application to Sagittarius A*”. In: *Astron. Astrophys.* 570, A7, A7. DOI: `10.1051/0004-6361/201424358`. arXiv: `1408.4743 [astro-ph.HE]`.

Mösta, Philipp et al. (Jan. 2014). “GRHydro: a new open-source general-relativistic magnetohydrodynamics code for the Einstein toolkit”. In: *Classical and Quantum Gravity* 31.1, 015005, p. 015005. DOI: `10.1088/0264-9381/31/1/015005`. arXiv: `1304.5544 [gr-qc]`.

Nakamura, T., K. Oohara, and Y. Kojima (1987). “General Relativistic Collapse to Black Holes and Gravitational Waves from Black Holes”. In: *Progress of Theoretical Physics Supplement* 90, pp. 1–218. DOI: `10.1143/PTPS.90.1`.

Narayan, R. et al. (Nov. 2012). “GRMHD simulations of magnetized advection-dominated accretion on a non-spinning black hole: role of outflows”. In: *Mon. Not. R. Astron. Soc.* 426, pp. 3241–3259. DOI: `10.1111/j.1365-2966.2012.22002.x`. arXiv: `1206.1213 [astro-ph.HE]`.

Nathanail, Antonios et al. (June 2020). “Plasmoid formation in global GRMHD simulations and AGN flares”. In: 495.2, pp. 1549–1565. DOI: `10.1093/mnras/staa1165`. arXiv: `2002.01777 [astro-ph.HE]`.

New, Kimberly C. B. et al. (1998). “Stable 3-level leapfrog integration in numerical relativity”. In: *Phys. Rev. D* 58. gr-qc/9801110, p. 064022.

Newman, E. T. et al. (June 1965). “Metric of a Rotating, Charged Mass”. In: *Journal of Mathematical Physics* 6.6, pp. 918–919. DOI: `10.1063/1.1704351`.

Newman, Ezra T. and Roger Penrose (1962). “An Approach to Gravitational Radiation by a Method of Spin Coefficients”. In: *J. Math. Phys.* 3.3. erratum in J. Math. Phys. 4, 998 (1963), pp. 566–578. DOI: `10.1063/1.1724257`.

Orszag, Steven A (1971). “On the elimination of aliasing in finite-difference schemes by filtering high-wavenumber components”. In: *Journal of Atmospheric Sciences* 28.6, pp. 1074–1074.

Parashar, Tulasi N., William H. Matthaeus, and Michael A. Shay (Sept. 2018). “Dependence of Kinetic Plasma Turbulence on Plasma β”. In: *Astrophys. J. Lett.* 864.1, L21, p. L21. DOI: `10.3847/2041-8213/aadb8b`. arXiv: `1807.11371 [physics.space-ph]`.

Parfrey, Kyle, Alexander Philippov, and Benoît Cerutti (Jan. 2019). “First-Principles Plasma Simulations of Black-Hole Jet Launching”. In: *Phys. Rev. Lett.* 122.3, 035101, p. 035101. DOI: `10.1103/PhysRevLett.122.035101`. arXiv: `1810.03613 [astro-ph.HE]`.

Pecora, F. et al. (Dec. 2018). “Ion diffusion and acceleration in plasma turbulence”. In: *Journal of Plasma Physics* 84.6, 725840601, p. 725840601. DOI: `10.1017/S0022377818000995`. arXiv: `1803.09647 [physics.plasm-ph]`.

Pecora, Francesco et al. (Sept. 2019). “Statistical Analysis of Ions in Two-Dimensional Plasma Turbulence”. In: 294.9, 114, p. 114. DOI: `10.1007/s11207-019-1507-6`. arXiv: `1908.02791 [physics.space-ph]`.

Pezzi, O. et al. (Apr. 2021). “Current Sheets, Plasmoids and Flux Ropes in the Heliosphere. Part II: Theoretical Aspects”. In: *Space Sci. Rev.* 217.3, 39, p. 39. DOI: `10.1007/s11214-021-00799-7`. arXiv: `2101.05007 [astro-ph.SR]`.

Porth, O. et al. (May 2017). “The black hole accretion code”. In: *Computational Astrophysics and Cosmology* 4, 1, p. 1. DOI: `10.1186/s40668-017-0020-2`. arXiv: `1611.09720 [gr-qc]`.

Porth, Oliver et al. (2017). “The black hole accretion code”. In: *Computational Astrophysics and Cosmology* 4.1, pp. 1–42.

Porth, Oliver et al. (Aug. 2019). “The Event Horizon General Relativistic Magnetohydrodynamic Code Comparison Project”. In: *Astrophys. J. Supp.* 243.2, 26, p. 26. DOI: `10.3847/1538-4365/ab29fd`. arXiv: `1904.04923 [astro-ph.HE]`.

Press, William H. et al. (2007). *Numerical Recipes 3rd Edition: The Art of Scientific Computing*. Third Edition. Cambridge University Press.

Pretorius, Frans (2006). “Simulation of binary black hole spacetimes with a harmonic evolution scheme”. In: *Class. Quantum Grav.* 23, S529–S552. eprint: `gr-qc/0602115`.

Radice, D. and L. Rezzolla (June 2012). “THC: a new high-order finite-difference high-resolution shock-capturing code for special-relativistic hydrodynamics”. In: *Astron. Astrophys.* 547, A26. DOI: `10.1051/0004-6361/201219735`. arXiv: `1206.6502 [astro-ph.IM]`.

Radice, D. and L. Rezzolla (Mar. 2013). "Universality and Intermittency in Relativistic Turbulent Flows of a Hot Plasma". In: *Astrophys. J.* 766, L10, p. L10. DOI: `10.1088/2041-8205/766/1/L10`. arXiv: `1209.2936 [astro-ph.HE]`.

Reissner, H. (1916). "Über die Eigengravitationn des elektrischen Felds nach der Einsteinshen Theorie". In: *Annalen der Physik* 50, pp. 106–120.

Reisswig, C. et al. (Mar. 2011). "Gravitational wave extraction in simulations of rotating stellar core collapse". In: *Phys. Rev. D* 83.6, 064008, p. 064008. DOI: `10.1103/PhysRevD.83.064008`. arXiv: `1012.0595 [gr-qc]`.

Rezzolla, L. and O. Zanotti (2013). *Relativistic Hydrodynamics*. Oxford, UK: Oxford University Press. ISBN: 9780198528906. DOI: `10.1093/acprof:oso/9780198528906.001.0001`.

Ripperda, B. et al. (Sept. 2019). "General-relativistic Resistive Magnetohydrodynamics with Robust Primitive-variable Recovery for Accretion Disk Simulations". In: *Astrophys. J., Supp.* 244.1, 10, p. 10. DOI: `10.3847/1538-4365/ab3922`. arXiv: `1907.07197 [physics.comp-ph]`.

Ripperda, B. et al. (Jan. 2022). "Black Hole Flares: Ejection of Accreted Magnetic Flux through 3D Plasmoid-mediated Reconnection". In: *Astrophys. J. Lett.* 924.2, L32, p. L32. DOI: `10.3847/2041-8213/ac46a1`. arXiv: `2109.15115 [astro-ph.HE]`.

Rowan, Michael E., Lorenzo Sironi, and Ramesh Narayan (Nov. 2017). "Electron and Proton Heating in Transrelativistic Magnetic Reconnection". In: *Astrophys. J.* 850.1, 29, p. 29. DOI: `10.3847/1538-4357/aa9380`. arXiv: `1708.04627 [astro-ph.HE]`.

Ruchlin, Ian et al. (2017). "Puncture initial data for black-hole binaries with high spins and high boosts". In: *Physical Review D* 95.2, p. 024033.

Sahraoui, F. et al. (June 2009). "Evidence of a Cascade and Dissipation of Solar-Wind Turbulence at the Electron Gyroscale". In: 102.23, 231102, p. 231102. DOI: `10.1103/PhysRevLett.102.231102`.

Scheel, Mark A. et al. (2006). "Solving Einstein's Equations With Dual Coordinate Frames". In: *Phys. Rev. D* 74, p. 104006. eprint: `gr-qc/0607056`.

Schneider, Kai and Marie Farge (2005). "Decaying two-dimensional turbulence in a circular container". In: *Physical review letters* 95.24, p. 244502.

Servidio, S. et al. (Mar. 2009). "Magnetic Reconnection in Two-Dimensional Magnetohydrodynamic Turbulence". In: *Phys. Rev. Lett.* 102.11, 115003, p. 115003. DOI: `10.1103/PhysRevLett.102.115003`.

Servidio, S. et al. (Jan. 2012). "Local Kinetic Effects in Two-Dimensional Plasma Turbulence". In: *Phys. Rev. Lett.* 108.4, 045001, p. 045001. DOI: `10.1103/PhysRevLett.108.045001`.

Servidio, Sergio et al. (2007). "Compressible turbulence in Hall magnetohydrodynamics". In: *Planetary and Space Science* 55.15, pp. 2239–2243.

Sgattoni, Andrea et al. (2015). "Optimising piccante-an open source particle-in-cell code for advanced simulations on tier-0 systems". In: *arXiv preprint arXiv:1503.02464*.

Shallcross, Gregory S, Rodney O Fox, and Jesse Capecelatro (2020). "A volume-filtered description of compressible particle-laden flows". In: *International Journal of Multiphase Flow* 122, p. 103138.

Shibata, M. (2016). *Numerical Relativity*. Singapore: World Scientific. ISBN: 978-981-4699-71-6. DOI: `10.1142/9692`.

Shibata, M. and T. Nakamura (Nov. 1995). "Evolution of three-dimensional gravitational waves: Harmonic slicing case". In: *Phys. Rev. D* 52, pp. 5428–5444. DOI: `10.1103/PhysRevD.52.5428`.

Shu, Chi-Wang et al. (2005). "Numerical convergence study of nearly incompressible, inviscid Taylor–Green vortex flow". In: *Journal of Scientific Computing* 24.1, pp. 1–27.

Sironi, Lorenzo and Benoît Cerutti (2017). "Particle acceleration in pulsar wind nebulae: PIC modelling". In: *Modelling Pulsar Wind Nebulae*. Springer, pp. 247–277.

Smarr, Larry and James W. York (May 1978). "Kinematical conditions in the construction of spacetime". In: *Phys. Rev. D* 17.10, pp. 2529–2552.

Smith, G. D. (1985). *Numerical Solution of Partial Differential Equations*. third. ISBN 0198596502. Oxford University Press.

Sperhake, Ulrich (2015). "The numerical relativity breakthrough for binary black holes". In: *Classical and Quantum Gravity* 32.12, p. 124011.

Springel, Volker (2016). "High performance computing and numerical modelling". In: *Star Formation in Galaxy Evolution: Connecting Numerical Models to Reality*. Springer, pp. 251–358.

Stone, J. M. et al. (Sept. 2008). "Athena: A New Code for Astrophysical MHD". In: *Astrophys. J.s* 178, pp. 137–177. DOI: 10.1086/588755. arXiv: 0804.0402.

Szilágyi, Béla (2014). "Key elements of robustness in binary black hole evolutions using spectral methods". In: *International Journal of Modern Physics D* 23.07, p. 1430014.

Teukolsky, Saul A (2015). "The kerr metric". In: *Classical and Quantum Gravity* 32.12, p. 124006.

The LIGO Scientific Collaboration et al. (Oct. 2017). "GW170814: A Three-Detector Observation of Gravitational Waves from a Binary Black Hole Coalescence". In: *Phys. Rev. Lett.* 119 (14), p. 141101. DOI: 10.1103/PhysRevLett.119.141101. URL: https://link.aps.org/doi/10.1103/PhysRevLett.119.141101.

Tichy, Wolfgang (Nov. 2009). "Long term black hole evolution with the BSSN system by pseudospectral methods". In: *Phys. Rev. D* 80 (10), p. 104034. DOI: 10.1103/PhysRevD.80.104034. URL: https://link.aps.org/doi/10.1103/PhysRevD.80.104034.

Tu, C. Y. and E. Marsch (Apr. 1997). "Two-Fluid Model for Heating of the Solar Corona and Acceleration of the Solar Wind by High-Frequency Alfven Waves". In: *Solar Physics* 171.2, pp. 363–391. DOI: 10.1023/A:1004968327196.

Unser, Michael (2000). "Sampling-50 years after Shannon". In: *Proceedings of the IEEE* 88.4, pp. 569–587.

Valentini, F. et al. (Aug. 2014). "Hybrid Vlasov-Maxwell simulations of two-dimensional turbulence in plasmas". In: *Physics of Plasmas* 21.8, 082307, p. 082307. DOI: 10.1063/1.4893301.

van der Holst, B. et al. (Dec. 2010). "A Data-driven, Two-temperature Solar Wind Model with Alfvén Waves". In: *Astrophys. J.* 725.1, pp. 1373–1383. DOI: 10.1088/0004-637X/725/1/1373.

Werner, G. R. et al. (Feb. 2018). "Non-thermal particle acceleration in collisionless relativistic electron-proton reconnection". In: 473.4, pp. 4840–4861. DOI: 10.1093/mnras/stx2530. arXiv: 1612.04493 [astro-ph.HE].

Wiaux, Yves, Laurent Jacques, and Pierre Vandergheynst (2007). "Fast spin±2 spherical harmonics transforms and application in cosmology". In: *Journal of Computational Physics* 226.2, pp. 2359–2371.

Winske, D. and N. Omidi (Jan. 1991). *Hybrid codes: Methods and applications*. Presented at the 4th International School for Space Simulation, Nara, Japan, 1-5 Apr. 1991.

Yee, Kane (May 1966). "Numerical solution of initial boundary value problems involving maxwell's equations in isotropic media". In: *IEEE Transactions on Antennas and Propagation* 14.3, pp. 302–307. ISSN: 0018-926X. DOI: 10.1109/TAP.1966.1138693.

York, James W. (1979). "Kinematics and Dynamics of General Relativity". In: *Sources of gravitational radiation*. Ed. by Larry L. Smarr. Cambridge, UK: Cambridge University Press, pp. 83–126. ISBN: 0-521-22778-X.

Younsi, Ziri et al. (Jan. 2020). "Modelling the polarised emission from black holes on event horizon-scales". In: *Perseus in Sicily: From Black Hole to Cluster Outskirts*. Ed. by Kieechi Asada et al. Vol. 342, pp. 9–12. DOI: `10.1017/S1743921318007263`. arXiv: `1907.09196 [astro-ph.HE]`.

Zhdankin, Vladimir (Dec. 2021). "Particle Energization in Relativistic Plasma Turbulence: Solenoidal versus Compressive Driving". In: 922.2, 172, p. 172. DOI: `10.3847/1538-4357/ac222e`. arXiv: `2106.00743 [astro-ph.HE]`.

Zhdankin, Vladimir et al. (Feb. 2017). "Kinetic Turbulence in Relativistic Plasma: From Thermal Bath to Nonthermal Continuum". In: 118.5, 055103, p. 055103. DOI: `10.1103/PhysRevLett.118.055103`. arXiv: `1609.04851 [physics.plasm-ph]`.

Zhdankin, Vladimir et al. (2019). "Electron and ion energization in relativistic plasma turbulence". In: *Physical review letters* 122.5, p. 055101.

Zlochower, Y. et al. (2005). "Accurate Black Hole Evolutions by Fourth-Order Numerical Relativity". In: *Phys. Rev. D* 72, p. 024021. eprint: `gr-qc/0505055`.